Implications of the Use of Cerium Oxide Nanoparticle Diesel Fuel-Borne Catalysts: From Transformation During Combustion Through Exposure to Plants and Soils

James Glennon Dale

Dissertation submitted to the faculty of the Virginia Polytechnic Institute and State University in partial fulfillment of the requirements for the degree of

Doctor of Philosophy
In
Geosciences

Michael F. Hochella Jr., Chair
Linsey C. Marr
F. Marc Michel
Madeline E. Schreiber
Peter J. Vikesland

March 23rd, 2017
Blacksburg, VA

Keywords: Ceria, cerium oxide, diesel additive, diesel fuel, fuel-borne catalyst, nanomaterials, nanotoxicology

Implications of the Use of Cerium Oxide Nanoparticle Diesel Fuel-Borne Catalysts: From Transformation During Combustion Through Exposure to Plants and Soils

James Glennon Dale

ACADEMIC ABSTRACT

The fate of nanoparticulate cerium oxide from the diesel fuel catalyst Envirox was studied from its presence in the additive to its transformations during combustion through its exposure to plants and soils using a broad range of analytical techniques. Envirox is a fuel-borne catalyst comprised of nanoparticles of cerium oxide suspended in kerosene. The particles suspended in Envirox were confirmed by synchrotron X-ray diffraction, dynamic light scattering, and electron microscopy to be 5-7 nm crystals of CeO_2 present as 15 nm aggregates. Significant changes to the particles were induced by the combustion process, resulting in 50-300 nm euhedral crystals of CeO_2 in the exhaust as discovered using high resolution transmission electron microscopy. Single particle electron diffraction of the emitted cerium oxide particles showed evidence of ordered oxygen vacancies, indicative of a superstructure. Variations in the engine operating load resulted in no significant differences in the emitted cerium oxide particles.

The mobility through soils and impacts on the plant *Brassica napus* (dwarf essex rape) of the emitted cerium oxide were compared to small and large CeO_2 nanoparticles as well as diesel particulate matter emissions with very low cerium. The small CeO_2 nanoparticles exhibited high mobility through soils and significant uptake and translocation in the plants. The large CeO_2 nanoparticles showed extremely low mobility in soils and no significant increase in cerium anywhere in the plants. Cerium emissions from a diesel engine utilizing Envirox was found to have moderate mobility through the soils as well as an increased association with the roots of the plants, though translocation of the cerium into the aboveground biomass was not statistically significant. Despite uptake and translocation of some materials by *B. napus*, exposure to these cerium sources at 100 ppm Ce in the topsoil showed no significant impacts on the growth or overall health of the plants when compared to unexposed control samples.

This dissertation shows that CeO_2 nanoparticles employed as catalysts suspended in diesel fuel are altered during their use resulting in changes to their mobility and interaction upon entering the environment. This dissertation lays the groundwork for a new approach to nanotoxicology.

Implications of the Use of Cerium Oxide Nanoparticle Diesel Fuel-Borne Catalysts: From Transformation During Combustion Through Exposure to Plants and Soils

James Glennon Dale

GENERAL AUDIENCE ABSTRACT

Understanding the environmental impacts – and subsequently the impacts on mankind – of the use of nanomaterials is an enormously complex problem. The bottom-up approach, whereby one can predict impacts from fundamental principals, is not practical because nanotechnology implementation into products is occurring far too rapidly and it is impossible for environmental toxicologists to keep pace. The properties of a nanomaterial are controlled by small changes to its physical/chemical properties that can be tuned to suit many different practical applications. During their use and subsequent release into the natural environment, nanomaterials are exposed to incredibly complex spaces that are capable of modifying the original nanomaterial still further. Thus, the originally produced nanomaterial will continue to evolve, and therefore change in its interaction with biotic and abiotic systems.

In this dissertation, we examine the use of nanoparticulate cerium oxide in fuel-borne catalysts as a case study. As a fuel-borne catalyst, nanoparticulate cerium oxide is employed to reduce carbon dioxide (a greenhouse gas and contributor to global climate change) and particulate matter (a known carcinogen) emissions from combustion in a diesel engine. Fuel-borne catalysts achieve this through the suspension of cerium oxide nanoparticles in the fuel, which go through the combustion process and exit the tailpipe with the rest of the diesel exhaust. Concerns over the emission of this emerging contaminant have resulted in its limited market penetration.

Here we show that the nanoparticulate cerium oxide in fuel-borne catalysts is substantially altered by the combustion process and is emitted as significantly larger particles in the exhaust. We suspected that the emitted cerium oxide would have different behavior in the environment from previously studied, laboratory synthesized cerium oxide nanoparticles. The behavior of emitted cerium oxide was compared with that of laboratory synthesized cerium oxide nanoparticles by exposure to the plant *Brassica napus*. The exposure experiments showed that cerium oxide emitted from the combustion of a fuel-borne catalyst did indeed behave differently in the environment, though none of the exposures proved toxic to the plants at the realistic concentrations utilized in the study.

DEDICATION

To the educators who led me to this moment.

ACKNOWLEDGEMENTS

First and foremost I thank my advisor, Mike Hochella. Without his steadfast support I would have never made it this far. You have been a constant inspiration and I hope that I can continue to reflect what you have taught me. Most of all, thank you for always encouraging me to see this through to the end, through all of the struggle and the hardship, and for trusting in my capabilities even when I did not.

Thank you to Chris Kim, my undergraduate advisor, for engaging me and so many other undergraduates in high quality research and introducing us to cutting edge techniques, intriguing and inspiring us to search for answers.

I thank Linsey Marr for your guidance, expertise, and your consistently concise and direct responses that always provided clarity when needed. To the rest of my committee, Marc Michel, Maddy Schreiber, and Peter Vikesland: Thank you for your interest, poignant questions, and direction over the years that helped steer me to the completion of this project.

I owe Steve Cox a great debt of gratitude for his many hours of getting his hands dirty with me working on the engine. To Nina Vance and Andrea Tiwari, thank you for sharing your wisdom with an atmospheric novice and always pointing me in the right direction.

Amalia Turner, thank you for taking the chance on such an extensive collaboration. It's hard to find a colleague to work so closely with and you have been incredibly generous with both your time and your friendship.

Thanks to Chris Winkler and Steve McCartney for your hours of undocumented support with the instruments at the NCFL. Without both of your support, the users would truly be lost in the dark.

Many thanks go out to so many more: the Greater Hochella Research Group, friends and colleagues through CEINT, and both office and lab mates over the years. Thank you all for your conversations, both scientific and non-scientific; for your friendship, both obligatory and non-obligatory; and for your assistance, both requested and unrequested. Thank you to the Geosciences support staff, the invisible hands behind the scenes keeping everything working.

Thank you to my parents, Glenn and Diane Dale, who have always been supportive of my unusual path. To my brother Matt, thank you for your incredible work ethic, which has occasionally rubbed off on me. Thanks to my dog, Bailey, for taking this cross country journey with me.

Finally I thank my wife, Dr. Sarah Mazza, for her unwavering support in all things. You make me a better scientist and a better person and I'm incredibly fortunate to have you in my life. I look forward to writing our next chapter together.

ATTRIBUTIONS

The work in this dissertation was completed with the help of numerous colleagues. Their contributions are detailed below.

Prof. Michael F. Hochella, Jr. (Dept. of Geosciences, Virginia Tech) is the primary advisor and Committee Chair. He provided guidance and support for all stages of the research.

Prof. Linsey Marr (Dept. of Civil and Environmental Engineering, Virginia Tech) is a committee member and co-principle investigator of the work in Chapter 2. Her expertise on atmospheric chemistry and particle sampling were critical to the success of the work.

Prof. Steve Cox (Dept. of Civil and Environmental Engineering, Virginia Tech) provided technical expertise to the establishing and maintenance of the engine and sampling apparatus.

Prof. Mitsu Murayama (Dept. of Materials Science and Engineering, Virginia Tech) provided his technical expertise on the TEM work for Chapter 3.

Dr. Marina Vance (former post-doc, Dept. of Civil and Environmental Engineering, Virginia Tech) provided insight and support into atmospheric particle sampling for the work in Chapter 2.

Dr. Sayako Inoue (post-doc, Dept. of Geosciences, Virginia Tech) performed the TEM work in Chapter 3.

Amalia Turner (Ph.D. candidate, Duke University) closely collaborated on the work in Chapter 3. She helped design the experiments, conduct day-to-day operations, and aided in the writing. Chapter 3 was successful in large part due to her contributions.

TABLE OF CONTENTS

LIST OF FIGURES

LIST OF TABLES

CHAPTER 1:
Introduction

1.1. SCIENTIFIC RESPONSIBILITY

Science and its resulting technological inventions form the cornerstone of modern civilization. Today we can hardly imagine what it would be like without things such as mobile phones, antibiotics, cars, and computers. Even though scientific progress is the foundation of today's society, science has created problems as well. Numerous examples of the dangers of unfettered implementation of technology have arisen over the last century. Some examples are overt, such as the creation of nuclear weapons, while others are not immediately evident as dangers at the time of their development. Often the latter cases are the result of an attempt to make life easier, such as the liberal application of the insecticide dichlorodiphenyltrichloroethane (DDT) to increase crop yields that was later discovered to be a carcinogen and have widespread environmental impact[1] and originally brought into the public's awareness by the publication of *Silent Spring* in 1962.[2] Many of these scientific mistakes are still in living memory and have had a worldwide impact for decades. In the case of tetraethyllead (TEL), used to increase the octane rating of petroleum fuels, the lead emissions were distributed globally through the atmosphere, eventually being detected in remote locations such as Antarctic snow[3] and Atlantic, Pacific, and Indian Ocean corals.[4] Other examples include ozone layer depletion from the use of chlorofluorocarbon (CFC) propellants[5] and anthropogenic global climate change induced by the release of greenhouse gases primarily from the burning of fossil fuels.[6] So far, all of these examples (except climate change) have displayed one significant commonality: Life on this planet is resilient and provided we recognize the

problem and take action to mitigate the harm, ecosystems can recover[7-9]. The response to these hazards in the past has been just that: a response. In order to maintain the trust of the public – the largest funding source of scientific research – it is the scientific community's responsibility to address potential risks of the technology it develops prior to widespread implementation.

With the acceptance of our responsibility and a renewed focus on preventing the widespread dissemination of new contaminants, we have to ask, "How can we prevent future harm?" It would be a difficult enough proposition to test new materials for toxicological effects on humans, but that would be the tip of the iceberg. Materials as manufactured may be transformed during their use or upon entering the environment, altering their toxicity or bioavailability. In the case of mercury exposure, elemental mercury is toxic but is not readily bioavailable, resulting in a relatively low threat. When mercury in the environment is transformed to methylmercury, the problem is significantly exacerbated by its absorption through the skin, resulting in increased bioaccumulation.[10] Other hazardous materials may be completely incidental to the desired process, such as the case of particulate matter, a carcinogenic and unintentional byproduct of incomplete combustion.[11] Exposure route plays a key role as well. Typical routes to human toxicity include dermal (direct skin contact), ingestion, and inhalation. Each route has its own relevant factors, but in general dermal exposure is considered less hazardous than ingestion, which in turn is considered less hazardous than inhalation due to the relative ease by which toxins can cross important barriers into the body. This is still just the beginning to the nearly infinite number of mechanisms that alter and control a materials potential risk. The environment is a complicated tapestry of interwoven interactions

where science is still trying to identify the threads, operating under the impression that given understanding of enough threads we will be able to see the whole picture. While this approach might work eventually, it is a daunting task ill-suited to the determination of the safety of new products as they arise.

This returns us to the question of how we broach the problem of identifying and testing potential threats to human and environmental health. By utilizing a single emerging contaminant as a test case, we will examine the process by which we identify potential health threats. As we will see, there is no one-size-fits-all approach to such complex questions. Instead, unique yet informed procedures must be developed on a case-by-case basis. While this body of work is not conclusive on its own, it substantially furthers our understanding of a single system and simultaneously establishes a framework for future studies of emerging contaminants, particularly within the field of nanotoxicology.

1.2. A FIELD OF EMERGING CONTAMINANTS

The field of nanoscience has grown rapidly over the last several decades since Richard Feynman's 1959 lecture *There's Plenty of Room at the Bottom* laid out the physicist's vision for what the field might become.[12] The study of the very small, typically defined as between 1 and 100 nm, promises revolutionary advances in nearly every field of science. In this size regime many materials exhibit novel properties due to their very high surface to bulk ratio and quantum mechanical effects. These properties can often be altered by changes to the material's physicochemical characteristics such as its size, shape, surface coating, charge, composition, etc. With a high degree of control

over the manufacturing process, nanomaterials can be synthesized to suit applications in nanomedicine, nanoelectronics, nanoremediation, nanolithography, and nanorobotics, to name a few. Nanoscience promises the synthesis of a vast number of novel materials, each with unique properties designed for a specific function. At the end of their useful life, like all waste, these nanomaterials will inevitably be released into the environment as emerging contaminants.

During a nanomaterial's useful life and subsequent disposal, it will likely undergo transformations induced by its changing environment. As noted previously, nanomaterial properties are highly sensitive to their physicochemical characteristics, thus the changes incurred could be expected to alter properties relevant to threat assessment. Additionally, in the case of a nanomaterial engineered to address health hazards, its intended use must be weighed against the threat it poses as an emerging contaminant. In order to make informed decisions regarding the use of novel nanomaterials, we can use the traditional toxicological principle

$$Risk = Probability \times Impact$$

to compare the risk of the use of a new material to not using that material. This simple mantra of toxicology defines risk as the probability that something might occur times its impact if it were to occur.

One nanomaterial has drawn much attention over the last couple decades: cerium oxide (CeO_2). Non-nanoscale or 'bulk' cerium oxide (ceria) has proven to be of very low toxicity with adverse health responses only seen in extremely high dose exposures.[13] Nanoscale cerium oxide (n-ceria) has found its way into numerous products and applications for a variety of purposes, taking advantage of various properties of the

nanomaterial. For example, n-ceria has found uses as polishing agents,[14] UV absorbent,[15] ceramic electrolytes,[16] and antioxidants.[17] One particularly intriguing use of n-ceria is as a fuel-borne catalyst (FBC). In this application, n-ceria promotes a more complete combustion of diesel fuel resulting in increased fuel efficiency and decreased diesel particulate matter (DPM) emissions.[18] It is believed that the high oxygen storage capacity of n-ceria – made possible by the conservation of its face-centered cubic crystal structure even when present as a nonstoichiometric oxide – enables this catalytic function.[19, 20] FBCs containing n-ceria provide an interesting test case: should we allow the widespread implementation of a nanomaterial to be employed in an effort to curb CO_2 and carcinogenic DPM emissions, replacing these emissions with the release of an emerging contaminant?

Fundamental studies of n-ceria properties and toxicity have been claiming to work on exactly that question for over a decade but we still have no definitive answer. Regulations in the United States remain in limbo, where FBCs containing n-ceria are prohibited by the EPA under the Clean Air Act for on-road use yet they seem to be implemented in some construction and mining sites. At the outset of my dissertation we were no closer to a definitive answer on whether or not the use of n-ceria FBCs to curb CO_2 and DPM emissions outweighed the risk of the emission of n-ceria, an emerging contaminant. Toxicology appeared to have a handle on the probability and impact of CO_2 and DPM emissions, but conclusions about n-ceria seemed hard to come by. Studies had shown the effects of n-ceria on plants and animals to range from detectably toxic[21, 22] to relatively benign at a broad range of concentrations.[23, 24] In the field of nanomedicine,

n-ceria has been probed for its use as a cancer treatment.[25] How could this single material be both beneficial and toxic?

1.3. THE NEED FOR CHARACTERIZATION

Nanoscience is a catch-all field of study based on size rather than the traditional scientific discipline boundaries. This enables nanoscience to transcend typically large barriers between disciplines such as physics, chemistry, materials science, and engineering to solve problems and answer questions. Unfortunately this also means that nanoscience lacks coherency amongst its researchers which has led to inconsistencies in the characterization of nanomaterials. As discussed above, subtle changes in a nanomaterial's characteristics can yield significant differences in displayed properties. This indicates the importance of full characterization of nanomaterials when conducting experiments. Based on the specific use of n-ceria FBCs – as surfactant-stabilized nanoparticulate cerium oxide suspended in diesel fuel during combustion in an engine – I hypothesized that significant transformations of the n-ceria was likely to occur during its use. It was unlikely that no transformation of the n-ceria would occur given that the particles were undergoing combustion, which I anticipated would result in an alteration to the surfactant coating at a minimum. In addition, the cerium particles were expected to be associated with the carbon in the particulate matter released alongside them in the exhaust.

In the second chapter of my dissertation, I investigate the transformation of cerium oxide nanoparticles in an FBC by characterizing the cerium before and after the combustion in a diesel engine. Understanding the phase of the emitted cerium would aid

in (1) determining the characteristics that control emitted cerium's behavior, (2) identifying relevant toxicological studies performed in the past, (3) modeling the dispersion of cerium from the use of FBCs, and (4) informing future studies on what particles would be most realistic in order to better target research regarding the health and safety of n-ceria FBC use. Previous studies of n-ceria FBCs had focused on the effects of these FBCs on known contaminants such as CO_2, DPM, and NO_x [26-28]. Several studies have examined the cerium emissions, though they were not conclusive. These studies lacked independent and direct measurement of cerium particle sizes [29, 30], significantly exceeded the manufacturer's dosage rate [30, 31], or had low quality transmission electron microscopy (TEM) imaging performed [31, 32].

Our work began with the selection and acquisition of a commercial n-ceria FBC, ensuring our results would be immediately relevant for at least a single product on the consumer market. Envirox, manufactured by Energenics Ltd., was selected of the three available n-ceria FBCs on the market due to it being the most widely used and previously studied of the options. The n-ceria found in Envirox was independently verified to be sub-10 nm CeO_2 crystals using synchrotron X-ray diffraction and high resolution (HR)TEM. Under the advisement of Drs. Linsey Marr and Steve Cox, a military surplus diesel engine/generator combination (genset) was purchased and we established a housing site for the setup in the yard of the Structures and Materials Laboratory on Plantation Road. The genset was restored to operating condition and a newly designed exhaust sampling apparatus was installed for the collection of combustion products directly from the exhaust stream. The sampled exhaust was diluted with compressed

breathing air (replicating the exhaust encountering ambient conditions upon exiting the tail pipe) and then sent to various instruments for sample preparation or direct analyses.

Exhaust samples from the engine were sent through a cascade impactor where they were size fractionated into three bins and impacted onto TEM grids. TEM analysis showed that the cerium particles were emitted as much larger 50-300 nm near-spherical single crystals of CeO_2 that showed evidence of ordered oxygen vacancies. The operating load of the engine appeared to have very little impact on the emission and transformation of the cerium particles. Surface coatings were inconsistently observed on the emitted cerium particles, being about 3-7 nm in thickness when they were present. Nearly all particles were discovered associated with turbostratic graphite (graphite composed of misaligned sheets). As we hypothesized, our findings provide evidence of dramatic changes to the n-ceria in FBCs occurring during combustion. Therefore it is improbable that the emitted cerium will interact in the environment in a manner similar to laboratory synthesized n-ceria like the materials previously used in toxicological studies. This work, titled "Transformation of Cerium Oxide Nanoparticles from a Diesel Fuel Additive during Combustion in a Diesel Engine" was published in *Environmental Science and Technology* in January 2017.

1.4. REALISTIC EXPOSURES

In Chapter 3 of my dissertation I investigate the transportation, bioavailability, translocation, and general toxicity of the cerium found in diesel emissions and compare it to both small (3-5 nm) and large (120-250 nm) n-ceria as well as low-cerium DPM generated without the n-ceria FBC. The small and large NPs were purchased from

chemical supply companies, are typical of other nanotoxicity studies, and resemble the NPs found in the additive and exhaust, respectively. The low-cerium PM was used to delineate the effects of the cerium in PM from the PM itself. Prior studies on the toxicity of n-ceria have made too many compromises on environmental relevance to be confident in the applicability of their results. The most obvious issue has been the particles themselves. As we discovered in Chapter 2, the particles found in the n-ceria FBC Envirox are significantly altered yet most nanotoxicological studies have utilized a range of sizes and surfactants that are not representative of the polydisperse and complex particles emitted in the exhaust. Many studies have performed hydroponic exposures which are likely to overestimate exposure and bioavailability. Exceedingly high concentrations well beyond those expected in realistic scenarios of 1000 ppm Ce or more are routinely used in order to induce toxicological effects in toxicity studies. All of these issues have made it difficult to extrapolate the findings of n-ceria nanotoxicity studies to the n-ceria FBC use case.

This study placed heavy emphasis on environmental relevance beginning with the primary exposure material collected from the exhaust of our genset operating with the n-ceria FBC Envirox. The plant *Brassica napus* (dwarf essex rape) was selected due to its use as a source of cooking oil and cattle silage, documented metal accumulation, rapid growth, and common use in toxicological experiments. Based on the size of the emitted particles, atmospheric dry deposition modeling predicted worst-case scenarios in urban environments of roughly 10 ppm Ce deposited annually to the roadside topsoil. Thus the exposures consisted of a topsoil addition of 100 ppm Ce increase over the background, while the low-cerium PM control dosage matched the total mass of the cerium PM

dosage. Composite water samples were collected at four intervals over the course of the 32 day exposure. At the completion of the exposure experiment, soil cores and plant materials were harvested for analysis of cerium concentration and TEM imaging.

The plants harvested at the conclusion of the experiment were examined and weighed. No visible differences were observed in leaf count or size and no evidence of spotting or discoloration existed. The dry masses of the plants, separated into above and below ground biomass, showed no statistical difference between any of the exposures or controls. Based on the masses and visual observations, it was concluded that exposure to cerium did not induce serious toxicological effects in *B. napus* over the course of the experiment. Cerium concentrations measured in the drainage water show that the small NPs are highly mobile while the large NPs are nearly completely immobile. The ceria emitted in the PM is mobile, but at a much lower rate than the small NPs. These trends appear in the soil centrations, with the small NPs showing signs of increased cerium concentration in the bottom of the soil and a slight depletion in the top soil, while the large NPs do not seem to travel at all. The ceria in the PM once again fall somewhere in between with some evidence of cerium increase in the soils below the top, though most of the cerium remains in the topsoil. Using root cerium concentrations as a proxy for bioavailability, the samples once again followed the mobility trends with small NPs being the most bioavailable, ceria in PM showing increased bioavailability, and large NPs at control levels. Aboveground biomass Ce concentrations represented translocated cerium and once again followed the mobility trends. The translocation of cerium decreased from small NPs to ceria in PM to large NPs which were equivalent to the controls. TEM

analysis has been unsuccessful in locating cerium in the roots of the samples. This work is currently in preparation for publication in *Environmental Science: Nano*.

While the sum of this work does not yet answer the broad question of whether or not it is safe to use n-ceria FBCs, it has moved us significantly closer to making an informed decision on a difficult and complex topic. We have shown that ceria nanoparticles from fuel-borne catalysts such as Envirox transform during their use and subsequent release into the environment in ways that impact their mobility, bioavailability, translocation, and therefore their toxicity. Through our exposure experiment we discovered that neither small nor large ceria NPs purchased from chemical supply companies adequately reproduce the trends of ceria in PM. We also saw that none of these exposures seemed to have a significant toxicological effect on the plant *B. napus* when exposed at realistic concentrations through a simulated atmospheric deposition exposure route. Still, this work is limited to a single plant and examined few toxicological endpoints and therefore is not sufficient to come to broad conclusions on the question of safety of n-ceria FBCs. Instead, this work comprises the core of a body of knowledge on the real world impacts of n-ceria emissions from FBC use on which others can build. It also establishes a framework by which researchers should identify emerging contaminants as they are expected to be found at the time of exposure, determine probable concentrations and exposure pathways, and carry out realistic experiments in order to answer difficult questions even in the absence of clear mechanistic understanding.

During my tenure at Virginia Tech, I collaborated on several projects on a wide range of topics. Three of these projects have resulted in publications, which are supplied

in the Appendices. Appendix A was a study led by Rui Ma, then working under Dr. Greg Lowry at Carnegie Mellon University, on the sulfidation of copper oxide nanoparticles. I provided TEM work and independent analysis that would corroborate their findings, showing that copper oxide NPs are rapidly transformed to copper sulfide at ambient temperatures under sulfate-reducing conditions. This work was published in *Environmental Science: Nano*. Appendix B is a study in which I worked with Drew Muscente, Dr. F. Marc Michel, and Dr. Shuhai Xiao to provide new insight into what were previously thought to be sponge spicule fossils. I collected and analyzed the synchrotron X-ray fluorescence (XRF) maps and X-ray absorption near edge structure (XANES) spectra. From this and other data, Drew concluded that these fossils could not be sponge spicules and instead offered several new hypotheses. The study was published in *Precambrian Research*. Appendix C is a study in which I collaborated with Astrid Avellan and John Stegemeier, working under Dr. Greg Lowry at Carnegie Mellon University, in order to characterize mercury at various points during petroleum refinement. I performed TEM analysis including energy dispersive spectroscopy (EDS) mapping, supporting the findings that mercury from oil processing plants should be treated as Hg-S compounds, predominately metacinnabar (ß-HgS) and mercury glutathione ($Hg(SR)_2$). This manuscript has been submitted to *Environmental Science and Technology*.

1.5 REFERENCES

1. Perfect, J., The environmental impact of DDT in a tropical agro-ecosystem. *Ambio* **1980**, 16-21.

2. Carson, R., Silent Spring. Greenwich, Connecticut. In Fawcett Publications: 1962.

3. Boutron, C. F.; Patterson, C. C., Relative levels of natural and anthropogenic lead in recent Antarctic snow. *Journal of Geophysical Research D* **1987,** *92*, (D7), 8454-8464.

4. Shen, G. T.; Boyle, E. A., Lead in corals: reconstruction of historical industrial fluxes to the surface ocean. *Earth and Planetary Science Letters* **1987,** *82*, (3-4), 289-304.

5. Molina, M. J.; Rowland, F. S., Stratospheric sink for chlorofluoromethanes: chlorine atom-catalysed destruction of ozone. *Nature* **1974,** *249*, (28), 810-812.

6. Baes, C.; Goeller, H.; Olson, J.; Rotty, R., Carbon Dioxide and Climate: The Uncontrolled Experiment: Possibly severe consequences of growing CO 2 release from fossil fuels require a much better understanding of the carbon cycle, climate change, and the resulting impacts on the atmosphere. *American Scientist* **1977,** *65*, (3), 310-320.

7. Lichter, J.; Caron, H.; Pasakarnis, T. S.; Rodgers, S. L.; Squiers Jr, T. S.; Todd, C. S., The ecological collapse and partial recovery of a freshwater tidal ecosystem. *Northeastern Naturalist* **2006,** *13*, (2), 153-178.

8. Wu, J.; Boyle, E. A., Lead in the western North Atlantic Ocean: completed response to leaded gasoline phaseout. *Geochimica et Cosmochimica Acta* **1997,** *61*, (15), 3279-3283.

9. Schrope, M., Successes in fight to save ozone layer could close holes by 2050. In Nature Publishing Group: 2000.

10. Morel, F. M.; Kraepiel, A. M.; Amyot, M., The chemical cycle and bioaccumulation of mercury. *Annual review of ecology and systematics* **1998,** *29*, (1), 543-566.

11. Dickhut, R.; Canuel, E.; Gustafson, K.; Liu, K.; Arzayus, K.; Walker, S.; Edgecombe, G.; Gaylor, M.; MacDonald, E., Automotive sources of carcinogenic polycyclic aromatic hydrocarbons associated with particulate matter in the Chesapeake Bay region. *Environmental Science & Technology* **2000,** *34*, (21), 4635-4640.

12. Feynman, R. P., There's plenty of room at the bottom. *Engineering and science* **1960,** *23*, (5), 22-36.

13. Graca, J. G.; Davison, F. C.; Feavel, J. B., Comparative Toxicity of Stable Rare Earth Compounds: II. Effect of Citrate and Edetate Complexing on Acute Toxicity in Mice and Guinea Pigs. *Archives of Environmental Health: An International Journal* **1962,** *5*, (5), 437-444.

14. Tsai, M.-S., Powder synthesis of nano grade cerium oxide via homogenous precipitation and its polishing performance. *Materials Science and Engineering: B* **2004,** *110*, (2), 132-134.

15. Yabe, S.; Sato, T., Cerium oxide for sunscreen cosmetics. *Journal of Solid State Chemistry* **2003,** *171*, (1), 7-11.

16. Chockalingam, R.; Amarakoon, V. R.; Giesche, H., Alumina/cerium oxide nano-composite electrolyte for solid oxide fuel cell applications. *Journal of the European Ceramic Society* **2008,** *28*, (5), 959-963.

17. Lee, S. S.; Song, W.; Cho, M.; Puppala, H. L.; Nguyen, P.; Zhu, H.; Segatori, L.; Colvin, V. L., Antioxidant properties of cerium oxide nanocrystals as a function of nanocrystal diameter and surface coating. *ACS nano* **2013,** *7*, (11), 9693-9703.

18. Park, B.; Donaldson, K.; Duffin, R.; Tran, L.; Kelly, F.; Mudway, I.; Morin, J.-P.; Guest, R.; Jenkinson, P.; Samaras, Z., Hazard and risk assessment of a nanoparticulate cerium oxide-based diesel fuel additive-a case study. *Inhalation toxicology* **2008,** *20*, (6), 547-566.

19. Ricken, M.; Nolting, J.; Riess, I., SPECIFIC-HEAT AND PHASE-DIAGRAM OF NONSTOICHIOMETRIC CERIA (CEO2-X). *Journal of Solid State Chemistry* **1984,** *54*, (1), 89-99.

20. Laachir, A.; Perrichon, V.; Badri, A.; Lamotte, J.; Catherine, E.; Lavalley, J. C.; El Fallah, J.; Hilaire, L.; Le Normand, F.; Quéméré, E., Reduction of CeO2 by hydrogen. Magnetic susceptibility and Fourier-transform infrared, ultraviolet and X-ray photoelectron spectroscopy measurements. *Journal of the Chemical Society, Faraday Transactions* **1991,** *87*, (10), 1601-1609.

21. Arnold, M.; Badireddy, A.; Wiesner, M.; Di Giulio, R.; Meyer, J., Cerium oxide nanoparticles are more toxic than equimolar bulk cerium oxide in Caenorhabditis elegans. *Archives of environmental contamination and toxicology* **2013,** *65*, (2), 224-233.

22. García, A.; Espinosa, R.; Delgado, L.; Casals, E.; González, E.; Puntes, V.; Barata, C.; Font, X.; Sánchez, A., Acute toxicity of cerium oxide, titanium oxide and iron oxide nanoparticles using standardized tests. *Desalination* **2011,** *269*, (1), 136-141.

23. Colon, J.; Hsieh, N.; Ferguson, A.; Kupelian, P.; Seal, S.; Jenkins, D. W.; Baker, C. H., Cerium oxide nanoparticles protect gastrointestinal epithelium from radiation-induced damage by reduction of reactive oxygen species and upregulation of superoxide dismutase 2. *Nanomedicine: Nanotechnology, Biology and Medicine* **2010,** *6*, (5), 698-705.

24. Hirst, S. M.; Karakoti, A.; Singh, S.; Self, W.; Tyler, R.; Seal, S.; Reilly, C. M., Bio-distribution and in vivo antioxidant effects of cerium oxide nanoparticles in mice. *Environmental toxicology* **2013,** *28*, (2), 107-118.

25. Wason, M. S.; Zhao, J., Cerium oxide nanoparticles: potential applications for cancer and other diseases. *Am J Transl Res* **2013,** *5*, (2), 126-131.

26. Kittelson, D. B., Engines and nanoparticles: a review. *Journal of aerosol science* **1998,** *29*, (5), 575-588.

27. Mayer, A.; Czerwinski, J.; Matter, U.; Wyser, M.; Scheidegger, G.; Kieser, D., VERT: Diesel nano-particulate emissions: Properties and reduction strategies. *SAE Technical Paper* **1998,** *980839*, 12.

28. Gandhi, H.; Piken, A.; Shelef, M.; Delosh, R., Labratory Evaluation of Three-Way Catalysts. *SAE Technical Paper* **1976,** *760201*.

29. Skillas, G.; Qian, Z.; Baltensperger, U.; Matter, U.; Burtscher, H., The influence of additives on the size distribution and composition of particles produced by diesel engines. *Combustion Science and Technology* **2000,** *154*, 259-273.

30. Okuda, T.; Schauer, J. J.; Olson, M. R.; Shafer, M. M.; Rutter, A. P.; Walz, K. A.; Morschauser, P. A., Effects of a Platinum− Cerium Bimetallic Fuel Additive on the Chemical Composition of Diesel Engine Exhaust Particles. *Energy & Fuels* **2009,** *23*, (10), 4974-4980.

31. Jung, H. J.; Kittelson, D. B.; Zachariah, M. R., The influence of a cerium additive on ultrafine diesel particle emissions and kinetics of oxidation. *Combustion and Flame* **2005,** *142*, (3), 276-288.

32. Gantt, B.; Hoque, S.; Fahey, K. M.; Willis, R. D.; Delgado-Saborit, J. M.; Harrison, R. M.; Zhang, K. M.; Jefferson, D. A.; Kalberer, M.; Bunker, K. L., Factors Affecting the Ambient Physicochemical Properties of Cerium-Containing Particles Generated by Nanoparticle Diesel Fuel Additive Use. *Aerosol Science and Technology* **2015,** *49*, (6), 371-380.

CHAPTER 2:

Transformation of Cerium Oxide Nanoparticles from a Diesel Fuel Additive during Combustion in a Diesel Engine

James G. Dale,*,† Steven S. Cox,‡ Marina E. Vance,‡ Linsey C. Marr,‡ and Michael F. Hochella, Jr.†,§

†The Center for NanoBioEarth, Department of Geosciences, Virginia Tech, Blacksburg, Virginia 24061, United States

‡Department of Civil and Environmental Engineering, Virginia Tech, Blacksburg, Virginia 24061, United States

§Geosciences Group, Energy and Environment Directorate, Pacific Northwest National Laboratory, Richland, Washington 99352, United States

Reprinted with permission from *Environmental Science and Technology*, **2017**, 51 (4), pp 1973-1980.

2.1. ABSTRACT

Nanoscale cerium oxide is used as a diesel fuel additive to reduce particulate matter emissions and increase fuel economy, but its fate in the environment has not been established. Cerium oxide released as a result of the combustion of diesel fuel containing the additive Envirox, which utilizes suspended nanoscale cerium oxide to reduce particulate matter emissions and increase fuel economy, was captured from the exhaust stream of a diesel engine and was characterized using a combination of bulk analytical techniques and high resolution transmission electron microscopy. The combustion process induced significant changes in the size and morphology of the particles; ~15 nm aggregates consisting of 5 to 7 nm faceted crystals in the fuel additive became 50 to 300 nm, near-spherical, single crystals in the exhaust. Electron diffraction identified the original cerium oxide particles as cerium (IV) oxide (CeO_2, standard FCC structure) with no detectable quantities of Ce(III), whereas in the exhaust the ceria particles had

additional electron diffraction reflections indicative of a CeO_2 superstructure containing ordered oxygen vacancies. The surfactant coating present on the cerium oxide particles in the additive was lost during combustion, but in roughly 30% of the observed particles in the exhaust, a new surface coating formed, approximately 2 to 5 nm thick. The results of this study suggest that pristine, laboratory-produced, nanoscale cerium oxide is not a good substitute for the cerium oxide released from fuel-borne catalyst applications and that future toxicity experiments and modeling will require the use/consideration of more realistic materials.

2.2. INTRODUCTION

In recent years, the explosive growth of the nanotechnology sector has come under scrutiny. Like many scientific breakthroughs, nanotechnology comes with risks of adverse effects to both humans and the environment. This is made more threatening by nanoparticle mobility, for example nanomaterials remaining suspended in the atmosphere over extended periods of time, and entering biological systems with relative ease. The utilization of nanomaterials in commercial products can provide great advantages, but it is important to understand the implications that the use of these materials will have on both human and environmental health before implementation and broad commercial acceptance. The fate, transport, and potential biotoxicity of nanomaterials is controlled by a variety of factors including (but not limited to): size, shape, chemical composition and atomic structure, surface coatings, and surface charge,[1] requiring the careful characterization of each material and product. To add to the complexity of the situation, the nanomaterial in question may be ephemeral as a result of the properties of the

nanomaterial itself, its particular environment, or both. Given all of these complicating factors, determining the fate of nanomaterials can be very difficult to predict. A classic example of this was reported by Kim et al.[2] who discovered that silver nanoparticles, sometimes used as an antimicrobial agent in clothing which can end up in wastewater treatment plants after laundering, is transformed to silver sulfide nanoparticles during sewage sludge formation. With the large variability in commercially employed nanomaterials and the wide range of factors controlling their fate, characterization of nanomaterials at various stages of their life cycles has become increasingly important.[3]

Cerium (di)oxide (ceria) nanoparticles (n-ceria) have found uses in a large number of highly diverse applications including polishing agents in the glass industry,[4] ceramic electrolytes in solid oxide fuel cells,[5] antioxidant agents in biomedical applications,[6, 7] and catalysts in diesel fuel.[8] The variety of uses is indicative of the many useful properties of cerium oxide. For example, when employed as a diesel fuel catalyst, n-ceria is used for its high oxygen storage capacity[9] and low activation energy for redox activity.[9] For this purpose, sub-10 nm ceria particles are ideal due to their high surface area (and therefore reactive sites) as well as maintaining their suspension in diesel fuel.[10] In this application, n-ceria particles are functionalized with a surfactant to prolong their suspension before combustion in a diesel engine, where they are exposed to exceedingly high temperatures and pressures (up to 2300 °C[11] and 200 bars[12]) followed by their emission into the environment as part of the diesel exhaust. Fuel additives containing n-ceria have been shown to significantly decrease carbonaceous particulate matter (PM) emissions while increasing fuel economy[13] by decreasing the light-off temperature of

carbon soot and promoting more complete (efficient) fuel burning, enabling users to meet increasingly strict emissions regulations.

Through personal communication with the manufacturer of the diesel fuel-borne catalyst (FBC) Envirox, their product has been consistently utilized in approximately 1% of diesel fuel in the EU. Based on data from the consulting group Wood Mackenzie, FuelsEurope reported that the EU consumed nearly 200 million metric tons of diesel fuel to meet their on-road demand in 2014.[14] At the 1% market penetration estimated and using the manufacturer's recommended concentration of 5 ppm Ce, this would result in the use of approximately 10 metric tons of cerium in the form of diesel FBCs across the EU annually. According to BP's Statistical Review, in 2015 the EU accounted for 14% of worldwide diesel consumption.[15] If one extrapolates these values to worldwide consumption, roughly 70 million metric tons of Ce initially present in nanoparticulate form could be emitted annually into our atmosphere. This scenario assumes that the mass of cerium emitted from an engine is equal to the mass put into the engine, though some studies indicate that the inclusion of a diesel particulate filter (DPF) in the exhaust stream may substantially reduce the emission of cerium used as a FBC.[16] Unfortunately the use of DPFs is not yet ubiquitous and their efficacy decreases with particle size beginning below 50 nm.[17] These values do not account for off-road uses (very likely a significant but unknown value) or the market share of similar products such as Eolys and Platinum Plus.

While many studies have characterized changes to the particulate matter and exhaust gases induced by ceria-based FBCs,[18-23] far fewer studies have focused on the fate of the cerium in the emissions and even less frequently is this paired with characterization of the

cerium as it is found in the additive. Skillas et al. determined that the bulk of cerium is released in the sub-50 nm size range.[24] However, their work provides no information about the specific additive used other than the concentration of cerium they used and it relies solely on bulk techniques. Jung et al. positively identified ceria in the exhaust stream of an engine burning the n-ceria catalyst Eolys DPX-9, but the amount of n-ceria added to the fuel was four times higher than recommended by the manufacturer.[25] Their results indicate that cerium is released as nanoparticles about 5 to 10 nm in diameter attached to aggregates 40 to 100 nm in size. Okuda et al. examined Platinum Plus, a bimetallic FBC comprised of platinum and cerium, and reported that cerium accounted for 10% of the $PM_{2.5}$ (particulate matter less than 2.5 microns in diameter) when the fuel was dosed at 40 ppm cerium (about seven times the manufacturer's recommended dose).[26] Further characterization by size showed that the cerium was predominantly found in the <250 nm size range (which constitutes a single size bin in their study) and rapidly dropped off with increasing size. Most recently, Gantt et al. used electron microscopy to characterize cerium emissions from a small engine utilizing Envirox.[27] They found that about 40% of the cerium particles were associated with micron-sized soot particles, the remainder of which were emitted as individual particles. The authors also report that the cerium particles were mostly about 75 nm, closely matching their predictions from a previous modeling paper,[20] but it is unknown how representative this size is in the absence of information about the number of particles examined. Therefore, while some characterization information of the combustion products of cerium-based FBCs exist in the literature, it is somewhat limited in scope and rarely includes

characterization of the uncombusted additive ceria which may, at least in part, account for the variations in results.

Toxicological studies indicate that cerium oxide's environmental and biological reactivity can be either beneficial,[28] toxic,[29] or have no apparent effect[30] depending on its physicochemical properties. The dearth of characterization information on environmentally relevant n-ceria is compounded by an underreporting of these properties in toxicological studies, rendering their findings impractical for predicting potential hazards.[31] In many nanotoxicity studies, characterization of the nanoparticles is typically inadequate and the particles themselves are not representative of what is expected to be released by the use of n-ceria containing products.[32] Detailed characterization of environmentally relevant n-ceria is needed to support studies of its toxicity and environmental impacts.

The objective of this research was to carefully characterize the transformation that n-ceria undergoes during combustion as a diesel fuel additive by closely examining its initial and terminal states. The cerium-bearing particles in the fuel additive were analyzed by transmission electron microscopy, dynamic light scattering, synchrotron X-ray diffraction, and inductively coupled plasma atomic emission spectroscopy in order to determine their size, morphology, crystallinity, chemical composition, and in-situ aggregation state. Particles in the exhaust were captured and analyzed by transmission electron microscopy and associated techniques to characterize these same physical and chemical traits. Variations in particle characteristics were also compared with engine operating conditions (a proxy for driving conditions). Results of this research will

contribute to relevant environmental and toxicological predictions surrounding the use of n-ceria.

2.3. MATERIALS AND METHODS

The work herein examines a single consumer product, Envirox, and details the transformation of ceria throughout this product's use. Envirox was selected due to its proven efficacy at reducing PM emissions and increasing fuel economy[13], as well as its wide implementation throughout Europe (particularly in London where an entire bus fleet adopted the additive). In contrast, in the United States n-ceria fuel additives are heavily regulated and limited to off-road use (e.g., farming, construction, and recreation). In this study, combustion of the n-ceria additive, diluted into diesel fuel at the manufacturer's recommended dose (1:4,000), was performed using a Kubota diesel generator (also known as a genset) in order to collect combustion products for characterization.

2.3.1. Diesel fuel additive

An independent confirmation of the properties of the cerium oxide particles contained within Envirox was performed through the combination of synchrotron X-ray diffraction (XRD), dynamic light scattering (DLS), and imaging using a transmission electron microscope (TEM). No sample preparation was required for the XRD, though a sample of diesel fuel was analyzed as a matrix blank to be subtracted from the background of the fuel/catalyst mixture data. Samples for DLS had to be diluted 10-fold due to their high concentration of suspended particles. The dilution was performed using hexane, a major component of the kerosene suspension matrix in Envirox. TEM analysis utilizes delicate equipment operating under high vacuum, necessitating the removal of the liquid hydrocarbon matrix. This removal was performed by diluting a sample of the additive in

hexane (1:10), adding the dilution dropwise to a SiN thin-film TEM grid, baking the grid in a vacuum oven at 80 °C and 0.033 atm overnight, and finally plasma cleaning the grid under high vacuum for 2 min. With temperatures well below the melting point of cerium oxide (2400 °C), the TEM sample preparation was not expected to cause any significant changes to the particles beyond aggregation and no evidence of alterations was observed in the TEM when compared with the results of the additional analytical techniques. The total concentration of cerium in the additive was determined by digesting 500 μL of Envirox in 20 mL of aqua regia at reflux for two hours before filtration by a 0.20 μm polycarbonate filter and dilution to 50 mL in preparation for analysis by ICP-AES. Analytical instrument models and additional details appear in the Supporting Information.

2.3.2. Diesel engine

The diesel engine used in this study was selected on the basis of several criteria: it had to be stationary, its size had to be comparable to that of an engine that would be found in a vehicle, and the load applied to the engine had to be adjustable. A Kubota V3300 diesel genset, combining a 32 kW (43 HP), 4-cylinder, turbocharged diesel engine with a 28 kW (38 HP) generator, met the requirements and was selected for use in this study. The engine operated at a fixed 1800 rpm with a manufacturer-stated power efficiency of 90%. The generator was connected to six 5600 W, 240 V industrial space heaters, enabling an electrical load to be applied to the engine by operating the space heaters in sequence from 0% (idle) to 81% actual load (Supplementary Table 2.1). The genset was housed in a shed to protect it and its operators from the weather while the exhaust was piped outside of the shelter via standard 2 inch (5.1 cm) OD steel exhaust pipe. No DPF

was used in this study due to the likelihood that the use of n-ceria FBCs will not come with the requirement of the use of a DPF. Standard EPA number 2 ultra-low sulfur diesel fuel (typical on-road diesel fuel available at gas stations) and 10W-30 lubricating oil were used for all experiments.

2.3.3. Characterization of the engine exhaust

The exhaust was sampled from two ports located 111.8 and 127.7 cm downstream of the engine's outlet. A piece of stainless steel tubing, 0.3175 cm OD, 25.4 cm long, with a 90-degree curve, was passed through the port and faced upstream to allow for isokinetic sampling of the exhaust. The exhaust was cooled and diluted to within the operating range of the gas-sampling instruments with air from a compressed gas cylinder at a ratio between 17:1 and 20:1 to a final flow rate of 17-20 L min^{-1}. Comparable dilution ratios have been used in other studies in order to condense and nucleate particles in a similar fashion to exhaust exiting the tail pipe and encountering ambient conditions.[33] The diluted exhaust then entered a Teflon sampling manifold where instrumentation siphoned off gas flow for analysis while simultaneously venting excess flow.

A three-stage cascade impactor (MPS-3, California Measurements, Sierra Madre, CA) was used to collect aerosols onto TEM grids in the following size ranges: 50 – 300 nm, 300 – 2,000 nm, and > 2,000 nm in aerodynamic diameter. Aerosol size distributions were measured in real time using a scanning mobility particle sizer (SMPS 3936, TSI, Shoreview, MN) for particles 4-750 nm in mobility diameter and an aerodynamic particle sizer (APS 3321, TSI, Shoreview, MN) for particles 500 nm-20 μm in aerodynamic diameter.

2.3.4. Electron microscopy analyses

Exhaust samples were extensively investigated by environmental scanning electron microscopy (ESEM) and TEM in order to locate and identify cerium-bearing particles, to measure the size distribution and the average particle size of cerium-bearing particles, to determine the crystallinity and structure of the cerium-bearing particles, and to describe other important features observed during analysis, such as shape and aggregation state. Exhaust particles were collected from the diluted exhaust (described above) onto 200 mesh lacey carbon gold or copper grids. Screening for Ce was performed on a FEI Quanta 600 field emission ESEM operating at 30 keV in backscatter mode to provide (Z)-contrast imaging. Bright spots in backscatter mode indicating the presence of heavy elements were analyzed with energy dispersive X-ray spectroscopy (EDS) to confirm the presence of cerium. Grids were then transferred to a TEM, either a JEOL 2100 or a FEI Titan 300, for further characterization of particles. Analysis on the JEOL 2100, operating at 200 keV, included high resolution (HR) imaging, selected area electron diffraction (SAED), and EDS mapping. The Titan, operating at 300 keV and capable of a smaller probe size, allowed for greater resolution of EDS and dark field (DF) imaging.

2.4. RESULTS AND DISCUSSION

2.4.1. Characterization of Envirox

Cerium oxide particles in Envirox were characterized by electron microscopy. Bright field transmission electron micrographs (Figure 2.1a) revealed that the cerium oxide particles are slightly elongated, faceted polyhedra between 5 to 7 nm along their long axis and 3 to 5 nm along their short axis. The particles exhibit lattice fringes, indicating that they are crystalline. A fast Fourier transform (FFT) of the micrographs produced

diffraction patterns (Figure 2.1b) from which d-spacings were measured (Figure 2.1c), confirming the particles are cerium (IV) oxide with no significant contribution from other crystalline materials, including cerium (III) oxide. Synchrotron XRD confirmed the chemical identity of the particles as CeO_2 (Supplementary Figure 2.1) and, using the Scherrer equation, the average crystallite size in suspension was estimated to be 7.8 nm as calculated from the (110) reflection, in reasonable agreement with the directly measured sizes in the TEM images. While the particles appear to be arranged into large, very loosely packed 50 to 200 nm aggregates in the TEM micrographs, DLS of the particles in suspension suggests that the additive contains clusters with an average hydrodynamic diameter of 15.6 nm. Wakefield et al. make it clear that the cerium oxide is present as sub-10 nm particles suspended in the additive and coated with a surfactant in order to maintain colloidal stability.[10] Together, the evidence indicates that the individual n-ceria crystals are approximately 3 to 7 nm in size and present as aggregates of roughly 15 nm as indicated by the DLS. The larger, very loose aggregates observed in the TEM images are likely an artifact of the TEM preparation methods which included vacuum drying, gentle heating, and brief plasma cleaning.

The safety data sheet (SDS) supplied with Envirox reports that the concentration of cerium in the additive is no more than 10% by weight.[34] Analysis by ICP-AES showed that the fuel additive has a concentration of approximately 19,300 ppm cerium or roughly 2.5% CeO_2 by weight. These findings verify and elaborate on the claims made by the manufacturer[10, 13] and reported in the literature[35] regarding the product's n-ceria content.

2.4.2. Electron Microscopy of Exhaust Particles

The HR-TEM micrographs in Figure 2.2 show representative ceria particles from the exhaust. Typically between zero and four ceria particles were found per grid square, with over 100 ceria particles being identified over approximately 200 grid squares (across 12 grids, 4 operating loads, and 3 impactor stages). Most of the material on the grids was carbon, consistent with previous reports of diesel emissions being composed of 30 to 50 nm primary particles of turbostratic graphite (graphite composed of misaligned graphene sheets).[36] Particles composed of heavier elements not including cerium were occasionally observed. Elemental compositions of these particles included Na, Mg, Al, Si, P, S, K, Ca, Fe, Ni, Zn, Sn, Pt, and much more rarely Ti, V, and W. These particles were typically comprised of several elements, with the exception of Fe (found with and without other elements), W (found only once as a pure element), and Ti and V (only found once and together). The elements and their modes of release observed in the exhaust are in agreement with previous studies.[37, 38]

The ceria particles found in the exhaust (Figure 2.2) were typically spherical to ellipsoidal with a maximum aspect ratio of 1.25 and a long axis that ranged from 60 to 300 nm in diameter. Assuming the particles are spheres, the increase in volume from additive to exhaust is approximately 1.1×10^5 nm^3 to 1.4×10^7 nm^3. This is a significant change from the particles in the additive; they have grown 1-2 orders of magnitude in diameter and approximately 120 times in volume from the initial aggregates. No particles containing ceria were identified with a diameter significantly less than 50 nm in the exhaust. If such particles existed they would be expected to be found either on their own (at a significantly reduced entrainment rate) or dotted on the surface of carbonaceous

material as shown by Jung[25] and Gantt[27]. While it is possible that particles below this threshold exist in the exhaust, it is expected that they are rare.

Most of the ceria particles exhibit lattice fringes across the entire particle (Figure 2.3c and d), indicating that they are single crystals, but they do not appear polyhedral as the n-ceria did before combustion (Figure 2.1a). Single particle SAED confirmed that the particles remain cerium (IV) oxide (Figure 2.4). By taking advantage of a double tilt sample holder used with the JEOL 2100 TEM, enabling the tilting of the sample stage along two axes simultaneously, diffraction of ceria particles was performed down major zone axes. In multiple particles, diffraction down the [-1 1 2] axis of CeO_2 revealed additional reflections between the fundamental reflections predicted for CeO_2 (Figure 2.4b), indicating long range ordering (and therefore the presence of a superstructure). These reflections were beam sensitive, disappearing after only a few minutes of electron beam exposure (Figure 2.4c). Similar superlattice reflections have been noted in cerium oxide crystals in the past under carefully controlled conditions.[39, 40] These studies concluded that the superlattice reflections arise from an ordered oxygen vacancy within the CeO_2 crystal structure. This suggests that the n-ceria particles showing a superstructure are slightly reduced, containing a fraction of Ce(III) that is sustainable by the CeO_2 crystal structure without substantially altering it.[8]

EDS spectra of the emitted ceria particles indicated the presence of impurities in no more than 10% of the particles analyzed. EDS maps were collected on the JEOL 2100 TEM for a subset of particles, paying particular attention to those that showed the presence of impurities (Supplementary Figure 2.3). These impurities were most commonly Ca and Si, but also included Zn, Ni, and Al, none of which were found

localized within the particles. High resolution EDS line scans were performed on the FEI Titan TEM to probe the surfaces of the ceria particles, particularly those which appeared to have a surface coating (e.g. Figure 2.3b and d), suggested by a sharp contrast change and lattice fringes ending a short distance from the particle edge. These surface coatings appeared in approximately a third of the particles identified, do not show a correlation to engine load, and vary in thickness from approximately 3 to 7 nm. The line scans showed no evidence of elements other than carbon and oxygen in the coatings, suggesting that the coating is a hydrocarbon. EDS mapping resulted in carbon contamination identified by a square carbon film where the probe rastered over the sample. Surface coatings, on the other hand, were present upon initial particle identification, they encapsulated the particle rather than covering a square area, and they weren't always present. These factors suggest that the particle coatings were unlikely to be the result of contamination from the electron beam.

Emitted ceria particles were discovered in an aggregated state of 40 to 60 nm crystals in an aggregate size of approximately 300 nm (Figure 2.2b) on two separate occasions. These particles were also confirmed to be cerium (IV) oxide and may be indicative of the process by which the large, near-spherical single crystals form from the original, individual nanoparticles. The temperature and pressure conditions within the cylinder of a diesel engine reach nearly 1000 °C and 120 bars,[41] with peaks approaching 2300 °C and 200 bars.[12, 42] The melting point of bulk ceria is approximately 2400 °C. Studies have shown that the melting point of a material often decreases as particle size decreases, such as with indium[43] and tin[44]. It is plausible that the in-cylinder conditions may result in the rapid melting and re-crystallizing of the n-ceria over short time scales. Sintering has

been observed in cerium oxide nanoparticles beginning at 750 °C and may also explain or contribute to the increase in particle size during combustion.[45]

Ceria was also identified within large carbonaceous aggregates that are on the order of 2 to 10 μm by (Z)-contrast imaging in the ESEM (Supplementary Figure 2.4b and d). The buried cerium particles appear to be similar in size and shape to the ceria particles found elsewhere in the exhaust. Additional characterization was not possible due to the fact that these particles were deeply buried within carbon, resulting in thick samples. This finding is supported by the work of Gantt et al.[27] who reported that 40% of the cerium present in their exhaust samples was in this micron-sized mode. The transport and fate of these 'buried' particles upon entering the environment is expected to be controlled by the carbon aggregates, although it is unknown what impact the cerium might have on chemical interactions, including toxicity, once released into the environment. Particle size distributions of the exhaust can be found in the Supporting Information.

2.4.3. Environmental implications

We have shown that the characteristics of cerium particles emitted from a representative diesel engine utilizing the commercially available additive Envirox are substantially altered during combustion and subsequent emission, and these changes appear to be unaffected by typical variations in the operating conditions of the engine. The alterations to the n-ceria are achieved over very short time periods, on the order of hundredths of a second (in-cylinder combustion) at high temperatures and pressures to several tenths of a second (flight time to exit the exhaust) at much lower temperatures and near atmospheric pressure. The alterations affect many of the properties of the ceria

particles: they grow in volume by two orders of magnitude, the surfactant is removed through combustion, a new carbonaceous coating reforms on approximately 30% of the particles, morphological alterations change the termination surfaces of the crystal, a restructuring of the internal crystallinity of the particles leads to superlattice formation in some of the crystals, and some of the ceria particles are found within large carbonaceous aggregates. All of these changes will very likely alter the reactivity, transport, and/or ultimate fate of these particles in the environment relative to the particles as found in the additive.

The alteration of engineered nanomaterials during their lifetimes, particularly upon entering the environment, is a known complication to hazard prediction.[3] Nanomaterials in anthropogenic and natural systems have been observed to undergo many types of alterations including sulfidation,[2, 46] redox reactions,[47-49] and dissolution.[50] The effect of these changes on environmental toxicity varies by both the mechanism and the nanomaterial being altered, making it difficult to predict the effect of a mechanism on the toxicity of a nanomaterial that has not been directly studied. In the case of n-ceria, the source and use of the particles has been shown to impact their toxicity, therefore it is important to characterize the emitted cerium particles in order to predict their toxicity.

The characterization of environmentally relevant n-ceria has been a long standing issue, especially regarding cerium used as a diesel fuel additive. In 2001, the Health Effects Institute evaluated the health risk posed by cerium diesel fuel additives and concluded that there was insufficient data regarding the fine and ultrafine n-ceria emissions to determine the risk.[51] As recently as 2014, similar sentiments were echoed by Collin et al., who identified the prediction and measurement of n-ceria in the environment as a

major data gap.[31] Kumar et al. noted that the source of n-ceria is critical to understanding its biological activity and called for more open data sharing and collaboration in order to address questions regarding the variability in toxicological responses to n-ceria exposure.[32] All of these reviews indicate that the characterization of n-ceria is critical to predicting its toxicity.

This work has identified many previously unexpected and unaccounted for alterations to the ceria nanoparticles that occur during the combustion of diesel fuel additives. The ultimate effects of these changes on the particles' interactions once emitted into the environment is unknown, but judging from the behavior of other nanomaterials, it is predicted to be significant. Many researchers conducting previous studies focusing on pristine nanoparticles from chemical supply companies or even within consumer products may be investigating particles that are nothing like those that are likely to be encountered in the environment. Future studies on the fate and toxicity of n-ceria entering the environment from diesel fuel additives need to consider the transformations that these particles are likely to undergo during their lifetimes and use more representative particles in order to provide meaningful/applicable results.

2.5. ACKNOWLEDGMENTS

This material is based upon work supported by the National Science Foundation (NSF) and the Environmental Protection Agency (EPA) under NSF Cooperative Agreement EF-0830093 and DBI-1266252, Center for the Environmental Implications of NanoTechnology (CEINT). Any opinions, findings, conclusions or recommendations expressed in this material are those of the author(s) and do not necessarily reflect the

views of the NSF or the EPA. This work has not been subjected to EPA review and no official endorsement should be inferred. This work was supported in part by the Institute for Critical Technology and Applied Science (ICTAS) through the ICTAS Graduate Student Fellowship Program, the Nanoscale Characterization and Fabrication Laboratory (NCFL), and the Virginia Tech Center for Sustainable Nanotechnology (VTSuN). This work used shared facilities at the Virginia Tech National Center for Earth and Environmental Nanotechnology Infrastructure (NanoEarth), a member of the National Nanotechnology Coordinated Infrastructure (NNCI), supported by NSF (ECCS 1542100). The authors would also like to thank Energenics Europe Limited for providing the Envirox^{TM} additive for these studies, Dr. Andrea Tiwari for her guidance and assistance in developing the sampling apparatus, and Drs. Chris Winkler and Mitsuhiro Murayama at ICTAS NCFL for their assistance with the TEM work. Finally, the authors would like to thank Dr. Sarah Mazza for her work on the abstract figure.

2.6. REFERENCES

1. Andreescu, D.; Bulbul, G.; Özel, R. E.; Hayat, A.; Sardesai, N.; Andreescu, S., Applications and implications of nanoceria reactivity: measurement tools and environmental impact. *Environmental Science: Nano* **2014,** *1*, (5), 445-458.

2. Kim, B.; Murayama, M.; Colman, B. P.; Hochella, M. F., Characterization and environmental implications of nano- and larger TiO2 particles in sewage sludge, and soils amended with sewage sludge. *Journal of Environmental Monitoring* **2012,** *14*, (4), 1129-1137.

3. Lowry, G. V.; Gregory, K. B.; Apte, S. C.; Lead, J. R., Transformations of nanomaterials in the environment. *Environmental science & technology* **2012,** *46*, (13), 6893-6899.

4. Jiang, M.; Wood, N. O.; Komanduri, R., On chemo-mechanical polishing (CMP) of silicon nitride (Si_3N_4) workmaterial with various abrasives. *Wear* **1998,** *220*, (1), 59-71.

5. Stambouli, A. B.; Traversa, E., Solid oxide fuel cells (SOFCs): a review of an environmentally clean and efficient source of energy. *Renewable and Sustainable Energy Reviews* **2002,** *6*, (5), 433-455.

6. Hirst, S. M.; Karakoti, A.; Singh, S.; Self, W.; Tyler, R.; Seal, S.; Reilly, C. M., Bio-distribution and in vivo antioxidant effects of cerium oxide nanoparticles in mice. *Environmental toxicology* **2013,** *28*, (2), 107-118.

7. Giri, S.; Karakoti, A.; Graham, R. P.; Maguire, J. L.; Reilly, C. M.; Seal, S.; Rattan, R.; Shridhar, V., Nanoceria: a rare-earth nanoparticle as a novel anti-angiogenic therapeutic agent in ovarian cancer. *PloS one* **2013,** *8*, (1), e54578.

8. Trovarelli, A., Catalytic properties of ceria and CeO2-containing materials. *Catalysis Reviews* **1996,** *38*, (4), 439-520.

9. Korner, R.; Ricken, M.; Nolting, J.; Riess, I., PHASE-TRANSFORMATIONS IN REDUCED CERIA - DETERMINATION BY THERMAL-EXPANSION MEASUREMENTS. *Journal of Solid State Chemistry* **1989,** *78*, (1), 136-147.

10. Wakefield, G.; Wu, X.; Gardener, M.; Park, B.; Anderson, S., Envirox™ fuel-borne catalyst: Developing and launching a nano-fuel additive. *Technology Analysis & Strategic Management* **2008,** *20*, (1), 127-136.

11. Zhao, H.; Ladommatos, N., Optical diagnostics for soot and temperature measurement in diesel engines. *Progress in Energy and Combustion Science* **1998,** *24*, (3), 221-255.

12. Eilts, P.; Stoeber-Schmidt, C.; Wolf, R., Investigation of Extreme Mean Effective and Maximum Cylinder Pressures in a Passenger Car Diesel Engine. *SAE Technical Paper* **2013**, 9.

13. Park, B.; Donaldson, K.; Duffin, R.; Tran, L.; Kelly, F.; Mudway, I.; Morin, J.-P.; Guest, R.; Jenkinson, P.; Samaras, Z., Hazard and risk assessment of a nanoparticulate cerium oxide-based diesel fuel additive-a case study. *Inhalation toxicology* **2008,** *20*, (6), 547-566.

14. FuelsEurope, *Statistical Report 2016* [Online]; Brussels, Belgium, 2016, https://www.fuelseurope.eu/uploads/Modules/Resources/graphs_fuels_europe-_2016_v12_web.pdf (accessed on January 20, 2017).

15. Petroleum, B., *BP Statistical Review of World Energy 2016* [Online]; London, UK, June 2016, https://www.bp.com/content/dam/bp/pdf/energy-economics/statistical-review-2016/bp-statistical-review-of-world-energy-2016-full-report.pdf (accessed January 20, 2017).

16. Ulrich, A.; Wichser, A., Analysis of additive metals in fuel and emission aerosols of diesel vehicles with and without particle traps. *Analytical and Bioanalytical chemistry* **2003,** *377*, (1), 71-81.

17. Mayer, A.; Czerwinski, J.; Scheidegger, P. *Trapping efficiency depending on particulate size*; 0148-7191; SAE Technical Paper: 1996.

18. Kittelson, D. B., Engines and nanoparticles: a review. *Journal of aerosol science* **1998,** *29*, (5), 575-588.

19. Mayer, A.; Czerwinski, J.; Matter, U.; Wyser, M.; Scheidegger, G.; Kieser, D., VERT: Diesel nano-particulate emissions: Properties and reduction strategies. *SAE Technical Paper* **1998,** *980839*, 12.

20. Gantt, B.; Hoque, S.; Willis, R. D.; Fahey, K. M.; Delgado-Saborit, J. M.; Harrison, R. M.; Erdakos, G. B.; Bhave, P. V.; Zhang, K. M.; Kovalcik, K., Near-Road Modeling and Measurement of Cerium-Containing Particles Generated by Nanoparticle Diesel Fuel Additive Use. *Environmental science & technology* **2014,** *48*, (18), 10607-10613.

21. Gandhi, H.; Piken, A.; Shelef, M.; Delosh, R., Labratory Evaluation of Three-Way Catalysts. *SAE Technical Paper* **1976,** *760201*.

22. Yao, H.; Yao, Y. Y., Ceria in automotive exhaust catalysts: I. Oxygen storage. *Journal of Catalysis* **1984,** *86*, (2), 254-265.

23. Kašpar, J.; Fornasiero, P.; Graziani, M., Use of CeO 2-based oxides in the three-way catalysis. *Catalysis Today* **1999,** *50*, (2), 285-298.

24. Skillas, G.; Qian, Z.; Baltensperger, U.; Matter, U.; Burtscher, H., The influence of additives on the size distribution and composition of particles produced by diesel engines. *Combustion Science and Technology* **2000,** *154*, 259-273.

25. Jung, H. J.; Kittelson, D. B.; Zachariah, M. R., The influence of a cerium additive on ultrafine diesel particle emissions and kinetics of oxidation. *Combustion and Flame* **2005,** *142*, (3), 276-288.

26. Okuda, T.; Schauer, J. J.; Olson, M. R.; Shafer, M. M.; Rutter, A. P.; Walz, K. A.; Morschauser, P. A., Effects of a Platinum− Cerium Bimetallic Fuel Additive on the Chemical Composition of Diesel Engine Exhaust Particles. *Energy & Fuels* **2009,** *23*, (10), 4974-4980.

27. Gantt, B.; Hoque, S.; Fahey, K. M.; Willis, R. D.; Delgado-Saborit, J. M.; Harrison, R. M.; Zhang, K. M.; Jefferson, D. A.; Kalberer, M.; Bunker, K. L., Factors Affecting the Ambient Physicochemical Properties of Cerium-Containing Particles Generated by Nanoparticle Diesel Fuel Additive Use. *Aerosol Science and Technology* **2015,** *49*, (6), 371-380.

28. Grulke, E.; Reed, K.; Beck, M.; Huang, X.; Cormack, A.; Seal, S., Nanoceria: factors affecting its pro-and anti-oxidant properties. *Environmental Science: Nano* **2014,** *1*, (5), 429-444.

29. Kitchin, K. T.; Grulke, E.; Robinette, B. L.; Castellon, B. T., Metabolomic effects in HepG2 cells exposed to four TiO 2 and two CeO 2 nanomaterials. *Environmental Science: Nano* **2014,** *1*, (5), 466-477.

30. Ma, Y.; Kuang, L.; He, X.; Bai, W.; Ding, Y.; Zhang, Z.; Zhao, Y.; Chai, Z., Effects of rare earth oxide nanoparticles on root elongation of plants. *Chemosphere* **2010,** *78*, (3), 273-279.

31. Collin, B.; Auffan, M.; Johnson, A. C.; Kaur, I.; Keller, A. A.; Lazareva, A.; Lead, J. R.; Ma, X.; Merrifield, R. C.; Svendsen, C., Environmental release, fate and ecotoxicological effects of manufactured ceria nanomaterials. *Environmental Science: Nano* **2014,** *1*, (6), 533-548.

32. Kumar, A.; Das, S.; Munusamy, P.; Self, W.; Baer, D. R.; Sayle, D. C.; Seal, S., Behavior of nanoceria in biologically-relevant environments. *Environmental Science: Nano* **2014,** *1*, (6), 516-532.

33. Abdul-Khalek, I.; Kittelson, D.; Brear, F. *The influence of dilution conditions on diesel exhaust particle size distribution measurements*; 0148-7191; SAE Technical paper: 1999.

34. *Envirox*^{TM} [Online]; Energenics Europe Ltd: Begbroke, UK, April 26, 2015, http://www.energenics.co.uk/wp-content/uploads/Envirox-SDS-rev-6-26Apr2015.pdf (accessed January 20, 2017).

35. Cassee, F. R.; van Balen, E. C.; Singh, C.; Green, D.; Muijser, H.; Weinstein, J.; Dreher, K., Exposure, health and ecological effects review of engineered nanoscale

cerium and cerium oxide associated with its use as a fuel additive. *Critical reviews in toxicology* **2011,** *41*, (3), 213-229.

36. Clague, A.; Donnet, J.; Wang, T.; Peng, J., A comparison of diesel engine soot with carbon black. *Carbon* **1999,** *37*, (10), 1553-1565.

37. Liati, A.; Schreiber, D.; Dimopoulos Eggenschwiler, P.; Arroyo Rojas Dasilva, Y., Metal particle emissions in the exhaust stream of diesel engines: an electron microscope study. *Environmental science & technology* **2013,** *47*, (24), 14495-14501.

38. Wang, Y.-F.; Huang, K.-L.; Li, C.-T.; Mi, H.-H.; Luo, J.-H.; Tsai, P.-J., Emissions of fuel metals content from a diesel vehicle engine. *Atmospheric Environment* **2003,** *37*, (33), 4637-4643.

39. Sharma, R.; Crozier†, P.; Kang, Z.; Eyring, L., Observation of dynamic nanostructural and nanochemical changes in ceria-based catalysts during in-situ reduction. *Philosophical Magazine* **2004,** *84*, (25-26), 2731-2747.

40. Crozier, P. A.; Wang, R.; Sharma, R., In situ environmental TEM studies of dynamic changes in cerium-based oxides nanoparticles during redox processes. *Ultramicroscopy* **2008,** *108*, (11), 1432-1440.

41. Lapuerta, M.; Armas, O.; Hernández, J., Diagnosis of DI Diesel combustion from in-cylinder pressure signal by estimation of mean thermodynamic properties of the gas. *Applied Thermal Engineering* **1999,** *19*, (5), 513-529.

42. Ahn, S. K.; Matsui, Y.; Kamimoto, T.; Matsuoka, S. *Measurement of flame temperature distribution in a DI diesel engine by means of image analysis of nega-color photographs*; 0148-7191; SAE Technical Paper: 1981.

43. Zhang, M.; Efremov, M. Y.; Schiettekatte, F.; Olson, E.; Kwan, A.; Lai, S.; Wisleder, T.; Greene, J.; Allen, L., Size-dependent melting point depression of nanostructures: nanocalorimetric measurements. *Physical Review B* **2000,** *62*, (15), 10548.

44. Lai, S.; Guo, J.; Petrova, V.; Ramanath, G.; Allen, L., Size-dependent melting properties of small tin particles: nanocalorimetric measurements. *Physical review letters* **1996,** *77*, (1), 99.

45. Zhou, Y.; Phillips, R. J.; Switzer, J. A., Electrochemical synthesis and sintering of nanocrystalline cerium (IV) oxide powders. *Journal of the American Ceramic Society* **1995,** *78*, (4), 981-985.

46. Ma, R.; Stegemeier, J.; Levard, C.; Dale, J. G.; Noack, C. W.; Yang, T.; Brown, G. E.; Lowry, G. V., Sulfidation of copper oxide nanoparticles and properties of resulting copper sulfide. *Environmental Science: Nano* **2014,** *1*, (4), 347-357.

47. Liu, Y.; Majetich, S. A.; Tilton, R. D.; Sholl, D. S.; Lowry, G. V., TCE dechlorination rates, pathways, and efficiency of nanoscale iron particles with different properties. *Environmental Science & Technology* **2005,** *39*, (5), 1338-1345.

48. Lok, C.-N.; Ho, C.-M.; Chen, R.; He, Q.-Y.; Yu, W.-Y.; Sun, H.; Tam, P. K.-H.; Chiu, J.-F.; Che, C.-M., Silver nanoparticles: partial oxidation and antibacterial activities. *JBIC Journal of Biological Inorganic Chemistry* **2007,** *12*, (4), 527-534.

49. Tiwari, A. J.; Morris, J. R.; Vejerano, E. P.; Hochella Jr, M. F.; Marr, L. C., Oxidation of C60 aerosols by atmospherically relevant levels of O3. *Environmental science & technology* **2014,** *48*, (5), 2706-2714.

50. Ma, R.; Levard, C.; Marinakos, S. M.; Cheng, Y.; Liu, J.; Michel, F. M.; Brown, G. E.; Lowry, G. V., Size-Controlled Dissolution of Organic-Coated Silver Nanoparticles. *Environmental Science & Technology* **2012,** *46*, (2), 752-759.

51. HEI, Evaluation of Human Health Risk from Cerium Added to Diesel Fuel. **2001**.

52. Wyckoff, R. W. G., *Crystal Structures*. Interscience Publishers: 1963.

2.7 FIGURES

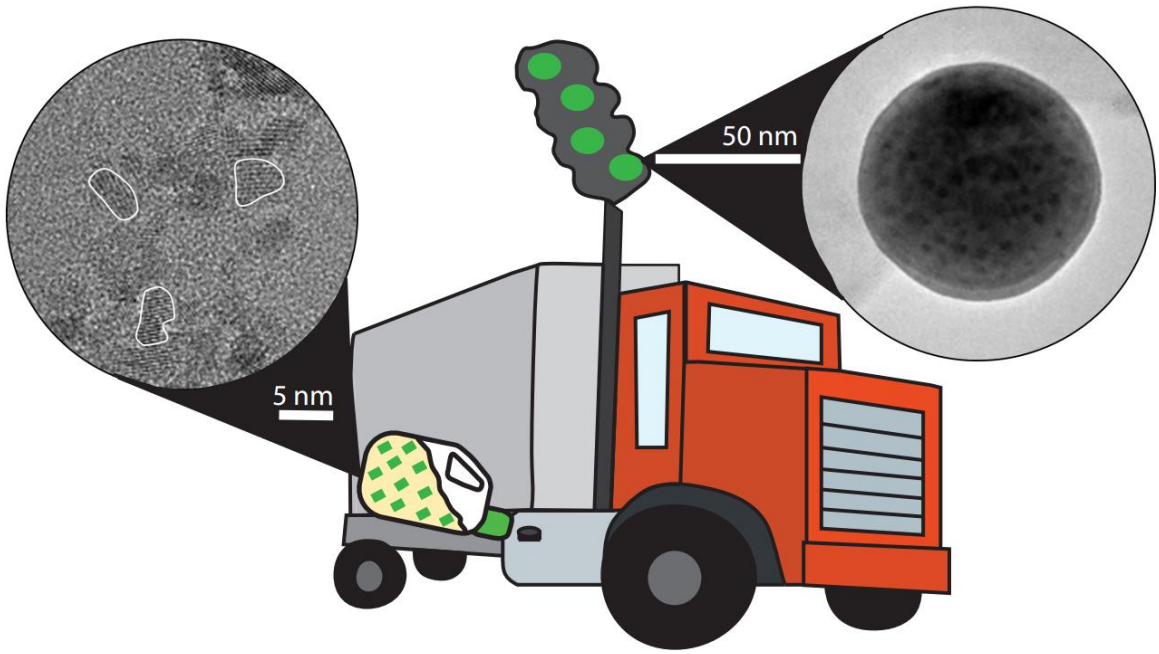

Figure 2.0. Abstract figure.

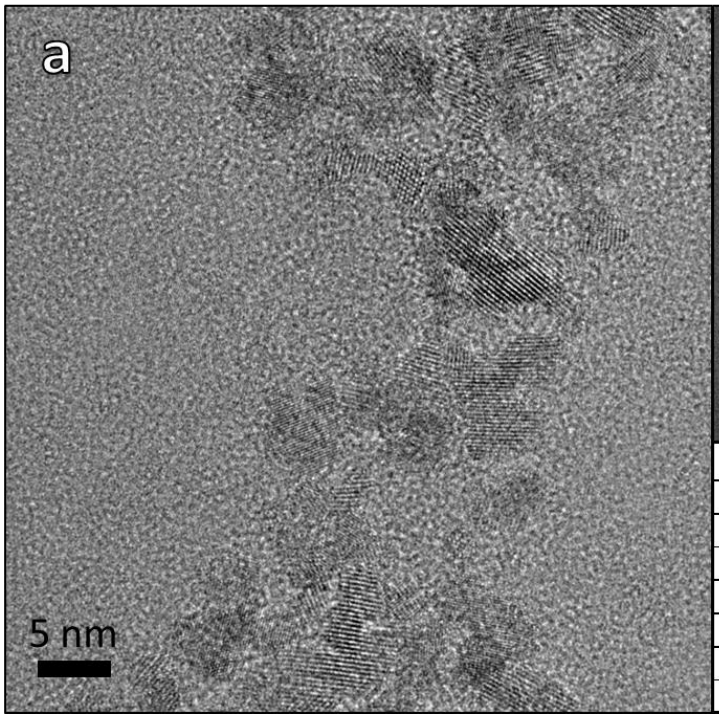

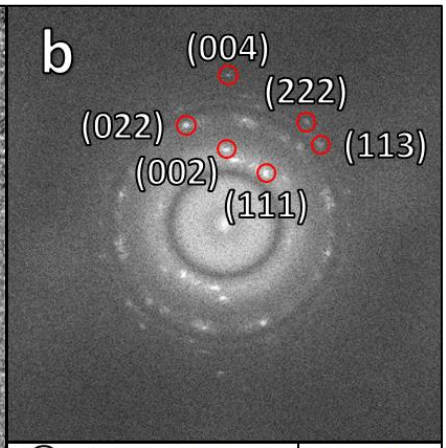

© Reference CeO_2		Envirox™
Plane	d-spacing	d-spacing
1 1 1	3.12	3.12
0 0 2	2.71	2.75
0 2 2	1.91	1.92
1 1 3	1.63	1.64
2 2 2	1.56	1.56
0 0 4	1.35	1.37

Figure 2.1. (a) HR-TEM image of the cerium oxide particles present in Envirox. (b) A fast Fourier transform (FFT) of the image in (a) with indexed spots labeled. (c) The table presents the crystallographic planes and their associated d-spacings of CeO_2 from Wyckoff[52] and compares these values with the d-spacings measured from the FFT in (b).

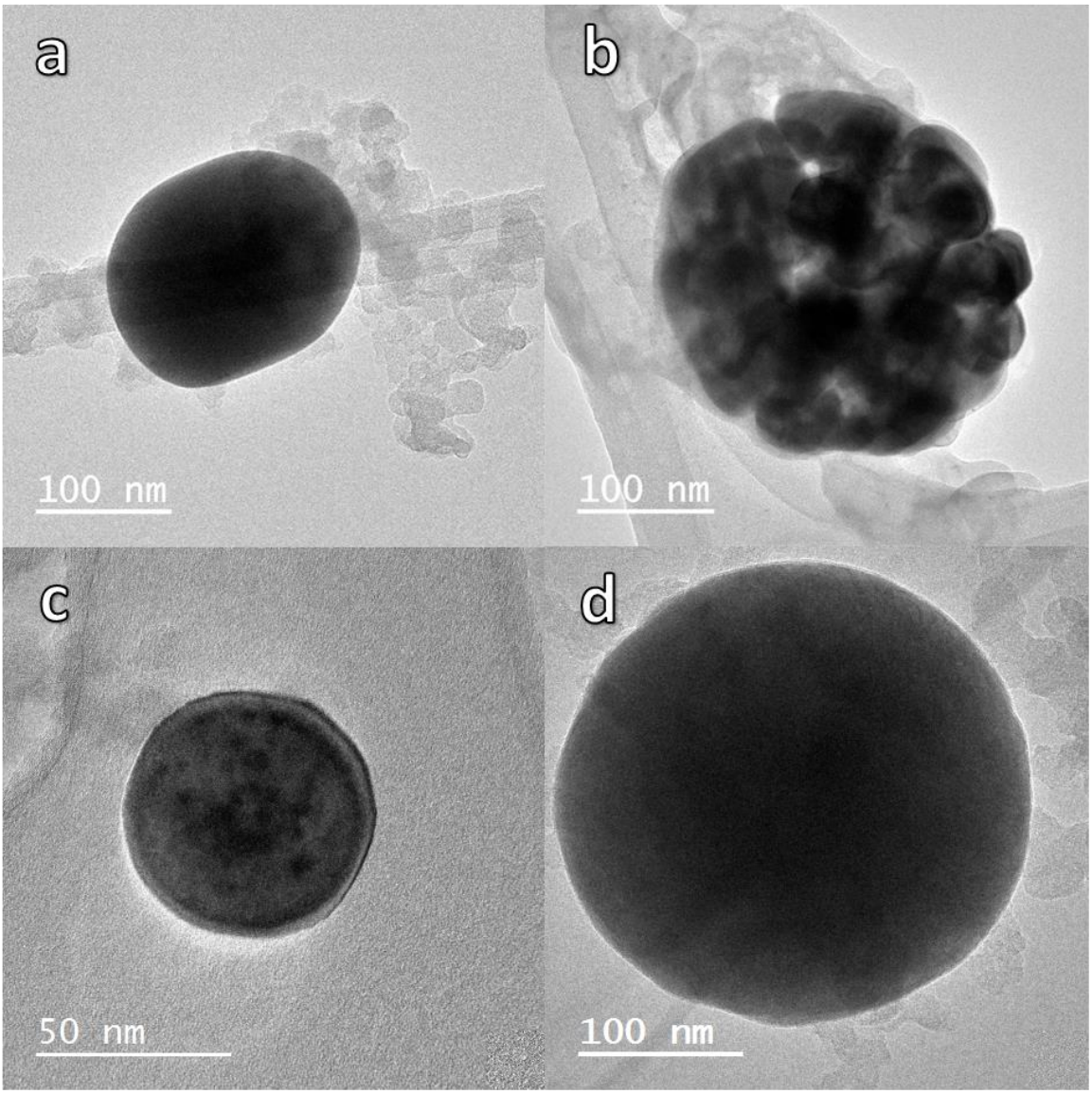

Figure 2.2. Representative ceria particles in the exhaust of a diesel engine using the additive Envirox. (a) An elongated particle, 155 by 195 nm, collected at engine idle (b) a 275 nm aggregate composed of numerous 50 to 70 nm single crystals of ceria collected at engine idle, (c) a 60 nm ceria particle collected at 27% engine load, and (d) a 280 nm ceria particle collected at 54% engine load.

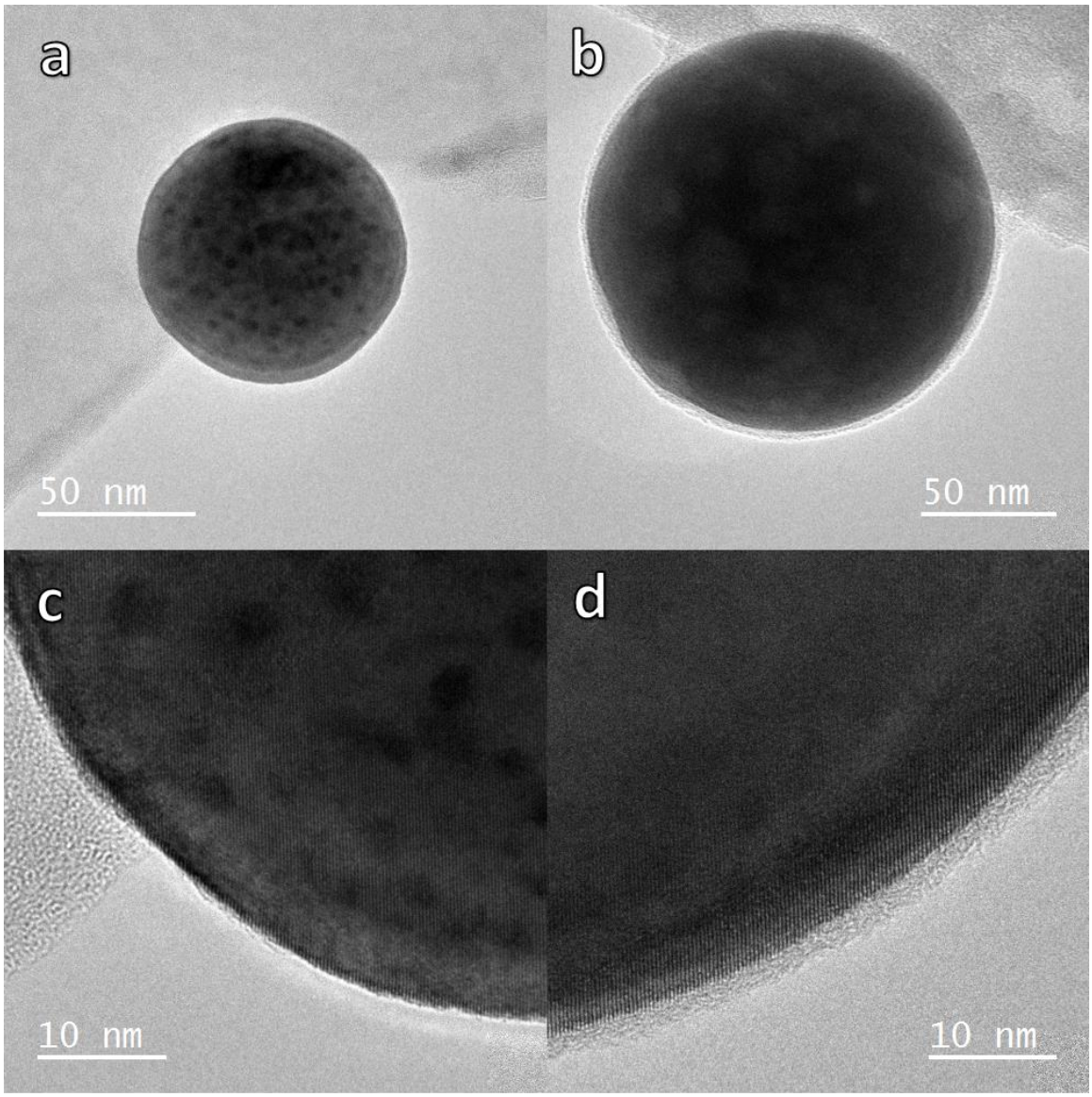

Figure 2.3. Ceria particles captured from the exhaust of a diesel engine using the additive Envirox. (a and b) Bright field images of two representative ceria particles, one without a surface coating, collected at 27% engine load (a) and one with a coating, collected at idle (b). (c and d) HR-TEM images of the particles in (a and b), respectively. Both particles exhibit lattice fringes.

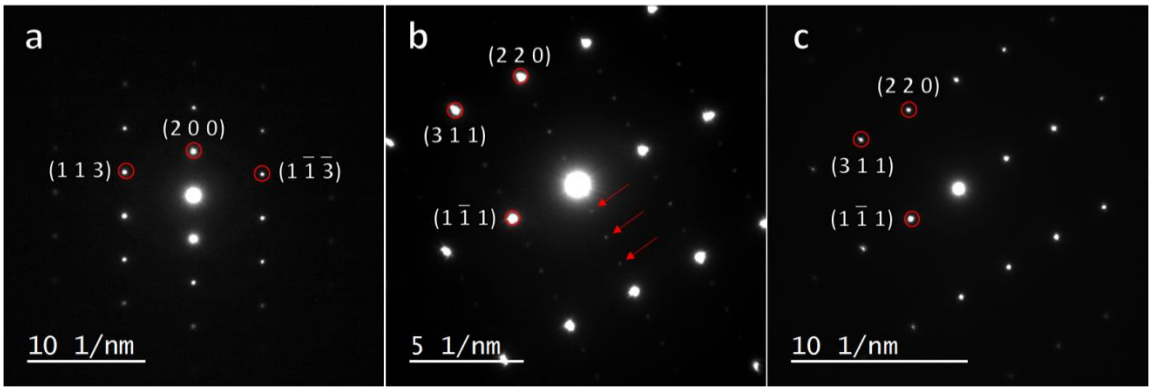

Figure 2.4. SAED of the particle from Figure 3 (a and c) down the (a) [0 3 -1] axis and (b and c) [-1 1 2] axis of the ceria particle. The pattern exhibited superlattice reflections (b, indicated by the arrows) that disappeared after several minutes of electron beam exposure (c).

2.8. SUPPORTING INFORMATION

2.8.1. Synchrotron-based XRD

X-ray diffraction of Envirox™ (Supplementary Figure 2.1) was performed on beamline 11-ID-B at the Advanced Photon Source (Argonne National Laboratory) operating at an energy of $\lambda = 0.2114$ Å (58.6 keV). Samples were suspended in 1.5 mm Kapton capillary tubes. The matrix background was removed from the data by collecting a pattern for diesel fuel (a reasonable substitute for the kerosene matrix) and subtracting it from the Envirox™ data. Additional background subtraction and peak matching using a Voigt profile was performed in Fityk[1] and crystal size was calculated using the Scherrer line-broadening equation,[2] with instrumental line-broadening measured from a CeO_2 model compound. The crystal size was determined to be 2.8 nm from the (111) reflection and 7.8 nm from the (200) reflection.

2.8.2. In-situ hydrodynamic size

Dynamic light scattering (DLS) was performed in order to measure the hydrodynamic size of the particles suspended within Envirox™. Measurements were made using a Malvern Zetasizer Nano ZS (Malvern, Worcestershire, UK) operating at 633 nm. The refractive indices of cerium oxide and kerosene were input as 2.2 and 1.39, respectively. Samples of Envirox™ were diluted 1:10 with kerosene (the suspension matrix in Envirox™). Results indicated that the size distribution of particles in Envirox™ is bimodal, with a Z-average of 15.60 (±0.84) nm diameter and a dispersity of 0.377 (±0.006).

2.8.3. Exhaust particle size characterization

The size distributions of all exhaust particles, as measured by both scanning mobility particle sizer (SMPS) and aerodynamic particle sizer (APS), at the various engine loads are presented in Supplementary Figure 2.4. Particle concentrations are highest at the lowest loads, idle and 27%, though the peak shifts from approximately 40 nm at idle to 15 nm at 27%. There is a significant reduction in particle concentration beginning at 54% load, possibly caused by increased dilution from the super charger. The primary peak is shifted even further downward, centered around 7 nm, though it no longer dominates the total emissions so strongly. Finally, at 81% load, no significant peaks appear in the size distribution. The APS data shows that particle count continues to drop off beyond the range of the SMPS, with nearly no particles being detected above 1 μm.

While particle size appears to shift with engine load, no significant variation of the ceria particles was observed over the various operating loads. Although the ceria in the exhaust accounts for 0.5% of the exhaust material by mass, due to its high relative density when compared to the hydrocarbons that make up the bulk of the exhaust particles, the ceria itself is not expected to have a significant impact on the overall particle distribution. The lack of a significant number of particles larger than 1 μm being released (Supplementary Figure 2.4b) indicates that the ceria found within large carbonaceous aggregates is unlikely to make up a significant proportion of the overall ceria released.

2.8.4. References

1. Wojdyr, M., Fityk: a general-purpose peak fitting program. *Journal of Applied Crystallography* **2010,** *43*, (5), 1126-1128.

2. Birks, L.; Friedman, H., Particle size determination from X-ray line broadening. *Journal of Applied Physics* **1946,** *17*, (8), 687-692.

2.9. SUPPLEMENTARY FIGURES

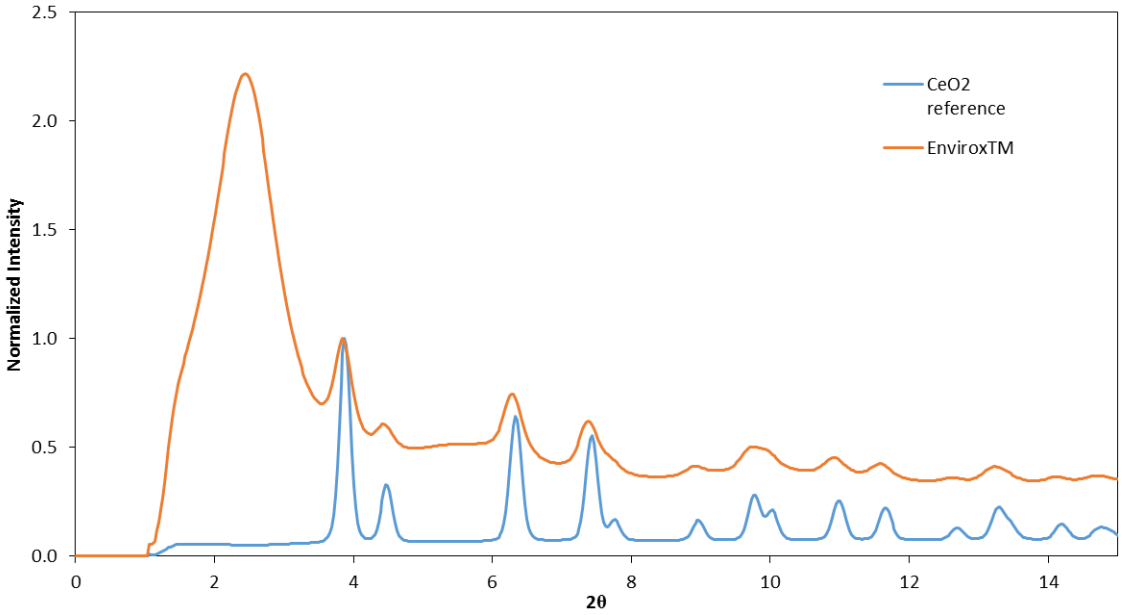

Supplementary Figure 2.1. Synchrotron XRD patterns of Envirox^{TM} and a CeO_2 reference material, plotted in 2θ vs. normalized intensity. Intensity was normalized to the (111) reflection.

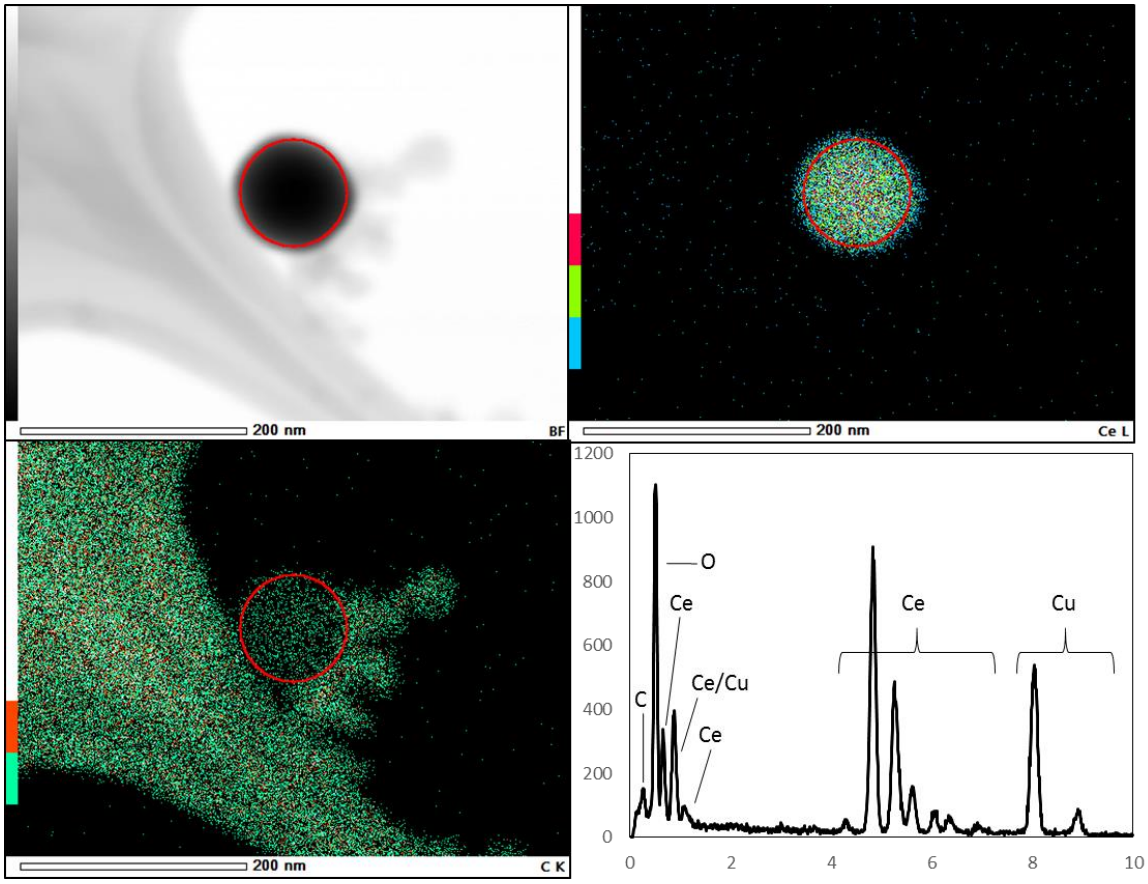

Supplementary Figure 2.2. EDS map and spectra of the ceria particle from Fig. 2.4c. The red ring indicates the region from which the spectrum is derived. The copper (in the spectrum) is most likely interference from the copper grid mesh.

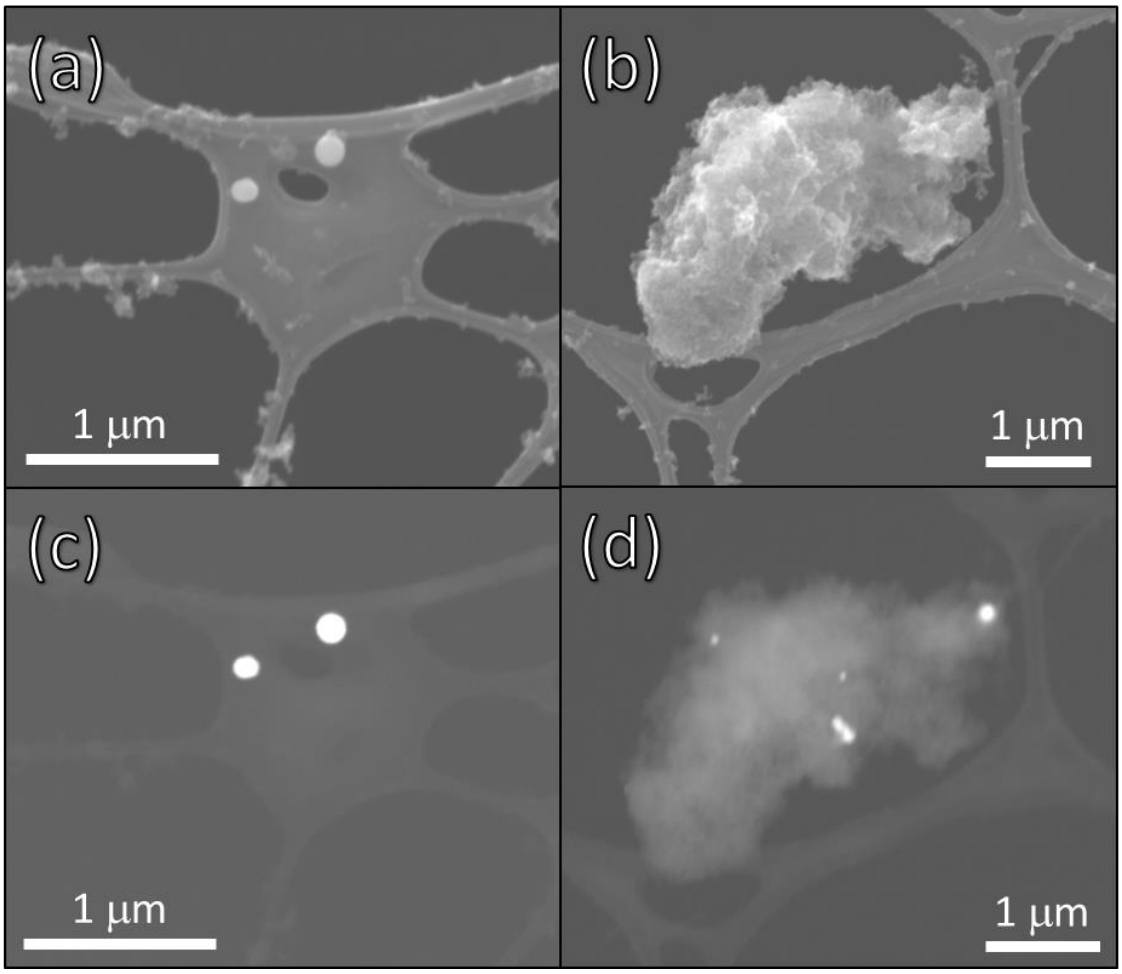

Supplementary Figure 2.3. Identification of cerium particles in diesel exhaust from an engine utilizing Envirox: (a and b) ESEM images showing two ceria particles and a large carbonaceous aggregate (approximately 3 to 4 microns) containing ceria buried within; (c and d) ESEM backscatter images of the same locations in (a and b), respectively.

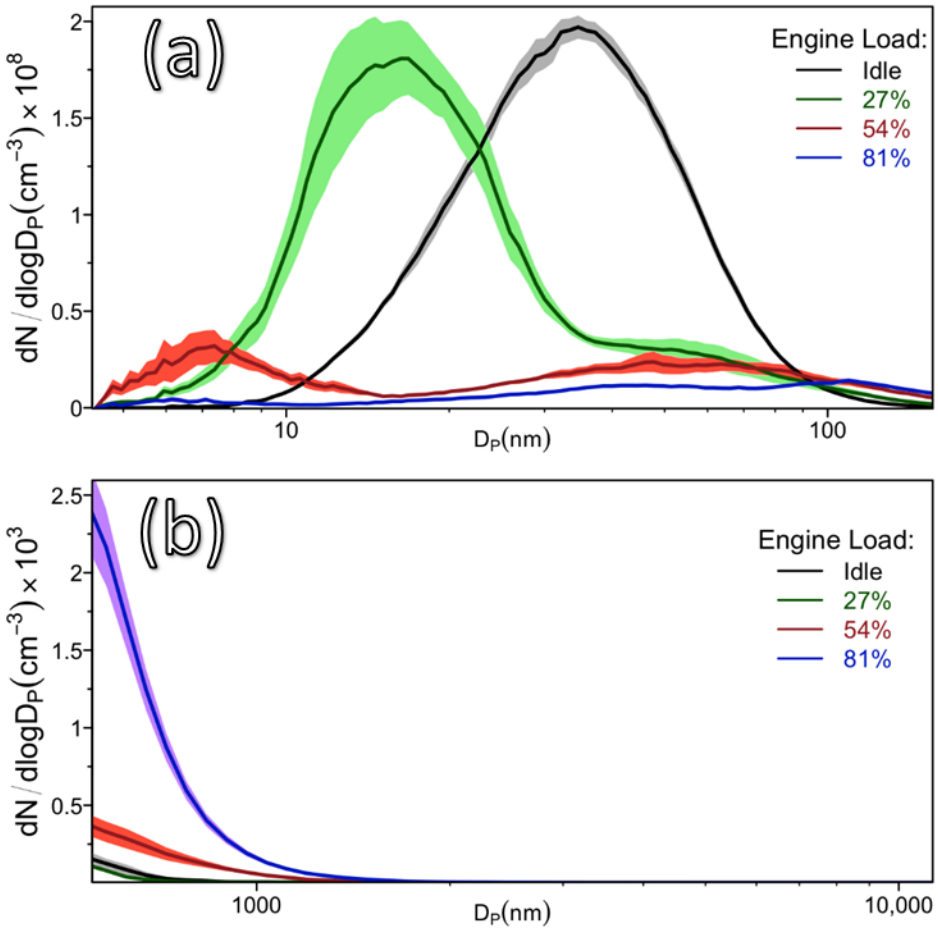

Supplementary Figure 2.4. Particle number size distribution (in diameter, D_p) of all exhaust particles over range 4 to 350 nm as measured by SMPS (a), and 500 to 10,000 nm as determined by APS (b).

2.10. SUPPLEMENTARY TABLES

Supplementary Table 2.1. Measured draw on the genset (kW) with sequential operation of the heaters.

Heaters	kW	Eff.	Load
1	4.5	5.0	13%
2	8.9	9.9	27%
3	13.4	14.9	40%
4	17.8	19.8	54%
5	21.6	24.0	65%
6	27.0	30.0	81%

CHAPTER 3:
Exposure of *Brassica napus* to Cerium Oxide Nanoparticles Released from a Diesel Engine using a Fuel-Borne Catalyst

James G. Dale[1], Amalia Turner[2], Sayako Inoue[1,3], Mitsu Murayama[3], Mark R. Wiesner[2], Michael F. Hochella, Jr.[1,4]

[1]Department of Geosciences, Virginia Tech, Blacksburg, VA 24061, United States

[2]Department of Civil and Environmental Engineering, Duke University, Durham, NC, 27708, United States

[3]Department of Material Science and Engineering, Virginia Tech, Blacksburg, VA 24061, United States

[4]Geosciences Group, Energy and Environment Directorate, Pacific Northwest National Laboratory, Richland, Washington 99352, United States

To be submitted to *Environmental Science: Nano*.

3.1. ABSTRACT

Cerium oxide emitted from the use of fuel-borne catalysts has been determined to significantly differ from the cerium oxide nanoparticles found in such products, suggesting that their behavior in the environment would differ as well. The effects of exposure on the plant *Brassica napus* to emitted cerium oxide were compared to two synthesized cerium oxide nanoparticles and diesel particulate matter emissions with very low cerium. Cerium concentrations were tracked using inductively coupled plasma optical emission spectroscopy in the plant biomass (separated into aboveground and belowground material) as well as through the soil and drainage water. Transmission electron microscopy was used to try to identify the location and phase of cerium oxide in the roots of exposed plants. The biomass of the plants was not significantly influenced by any of the exposures and visual observations provided no indications of a negative

response in the plants. Mobility of cerium as determined by the concentrations found in the drainage water and the soil column indicated that the small nanoparticles were the most mobile, the emitted cerium showed signs of delayed mobility, and the large nanoparticles were not significantly mobile. The root association and potential uptake as measured by the cerium concentration in the belowground biomass showed the same trend, with uptake decreasing from small nanoparticles to emitted cerium, to large nanoparticles, which were on par with the control. Translocation was determined by the cerium concentration in the aboveground biomass and followed the same trend with evidence of significant translocation of the small nanoparticles, the possibility that there may be some translocation of the emitted cerium, and no significant translocation of the large nanoparticles. The results show that while none of the exposures appeared significantly toxic to *B. napus*, the behavior of emitted cerium is not captured by the synthesized nanoparticles and therefore they make poor substitutes in toxicity experiments.

3.2. INTRODUCTION

As nanotechnology continues to penetrate the market, nanomaterials (NMs) will inevitably enter the environment at increased rates. While biological systems have evolved in the presence of many naturally occurring nanomaterials (resulting in some resistance), these same systems are evolutionarily ill-equipped to tolerate the influx of novel anthropogenic nanomaterials.[1] Investigation of the effects of these emerging contaminants is critical because of the possibility that they may be taken up by biological systems (bioavailable) and concentrated up the food chain (bioaccumulated). These types

of interactions can, on medium to long time scales, result in ecosystem collapse similar to that induced by the widespread use of the insecticide dichlorodiphenyltrichloroethane (DDT).[2] In order to protect human health, we must protect environmental health. Past studies on the engineered nanomaterial (ENM)/biological interface have tended to focus on fundamental questions regarding pathways and mechanisms, leaving the broader impact of nanotechnologies still in question. As Chichiriccò and Poma concluded in their recent review of the toxicity of NMs in plants, "While it remains important to study the basic mechanisms of the interaction of NMs with plants, our priority is to weigh up the potential benefits of NMs for plants and humans against the risk of exposing terrestrial ecosystems to particles that are small and potentially reactive."[3]

One significant hurdle in the field of nanotoxicology has been the recurrence of contradictory results. This has typically been attributed to the variability in the exposure materials. NM behavior is closely controlled by their physicochemical properties, meaning small variations in the NM can yield significantly different toxicological results. For example, the effect of organic matter on CeO_2 NPs has been shown to reduce toxicity[4] while another study found that organic matter increased CeO_2 NPs' association with plant roots, suggesting that the organic matter-mediated particles may have an increased toxic effect.[5] The number of variables that need to be understood in order to make accurate predictions regarding a new NMs toxicity is unfeasible within the timeframes in which decisions about their use need to be made.

Nanoparticulate cerium oxide provides a unique opportunity to investigate the environmental impacts of a NM. In its use as a diesel fuel catalyst, n-ceria suspended in the fuel increases fuel efficiency and substantially decreases diesel particulate matter

(DPM) emissions.[6] DPM is a known carcinogen that consists of the uncombusted exhaust products from a diesel engine and contributes to air pollution and its associated health hazards.[7] Concerns over the release of n-ceria into the environment have prevented widespread implementation of FBCs. The effect of n-ceria on plants has been studied, but suffers from many of the standard issues in nanotoxicology. In the case of n-ceria FBCs, it has recently been shown that the n-ceria are significantly altered before being emitted into the environment along with DPM.[8, 9] These changes are likely to impact the way the n-ceria interacts in the environment and may have impact on their toxicity.

The goal of this study was to compare the effects of cerium in DPM to small Ce NPs, large Ce NPs, DPM without Ce on the growth of *Brassica napus*, as well as determine the uptake and translocation of the different cerium materials by the plants during a month long exposure experiment. These results were supported and contextualized with information regarding the transport and transformation of the cerium oxide nanoparticles in soil and water. Plant growth comparisons were made based on the dried biomasses of the plants, separated into aboveground (shoots) and belowground (roots) biomass. Cerium concentrations were determined by inductively coupled plasma atomic emission spectroscopy and additional characterization of the cerium was performed using scanning and transmission electron miscroscopies. The results of this work will aid in assessing the veracity of studies using 'pristine' cerium oxide nanoparticles to simulate fuel additive byproducts and provide insight into how to perform more environmentally relevant nanotoxicology experiments.

3.3. MATERIALS AND METHODS

3.3.1. Experimental Overview

The study herein compares the effects of *Brassica napus* plant exposure to one control and four cerium oxide treatments in aged soil. The cerium oxide treatments included two commercial cerium oxide nanoparticle suspensions, cerium oxide nanoparticles in DPM from the use of Envirox, and very low cerium DPM (generated in the absence of Envirox). Figure 3.1 provides a schematic for the experiments performed within this study. Six replicates were performed for each treatment, consisting of a single plant pot containing 20 *B. napus* seedlings from which total biomass was analyzed. *B. napus* seeds were germinated then planted into control soils where they were then dosed with cerium levels of approximately 100 ppm over the background via a topsoil addition. The plants were lightly watered twice per day with a 10% Hoagland solution over the course of the 32-day exposure. The drainage water was collected after 1, 8, 22, and 32 days to analyze for cerium concentration. At the conclusion of the 32-day exposure, the roots and shoots were separated and collected, a soil core was sampled and divided into 3 depth bins, and a section of the above-below ground junction as well as a lateral root were harvested and prepared for electron microscopy. Biomass not used for electron microscopy was dried, weighed, and digested in order to determine cerium concentrations.

3.3.2. Exposure Materials

The five treatments used in this study were: control soil, very low cerium diesel particulate matter (DPM), diesel particulate matter containing ceria (CeDPM), small cerium oxide nanoparticles (SmNPs), and large cerium oxide nanoparticles (LaNPs). The

four cerium oxide treatments were mixed with control soil prior to dosing, as described below.

The control soil used in this study consisted of a 30%/45%/25% mixture of Sandhills/Clay/Topsoil purchased from Sands & Soils in Durham, NC, air-dried and dry-sieved to >2 mm. The soil mixture had an average content of 19.6% clay, 24.3% silt, and 56.1 % sand, with an overall texture characterized as sandy loam. This soil mixture is the same as that used in the 2015-2016 wetland mesocosm experiments at Duke University and was used as the base soil for all replicates and controls in this experiment.

Both DPM and CeDPM were collected from a 32 kW Kubota V3300 diesel engine and 28 kW generator combined unit (genset), with further details of the genset described previously by Dale et al.[8] The genset was run for intervals of 4 to 8 hours between particulate matter collections. Particulate matter was collected by removing segments of the 2" exhaust pipe, allowing them to cool to room temperature, and scraping their interior walls using a 1.5" metal wire wheel brush. Collections were performed at four different engine operating loads: idle (0%), 27%, 54%, and 81%. The particulate matter was collected separately from each load to be combined later. The CeDPM was generated by the addition of the commercial product Envirox to the fuel at the manufacturer's recommended dosage of 4000:1. The characterization of cerium emission products have been performed on this system by Dale et al.[8] and on another engine setup by Gantt et al.,[9] which suggest the emitted cerium is found as cerium (IV) oxide predominately in the 50 to 300 nm size range and also in the >1 μm size range. The average concentration of cerium in the CeDPM (averaged across all loads) was 3342.4 ± 660.4 ppm Ce. In order to collect the very low cerium DPM, the engine was purged of

fuel, a new fuel tank was installed, the engine was operated for 16 hours with additive-free fuel, and then a new exhaust manifold was installed. DPM was collected in the same manner as CeDPM and had a concentration of 59.3 ppm Ce. EPA number 2 ultralow sulfur diesel (standard for on-road use) and 10W-30 lubricating oil were used for all DPM generation.

The small and large cerium oxide nanoparticles were purchased as aqueous suspensions from chemical supply companies. The SmNP suspension was acquired from Nyacol Nano Technologies, Inc. (Ashland, MA) and was reported by the manufacturer as 10-30 nm acetate-stabilized CeO_2 nanoparticles suspended in water at 30 wt%. Independent characterization using TEM and ICP-MS at Duke University determined the primary particle size to be 3.8 +/- 1.1 nm and the cerium concentration to be 267.8 g/L. The LaNP suspension was acquired from Alfa Aesar (Ward Hill, MA) and was reported by the manufacturer as 750-nm CeO_2 particles dispersed in water with an undisclosed dispersant at 20 wt%. The primary particle size determined through independent analysis was 185.3 +/- 63.7 nm, and the concentration was 111 g/L. Both nanoparticle suspensions were further diluted in 10% Hoagland solution to create stock suspensions of 100 ppm Ce.

3.3.3. B. napus *Germination and Planting*

Dwarf Essex Rape (*Brassica napus*) was selected for these experiments due to its widespread use as a crop plant,[10] properties as a metal accumulator,[11] and common use in toxicological studies.[12, 13] Recent studies have demonstrated that *B. napus* is capable of translocating nanomaterials from its roots to the aboveground plant biomass in hydroponic systems.[14, 15] *B. napus* seeds were purchased from Ernst Conservation Seeds,

Inc. (Meadville, Pennsylvania). Seeds were soaked in deionized water for 3 hours, then rinsed and deposited on filter paper where they were kept moist with deionized water four days prior to planting. Germinating seeds were protected from contamination using plastic petri dishes sealed shut with Aquapore tape between wettings. Seedlings were selected for planting based on two criteria: a root length of at least 1.5 cm and testa (seed coat) no longer covering plumula (first bud).

Each replicate consisted of a 4" square plant pot lined with a woven plastic mesh root barrier to decrease soil loss and prevent the plant roots from crossing into the drainage water. The pots were each filled with 425 g dry weight control soil wetted with 50 mL of 10% Hoagland solution. Selected seedlings were evenly distributed over 4 rows and 5 columns resulting in 20 plants per replicate. A glass rod was plunged into the soil to a depth of 1.5 cm to create the holes in which the seedlings were planted and the holes were backfilled with control soil over the base of the seedlings. Seedlings were allowed to adjust to the moist control soil for 4-20 hours before dosing, and all seedlings were observed to phototrope by the time of dosing. Drainage water was collected by the attachment of a plastic zip-top bag to the plant pot and contained within a second plant pot in order to create space and prevent saturation of the soil with 10% Hoagland solution. The plant pots were housed in a 1.2 m x 0.91 m x 1m Model M-13 reach-in growth chamber in Duke University's Phytotron facility where the temperature and light cycle were regulated to a constant 20 °C and 16/8 hours light/dark, respectively. The plants were lightly watered with 10% Hoagland solution twice daily by Phytotron staff to keep the pots moist but not saturated.

3.3.4. Dosing and Watering

Cerium oxide nanoparticle dosing for the SmNP, LaNP, and CeDPM treatments consisted of the surface application of 25 g dry weight control soil with a concentration of approximately 100 ppm cerium above the control soil in order to simulate the atmospheric deposition of emission byproducts from n-ceria FBCs onto terrestrial surfaces. The concentration was selected based on worst-case scenario calculations wherein an n-ceria FBC was utilized in every heavy-duty diesel vehicle in an urban city area. The calculations also assumed that these vehicles emitted 100% of the cerium put into the engines and that the cerium accumulated in the top layer of soil for 10 years with no significant mobilization. This value struck a balance between realistic exposure concentrations and maintaining detectable limits.

Based on the average Ce concentration of 3400 ppm in the exhaust material, it was calculated that 0.78 g of exhaust material needed to be added to each 25 g dry weight soil amendment in order to achieve an increase of 100 ppm cerium. The 0.78 g of CeDPM was measured evenly from CeDPM from the four engine operating loads and combined with control soil to reach a combined soil/CeDPM weight of 25 g dry weight. For the DPM exposure, an equal mass was measured for comparison with the CeDPM. It is worth noting that a significant reason for using n-ceria FBCs is their ability to reduce DPM emissions 1-3 orders of magnitude.

All replicates were watered with 25 mL of 10% Hoagland solution immediately after surface application of the 25 g CeDPM/soil, DPM/soil, or control soil. For the commercial SmNP and LaNP exposures, 25g control soil was surface applied to each replicate followed by direct addition of 25 mL of 100 ppm Ce suspension in 10% Hoagland solution. In all cases, this first watering of 25 mL was spread evenly over the

top layer of soil, and care was taken to rinse any soil particles off of aboveground portions of plants.

3.3.5. Sample Collection

Drainage "water" was collected to determine the mobility of cerium through soil pore water channels. Drainage samples were collected by removing the plastic bags between plant pots and replacing them with new bags after 1, 8, 22, and 32 days for each replicate. The volume collected at each time point was the total amount of drainage "water" collected since the previous time of collection. The samples were stored in a refrigerator at 1.4 °C prior to analysis.

All plant and soil samples were collected over a two-day period at the conclusion of the 32-day exposure period. Soil samples were collected to determine the mobility of cerium downward through soils, and plant biomass was compared to generally assess the overall effects of the exposures on plant growth. The cerium concentration in the belowground biomass remaining after washing provided the amount of root-associated cerium (both on and in the roots) while the cerium concentration in the aboveground biomass confirmed (but did not disprove) if cerium was bioavailable – that is, able to cross the biological interface and enter the plant – and translocate into the aerial portions of the plant for each n-ceria exposure.

The aboveground plant biomass was collected by cutting the shoots at the soil level. Next, the soil block was removed from the plant pot along with the mesh root barrier. A soil core was collected from the block by cutting away 1 cm of soil from the edge, avoiding any primary roots, and then cutting out a 1 cm x 1 cm square section of soil down the depth of the soil block with a razor blade. The soil core was then separated

by depth into three sections: the top 1 cm, the next 2 cm, and everything below 3 cm (with a maximum depth of 5 cm). The soils were stored at room temperature prior to analysis. Belowground biomass was harvested from the soil block by washing away the soil with DI water.

The plant biomass was rinsed multiple times in DI water to remove debris and loosely associated cerium oxide particles. Aboveground biomass was first rinsed in a bath of DI, then in a water bath containing ~1% Dawn dish soap, followed by two rinses in DI water baths. Leaves and stems were gently rubbed to remove surface-adhered particles. The belowground biomass was first cleared of soil by gently spraying with DI water, followed by rinsing and gentle agitation in 3 consecutive DI water baths. Rinsing with water has been previously shown to remove over 90% of cerium nanoparticles in just three washes [16]. The belowground biomass (roots) were also picked clean of any visible organic debris using tweezers during rinsing. The belowground portion and about 0.5 cm of the aboveground biomass of one plant from each replicate was set aside after rinsing for analysis by TEM. The remaining plant biomass samples were segregated by above and below ground biomass for each replicate before drying overnight at 70 °C. Dried samples were weighed, crushed, and stored for future analysis at room temperature.

3.3.6. Sample Digestion

All water, soil, and biomass samples were digested using a modified EPA Method 3050B procedure to prepare samples for the measurement of cerium concentrations by ICP-OES. The digestion of a CeO_2 nanoparticle standard showed that this method had between 89-92% recovery of cerium.

Water samples were allowed to settle for a minimum of 24 hours before decanting into a separate container where volumes were approximated by mass. 5 mL aliquots of water samples were digested by the addition of 5 mL H_2O_2, which was maintained at room temperature for 30 minutes before increasing to 80 °C for 30 minutes. Next, 12 mL HCl and 4 mL HNO3 were added, the temperature increased to reflux at 100 ± 5 °C, and the vessel was loosely capped with a watch glass for at least 2 hours. Upon completion, the samples were cooled, passed through a 0.22 µm PTFE filter, and diluted to 50 mL.

Soil samples were homogenized in order to ensure representative samples were analyzed. 220-270 mg of each sample was dried at 70 °C overnight and then digested with 5 mL of H_2O_2 for 30 minutes at room temperature followed by 30 minutes at 80 ± 5 °C. Next, 12 mL HCl and 4 mL HNO3 were added and the temperature increased to reflux at 100 ± 5 °C and the vessel loosely capped with a watch glass for at least 2 hours. Digested samples were then cooled, filtered through a 0.22 µm, and diluted to 50 mL.

Biomass samples were ashed at 550 °C overnight in a muffle furnace to remove organic compounds and enable greater recovery rates in subsequent digestions. Each biomass sample was digested in its entirety for ICP-OES analysis. 5 mL H_2O_2 was added and maintained at room temperature for 30 minutes before increasing to 80 ± 5 °C for 30 minutes. Next, 15 mL HCl and 5 mL HNO3 were added, the temperature increased to reflux at 100 ± 5 °C, and the vessel loosely capped with a watch glass for at least 2 hours. Digested samples were then cooled, filtered through 0.22 µm, and diluted to 50 mL.

3.3.7. TEM Preparation and Analysis

One fresh belowground sample from each replicate was collected, rinsed, and placed in a bath of DI water overnight. Samples were then prepared for TEM analysis

through a gradual process of prefixing, fixing, dehydration, and resin embedding, as described by Stegemeier et al.[17] Briefly, a 1-cm portion of the junction between above- and belowground biomass (i.e., the root/shoot junction) and five lateral root tips (~1 cm) were sliced from each plant while submerged in a prefixitive solution of 0.1 M phosphate buffered 3.0% glutaraldehyde (pH 7.0). The segments were then placed in a 15-mL syringe and degassed in the same solution by application of a gentle vacuum until the segments sank to the bottom of the syringe. The segments then sat in the prefixative solution at room temperature for 2 hours, after which they were refrigerated at 4 °C for 1 week. The segments were then fixed in 1% OsO4 for 1 hr, followed by two 10-minute rinses in 0.1 M phosphate buffer. Segments were then dehydrated in series with 30, 50, 70, 90, 95, and 4x 100% EtOH for 15-20 minutes each. Finally, the segments were embedded in Spurr's Resin through a series of 2:1, 1:1, 1:2 EtOH: Spurr's Resin followed by 3x 100% Spurr's resin. Each embedding step lasted 5-14 hours, during which the segments were gently agitated in the resin mixture using a rotary mixer on low speed. The embedded segments were then cured for 24 hours at 60 °C, and thin sections were obtained using an ultramicrotome and deposited on hexagonal copper grids.

TEM analysis of the thin sections was conducted on a JEOL 2100 operating at 200 keV.

3.4. RESULTS AND DISCUSSION

All statistical analyses were performed assuming normal distributions using two-tailed tests at $\alpha = 0.05$ (95% confidence interval). Replicates were analyzed for outliers

using a Grubbs' test which required the rejection of no more than one data point per set. Between sets of data, Welch's t-tests were used to determine statistical significance of the measured differences. The plants from two replicates (one control and one CeDPM exposure) died over the course of the growth period (all plants in a single plant pot were dead). These replicates were not included in the biomass and cerium concentrations tabulated in the biomass datasets. One replicate from each exposure was lost during ashing of the plants in preparation for measuring the cerium concentration. The number of replicates was $n = 6$, except for the plant masses of the control and CeDPM exposures where n = 5 (due to the dead replicates), and except for the biomass cerium concentrations where $n = 4$ (due to loss from the ashing process, outliers, and dead replicates). Only a few more replicates are missing as noted in the data tables. The raw data can be found in the Supplementary Information Tables 3.1-4.

3.4.1. Biomass and General Observations

The replicates had no observable differences in the health of the plants, including number of leaves, plant height, coloration, or spotting. This lack of observable differences combined with the growth issues in single replicates from two different exposures, one of which was a control exposure, suggests that the dead replicates are not due to the exposures but more likely an issue with watering and drainage. Most replicates had between 1-3 individual plants that did not appear in good health at the conclusion of the experiment. This was observed for all exposures including the control.

The above and below ground dried biomass replicates were averaged and compared between exposures (Figure 3.2). The overall average for all exposures' aboveground biomass was 1.902 ± 0.068 g and 0.406 ± 0.033 g for the belowground

biomass. A one-way analysis of variance (ANOVA) indicated that the null hypothesis (that the samples come from the same population) should be accepted, suggesting that the exposures did not have a significant impact on the growth of the plants. The largest difference from the overall mean in the aboveground material was the CeDPM exposure, below the overall mean at 1.811 ± 0.096 g. The highest mean for aboveground biomass was the control at 1.956 ± 0.187 g. In the belowground material, the largest difference from the overall mean was the LaNP exposure which had a higher mean mass of 0.460 ± 0.071 g. The lowest belowground biomass was the SmNP exposure with a mean of 0.378 ± 0.075 g.

Even on the nanoscale, cerium oxide is generally considered non-toxic. In these experiments, no significant differences in the growth or overall health of the plants were discovered either visibly or statistically. The variability in biomass between replicates was small and a one-way ANOVA test indicated that the samples were drawn from populations with the same mean values. In other works, exposure to n-ceria has been shown to increase root length and biomass in cilantro[18], soybean[19], wheat[20] and alfalfa[19]. However, this effect is inconsistent across species, with evidence of root length and biomass decreases in tomato[19] and corn[21] as well as no significant biomass impacts on radish[22] after exposure to n-ceria. Typically, at moderate exposure concentrations of 500 ppm cerium or less, n-ceria hasn't been observed to induce broad level toxicity responses.[19, 23] At concentrations above 500 ppm Ce, n-ceria exposure has been shown to reduce yields and degrade nutritional value in corn[21] and soybean[24]. At the exposure concentration in this experiment, which represents a high exposure scenario from the

atmospheric deposition of ceria released from diesel emissions, no significant broad level toxicological impact was observed, in line with the previous data.

3.4.2. Cerium concentration in the water

The cerium concentration from water samples collected on days 1, 8, 22, and 32 of the exposure experiment are presented in SI Table 3.1. Due to high variability between replicates, the cerium concentrations in the water do not provide any statistically significant information on differences between the exposures. The presence of cerium in the breakthrough (drainage) water was highly inconsistent both within the replicates of a single exposure and across exposures. Over the course of the experiment, cerium was detected in the water of at least one replicate from every exposure. The control and DPM exposures each had a total of three replicates (out of a total of 24 measurements) containing measurable cerium concentrations, with no more than one detection on any given collection day and a maximum concentration of 0.33 ppm cerium. Even with the large variability, based on the mean, maximum value, and total number of replicates with detectable Ce, trends could be identified.

The LaNP exposure only had one replicate with observable cerium over the course of the experiment. The one detectable replicate came from the first day of collections. The lack of quantifiable cerium in the drainage water of the LaNP replicates indicates that the large ceria nanoparticles have a low mobility in the aquatic phase.

The SmNP exposure had the most consistently detectable cerium concentration with measureable concentrations in 5-6 replicates collected in each of the first three collection days. The cerium concentration tapers off quickly with an average of 9.44

ppm Ce on day 1, 2.16 ppm Ce on day 8, 1.23 ppm Ce on day 22, and only a single detectable replicate on day 32 at 0.23 ppm Ce. This suggests that the small ceria nanoparticles are highly mobile in the aquatic phase, resulting in the particles passing through the system rapidly. Though there was large variability between replicates, the decay trend remains relatively clear within the individual replicates.

The CeDPM had relatively few replicates producing measurable quantities of cerium but having at least one on every collection day. Samples collected on days 1, 22, and 32 had one replicate with detectable cerium, while on day 8 three replicates produced measurable cerium. All of the cerium concentrations measured in water for the CeDPM exposure were relatively low, with none above double the detection limit (0.44 ppm). Replicate 6, which had its plants die over the course of the experiment, had the highest total mass of cerium eluted for the CeDPM exposure at approximately 4.8% of the dosage. Two other replicates never had measurable cerium in the drainage water. This suggests that the CeDPM had a mobility somewhere between the LaNP and SmNP exposures and that it did not pass through the system fast enough to significantly elute out after the first day.

3.4.3. Cerium concentration in the soil

Soil samples were collected at the termination of the exposure experiments on day 32. The soil samples were separated by depth into three compartments or bins measured from the top of the soil at depths of 0-1 cm, 1-3 cm, and >3 cm. Soils from each bin were homogenized prior to analysis in order to assess the mobility of cerium through the soil. Cerium concentrations in the soils are presented in Figure 3.3.

The control soils provide a background concentration and show moderate variability between replicates with very little difference between the depth bins. The average cerium concentration in the control soil was 17.2 ± 2.7 ppm. From the concentration of cerium in the DPM, the increase of cerium in the dosing soil was expected to be less than 2 ppm. The cerium concentrations of the depth profile from the DPM replicates show slightly elevated concentrations compared to the control at 20.4 ± 1.9. A t-test indicated that the DPM exposure only had a statistically significant difference from the control in the top 0-1 cm.

The LaNP exposure exhibited a slightly increased cerium concentrations that were statistically different from the control in both the top 1 cm of soil at 24.0 ± 5.3 ppm Ce and the >3 cm soil at 21.3 ± 1.8 g. One replicate in the top 0-1 cm had a substantially increased cerium concentration and was removed after being rejected by a Grubbs' test for outliers. The overall average for the LaNP soils was 21.4 ± 2.8 ppm Ce and the concentrations of cerium by depth were consistent with the low mobility indicated by the water samples.

SmNP exposed soils contained significantly elevated cerium concentrations in the top 1 cm at 33.4 ± 8.2 ppm Ce. Additionally, the deepest bin at >3 cm contained significantly increased cerium concentrations with an average of 27.7 ± 5.2 ppm Ce, providing evidence of substantial downward mobility of the small ceria nanoparticles. The soil data remain consistent with the water data, indicating that the SmNPs have a relatively high mobility through the system. The relatively large error values are also consistent with the water samples, indicating that while trends may be apparent, these complex systems are not easily simplified to single values.

Soils exposed to CeDPM contain the most elevated cerium concentrations in the top 1 cm at 36.6 ± 9.4 ppm Ce. The CeDPM soil from 1-3 cm depth showed no evidence of significantly increased cerium concentrations, while the soil at a depth >3 cm was once again significantly elevated over the control to an average of 23.2 ± 3.4. The increase of cerium in the CeDPM exposed soils appears to be in line with the water data trends, with most of the material remaining in the top soil but a moderate mobility results in a quantifiable increase in the deepest soil.

The water data support the soil data in indicating the relative mobility of cerium from the various sources. Both sets of data suggest that (1) the small ceria NPs are highly mobile, moving downward through the soil and being regularly detected in the water; (2) the cerium from diesel exhaust is moderately mobile, being detectable at depth in the soil and occasionally in the water; and (3) the large ceria NPs do not appear to be significantly mobile, with soil concentrations not significantly above the background and only being detectable in 1 of 24 water replicates.

Increasing mobility decreases concentration (by dilution), which also increases the overall area of exposure resulting in greater contact with biological interfaces, improving the opportunity for nanoparticle uptake. The mobility of nanoparticles through porous media is controlled by their physicochemical properties such as size, shape, surface charge, and surfactant coating. The transport of n-ceria through saturated porous media may be altered by transformations induced by the local environment, such as aggregation and dissolution. Aggregation of n-ceria induced by ionic strength changes has been shown to reduce mobility[25, 26], while humic acid, a substitute for natural organic matter, results in a stabilizing effect that increases n-ceria mobility.[27] Several studies

have shown that variations in the media composition alter n-ceria mobility; for example n-ceria has been observed to be more mobile in quartz rather than loamy sands[26] and various soils have shown significantly different retentions of n-ceria.[28] In light of these complicating factors, the variability in mobility between ceria exposures in this study appears to fall within an expected range of values. These results are unable to determine the mechanism resulting in differing mobility, but due to the use of a single soil, conditions unlikely to promote significant dissolution, and the differences in surfactants between exposure materials, it seems likely that aggregation and hydrophobicity differences as a result of the various surfactants may be a key controlling factor.

3.4.4. Cerium concentration in the biomass

Cerium concentrations in the above and below ground plant biomasses were measured separately, calculated based on dry mass, and are presented in Figure 3.4. The concentrations in the belowground biomass provide approximations of cerium exposure that the plants had to endure, while the concentration in the aboveground biomass represents cerium that was taken up and translocated to the aerial portions of the plant, providing insight into bioavailability.

In the roots of the control plants, the cerium concentration was slightly elevated over the background soil concentration at 20.7 ± 1.0 ppm Ce (compared to the 17.2 ± 2.7 ppm Ce in the soil). The DPM and LaNP exposures had root cerium concentrations of 22.9 ± 3.2 and 20.1 ± 3.3 ppm Ce, respectively, very similar to their respective topsoil concentrations but not statistically different from the control roots. The roots from the SmNP exposure were significantly increased over its topsoil concentration at 121.0 ± 37.9 ppm Ce (compared to 33.4 ± 8.2 ppm Ce in its topsoil). Roots from the CeDPM

exposure were significantly elevated and in accordance with its soil concentration, resulting in 34.7 ± 9.2 ppm Ce. All of the exposures appear to mirror their topsoil cerium concentrations in the plant roots except for the SmNPs, which appear to be highly associated with the roots at an average rate of nearly 4x the replicates' respective topsoil concentrations.

An increase in the cerium concentration of the aboveground biomass indicates that the cerium was taken up and translocated to the aerial portion of the plant from the roots. The control shows that there is a significant decrease in aboveground concentration even with a relatively substantial belowground concentration, only containing 1.7 ± 0.6 ppm Ce in its aboveground biomass. The DPM exposure likewise had a very low transference of cerium into the aboveground biomass at 1.0 ± 0.2 ppm Ce. Plants exposed to LaNP also had very low cerium concentrations at only 1.3 ± 0.1 ppm Ce. Neither the DPM nor the LaNP exposure contained a statistically different concentration of cerium than the control in their aboveground biomasses. The SmNPs showed nearly an order of magnitude increase over the control in the aboveground biomass at 11.2 ± 0.6 ppm Ce. This is also approximately an order of magnitude lower than its root concentration. The CeDPM shoots show evidence of a slightly elevated cerium concentration at 2.2 ± 0.3 ppm Ce, though is wasn't statistically different from the control. It would appear that there is a barrier to translocation of Ce from the roots to the shoots in *B. napus* that decreases the cerium concentration by roughly 1 order of magnitude. Still, the significantly higher association of SmNP cerium to the plant roots accounts for most of the difference in the aboveground biomass as well. This

magnification from the soil to the roots implies that the SmNPs have a higher affinity for the roots than the other cerium exposure materials.

Significant impacts of nanoparticle exposure via soils begin with root contact. Similar to the SmNP and CeDPM exposures, n-ceria exposure has been observed to result in Ce-root association correlated to exposure concentration in cilantro[18], rice[29], wheat[20, 30]. Unsurprisingly, the root-associated cerium has been shown to increase with increasing exposure concentrations in rice[29] and cilantro[18]. While corn,[21, 31] rice,[29] and wheat[29] do not appear to significantly translocate cerium nanoparticles from their roots to the aerial portions of the plant, many other plants have been shown to translocate cerium from nanoparticle exposure including cilantro,[18] cucumber,[16] and soybean.[32 18] In addition, it has been shown that tomato[23] and radish[22] accumulate cerium from nanoparticle exposure in the edible portions of the plants. Lopez-Moreno et al. [19] used X-ray absorption spectroscopy to analyze the valence state of cerium present in four different plants after uptake of CeO_2 nanoparticles and determined that there was no detectable Ce(III), suggesting that the nanoparticles were taken up relatively untransformed. From our results, *Brassica napus* appears to be capable of significant uptake and translocation of n-ceria, though differences in the particles' characteristics appear to control the bioavailability and translocation of cerium.

3.4.5. Cerium distribution and mass balance

The overall distribution of cerium to the three primary partitions – soil, water, and plant –was calculated based on the averages for each exposure material. The data and explanation of calculations are provided in the Supplementary Information. The results

show that regardless of the exposure, the soil retains the bulk of the cerium at a minimum of 82% (from the small ceria nanoparticles). The water held 17% of the cerium from the small ceria nanoparticles, which reflects 1% from the cerium emissions. The plants themselves (combined into a single sum) represent a negligible amount of the cerium added, representing at a maximum of 1% of the cerium from the small ceria nanoparticles and 0% for all of the other exposures. Both the large ceria nanoparticles and the low-Ce DPM had negligible partitioning of cerium to the plants and water, with effectively 100% of their added cerium being found in the soil. These calculations show\ that regardless of the mobility of the particles, the soil acts as the largest sink for n-ceria and that elevated concentrations of cerium in the plants represent a tiny fraction of the overall cerium from the exposures.

From the concentration of the dosages multiplied by either the mass or volume (for the emitted cerium or commercial cerium, respectively) of the dose, 2.5 mg of cerium was expected to be added to each replicate above the background concentration.. Mass balance calculations were performed by totaling the cerium increase over the background (as determined by the control replicates) from the water, soil, and biomass. Replicates exposed to small nanoparticles had an average of 5.0 mg Ce above the background, double the expected total mass of cerium. The emitted cerium was also above the expected total cerium mass at 3.3 mg cerium between the water, soil, and biomass compartments. This excess of cerium is likely due to the large uncertainty regarding the soil depth bins and their relative makeup of the overall soil mass, potentially over representing the bins with elevated cerium concentrations, e.g. the top and bottom depth bins. Only 62% of the cerium added was accounted for from the large

ceria nanoparticle exposures across all of the analyzed partitions – soil, water, and plant. This indicates that significant differences between the large ceria nanoparticle exposure and the other two cerium exposures result in differences in accounting of the cerium by mass. It is possible that the large ceria nanoparticles are not being accurately accounted for due to a preferential transport path that avoided the sampling protocols used here. Additionally, the large nanoparticles may be more difficult to detect, resisting digestion and analysis due to their size, aggregation state, surface area, or other factors, resulting in the under reporting that appears to pervade the large nanoparticle samples.

3.5. CONCLUSIONS

This study compared the effects of exposure to various forms of cerium oxide nanoparticles on the plant *Brassica napus*, focusing on the differences between n-ceria emitted from the exhaust of a diesel engine using a fuel-borne catalyst, a small ceria nanoparticle produced by a chemical supply company resembling the particles found in the catalyst, and a large ceria nanoparticle close in size to the emitted ceria also purchased from a chemical supply company. In summary, the two commercially-produced nanoparticles displayed significantly different behavior with the SmNPs appearing to be highly mobile and showing evidence of bioavailability and translocation while the LaNPs appeared to have a low mobility and showed no evidence of bioavailability or translocation. Ceria particles found in DPM from the use of a diesel fuel-borne catalyst displayed behavior between the two commercial endpoints, with lower but measurable mobility and root association. Bioavailability and translocation of the cerium in DPM was not as evident, with an elevated cerium concentration in the

aboveground plant that was not statistically different from the control. The substantial differences between the cerium concentrations in the aboveground and belowground biomass are likely the result of biological barriers. This barrier is most likely to occur at either (1) the root surface, preventing the uptake of the nanoparticles and resulting in deposition onto the root but preventing the cerium from becoming bioavailable, or (2) between the root and shoot, where contaminants may be filtered from translocating into the aerial portion of the plant. None of the exposures appeared to have significant adverse effects on the overall health of the plants, though more toxicological endpoints need to be assessed to make such a broad determination.

The results of this work demonstrate that traditionally studied cerium oxide NPs – those purchased from chemical supply companies, suspended in liquids, and coated in surfactants – are unlikely to capture the trends that would occur from exposure to ceria particles released by the use of n-ceria fuel-borne catalysts. The efficacy of such catalysts in reducing carcinogenic DPM emissions and increasing fuel efficiency has been proven, but concern over the potential health impacts has prevented their widespread adoption. In order to address these concerns, it is critical that realistic emissions scenarios be studied using representative particles. To do this, future studies must take into account:

- The particles – it is well known that numerous variables control the behavior of nanoparticles and we have demonstrated that the behavior of n-ceria emissions byproducts is not well captured by commercial counterparts.
- Emissions routes – particles that are transported through the air can travel great distances and will likely be modified en route; particles in aquatic

environments are likely to aggregate and are also exposed to a broad range of chemical conditions; and particles in soils will interact with soil solutions, as well as a complex variety of organic and inorganic matter.

- Concentrations – past studies have often utilized concentrations well above the worst-case scenarios primarily to ensure detection and induce toxicological effects which may not be representative of realistic scenarios.

Through the use of modern analytical techniques combined with innovative experimental setups, it is possible to elucidate the environmental and health impacts of the use of n-ceria fuel-borne catalysts. If n-ceria FBCs are determined to be safe, their widespread use will result in a significant improvement in air quality through the reduction of soot emissions and its associated human health benefits, and knowing that we are not introducing another contaminant into the atmosphere, surface water, or soils.

3.6 REFERENCES

1. Handy, R. D.; Owen, R.; Valsami-Jones, E., The ecotoxicology of nanoparticles and nanomaterials: current status, knowledge gaps, challenges, and future needs. *Ecotoxicology* **2008,** *17*, (5), 315-325.

2. Perfect, J., The environmental impact of DDT in a tropical agro-ecosystem. *Ambio* **1980**, 16-21.

3. Chichiriccò, G.; Poma, A., Penetration and toxicity of nanomaterials in higher plants. *Nanomaterials* **2015,** *5*, (2), 851-873.

4. Van Hoecke, K.; De Schamphelaere, K. A.; Van der Meeren, P.; Smagghe, G.; Janssen, C. R., Aggregation and ecotoxicity of CeO 2 nanoparticles in synthetic and natural waters with variable pH, organic matter concentration and ionic strength. *Environmental Pollution* **2011,** *159*, (4), 970-976.

5. Schwabe, F.; Schulin, R.; Limbach, L. K.; Stark, W.; Bürge, D.; Nowack, B., Influence of two types of organic matter on interaction of CeO 2 nanoparticles with plants in hydroponic culture. *Chemosphere* **2013,** *91*, (4), 512-520.

6. Park, B.; Donaldson, K.; Duffin, R.; Tran, L.; Kelly, F.; Mudway, I.; Morin, J.-P.; Guest, R.; Jenkinson, P.; Samaras, Z., Hazard and risk assessment of a nanoparticulate cerium oxide-based diesel fuel additive-a case study. *Inhalation toxicology* **2008,** *20*, (6), 547-566.

7. Peters, A.; Von Klot, S.; Heier, M.; Trentinaglia, I.; Hörmann, A.; Wichmann, H. E.; Löwel, H., Exposure to traffic and the onset of myocardial infarction. *New England Journal of Medicine* **2004,** *351*, (17), 1721-1730.

8. Dale, J. G.; Cox, S. S.; Vance, M. E.; Marr, L. C.; Hochella, M. F., Transformation of cerium oxide nanoparticles from a diesel fuel additive during combustion in a diesel engine. *Environmental Science & Technology* **2017**.

9. Gantt, B.; Hoque, S.; Fahey, K. M.; Willis, R. D.; Delgado-Saborit, J. M.; Harrison, R. M.; Zhang, K. M.; Jefferson, D. A.; Kalberer, M.; Bunker, K. L., Factors affecting the ambient physicochemical properties of cerium-containing particles generated by nanoparticle diesel fuel additive use. *Aerosol Science and Technology* **2015,** *49*, (6), 371-380.

10. Government, A., The Biology of *Brassica napus* L. (canola). In Ageing, D. o. H. a., Ed. 2008.

11. Ebbs, S.; Lasat, M.; Brady, D.; Cornish, J.; Gordon, R.; Kochian, L., Phytoextraction of cadmium and zinc from a contaminated soil. *Journal of Environmental Quality* **1997,** *26*, (5), 1424-1430.

12. Fernández, M. D.; Cagigal, E.; Vega, M. M.; Urzelai, A.; Babín, M.; Pro, J.; Tarazona, J. V., Ecological risk assessment of contaminated soils through direct toxicity assessment. *Ecotoxicology and environmental safety* **2005,** *62*, (2), 174-184.

13. Cui, J.; Zhang, R.; Wu, G. L.; Zhu, H. M.; Yang, H., Salicylic acid reduces napropamide toxicity by preventing its accumulation in rapeseed (Brassica napus L.). *Archives of environmental contamination and toxicology* **2010,** *59*, (1), 100-108.

14. Larue, C.; Pinault, M.; Czarny, B.; Georgin, D.; Jaillard, D.; Bendiab, N.; Mayne-L'Hermite, M.; Taran, F.; Dive, V.; Carrière, M., Quantitative evaluation of multi-walled carbon nanotube uptake in wheat and rapeseed. *Journal of hazardous materials* **2012,** *227*, 155-163.

15. Zhang, J.; Pan, L.; Lv, M.; Aldalbahi, A.; Xie, T.; Li, A.; Tai, R.; Huang, Q.; Fan, C.; Zhao, Y., Transportation and fate of gold nanoparticles in oilseed rape. *RSC Advances* **2015,** *5*, (90), 73827-73833.

16. Zhang, Z.; He, X.; Zhang, H.; Ma, Y.; Zhang, P.; Ding, Y.; Zhao, Y., Uptake and distribution of ceria nanoparticles in cucumber plants. *Metallomics* **2011,** *3*, (8), 816-822.

17. Stegemeier, J. P.; Schwab, F.; Colman, B. P.; Webb, S. M.; Newville, M.; Lanzirotti, A.; Winkler, C.; Wiesner, M. R.; Lowry, G. V., Speciation matters: Bioavailability of silver and silver sulfide nanoparticles to alfalfa (Medicago sativa). *Environmental science & technology* **2015,** *49*, (14), 8451-8460.

18. Morales, M. I.; Rico, C. M.; Hernandez-Viezcas, J. A.; Nunez, J. E.; Barrios, A. C.; Tafoya, A.; Flores-Marges, J. P.; Peralta-Videa, J. R.; Gardea-Torresdey, J. L., Toxicity assessment of cerium oxide nanoparticles in cilantro (Coriandrum sativum L.) plants grown in organic soil. *Journal of agricultural and food chemistry* **2013,** *61*, (26), 6224-6230.

19. Lopez-Moreno, M. L.; de la Rosa, G.; Hernandez-Viezcas, J. A.; Peralta-Videa, J. R.; Gardea-Torresdey, J. L., X-ray Absorption Spectroscopy (XAS) Corroboration of the Uptake and Storage of CeO2 Nanoparticles and Assessment of Their Differential Toxicity in Four Edible Plant Species. *Journal of Agricultural and Food Chemistry* **2010,** *58*, (6), 3689-3693.

20. Rico, C. M.; Lee, S. C.; Rubenecia, R.; Mukherjee, A.; Hong, J.; Peralta-Videa, J. R.; Gardea-Torresdey, J. L., Cerium oxide nanoparticles impact yield and modify nutritional parameters in wheat (Triticum aestivum L.). *Journal of agricultural and food chemistry* **2014,** *62*, (40), 9669-9675.

21. Zhao, L.; Sun, Y.; Hernandez-Viezcas, J. A.; Hong, J.; Majumdar, S.; Niu, G.; Duarte-Gardea, M.; Peralta-Videa, J. R.; Gardea-Torresdey, J. L., Monitoring the environmental effects of CeO2 and ZnO nanoparticles through the life cycle of corn (Zea mays) plants and in situ μ-XRF mapping of nutrients in kernels. *Environmental science & technology* **2015,** *49*, (5), 2921-2928.

22. Zhang, W.; Ebbs, S. D.; Musante, C.; White, J. C.; Gao, C.; Ma, X., Uptake and accumulation of bulk and nanosized cerium oxide particles and ionic cerium by radish (Raphanus sativus L.). *Journal of agricultural and food chemistry* **2015,** *63*, (2), 382-390.

23. Wang, Q.; Ma, X.; Zhang, W.; Pei, H.; Chen, Y., The impact of cerium oxide nanoparticles on tomato (Solanum lycopersicum L.) and its implications for food safety. *Metallomics* **2012,** *4*, (10), 1105-1112.

24. Peralta-Videa, J. R.; Hernandez-Viezcas, J. A.; Zhao, L.; Diaz, B. C.; Ge, Y.; Priester, J. H.; Holden, P. A.; Gardea-Torresdey, J. L., Cerium dioxide and zinc oxide nanoparticles alter the nutritional value of soil cultivated soybean plants. *Plant Physiology and Biochemistry* **2014,** *80*, 128-135.

25. Limbach, L. K.; Bereiter, R.; Müller, E.; Krebs, R.; Gälli, R.; Stark, W. J., Removal of oxide nanoparticles in a model wastewater treatment plant: influence of agglomeration and surfactants on clearing efficiency. *Environmental science & technology* **2008,** *42*, (15), 5828-5833.

26. Petosa, A. R.; Öhl, C.; Rajput, F.; Tufenkji, N., Mobility of nanosized cerium dioxide and polymeric capsules in quartz and loamy sands saturated with model and natural groundwaters. *Water research* **2013,** *47*, (15), 5889-5900.

27. Lv, X.; Gao, B.; Sun, Y.; Shi, X.; Xu, H.; Wu, J., Effects of humic acid and solution chemistry on the retention and transport of cerium dioxide nanoparticles in saturated porous media. *Water, Air, & Soil Pollution* **2014,** *225*, (10), 2167.

28. Cornelis, G.; Kirby, J. K.; Beak, D.; Chittleborough, D.; McLaughlin, M. J., A method for determination of retention of silver and cerium oxide manufactured nanoparticles in soils. *Environmental Chemistry* **2010,** *7*, (3), 298-308.

29. Rico, C. M.; Hong, J.; Morales, M. I.; Zhao, L.; Barrios, A. C.; Zhang, J.-Y.; Peralta-Videa, J. R.; Gardea-Torresdey, J. L., Effect of cerium oxide nanoparticles on rice: a study involving the antioxidant defense system and in vivo fluorescence imaging. *Environmental science & technology* **2013,** *47*, (11), 5635-5642.

30. Wild, E.; Jones, K. C., Novel method for the direct visualization of in vivo nanomaterials and chemical interactions in plants. *Environmental science & technology* **2009,** *43*, (14), 5290-5294.

31. Birbaum, K.; Brogioli, R.; Schellenberg, M.; Martinoia, E.; Stark, W. J.; Gunther, D.; Limbach, L. K., No Evidence for Cerium Dioxide Nanoparticle Translocation in Maize Plants. *Environmental Science & Technology* **2010,** *44*, (22), 8718-8723.

32. López-Moreno, M. L.; de la Rosa, G.; Hernández-Viezcas, J. Á.; Castillo-Michel, H.; Botez, C. E.; Peralta-Videa, J. R.; Gardea-Torresdey, J. L., Evidence of the differential biotransformation and genotoxicity of ZnO and CeO2 nanoparticles on soybean (Glycine max) plants. *Environmental science & technology* **2010,** *44*, (19), 7315.

3.7. FIGURES

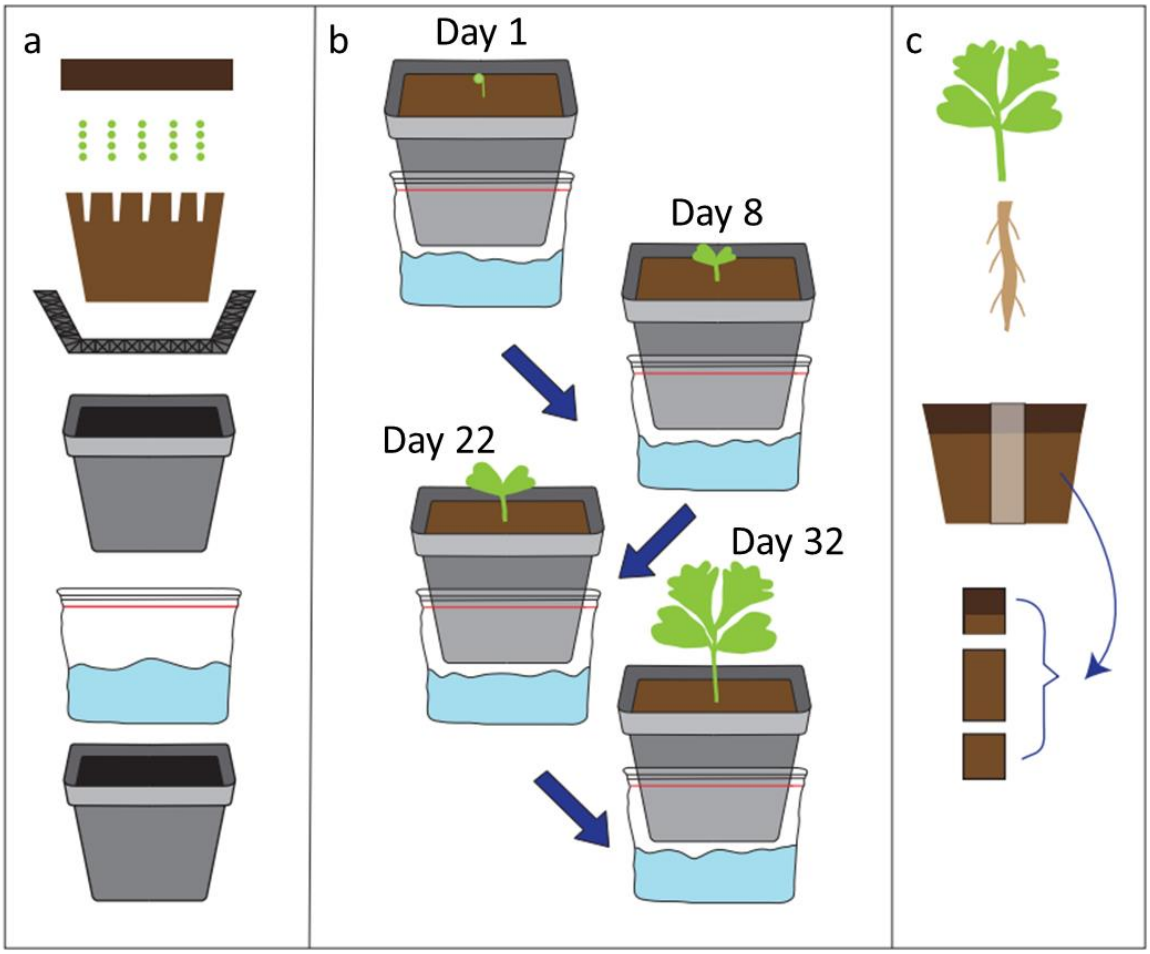

Figure 3.1. Diagram overview of the exposure experiment. (a) Shows the construction of each replicate, comprised (from bottom to top) of a 4" plant pot, zip-top bag for water collection, another 4" plant pot, mesh root barrier, 425 g control soil, 20 *B. napus* seedlings, and 25 g of exposure soil. (b) Indicates the days in which the drainage water was collected. (c) Shows the harvesting of the biomass and soil core samples at the completion of the experiment on day 32.

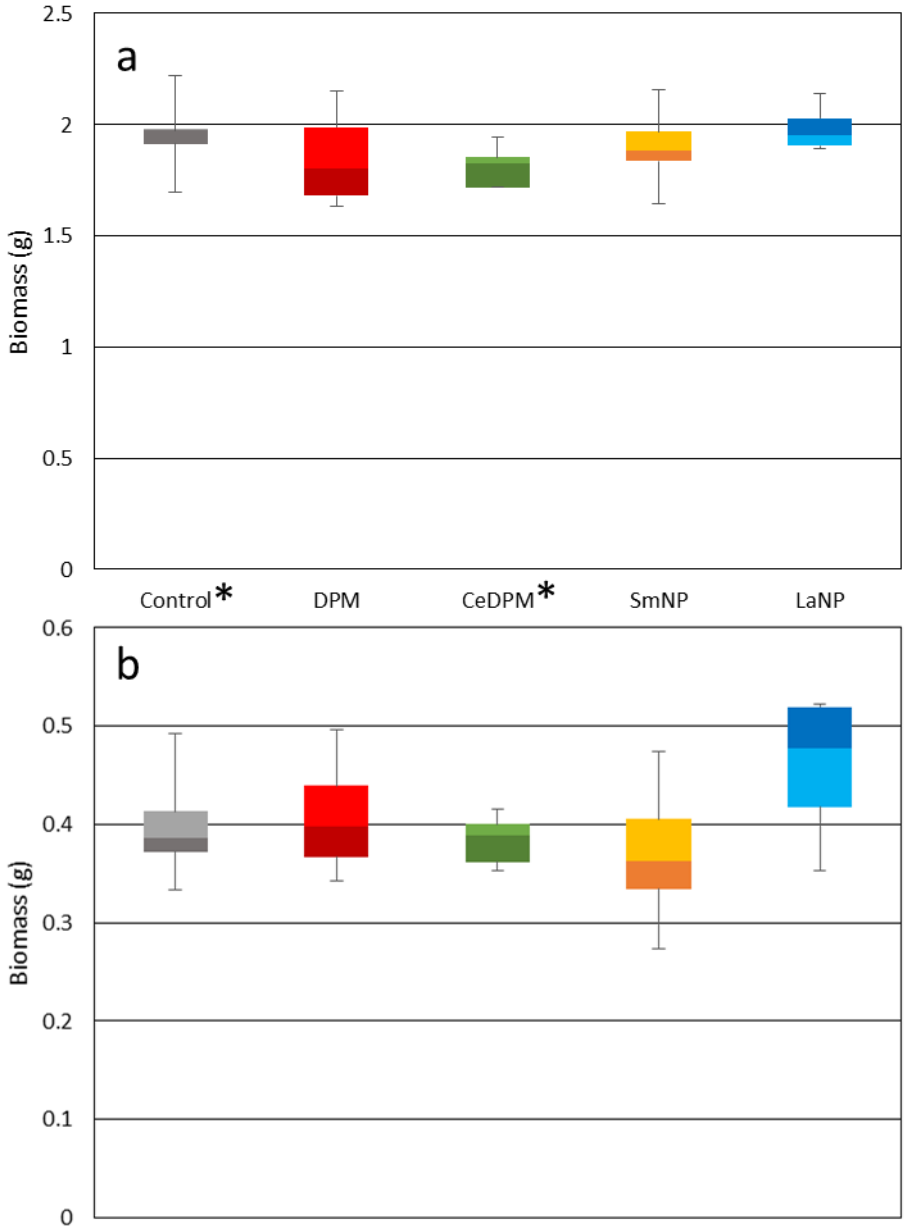

Figure 3.2. Biomass in grams of the (a) aboveground and (b) belowground plant material for each exposure. None of the exposures were statistically different from the control. N = 6 except where *: N = 5.

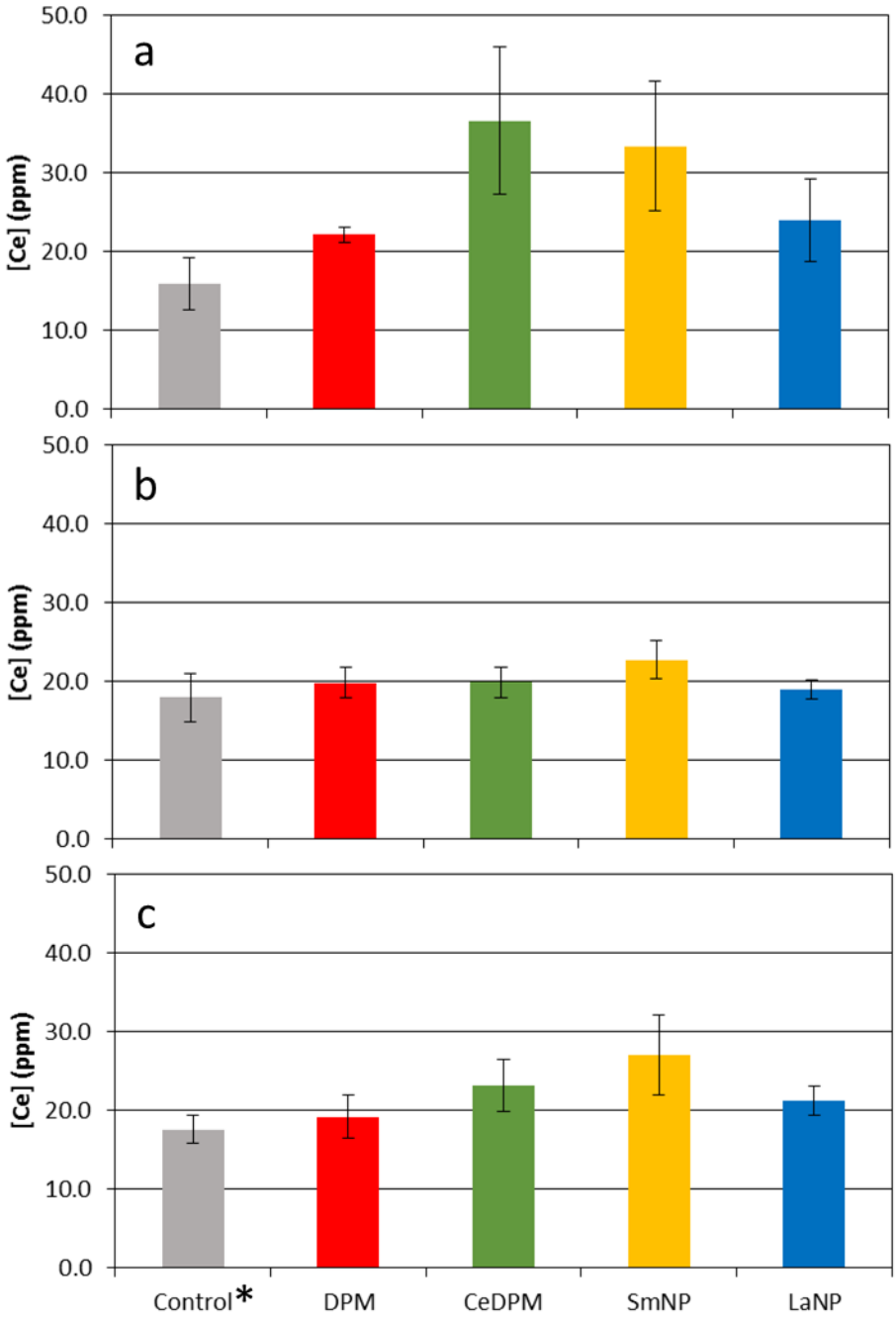

Figure 3.3. Concentration of cerium in the soil for each exposure at depths of (a) < 1 cm, (b) 1-3 cm, and (c) > 3 cm. Cerium concentrations were increased above the control for the CeDPM, SmNP and LaNP in (a) the top 1 cm, and for CeDPM and SmNP in (c) the soil > 3 cm. No exposures exhibited statistically differing cerium concentrations in (b) the middle soil. N = 6 except where *: N = 5.

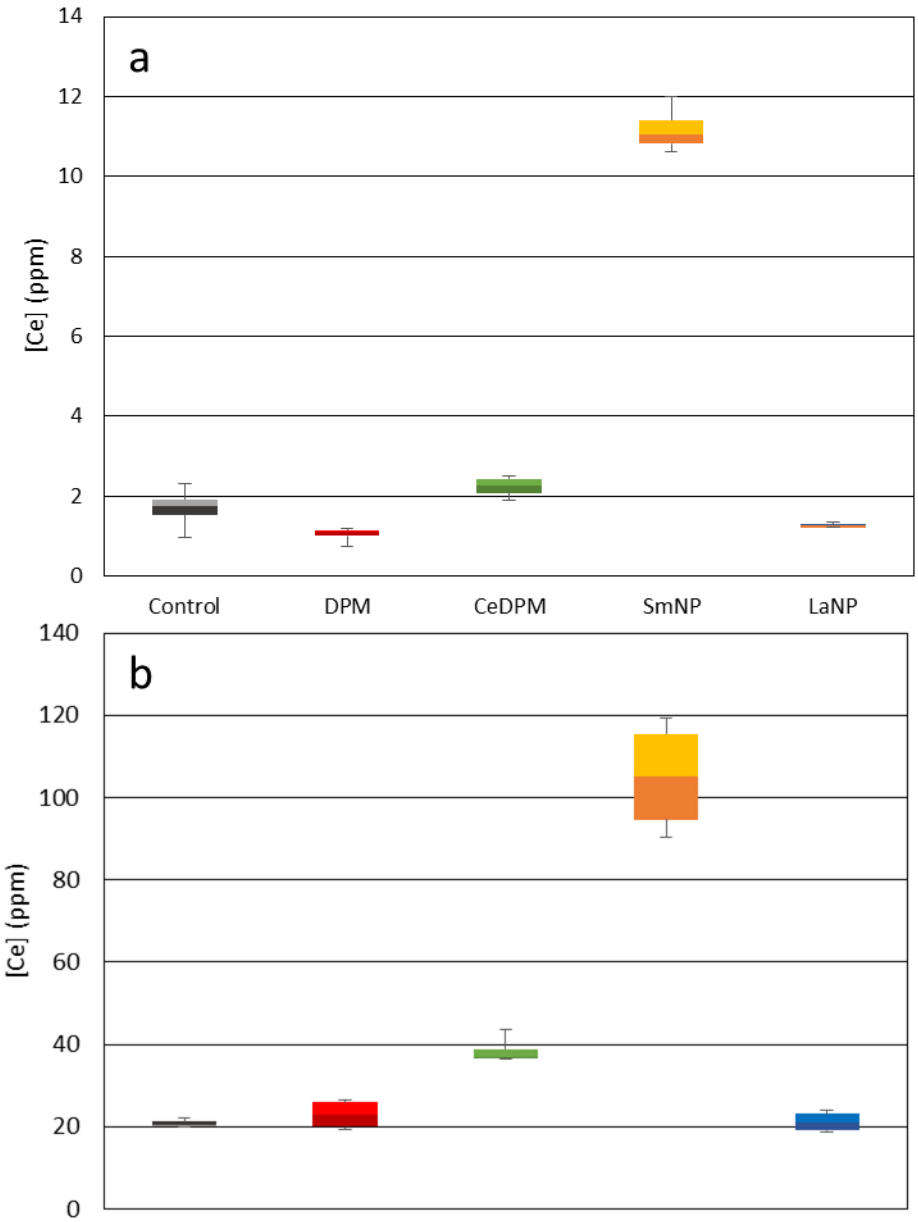

Figure 3.4. Concentration of cerium in the (a) aboveground and (b) belowground biomass. (b) Shows significant increases in root-associated cerium for the CeDPM and SmNP exposures. (a) Indicates that while the SmNP translocate into the aerial portion of the plants, the CeDPM does not seem to do so significantly. N = 4.

3.8. SUPPLEMENTARY INFORMATION

3.8.1. Soil exposure concentration

From the mass concentration modeling conducted by Gantt et al.,[1] the slope of the line over distance was used to determine the loss of cerium per meter. The slope was extracted from the graph and determined to be approximately 1.2 $\mu g/m^3$ per m from the source (the road). This value represents the mass concentration of cerium lost on average over each meter of ground (in the range of approximately 30 to 60 meters) to dilution and deposition. No time factor is included in these values, so in order to determine a deposition per unit time, the wind speed was utilized. The calculations performed by Gantt et al. used a wind speed of 1 m/s. From this value, it was assumed that the concentration in the cube of air is refreshed every second, resulting in a loss of 1.2 μg per m (from the cubic meter of soil above it) every second. Extrapolated to one year, this results in a loss of approximately 3760 mg per year into a square meter of soil. Soil density is highly variable based on a number of factors and for these calculations a density of 1.3 g/cm^3 was selected. Similarly, the definition of the depth of 'topsoil' is highly variable and was set to 2 cm for this calculation. Assuming the cerium loss is entirely due to deposition, over the course of one year, the expected topsoil concentration in a square meter of soil would be expected to increase by approximately 145 ppm Ce. This value was rounded down to 100 ppm Ce.

3.8.2. Distribution and mass balance calculations

The calculations for the distribution and mass balance of cerium were performed using the mean values for each exposure. The mean cerium mass was calculated for the soil at each depth bin. The mass of soil per bin was calculated by assuming that the total

original soil mass (450 g) was evenly distributed by depth and that the average depth of a replicate was 4.5 cm. By this method, the top bin (0-1 cm) was determined to be 22%, the middle (1-3 cm) 44%, and the bottom (>3 cm) 33% of the total soil mass. The total mass of cerium per bin was extrapolated from these values and the background mass (determined from the control) was subtracted. Volumes of water collected were recorded and averaged in order to extrapolate the mean mass of cerium per exposure and was summed for all four collections. Again, the control mass was subtracted. Finally, the mean mass of the plants was multiplied by the mean cerium concentration, summed, and the control was subtracted. To arrive at distributions between the partitions, the three partitions were summed to determine the total recovered cerium mass above the background.

3.8.3. References

1. Gantt, B.; Hoque, S.; Fahey, K. M.; Willis, R. D.; Delgado-Saborit, J. M.; Harrison, R. M.; Zhang, K. M.; Jefferson, D. A.; Kalberer, M.; Bunker, K. L., Factors affecting the ambient physicochemical properties of cerium-containing particles generated by nanoparticle diesel fuel additive use. *Aerosol Science and Technology* **2015,** *49*, (6), 371-380.

3.9. SUPPLEMENTARY TABLES

Supplementary Table 3.1. Dried biomass of the above and below ground plant material from each replicate of all five exposures. The control 3 and CeDPM 6 replicates were dead at the conclusion of the experiment.

		Biomass (g)					
		Replicates					
		1	2	3	4	5	6
Control	Aboveground	2.222	1.698	1.465	1.975	1.974	1.914
	Belowground	0.492	0.372	0.620	0.386	0.413	0.333
DPM	Aboveground	1.820	1.781	2.151	1.632	2.044	1.648
	Belowground	0.413	0.496	0.448	0.343	0.362	0.383
CeDPM	Aboveground	1.718	1.718	1.827	1.852	1.944	0.824
	Belowground	0.353	0.389	0.416	0.361	0.400	0.068
SmNP	Aboveground	2.156	1.992	1.864	1.899	1.828	1.642
	Belowground	0.474	0.360	0.367	0.273	0.418	0.326
LaNP	Aboveground	1.891	1.991	1.901	2.040	1.918	2.141
	Belowground	0.353	0.436	0.412	0.522	0.519	0.520

Supplementary Table 3.2. Concentration of cerium in the drainage water on days 1, 8, 22, and 32 of the exposure experiment for each of the 6 replicates and 5 exposures. Most of the samples fell below the detection limit.

		[Ce] in Drainage Water (ppm)					
		Replicates					
		1	2	3	4	5	6
Control	Day 1	0.00	0.00	0.00	0.00	0.00	0.00
	Day 8	0.33	0.00	0.00	0.00	0.00	0.00
	Day 22	0.27	0.00	0.00	0.00	0.00	0.00
	Day 32	0.00	0.00	0.00	0.00	0.00	0.00
DPM	Day 1	0.00	0.00	0.00	0.00	0.00	0.00
	Day 8	0.00	0.00	0.00	0.00	0.00	0.00
	Day 22	0.00	0.00	0.19	0.00	0.00	0.00
	Day 32	0.00	0.00	0.00	0.00	0.00	0.00
CeDPM	Day 1	0.00	0.00	0.00	0.00	0.27	0.00
	Day 8	0.00	0.00	0.00	0.24	0.22	0.35
	Day 22	0.00	0.00	0.35	0.00	0.00	0.00
	Day 32	0.00	0.00	0.00	0.00	0.00	0.30
SmNP	Day 1	3.02	4.38	22.84	1.92	21.50	2.95
	Day 8	1.52	0.69	2.34	0.45	6.13	1.18
	Day 22	1.13	0.60	4.46	0.00	0.42	0.75
	Day 32	0.23	0.00	0.00	0.00	0.00	0.00
LaNP	Day 1	0.00	0.00	0.00	0.00	0.25	0.00
	Day 8	0.00	0.00	0.00	0.00	0.00	0.00
	Day 22	0.00	0.00	0.00	0.00	0.00	0.00
	Day 32	0.00	0.00	0.00	0.00	0.00	0.00

Supplementary Table 3.3. Concentration of cerium in each of three depth bins of the soils, separated into the top 0-1 cm, 1-3 cm, and >3 cm, for all five exposures and each of the six replicates.

		[Ce] in Soils (ppm)					
		Replicates					
		1	2	3	4	5	6
Control	Top (0-1 cm)	10.40		18.06	15.82	18.62	16.94
	Middle (1-3 cm)	14.11		17.87	17.99	22.68	17.38
	Bottom (>3 cm)	15.45		18.15	18.06	19.98	16.45
DPM	Top (0-1 cm)	22.06	21.49	21.91	21.12	22.82	23.73
	Middle (1-3 cm)	20.07	18.74	21.09	19.48	19.94	15.63
	Bottom (>3 cm)	22.84	16.27	19.99	17.35	19.47	15.46
CeDPM	Top (0-1 cm)	32.54	31.12	26.39	35.31	52.83	41.67
	Middle (1-3 cm)	22.67	20.04	16.76	20.38	19.99	19.48
	Bottom (>3 cm)	20.33	22.42	24.89	22.21	29.12	20.30
SmNP	Top (0-1 cm)	34.65	36.91	46.82	22.64	29.47	29.67
	Middle (1-3 cm)	25.21	21.78	25.51	19.51	23.64	20.91
	Bottom (>3 cm)	24.15	23.72	23.62	32.74	23.95	34.50
LaNP	Top (0-1 cm)	25.27	18.50	21.42	33.67	23.88	21.26
	Middle (1-3 cm)	18.79	17.90	17.63	20.29	20.69	18.94
	Bottom (>3 cm)	18.54	23.18	21.19	22.67	22.31	19.63

Supplementary Table 3.4. Concentration of cerium in the plant biomass, separated into the above and belowground material. All of the second replicates were lost during the ashing step. The control 3 and CeDPM 6 replicates are not shown because the plants in those two replicates were dead at the conclusion of the experiment.

		[Ce] in Plant Biomass (ppm)				
		Replicates				
		1	2	3	4	5	6
Control	Aboveground	1.71			0.96	2.31	1.78
	Belowground	20.01			20.99	22.02	19.83
DPM	Aboveground	2.47		1.10	1.20	1.14	0.73
	Belowground	23.00		26.35	20.27	19.15	25.76
CeDPM	Aboveground	2.41		2.50	2.13	1.90	
	Belowground	36.52		43.65	37.25	23.54	
SmNP	Aboveground	15.96		10.89	10.62	11.21	12.01
	Belowground	114.27		96.06	90.30	119.26	185.19
LaNP	Aboveground	1.53		1.22	1.20	1.28	1.35
	Belowground	15.73		23.83	18.76	19.13	22.81

APPENDIX A:

Sulfidation of copper oxide nanoparticles and properties of resulting copper sulfide

Rui Ma,[abh] John Stegemeier,[ab] Clément Levard,[bc] James G. Dale,[bd] Clinton W. Noack,[a] Tiffany Yang,[ab] Gordon E. Brown Jr.[efg] and Gregory V. Lowry[*ab]

[a]Department of Civil & Environmental Engineering, Carnegie Mellon University, USA.
[b]Center for Environmental Implications of Nanotechnology (CEINT), USA
[c]Aix-Marseille Université, CNRS, IRD, CEREGE UM34, 13545 Aix en Provence, France
[d]Department of Geosciences, Virginia Tech, USA
[e]Department of Geological & Environmental Sciences, Stanford University, USA
[f]Stanford Synchrotron Radiation Lightsource, SLAC National Accelerator Laboratory, USA
[g]Department of Photon Science, SLAC National Accelerator Laboratory, Menlo Park, CA, USA
[h]Ecological Environment Institute, Chinese Academy for Environmental Planning, Beijing, China

Reprinted with permission from *Environmental Science: Nano*, 2014, 1, 347-357.

A.1. NANO IMPACT

Metal and metal oxide nanomaterials that find their way into reducing environments such as wastewater treatment plants or subaquatic sediments may potentially become sulfidized. The properties of the sulfidized materials will control their fate and toxicity so those properties must be determined. This work describes the sulfidation of CuO nanoparticles, and determines the properties of the sulfidized copper product under environmental conditions that are relevant to predicting fate and toxicity, *e.g.* solubility. This enhances our understanding of the behavior of these nanomaterials in important environmental compartments, and better enables predictions of their interactions with natural systems.

A.2. ABSTRACT

Many nanoparticles (NPs) are transformed in the environment, and the properties of the transformed materials must be determined to accurately assess their environmental risk. Sulfidation is expected to alter the speciation and properties of CuO NPs significantly. Here, commercially available 40 nm CuO NPs were characterized and sulfidized in water by inorganic sulfide, and the properties of the resulting products were determined. X-ray absorption spectroscopy, X-ray diffraction, and transmission electron microscopy indicate that CuO (tenorite) is sulfidized by inorganic sulfide to several copper sulfide (Cu_xS_y) species including crystalline CuS (covellite), and amorphous (Cu_xS_y) species at ambient temperature. Some Cu(II) was reduced to Cu(I) during sulfidation, coupled with sulfide oxidation to sulfate, resulting in the formation of small amounts of several copper sulfate hydroxide species as well. The extent of sulfidation depends on the sulfide to CuO molar concentration ratio used. At the highest S/Cu molar ratio of 2.16, 100% sulfidation was not reached in 7 days, as evidenced by the persistence of small amounts of CuO in the NPs. Sulfidation increased the fraction of copper passing a 3 kDa MWCO filter representing soluble forms of Cu and any small CuxSy clusters compared to the pristine CuO NPs at environmentally relevant neutral pH. This high solubility is a result of oxidative dissolution of Cu_xS_y, formation of relatively more soluble copper sulfate hydroxides, and the formation of small CuS nanoclusters that pass the 3 kDa MWCO filter. These findings suggest that sulfidation of CuO may increase its apparent solubility and resulting bioavailability and eco-toxicity attributed to toxic Cu^{2+}.

A.3. INTRODUCTION

Copper-based nanoparticles (NPs) are being used in products or technologies like semiconductors, heat transfer fluids, catalysts, batteries, solar cells and biocides.[1–6] Copper based NPs such as CuO and elemental Cu(0) were found to be among the top five most reported metal NPs in recent (2011) nanotechnology patents, indicating the potential for an increasing use of these NPs.[7] Their widespread uses will likely lead to subsequent release into the environment, and will raise concern about their potential toxicity. Nano Cu(0) was reported to have a thin oxide layer when exposed to air, where the Cu(0) is oxidized to form Cu_2O and then ultimately to CuO in an aerobic environment.[8] Hence, CuO NPs are an environmentally relevant form of copper for assessing the risks of nano copper products.

The toxicity of CuO NPs to a variety of organisms has been studied extensively. According to a recent critical review, CuO NPs are toxic to crustaceans, algae, fish and bacteria, but typically requires higher doses than Cu^{2+} ions to achieve the same effects. Cu^{2+} was found to be more toxic to all organisms except for yeast and mammalian cells in vitro.[9] Although Cu(0) NPs can catalyze the formation of reactive oxygen species (ROS), leading to toxicity.[10,11] CuO dissolution to release Cu^{2+} accounted for most of the observed toxicity in vitro and in vivo.[12] This indicates that the ability of the NPs to release Cu^{2+} plays a key role in copper NP toxicity.

The dissolution of CuO NPs resulting in the release of Cu^{2+} ions is pH dependent. The dissolution minimum is expected at near neutral pH (6–8). However, the solubility is significantly higher at lower pH (4–5). Dissolution of CuO NPs is also promoted by strong ligands such as amino acids,[11,13] even at neutral pH. This behavior makes CuO

NPs one of the more toxic metal oxides NP in cell culture media (containing amino acids).[14]

Sulfidation is an important transformation of many metal and metal oxide NPs. This is because sulfidation has been demonstrated to affect NP chemical composition,[15,16] to reduce ion release,[16,17] and to significantly decrease the toxicity of Ag NPs to a range of organism types.[15,18] Ag, ZnO, and CuO NPs all contain class B soft metals[19] and are likely to sulfidize once released into the environment. Donner et al. showed that 74–92% of the Cu is present as Cu(I) and Cu(II) sulfide (chalcocite and covellite, respectively) in fresh biosolids that had been amended with CuO NPs, but these inorganic Cu-sulfide species were transformed to Cu–organic sulfur complexes and Cu(II) sulfide in aged biosolids.[20] Dimkpa et al. showed that exposure of plant roots to CuO NPs resulted in bioaccumulation of Cu_2S, Cu–cysteine complexes, and CuO NPs in the plant.[21] Based on these previous findings, it is important to understand the sulfidation products of CuO NPs, and the impact of sulfidation on the dissolution of these NPs to form Cu ions under environmentally relevant conditions.

Copper sulfides (Cu_xS_y), the sulfidized product of CuO, have been successfully synthesized in the laboratory and occur naturally. An array of crystalline copper sulfide phases are stable at room temperature, including covellite (CuS), yarrowite ($Cu_{1.12}S$), spionkopite ($Cu_{1.39}S$), geerite ($Cu_{1.6}S$), anilite ($Cu_{1.75}S$), digenite ($Cu_{1.8}S$), djurlite ($Cu_{1.95}S$), and chalcocite (Cu_2S),[22] which have different optical and electrical properties.[23] Controlled syntheses of copper sulfides have shown that sulfidation occurs via a Kirkendall mechanism: formation of nano CuS hollow structures (Kirkendall diffusion) by reacting Cu_2O with Na_2S.[24,25] Luther et al. reported a mechanism of reduction of

dissolved Cu^{2+} and formation of very small (Cu(I)S(−I)) tetrameric clusters.[26] Data gaps still exist about how CuO NPs transform in the presence of sulfide (S^{2-}/HS^-) in water at ambient temperature and about the properties of the partially and fully sulfidized CuO NPs, including chemical composition, surface properties, size, morphology, and crystal structure. More information is also needed on the potential dissolution (re-oxidation) of copper sulfide species under environmental conditions (*i.e.* ambient temperature, neutral pH, and low ionic strength).

In this study we sulfidized commercially available CuO NPs using different S/Cu molar ratios. The pristine CuO NPs and the resulting sulfidized Cu_xS_y/CuO NPs were extensively characterized. The objectives of this study were to (1) provide mechanistic insights about the transformation of CuO in the presence of sulfide in aqueous solution; and (2) determine the properties and solubility of the resulting sulfidized nanoparticles. The pristine and sulfidized particles were characterized using transmission electron microscopy (TEM), dynamic light scattering (DLS), thermo gravimetric analysis (TGA), X-ray diffraction (XRD), and synchrotron based X-ray absorption spectroscopy (XAS). Their dissolution rate was determined by measuring ion release by inductively coupled plasma mass spectrometry (ICP-MS).

A.4. MATERIALS AND METHODS

A.4.1. CuO NPs

The CuO NPs (40 nm) were purchased from US Research Nanomaterials, Inc. (Houston, TX). The primary particle size is ~40 nm and the particles are generally spherical. The N_2-BET specific surface area provided by the manufacturer is 20 $m^2\ g^{-1}$.

The particles were used as received. The manufacturer claims that the CuO NPs contain no organic capping agent. This was confirmed by thermo gravimetric analysis (TGA) as described below. The crystal structure of the initial CuO NPs is described in the results section.

A.4.2. Sulfidation of CuO nanoparticles

Sulfidation of CuO NPs was conducted following similar procedures as previously described for sulfidation of ZnO NPs.[16] In order to minimize the oxidation of sulfide by dissolved oxygen in a typical experiment, all solutions were prepared using N_2-purged DI water and N_2-purged headspace. The CuO NPs were suspended in deoxygenated water by sonicating in an ice-bath with a micro tip sonicator (Branson Model 250) at a power input of 10 W for 8 minutes. The dispersed CuO NPs (100 mg L^{-1}) in 10 mM NaNO3 electrolyte were reacted with sulfide (Na_2S) in N_2-purged 50 mL propylene Falcon tubes. The S/Cu molar ratio was varied from 0.21 to 2.16 to investigate the properties of NPs sulfidized to different extents. The exact S/Cu ratios used are listed in S. Table A.1.[†] The initial pH of the solution during sulfidation was approximately 12 due to addition of sodium sulfide. The pH of the tubes was adjusted to 11.9 using NaOH and HCl, and the tubes were sealed and were allowed to rotate in the dark for 7 days. Then the resulting solutions were centrifuged at 4000 g for 20 min. Supernatants were carefully decanted and DI water was added. The NPs were re-suspended in sulfide-free DI water, and then the tubes were centrifuged again and the supernatants were decanted. These steps were repeated three times to remove residual sulfide in solution. Finally, the sulfidized CuO NPs were suspended in deoxygenated DI water. A portion of each of the slurries was allowed to dry and was kept for characterization as described below.

A.4.3. Characterization of the pristine and sulfidized CuO

Characterization was performed on NPs that had been washed, dried, and re-dispersed in 10 mM $NaNO_3$ at pH = 7.5. The sizes of the NPs were measured by dynamic light scattering (DLS) and TEM bright field imaging. DLS measurements were made using an ALV/CGS-3 compact goniometer system equipped with a 22 mW HeNe Laser (λ = 632.8 nm) at a scattering angle of 90°. TEM images were taken using a JEOL 2100 transmission electron microscope at an accelerating voltage of 200 kV. The TEM samples were mounted on lacy carbon film on 300 mesh gold grids (Ted Pella, Inc.). Samples were prepared by placing one drop of a NP suspension in ethanol using a 'drop and wick' technique.

Thermo gravimetric analysis (TGA) was conducted using a SDT Q600 TGA (TA Instruments, New Castle, DE). Approximately 20 mg of the NPs was placed in the TGA holder. The particles were heated at a rate of 2 °C min^{-1} from ambient temperature up to 400 °C in air, and the weight change upon heating was recorded.

X-ray absorption spectroscopy (XAS) and X-ray diffraction (XRD) (both laboratory and synchrotron-based XRD) were used to assess structural/speciation differences among the NPs. XAS measurements were conducted at the Stanford Synchrotron Radiation Lightsource (SSRL) on beamline 11-2 to determine the speciation of pristine and sulfidized CuO NPs. Samples were pelletized after diluting with glucose to achieve an optimized absorption edge jump ($\Delta\mu$) of 1 at the Cu K-edge (8988 eV). XAS spectra were collected at room temperature in transmission mode. Data were analyzed using the SixPACK software package, version 0.68.[13] XAS scans were energy calibrated using a metallic Cu foil, background subtracted with E0 defined as 8988 eV,

converted to frequency (k) space, and weighted by k^3. Linear combination fitting (LCF) using a three copper model compounds (CuS, Cu_2S & CuO) was performed on the spectra to obtain quantitative speciation information by using least-squares. To better understand the CuO to Cu_xS_y transformation, the spectra were converted into *R* space *via* Fourier transform and the first shell was fit using two theoretical scattering paths (Cu–S & Cu–O) that were generated by IFEFFIT through Sixpack.[13]

Powder X-ray diffraction was first used to identify the crystal structure of the pristine CuO NPs. Diffraction patterns of these materials were collected using a laboratory-based Panalytical X-ray diffractometer, operating in the Bragg configuration using Cu Kα radiation (λ = 1.5418 Å) from 10° to 90° at a scanning rate of 0.2° min^{-1} for the identification of crystalline phases.

The XRD patterns for copper sulfide model compounds (CuS and Cu_2S) and the sulfidized samples were collected using synchrotron-based XRD at SSRL on beamline 11-3. Incident X-rays (0.9744 Å, 12 735 eV) were focused using a bent cube root I-beam Si (311) monochromator. A MAR345 area detector positioned 120 mm downstream of the sample was used to collect diffraction scans with a dwell time of 90 s. The collected images were converted into *q* space using Area Diffraction Machine (open source) software.

A.4.4. Dissolution measurements

Dissolution of CuO NPs and the sulfidized NPs was measured by quantifying the concentration of dissolved copper in solution with a known initial concentration of total Cu of ~1 mM, *i.e.* CuO (80 mg L^{-1}) and Cu_xS_y (100 mg L^{-1}). Two sets of dissolution experiments were conducted to investigate the effect of dissolved oxygen on the rate and

extent of dissolution of the sulfidized NPs. One set was performed with a dissolved oxygen (DO) concentration of 8.3 mg L^{-1}. The other set used N_2-purged deoxygenated water and was conducted in a glove box with N_2 headspace.

To measure the extent of dissolution of the NPs for different reaction times, the washed NPs were diluted into 200 mL serum bottles. $NaNO_3$ was added to provide a 10 mM background concentration to maintain uniform ionic strength in all reactors. HEPES buffer (2 mM) was used to provide an initial pH of 7.4 in all reactors. The serum bottles were capped and agitated on an end-over-end rotator at 30 rpm in the dark at room temperature (20 °C).

At time points from 1 h to 2 weeks, samples were taken from the reactors. At each time point, 7 mL of solution was removed for analysis. Particles were separated using Amicon ultra-15 filters (MWCO 3 kDa). The ultra filters were centrifuged at 3000 g for 20 minutes and a 5 mL aliquot of the filtrate was collected for analysis. Control studies with 1 and 3 mg L^{-1} Cu^{2+} indicated that Cu ion ($Cu(NO_3)_2$) retention by the ultra filtration membranes can be neglected.

The samples were digested by adding concentrated HNO3 to reach 5% acid content. Each sample was analyzed by inductively coupled plasma mass spectrometry (ICP-MS) to determine the concentration of dissolved copper in solution. A multi-element calibration standard (10 mg L^{-1} with 5% HNO_3, Agilent Technologies) was diluted with 5% HNO_3 to make the desired calibration standards.

A.4.5. Modeling the solubility of Cu solids

Experimentally determined copper solubilities were compared to thermodynamic equilibrium for crystalline mineral phases identified by XRD using the general chemical

equilibrium model MINEQL+ Version 4.5. Calculations used a constant total Cu of 1.25 mM, derived from the initial 100 mg L^{-1} CuO nanoparticles used in solubility experiment, assuming complete conversion to the mineral of interest. For copper-sulfide and copper-sulfate-hydroxide solids, the total S(−II) or total S(VI) was set to the stoichiometric ratio of the solid, *e.g.* for covellite (CuS) TOTS(−II) = 1.25 mM, for chalcocite (Cu_2S) TOTS(−II) = 0.625 mM, and for brochantite ($Cu_4SO_4(OH)_6$) TOTS(VI) = 0.3125 mM. Copper solubility was considered for each solid separately with each mineral of interest included in the model as dissolved and capable of precipitating. Conditions of the dissolution experiments (pH 7.4, I = 10 mM $NaNO_3$, 20.0 °C) were fixed in the model. Oxidation–reduction reactions of copper and sulfur were ignored. Equilibrium solubility of Cu for each mineral was the resulting sum of dissolved Cu species.

A.5. RESULTS AND DISCUSSION

A.5.1. Characterization of the pristine CuO NPs

The CuO NPs are roughly spherical particles ~30–50 nm in diameter as determined by TEM (Fig. A.1). XRD data showed that the initial CuO NPs are crystalline, and the XRD pattern matches that of tenorite (Fig. A.1). The relatively broad diffraction peaks are consistent with the TEM images indicating that the CuO is in the nano size range.

The total weight loss upon heating the NPs in air to 400 °C is 3.2% (S. Fig. A.1[†]). The weight loss from the initial temperature to approximately 100 °C is attributed to evaporation and removal of surface-bound water. Loss of water (before reaching 100 °C)

accounted for 2.5% of the total mass. The weight loss during 100 to 200 °C was 0.74%, which is consistent with the manufacturer's claim of limited organic capping agents. Also, there was no further phase transformation of the CuO NPs upon heating to 400 °C.

Because sulfidation occurred in aqueous solution, the NPs were also characterized in water. The intensity-averaged hydrodynamic diameter of the CuO NPs in 10 mM $NaNO_3$ at pH 7.5 is centered at 587 nm (Fig. A.1). This is larger than the aggregates observed by TEM (Fig. A.1), and indicates that the initial NPs were further aggregated in solution, consistent with the absence of a capping agent.

A.5.2. Sulfidation of CuO NPs

Copper speciation in pristine CuO NPs and the sulfidized NPs were characterized using XRD and XAS. Both lab-based (λ = 1.5418 Å) and synchrotron-based XRD (λ = 0.9744 Å) were used. To compare the XRD patterns on the same basis, the lab-based XRD spectra were converted to 2θ space corresponding to the synchrotron energy using Bragg's equation. The noisy XRD patterns collected on the lab-based instrument resulted from the lower flux of X-rays in the lab-based XRD compared to synchrotron XRD. The initial CuO NPs were identified as tenorite. Upon addition of sulfide, several new phases appeared in the sulfidized NPs with corresponding disappearance of the tenorite. The predominant phase was identified by XRD as CuS (covellite), which was confirmed by both comparison of the S/Cu 2.16 sample with a CuS model compound in Fig. A.2, and by peak matching (with ICDD-no. 1074-1234, covellite CuS) from the mineral database (S. Fig. A.2[†]). Sulfidation to CuS increased with increasing S/Cu ratios.

The small peaks in the XRD pattern of the most sulfidized sample indicate the presence of other minor phases in addition to CuS. A more detailed view of the XRD

pattern of the most sulfidized sample (S/Cu 2.16) is shown in Fig. A.3. Besides covellite (CuS), three copper sulfate hydroxides, more or less hydrated, were identified. They are brochantite (ICSD (Inorganic Crystal Structure Database) 64688): $Cu_4(SO_4)(OH)_6$, posnjakite (ICSD 100276): $Cu_4(SO_4)(OH)_6(H_2O)$ and langite (ICSD 030724): $Cu_4(SO_4)(OH)_6(H_2O)$. The presence of sulfate minerals indicates oxidation of some of the sulfide to sulfate in the sulfidation process, potentially during drying. Because dissolved oxygen was removed prior to the sulfidation process, Cu(II) was the likely oxidant for sulfide oxidation, resulting in formation of Cu(I). This reduction of Cu(II) to Cu(I) by sulfide has been previously observed by Luther et al.[26]

Additional structural characterization of the sulfidized materials was carried out using XAS (Fig. A.4). The extended X-ray absorption fine structure (EXAFS) spectra (Fig. A.4a) clearly show a steady decrease in CuO-oscillations and the appearance of Cu–S oscillations with increasing sulfide concentration. Linear combination fitting (LCF) for *k* from 2 to 9 was conducted to identify the relevant phases for each sample (CuO, Cu_2S or CuS). The best fits were obtained by including all three (CuO, Cu_2S and CuS) of the model compounds used (S. Fig. A.3 and S. Table A.2[†]). This result suggests incomplete sulfidation and a mixture of covellite and chalcocite as reaction products. However, the linear combination fits were poor, especially for the NPs that had been sulfidized with a Cu/S ratio of less than ~1 (*i.e.* S/Cu ratios of 0.43, 0.63, and 0.86). The fits were somewhat better ($R < 0.15$) for the materials that were least sulfidized and those with S/Cu > 0.94. The relatively poor fits, especially for the intermediate Cu/S ratios, suggest that either Cu_xS_y phases other than CuS and Cu_2S had formed which were not among the model compounds used, or that the CuS and Cu_2S formed was poorly ordered and

therefore different than the crystalline CuS and Cu_2S model compounds. The broadness of the Fourier transformed EXAFS spectra is consistent with poorly ordered materials. The most sulfidized material (S/Cu = 2.16) had only one peak in the FT corresponding to the expected Cu–S bond distance for copper sulfide (Fig. A.4b). In contrast, the crystalline model compounds used all have FT features over an $R + \Delta R$ range of 6–8 Å indicating longer range order (Fig. A.4b). This difference in long-range order may explain the relatively poor linear combination fits. In addition, the copper sulfate hydroxides identified by XRD were not represented in the model compound library used for LCF. To confirm the transition from CuO to CuS upon sulfidation, the first shell was fit using theoretical scattering paths generated by SixPack for Cu–S and Cu–O shells fixed at 1.95 and 2.25 Å, respectively. The Debye–Waller and the sigma parameters were set to 0.9 and 0.008, respectively. There is a clear decrease in the Cu–O coordination number while a simultaneous increase in the Cu–S coordination number as the particles become increasingly sulfidized (Fig. A.4c). Even though a clear distinction between covellite and chalcocite was not possible, it is certain from XAS that the Cu–O character of the particles is readily replaced by Cu–S and it is relatively poorly ordered material.

The oxidation state of Cu in Cu_xS_y species can vary from +I to +II. Both Cu_2S (chalcocite) and CuS (covellite) have been described as containing predominantly Cu(I).[26,27] The XANES region of our XAS data suggest that this is not the case for the Cu_xS_y formed here. There was more than a 2 eV difference between the *K* edge of a Cu_2S model compound and that of the Cu_xS_y formed here at S/Cu = 2.16 (S. Fig. A.3[†]). The oxidation state of Cu in the most sulfidized particles is therefore greater than one, so at least some, if not all, of the Cu in the sulfidized material is Cu(II).[28]

The EXAFS suggested that for higher S/Cu ratios Cu is primarily bound to S. This Cu–S phase was poorly ordered as evidenced by the lack of order after $R + \Delta R$ over 2.5 Å. XRD results showed formation of CuS, primarily. TEM analysis was performed to further assess the structure and morphology of the CuS phases formed.

TEM analysis of the pristine CuO NPs and the most sulfidized NP (S/Cu 2.16) (Fig. A.5) show that the average size of the CuO NPs is 30–50 nm (Fig. A.5a) and that they are crystalline (Fig. A.5b). TEM images of the S/Cu 2.16 NPs indicated a range of NP sizes and the presence of both poorly ordered (Fig. A.5c) and crystalline phases (Fig. A.5d). Additional TEM images are provided in the ESI† (S. Fig. A.4). In some cases, the sizes and range of sizes for the sulfidized NPs were found to be similar to those of the pristine CuO NPs, which suggests a direct solid–fluid sulfidation process in water at pH = 11.9 and the Cu/S ratios used here. The wide distribution of NP sizes (S. Fig. A.4†) also suggests that a dissolution/precipitation mechanism is also occurring.

To confirm the identity of the crystalline phases in Fig. A.5, the d-spacing of the lattice fringes was determined in selected regions using Gatan DigitalMicrograph. The d-spacings determined for the pristine CuO particles in Fig. A.5a and b were 2.30 Å and 2.50 Å, corresponding with tenorite's two primary peaks. Analysis of Fig. A.5d yielded a d-spacing of 3.05 Å, which is consistent with the (102) plane for covellite (CuS). The d-spacings for other crystalline materials in the TEM were 2.80 Å, which is also consistent with the CuS (covellite) (103) plane. The presence of some crystalline CuS is consistent with the presence of covellite peaks in the XRD pattern.

A.5.3. Dissolution

The rate and extent of dissolution of the pristine CuO NPs and the sulfidized NPs were determined at neutral pH in 10 mM $NaNO_3$ (Fig. A.6). In the presence of dissolved oxygen, after 2 weeks, dissolution of CuO and CuO/CuS NPs apparently reaches equilibrium. This time scale is longer than that observed for ZnO/ZnS NP dissolution but similar to that of Ag NP oxidative dissolution.[29,30] CuO does not dissolve significantly at neutral pH without ligands present (e.g., amino acids). The highest measured dissolved copper released by CuO NPs was only 0.02 mg L^{-1}. The partially and fully sulfidized particles have a higher apparent solubility than CuO. This result contrasts with expectations for metal sulfides and with previous studies which showed that sulfidation reduces dissolution and ion release from ZnO and Ag NPs.[16,30] Wang et al. also found lower solubility of sulfidized CuO NPs compared to pristine CuO NPs, as well as reduced cytotoxicity of CuS compared to CuO NPs in RPMI 1640 medium.[31] It also contradicts calculated solubility expected for the sulfide minerals Cu_2S and CuS compared to CuO[32] under the conditions used for dissolution (Table A.1).

Both the solubility and the rate of dissolution increased with increased sulfidation. The most sulfidized particles (S/Cu 2.16) (~85% sulfidized Cu) have the highest solubility of 2.9 mg L^{-1} (4.6×10^{-5} M). This solubility is much higher than the modeled values for either crystalline CuS or crystalline Cu_2S (Table A.1). It is also higher than expected for poorly crystalline $Cu_{1.18}S$.[33] This solubility is more consistent with that predicted for the high solubility Cu sulfate hydroxide species identified by XRD and may explain the higher than expected solubility. However, it appears from XRD that these sulfate hydroxide species are not a large fraction of the solids formed. Moreover, the washing processes prior to the measurement of solubility should have partially or

completely removed these soluble species. Assuming that the DI water rinse solutions come to equilibrium with small fraction of the total solid mass as Cu–SO_4–OH minerals, complete dissolution could be achieved during the first or second rinse. If equilibrium is not obtained due to kinetic limitations, the most likely solid to remain is the less soluble brochantite. Copper solubility observed for the S/Cu = 0.22 dissolution experiment, approximately 0.3 mg L^{-1}, could be explained by a small fraction of brochantite in the solid phase. However, the solubility measured in the more sulfidized systems cannot be reconciled by thermodynamics of observed crystalline phases. Therefore, dissociation of Cu^{2+} from crystalline CuS or copper sulfate hydroxide alone is not likely controlling the solubility for the sulfidized NPs in our experiments. The high dissolved copper concentration could result from either a higher apparent solubility due to formation of poorly ordered Cu_xS_y phases, the presence of very small CuS nanoclusters, or oxidative dissolution of the formed CuS NPs according to eqn (1) and (2).

$$Cu_2S + 2.5O_2 + 2H^+ = 2Cu^{2+} + SO_4^{2-} + H_2O \quad (1)$$

$$CuS + 2O_2 = Cu^{2+} + SO_4^{2-} \quad (2)$$

In order to evaluate the potential for oxidative dissolution, the dissolution of the NPs was also measured after purging the dissolved oxygen from the water (Fig. A.6 bottom). The dissolution rate and extent was lower for S/Cu ratios of 0.43, 0.62, and 2.16 compared to dissolution in the presence of DO. Thus, it appears that an oxidative dissolution mechanism occurs in the dissolution of sulfidized CuO NPs when dissolved

oxygen is present. This is consistent with a the finding of Wang et al.,[31] who showed that addition of H_2O_2 to the sulfidized CuO NPs rapidly solubilized those particles.

Non-zero dissolved Cu concentrations without dissolved oxygen was also noted. In the absence of oxygen, solubility equilibrium was reached rapidly: within 1 h for S/Cu 2.16 and within 100 h for other ratios. Because oxidative dissolution was excluded under anoxic conditions, the apparent rapid dissolution is most likely due to the combination of 1) presence of poorly ordered, higher solubility phases, 2) presence of copper sulfate hydroxide species, and 3) formation of very small clusters of CuS (*e.g.* tetrameric Cu–S structures noted by Luther et al.[26]) that can pass through the filter with a MWCO of 3 kDa. The latter suggestion is most consistent with the non-zero initial concentration in the dissolution experiments. Small (passing a 3 kDa MWCO filter) metal sulfide clusters were previously found to account for more than 40% of the total metal in river water in Connecticut, USA.[35]

A.5.4. Mechanistic insights on the sulfidation process

Information from the combined XAS, XRD, TEM, and dissolution measurements provide some mechanistic insights on sulfidation of CuO NPs. EXAFS indicates the presence of poorly ordered Cu_xS_y. XRD shows the presence of some crystalline CuS (covellite) as well as copper sulfate hydroxide phases. TEM confirms a mixture of poorly ordered and crystalline CuS phases. TEM also indicates that some of the sulfidized NPs are similar in size to that of the pristine CuO NPs, while others are not, suggesting that sulfidation occurs through dissolution and reaction with sulfide as well as a direct solid–fluid sulfidation. This kind of Kirkendall effect was demonstrated previously for copper sulfidation in organic solvents under an argon atmosphere[36] and in water under mild

conditions.[24,25] This study suggests that this mechanism is also occurring for sulfidation in water under the conditions used here. Dissolution measurements show the possibility of formation of small clusters (<1 nm).

A potential set of reactions for the sulfidation of CuO consistent with the species identified are given in eqn (3) through (6).

$$8CuO + 5S^{2-} + 8H^{+} = 4Cu_2S + SO_4^{2-} + 4H_2O \quad (3)$$

$$CuO + S^{2-} + 2H^{+} = CuS + H_2O \quad (4)$$

$$8Cu^{2+} + 5S^{2-} + 4H_2O = 4Cu_2S + SO_4^{2-} + 8H^{+} \quad (5)$$

$$Cu^{2+} + S^{2-} = CuS \quad (6)$$

Eqn (3) and (5) are redox reactions in which Cu(II) is reduced to Cu(I) while S(−II) in sulfide is oxidized to S(VI) in sulfate. Eqn (4) and (6) are not redox reactions. The standard Gibbs free energy of reaction of eqn (3) and (4) are −1432 and −246.8 kJ mol^{-1}, respectively. For eqn (4) under our reaction conditions, $\Delta G_r = \Delta G_r^0 + RT \log(1/([S_{2-}][H^+]_2)) = -92.63$ kJ mol^{-1} indicating a spontaneous reaction. Thus, the formation of CuS and Cu2S are thermodynamically favorable. At pH 11.9 and for all S/Cu ratios, the free Cu^{2+} ion concentration is extremely low (as calculated by MINEQL+). Hence eqn (3) and (4) may be the major pathways for sulfidation under the experimental conditions used here. However, the formation of larger CuS particles than the initial CuO and small CuS clusters suggests that the dissolution and precipitation reaction pathways in eqn (5) and (6) are also active to some degree. The proposed sulfidation process is summarized in Fig. A.7.

A.5.5. Environmental implications

Sulfidation and its impacts on the properties of the sulfidized NPs have important environmental implications. Transformations and the environmental risks of metal and metal oxide NPs are often controlled by sulfidation reactions.[17,37–39] The facile sulfidation of commercial 40 nm CuO NPs at ambient temperature in water to form a variety of Cu_xS_y NPs, soluble copper-hydroxide-sulfates, and likely the formation of Cu_xS_y nanoclusters suggests that these different copper sulfide species may be those likely found in the environment, rather than the pristine CuO NPs. This finding is consistent with expectations based on previous studies showing that copper sulfide is the predominant form of copper in sediment under sulfate-reducing conditions, and in sewer pipes and wastewater treatment plants.[40–42]

Sulfidation increased the dissolved fraction of copper compared to the pristine CuO NPs under environmentally relevant neutral pH. This finding is opposite to that found for Ag and ZnO NPs after sulfidation, where sulfidation decreases solubility and metal availability. The increased release of Cu^{2+} and/or CuS nanoclusters from sulfidized NPs compared to CuO NPs suggests that toxicity studies with pristine CuO may be misleading in environments where sulfidation is expected, considering the complex mixture of sulfidized products that may be formed at pH and redox potentials expected in the environment (Fig. A.8) and their potentially different toxicity to organisms.

The formation of some small Cu_xS_y structures (5–10 nm) and nanoclusters (<1 nm) were observed by TEM or implied in the dissolution experiments. If these structures are formed during sulfidation of CuO in the environment, they may have different transport properties. Both the pristine and sulfidized NPs aggregated (intensity average

size of 587 and 487 nm, respectively in 10 mM $NaNO_3$) and rapidly settled from solution (within 30 min). However, the smaller and poorly crystalline Cu_xS_y structures formed may have increased mobility and higher bioavailability compared with the larger particles of CuO or CuS formed.

Sulfidation has proved to be an important transformation for some metal and metal oxide nanoparticles. This study suggests that CuO may become sulfidized in the environment, and that the resulting properties relevant to toxicity, *e.g.* solubility, will be affected. Thus it is prudent to use environmentally transformed nanoparticles in fate, transport, and toxicity studies rather than focusing solely on the pristine materials.

However the implications of sulfidation differ for Ag, ZnO, and CuO NPs, with sulfidation decreasing the solubility of Ag and ZnO NPs, but increasing apparent solubility for CuO. Studies are also still needed to (1) identify the nature of the Cu_xS_y nanoclusters, (2) assess the toxicity of sulfidized CuO NPs and Cu_xS_y nanoclusters; (3) assess the stability of very small metal sulfide clusters (Ag, Zn, and Cu) against oxidation under environmental and biological conditions; and (4) assess how sulfidation of CuO NPs occurs in situ at relevant CuO/S concentration ratios, and how this affects their bioavailability (*e.g.*, plant uptake) under realistic exposure scenarios.

A.6. ACKNOWLEDGEMENTS

This material is based on work supported by the US EPA Science to Achieve Results program (R834574), Transatlantic Initiative for Nanotechnology and the Environment (TINE), and the National Science Foundation (NSF and the Environmental Protection Agency (EPA) under NSF Cooperative Agreement EF-0830093, Center for

the Environmental Implications of Nanotechnology (CEINT). Any opinions, findings, conclusions or recommendations expressed in this material are those of the author(s) and do not necessarily reflect the views of the NSF or the EPA. This work has not been subjected to EPA review and no official endorsement should be inferred. Portions of this research were carried out at the Stanford Synchrotron Radiation Lightsource (SSRL) beamline 4-3 and 11-2, a national user facility operated by Stanford University on behalf of the U.S. Department of Energy, Office of Basic Energy Sciences. We also thank the beamline scientists at SSRL (BL 4-3 and 11-2) for their support. The authors also acknowledge use of the facilities and the assistance of Christopher Winkler at the Nanoscale Characterization and Fabrication Laboratory at Virginia Polytechnic Institute.

A.7. REFERENCES

1 E. Ebrahimnia-Bajestan, H. Niazmand, W. Duangthongsuk and S. Wongwises, *Int. J. Heat Mass Transfer*, 2011, 54, 4376–4388.

2 K. Guo, Q. Pan, L. Wang and S. Fang, *J. Appl. Electrochem.*, 2002, 32, 679–685.

3 S. Magdassi, M. Grouchko and A. Kamyshny, *Materials*, 2010, 3, 4626–4638.

4 A. Saha, D. Saha and B. C. Ranu, *Org. Biomol. Chem.*, 2009, 7, 1652–1657.

5 K. Sahithi, M. Swetha, M. Prabaharan, A. Moorthi, N. Saranya, K. Ramasamy, N. Srinivasan, N. C. Partridge and N. Selvamurugan, *J. Biomed. Nanotechnol.*, 2010, 6, 333–339.

6 Y. Wu, C. Wadia, W. L. Ma, B. Sadtler and A. P. Alivisatos, *Nano Lett.*, 2008, 8, 2551–2555.

7 M. E. Leitch, E. Casman and G. V. Lowry, *J. Nanopart. Res.*, 2012, 14.

8 I. A. Mudunkotuwa, J. M. Pettibone and V. H. Grassian, *Environ. Sci. Technol.*, 2012, 46, 7001–7010.

9 O. Bondarenko, K. Juganson, A. Ivask, K. Kasemets, M. Mortimer and A. Kahru, *Arch. Toxicol.*, 2013, 87, 1181–1200.

10 A. J. Bone, B. P. Colman, A. P. Gondikas, K. M. Newton, K. H. Harrold, R. M. Cory, J. M. Unrine, S. J. Klaine, C. W. Matson and R. T. Di Giulio, *Environ. Sci. Technol.*, 2012, 46, 6925–6933.

11 C. Gunawan, W. Y. Teoh, C. P. Marquis and R. Amal, *ACS Nano*, 2011, 5, 7214–7225.

12 H. Y. Zhang, Z. X. Ji, T. Xia, H. Meng, C. Low-Kam, R. Liu, S. Pokhrel, S. J. Lin, X. Wang, Y. P. Liao, M. Y. Wang, L. J. Li, R. Rallo, R. Damoiseaux, D. Telesca, L. Madler, Y. Cohen, J. I. Zink and A. E. Nel, *ACS Nano*, 2012, 6, 4349–4368.

13 S. M. Webb, *Phys. Scr., T*, 2005, 115, 1011–1014.

14 H. L. Karlsson, P. Cronholm, J. Gustafsson and L. Moller, *Chem. Res. Toxicol.*, 2008, 21, 1726–1732.

15 C. Levard, E. M. Hotze, B. P. Colman, A. L. Dale, L. Truong, X. Y. Yang, A. J. Bone, G. E. Brown, R. L. Tanguay, R. T. Di Giulio, E. S. Bernhardt, J. N. Meyer, M. R. Wiesner and G. V. Lowry, *Environ. Sci. Technol.*, 2013, 47, 13440–13448.

16 R. Ma, C. Levard, F. M. Michel, G. E. Brown and G. V. Lowry, *Environ. Sci. Technol.*, 2013, 47, 2527–2534.

17 J. Y. Liu, K. G. Pennell and R. H. Hurt, *Environ. Sci. Technol.*, 2011, 45, 7345–7353.

18 B. C. Reinsch, C. Levard, Z. Li, R. Ma, A. Wise, K. B. Gregory, G. E. Brown and G. V. Lowry, *Environ. Sci. Technol.*, 2012, 46, 6992–7000.

19 R. G. Pearson, *J. Chem. Educ.*, 1968, 45, 643–648.

20 E. Donner, D. L. Howard, M. D. de Jonge, D. Paterson, M. H. Cheah, R. Naidu and E. Lombi, *Environ. Sci. Technol.*, 2011, 45, 7249–7257.

21 C. O. Dimkpa, D. E. Latta, J. E. McLean, D. W. Britt, M. I. Boyanov and A. J. Anderson, *Environ. Sci. Technol.*, 2013, 47, 4734–4742.

22 P. Leidinger, R. Popescu, D. Gerthsen, H. Lunsdorf and C. Feldmann, *Nanoscale*, 2011, 3, 2544–2551.

23 S. H. Jiao, L. F. Xu, K. Jiang and D. S. Xu, *Adv. Mater.*, 2006, 18, 1174.

24 H. T. Zhu, J. X. Wang and D. X. Wu, *Inorg. Chem.*, 2009, 48, 7099–7104.

25 Z. H. Yang, D. P. Zhang, W. X. Zhang and M. Chen, *J. Phys. Chem. Solids*, 2009, 70, 840–846.

26 G. W. Luther, S. M. Theberge, T. F. Rozan, D. Rickard, C. C. Rowlands and A. Oldroyd, *Environ. Sci. Technol.*, 2002, 36, 394–402.

27 S. W. Goh, A. N. Buckley, R. N. Lamb, R. A. Rosenberg and D. Moran, *Geochim. Cosmochim. Acta*, 2006, 70, 2210–2228.

28 P. Kumar, R. Nagarajan and R. Sarangi, *J. Mater. Chem. C*, 2013, 1, 2448–2454.

29 I. A. Mudunkotuwa, T. Rupasinghe, C. M. Wu and V. H. Grassian, *Langmuir*, 2012, 28, 396–403.

30 C. Levard, B. C. Reinsch, F. M. Michel, C. Oumahi, G. V. Lowry and G. E. Brown, *Environ. Sci. Technol.*, 2011, 45, 5260–5266.

31 Z. Wang, A. von dem Bussche, P. K. Kabadi, A. B. Kane and R. H. Hurt, *ACS Nano*, 2013, 7, 8715–8727.

32 G. E. Lagos, C. A. Cuadrado and M. V. Letelier, *J. – Am. Water Works Assoc.*, 2001, 93, 94–103.

33 D. Shea and G. R. Helz, *Geochim. Cosmochim. Acta*, 1989, 53, 229–236.

34 A. H. Zittlau, Q. Shi, J. Boerio-Goates, B. F. Woodfield and J. Majzlan, *Chem. Erde*, 2013, 73, 39–50.

35 T. F. Rozan, G. Benoit and G. W. Luther, *Environ. Sci. Technol.*, 1999, 33, 3021–3026.

36 G. Cheng and A. R. H. Walker, *Anal. Bioanal. Chem.*, 2010, 396, 1057–1069.

37 R. Kaegi, A. Voegelin, C. Ort, B. Sinnet, B. Thalmann, J. Krismer, H. Hagendorfer, M. Elumelu and E. Mueller, *Water Res.*, 2013, 47, 3866–3877.

38 E. Lombi, E. Donner, E. Tavakkoli, T. W. Turney, R. Naidu, B. W. Miller and K. G. Scheckel, *Environ. Sci. Technol.*, 2012, 46, 9089–9096.

39 G. V. Lowry, K. B. Gregory, S. C. Apte and J. R. Lead, *Environ. Sci. Technol.*, 2012, 46, 6893–6899.

40 A. F. Hofacker, A. Voegelin, R. Kaegi, F. A. Weber and R. Kretzschmar, *Geochim. Cosmochim. Acta*, 2013, 103, 316–332.

41 A. E. Lewis, *Hydrometallurgy*, 2010, 104, 222–234.

42 F. A. Weber, A. Voegelin, R. Kaegi and R. Kretzschmar, *Nat. Geosci.*, 2009, 2, 267–271.

A.8. FIGURES

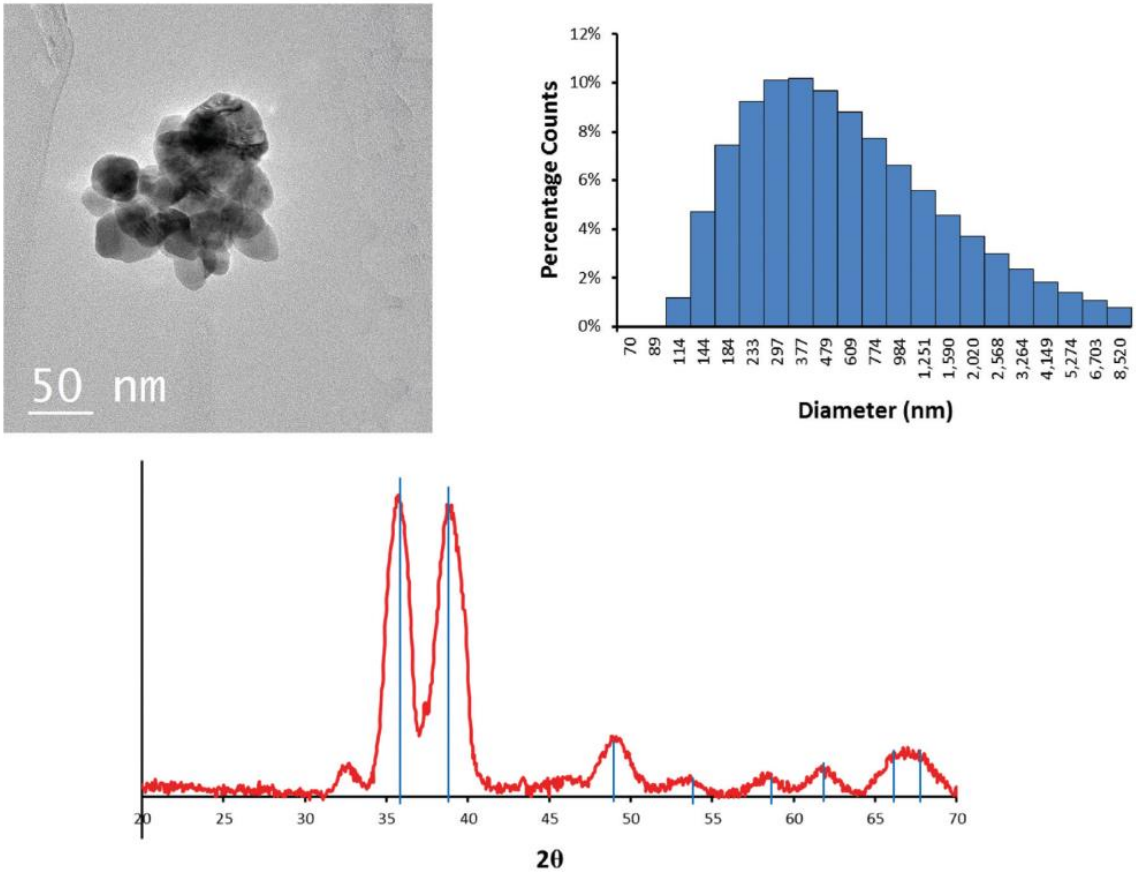

Figure A.1. TEM image of the CuO NPs (top left), intensity averaged hydrodynamic diameter histogram (top right) of particles in 10 mM $NaNO_3$ at pH = 7.5 measured by DLS, and the XRD pattern (bottom) of the pristine CuO NPs. Blue lines are peak matches for tenorite.

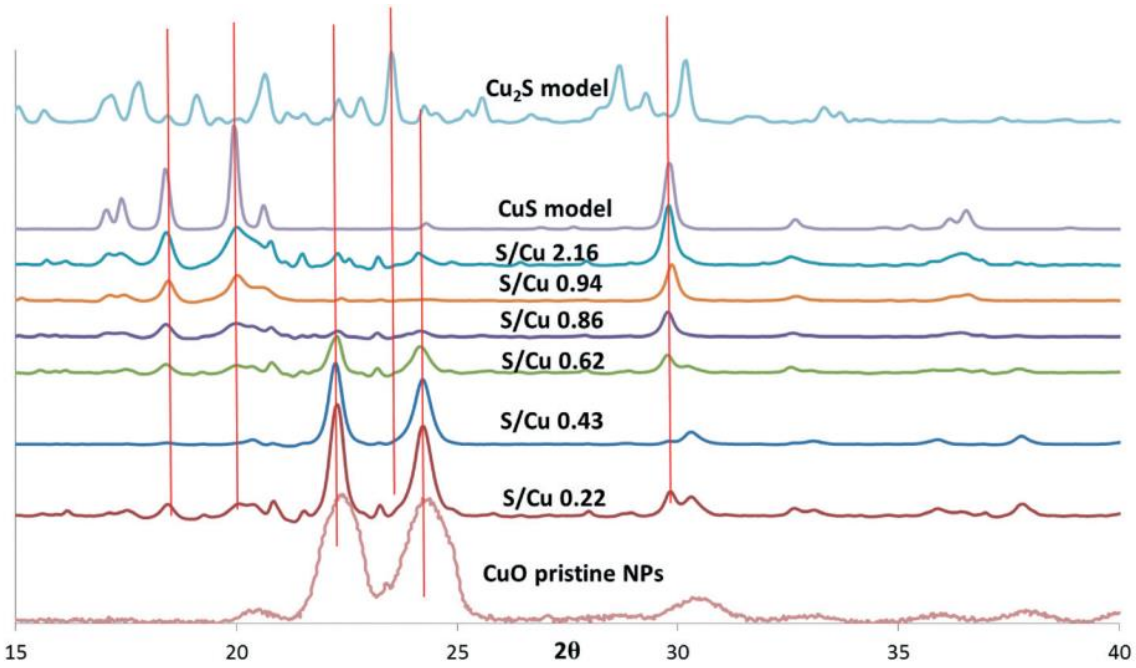

Figure A.2. XRD patterns of CuO NPs, Cu_2S, and CuS model compounds, and sulfidized particles with S/Cu ratios ranging from 0.22 to 2.16. Spectra of CuO model compounds were taken using lab-based XRD with Cu Kα incident X-rays (λ = 1.5418 Å). The spectra were converted to d spacing using Bragg's equation (λ = 2d sin θ). Then the synchrotron X-ray energy (λ = 0.9744 Å) was used to calculate the corresponding 2θ values. The intensities of the lab-based XRD patterns were scaled up by 1000 times to display on the same graph with synchrotron XRD patterns.

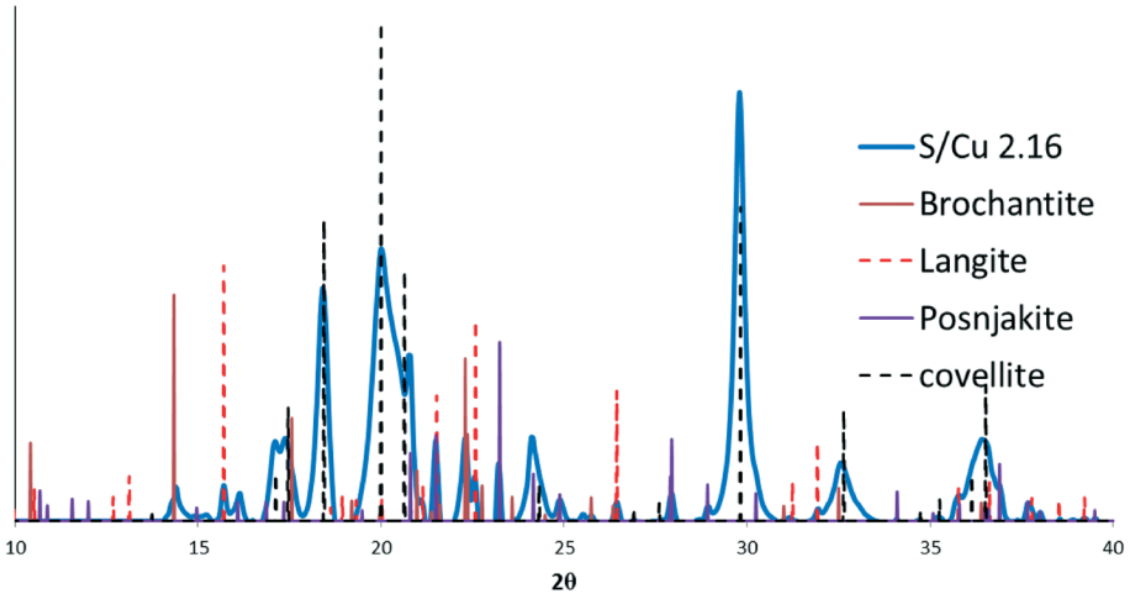

Figure A.3. Peak matching results showing a mixture of CuS (covellite) and a copper sulfate hydroxides and two copper sulfate hydroxide hydrates: brochantite (64688): $Cu_4(SO_4)(OH)_6$; posnjakite (100276): $Cu_4(SO_4)(OH)_6(H_2O)$; and langite (030724): $Cu_4(SO_4)(OH)_6(H_2O)$.

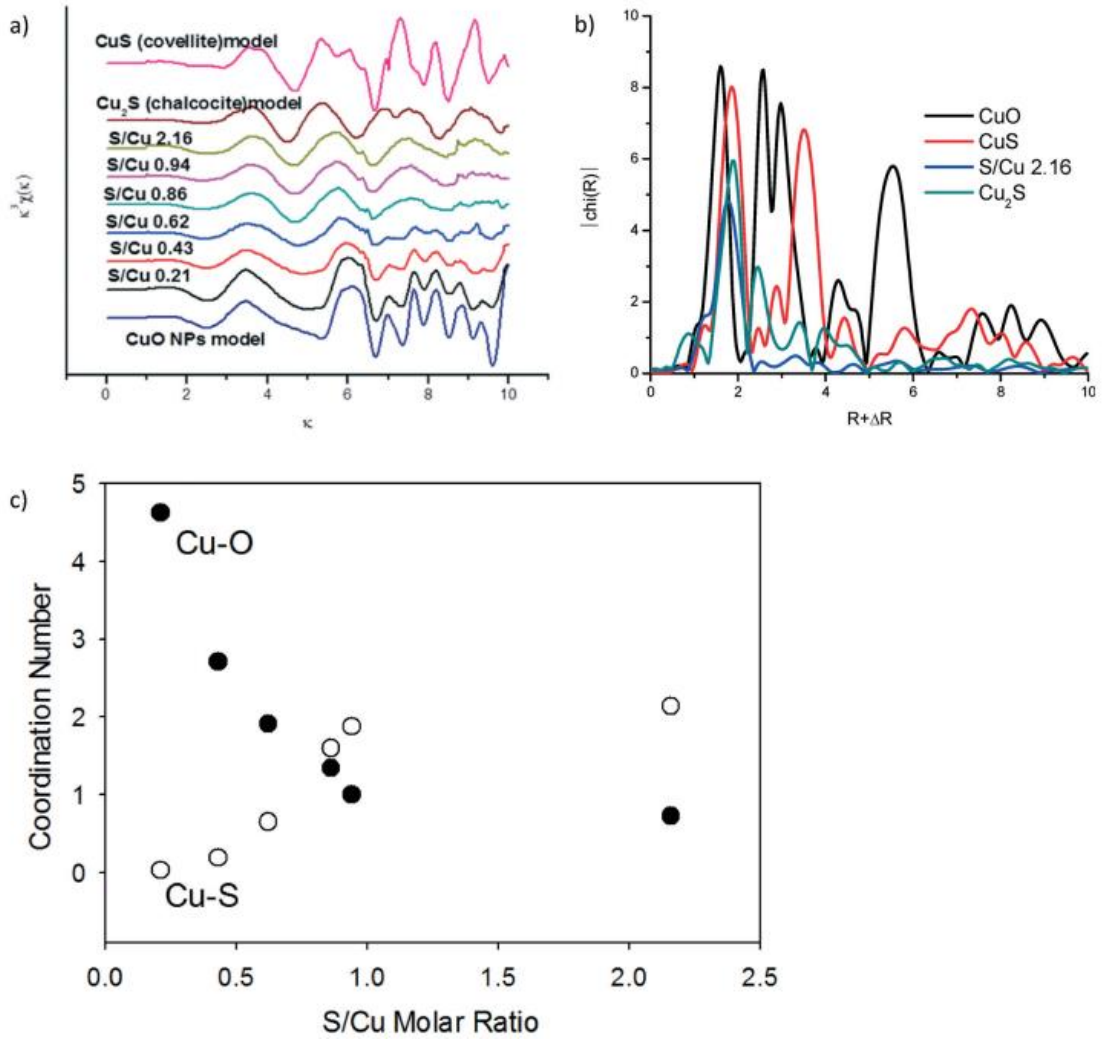

Figure A.4. (a) EXAFS spectra of CuO, Cu_2S (chalcocite), and CuS (covellite) model compound, and the partially sulfidized CuO particles for S/Cu from 0.22 to 2.16. (b) Fourier transformed EXAFS of the model compounds and the most sulfidized sample: S/Cu 2.16. (c) Fitted coordination numbers for theoretical Cu–S and Cu–O scattering paths for the partially sulfidized CuO particles for S/Cu from 0.22 to 2.16.

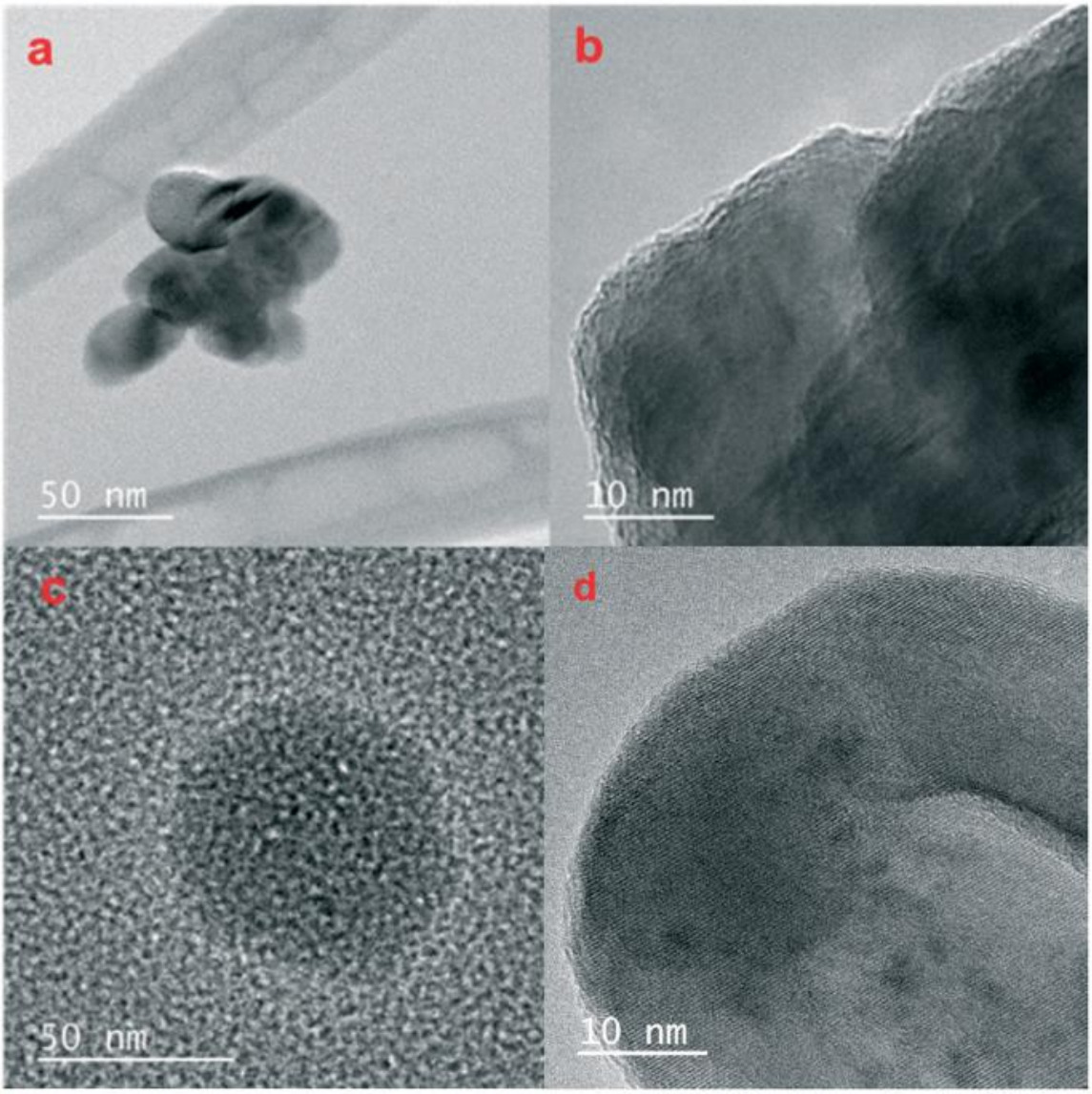

Figure A.5. TEM images of the pristine CuO NPs showing a) primary particle size of CuO is 30–50 nm, b) crystalline nature of the CuO material, c) poorly ordered Cu_xS_y phases formed upon sulfidation, and d) crystalline Cu_xS_y phases including CuS as determined from lattice fringe d-spacings of 3.05 Å.

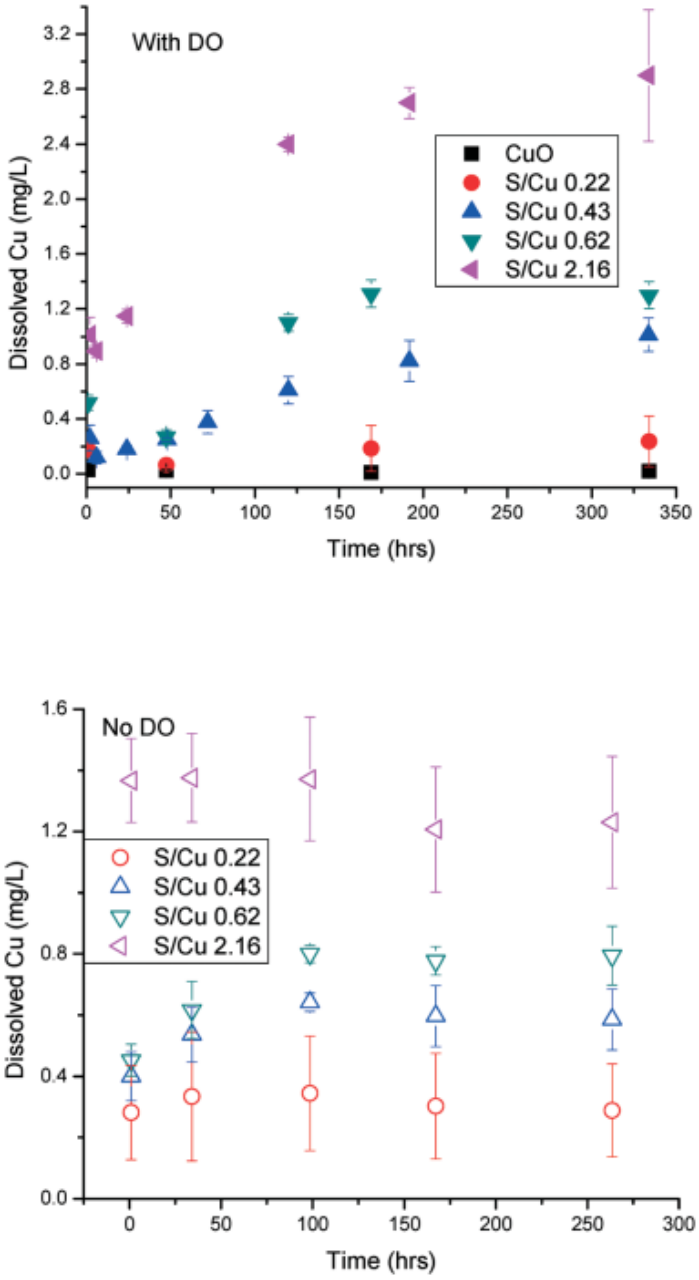

Figure A.6. Dissolution of pristine CuO NPs and sulfidized CuO NPs (S/Cu 0.22, 0.43, 0.62, and 2.16) over two weeks in the presence of dissolved oxygen (top) and with deoxygenated water (bottom). The initial concentration of particles was 100 mg L^{-1}, in 10 mM $NaNO_3$ and 2 mM HEPES buffer. The solution pH for all dissolution studies was 7.4. The error bar indicates ±standard deviation of duplicate reactors. Note that the y-axis scales are not the same in both figures to better indicate the slope of the dissolution curve.

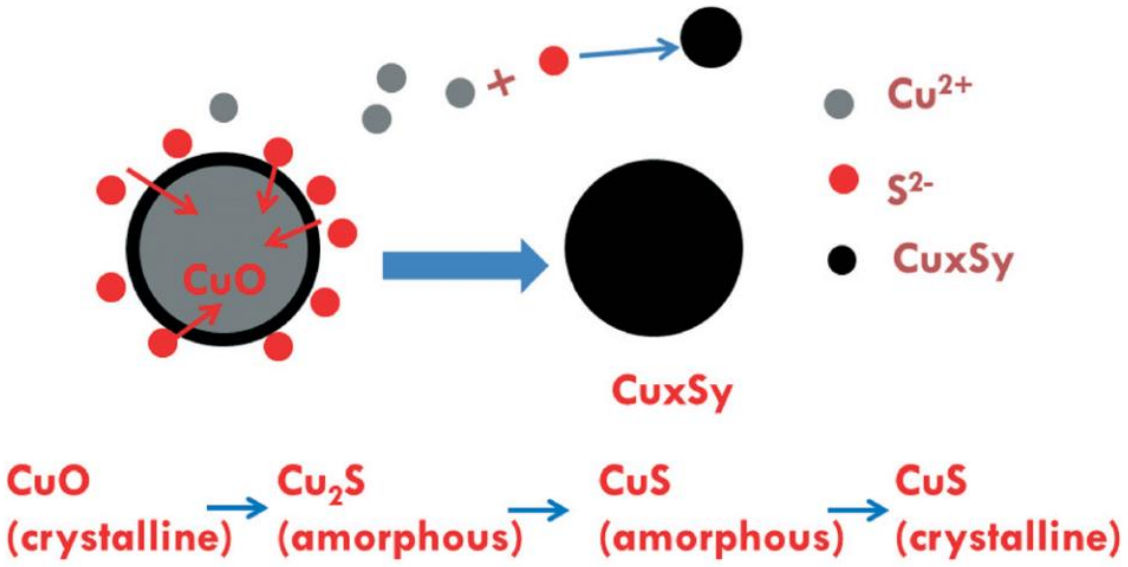

Figure A.7. Proposed sulfidation process of CuO NPs with the dominant pathway being direct solid–fluid sulfidation accompanied by a lower amount of dissolution–precipitation formation of small Cu_xS_y clusters.

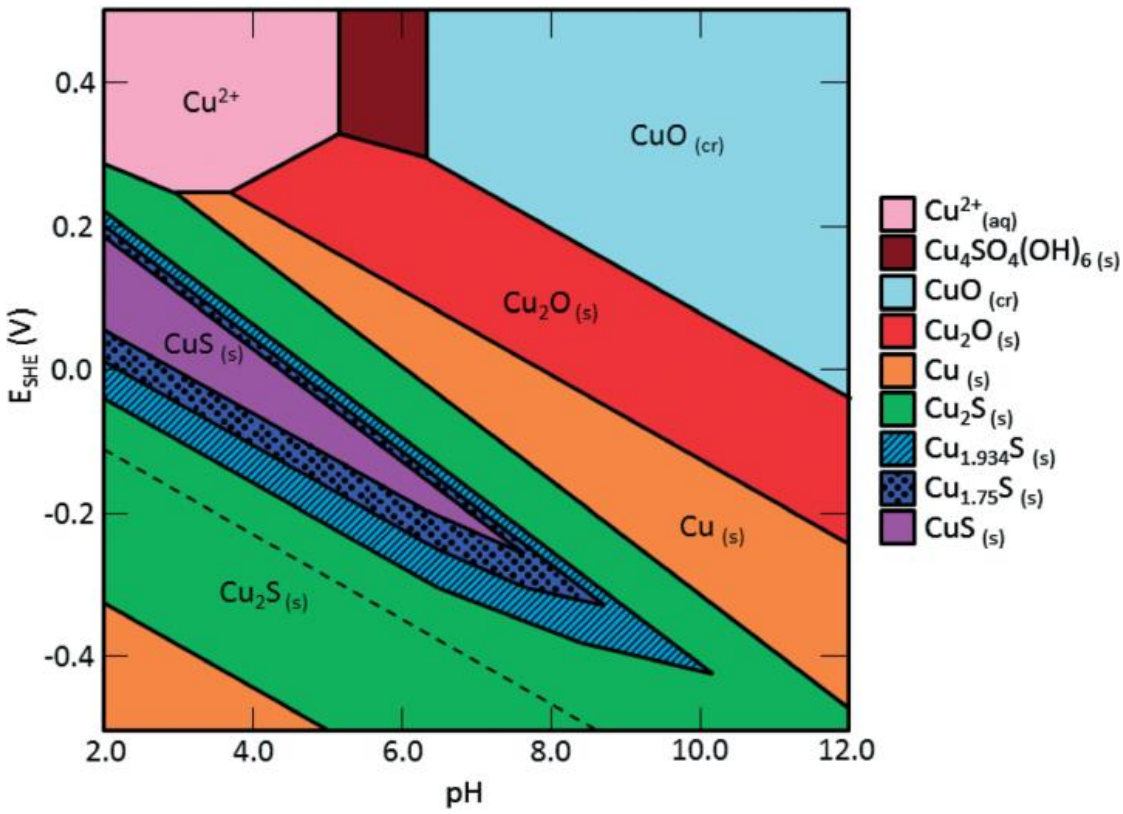

Figure A.8. Pourbaix diagram of the Cu–O–S system generated by Hydromedusa. $[HS^{-}]_{tot}$ = 2 mM, $[Cu]_{tot}$ = 1 mM, $[Na^{+}]$ = $[NO^{3-}]$ = 10 mM. Under the conditions of the sulfidation used here and at environmentally relevant pH and Eh, there are a number of non-stoichiometric Cu_xS_y species that may form.

A.9. TABLES

Table A.1. Equilibrium solubility of crystalline copper solids identified by XRD calculated using MINEQL+ Version 4.5 at TOTCu = 1.25 mM, stoichiometric total sulfur, pH 7.4, I = 10 mM $NaNO_3$, and 20 °C while excluding oxidation–reduction reactions. Solubility products (K_{sp}) were part of standard MINEQL+ database unless otherwise noted. Values for amorphous CuS (am-CuS) were calculated by hand (see ESI) and represent results for unit activity of both solid phases involved in the proposed reaction

Solid	Log K_{sp}	$\sum[Cu]_{diss}$ (M)	Dominant aq. species (% total)
Tenorite	7.644[a]	2.45×10^{-7}	Cu^{2+} (67), $CuOH^+$ (30)
Covellite	−22.300[b]	1.91×10^{-15}	Cu^{2+} (68), $CuOH^+$ (31)
am-CuS	−18.90[c,d]	8.49×10^{-14}	N/A
Chalcocite	−34.920[e]	8.39×10^{-15}	Cu^+ (100)
Brochantite	15.220[f]	5.41×10^{-6}	Cu^{2+} (65), $CuOH^+$ (30)
Langite	17.489[g]	1.52×10^{-5}	Cu^{2+} (62), $CuOH^+$ (29)
Posnjakite	17.6[h,i]	1.25×10^{-5}	Cu^{2+} (63), $CuOH^+$ (29)

[a] $CuO + 2H^+ = Cu^{2+} + 2H_2O$. [b] $CuS + H^+ = Cu^{2+} + HS^-$. [c] $H^+ + 0.15S_{(s)} + 0.85Cu_{1.18}S = Cu^{2+} + HS^-$. [d] Log K_{sp} taken from Shea and Helz.[33] [e] $Cu_2S + H^+ = 2Cu^+ + HS^-$. [f] $Cu_4SO_4(OH)_6 + 6H^+ = 4Cu^{2+} + SO_4^{2-} + 6H_2O$. [g] $Cu_4SO_4(OH)_6{\cdot}H_2O + 6H^+ = 4Cu^{2+} + SO_4^{2-} + 7H_2O$. [h] $Cu_4SO_4(OH)_6{\cdot}H_2O + 6H^+ = 4Cu^{2+} + SO_4^{2-} + 7H_2O$. [i] Log K_{sp} taken from Zittlau *et al.*[34]

A.10. SUPPLEMENTARY INFORMATION

A.10.1. Calculation of solubility of the amorphous $Cu_{1.18}S$ phase

Poorly crystalline copper sulfide is a potential source of observed copper solubility that significantly exceeded thermodynamic predictions for crystalline solids. Using the solubility equilibria developed by Shea and Helz[1] copper solubility was predicted based on the following reaction:

$$H^+ + \frac{x-1}{x} S_{(s)} + \frac{1}{x} Cu_x S \leftrightarrow Cu^{2+}_{(aq)} + HS^-_{(aq)} \quad \text{(R1)}$$

Data for x = 1.18 are provided by Shea and Helz and are used in this calculation (i.e., pK_{sp} = 18.9). Assuming the activity of the sulfide solid to be unity, the solubility relationship from (R1) can be described by:

$$K_{sp} = \frac{\{Cu^{2+}_{(aq)}\}\{HS^-_{(aq)}\}}{\{H^+\}\{S_{(s)}\}^{\frac{x-1}{x}}} \quad \text{(E1)}$$

Solving this equation for the ion product of copper and bisulfide at experimental pH and assuming that the activities of copper and bisulfide are equal in solution, the free copper (and bisulfide) activity can be expressed as a function of elemental sulfur activity, which Shea and Helz note may not necessarily be unity.

$$\{Ce^{2+}_{(aq)}\} = \sqrt{(K_{sp}\{H^+\}\{S_{(s)}\}^{\frac{x-1}{x}}} = \{HS^-_{(aq)}\} \quad \text{(E2)}$$

With thermodynamic data taken from Benjamin[2], the total copper solubility (Cu_T) can be calculated after accounting for complexation with hydroxide and bisulfide.

$$Cu_T = \left[Cu^{2+}_{(aq)}\right] + [CuOH^+] + [Cu(OH)^0_2] + [Cu(OH)^-_3] + [Cu(OH)^{2-}_4] + [Cu(HS)^-_3] \quad \text{(E3a)}$$

$$Cu_T = \left\{Cu^{2+}_{(aq)}\right\} \cdot \left(\frac{1}{\gamma_2} + \frac{\beta_1^{OH}\{OH^-\}}{\gamma_1} + \frac{\beta_2^{OH}\{OH^-\}^2}{\gamma_0} + \frac{\beta_3^{OH}\{OH^-\}^3}{\gamma_1} + \frac{\beta_4^{OH}\{OH^-\}^4}{\gamma_2} + \frac{\beta_3^{HS}\{HS^-\}^3}{\gamma_1}\right) \quad \text{(E3b)}$$

Substituting (E2) into (E3b), the total dissolved copper can be expressed as a function of elemental sulfur activity. Evaluating this expression between $-8 \leq \log\{S_{(s)}\} \leq 0$ shows that the maximum copper solubility for poorly crystalline $Cu_{1.18}S$ is 8.49×10^{-14} M. Figure 1 illustrates the log-log linear relationship between soluble copper and elemental sulfur activity described by this model.

A.10.2. References

1 Shea, Damian, and George R. Helz. "Solubility product constants of covellite and a poorly crystalline copper sulfide precipitate at 298 K." *Geochimica et Cosmochimica Acta* 53.2 (**1989**): 229-236.

2 Benjamin, Mark M. *Water chemistry*. New York: McGraw-Hill, 2002.

A.11. SUPPLEMENTARY FIGURES

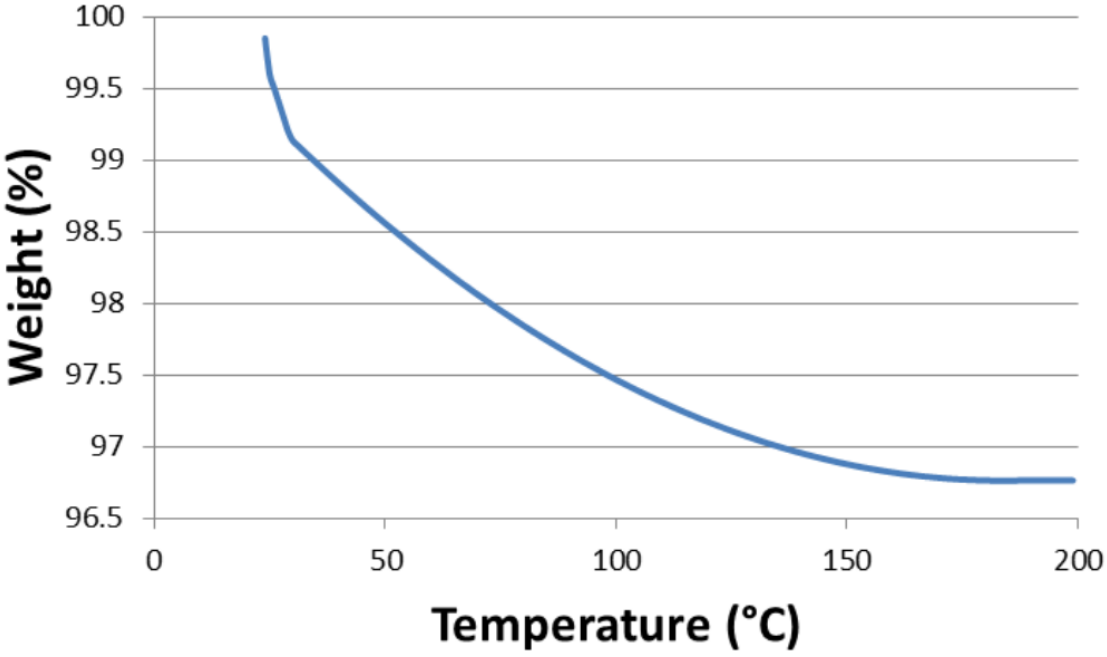

Supplementary Figure A.1. Weight (%) loss upon heating in air using TGA.

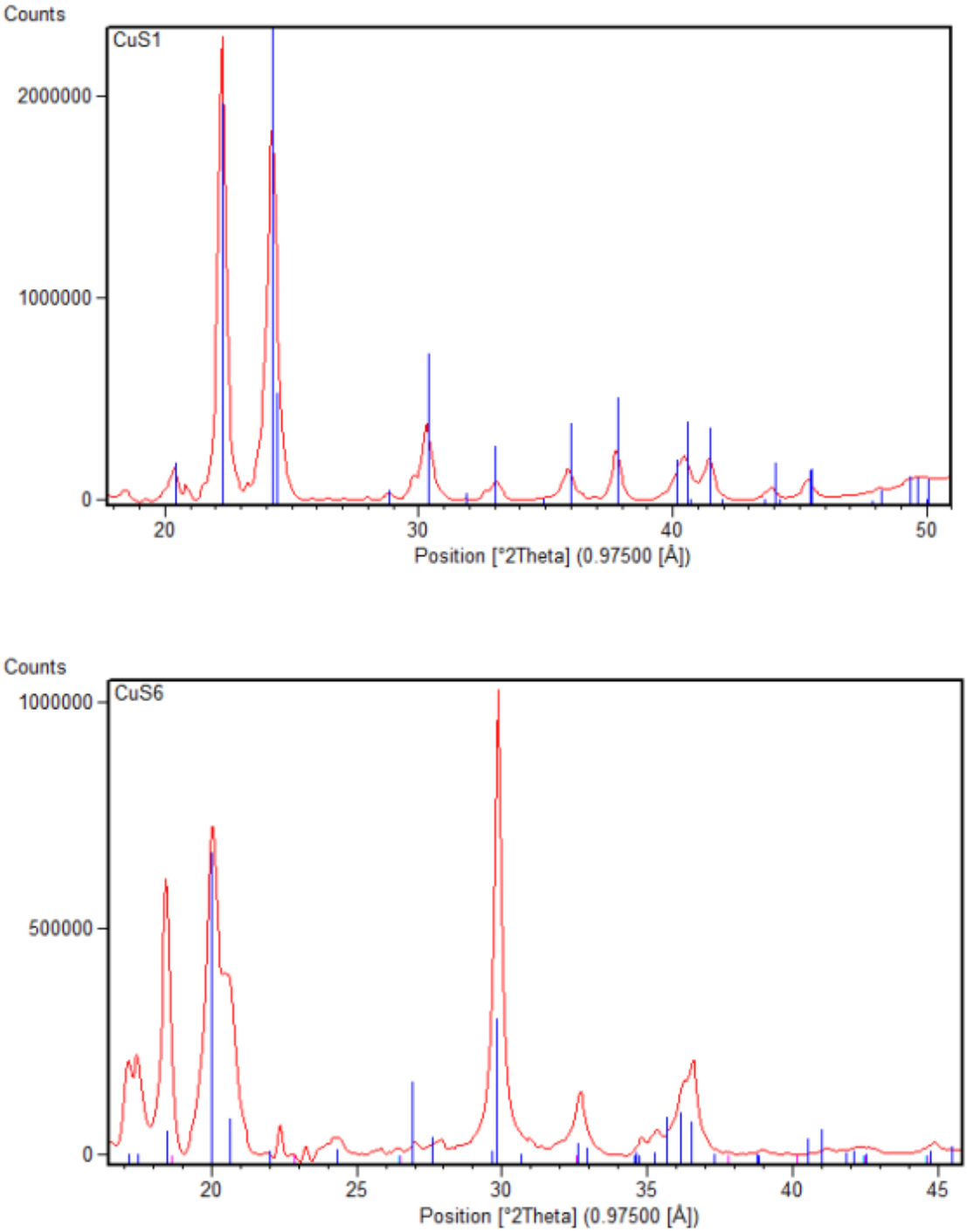

Supplementary Figure A.2. CuS 1 (S/Cu 0.22, top) and CuS 6 (S/Cu 2.16, bottom) XRD peak matching using X'pert High Scores. Red peaks were measured and blue spikes indicate matches for tenorite (top) and for covellie (bottom) taken from the mineralogy database.

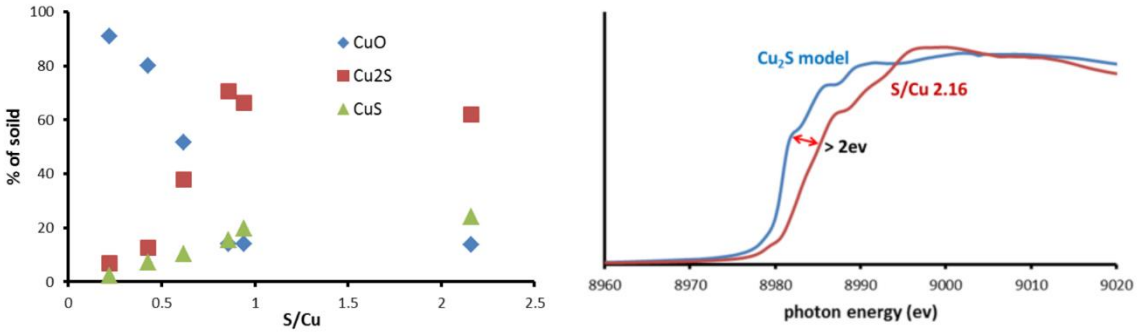

Supplementary Figure A.3. Percentage (left) of CuO and CuS as a function of the S/Cu ratio. The normalized Cu K edge XANES region of the XAS spectra (right) for Cu_2S and S/Cu 2.16.

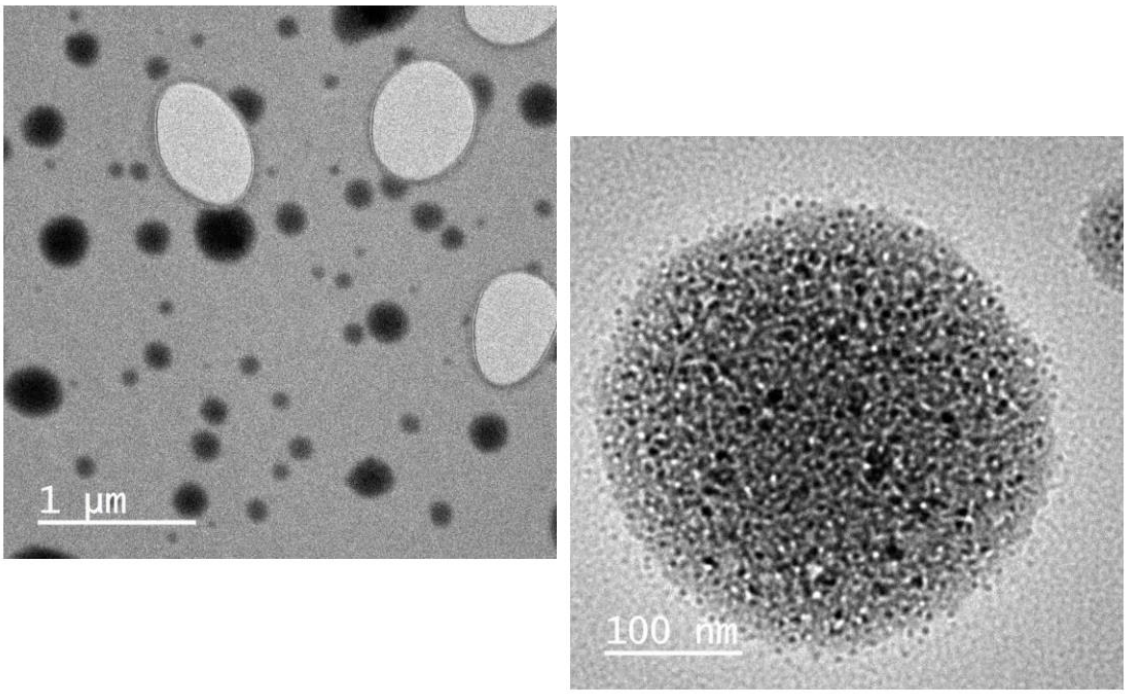

Supplementary Figure A.4. TEM images of relatively amorphous particles in the fully sulfidized Cu_xS_y (Cu/S ratio of 2.16). There is a range of NP aggregates sizes and the particles are highly beam sensitive. Dark spots tended to form with time in the beam.

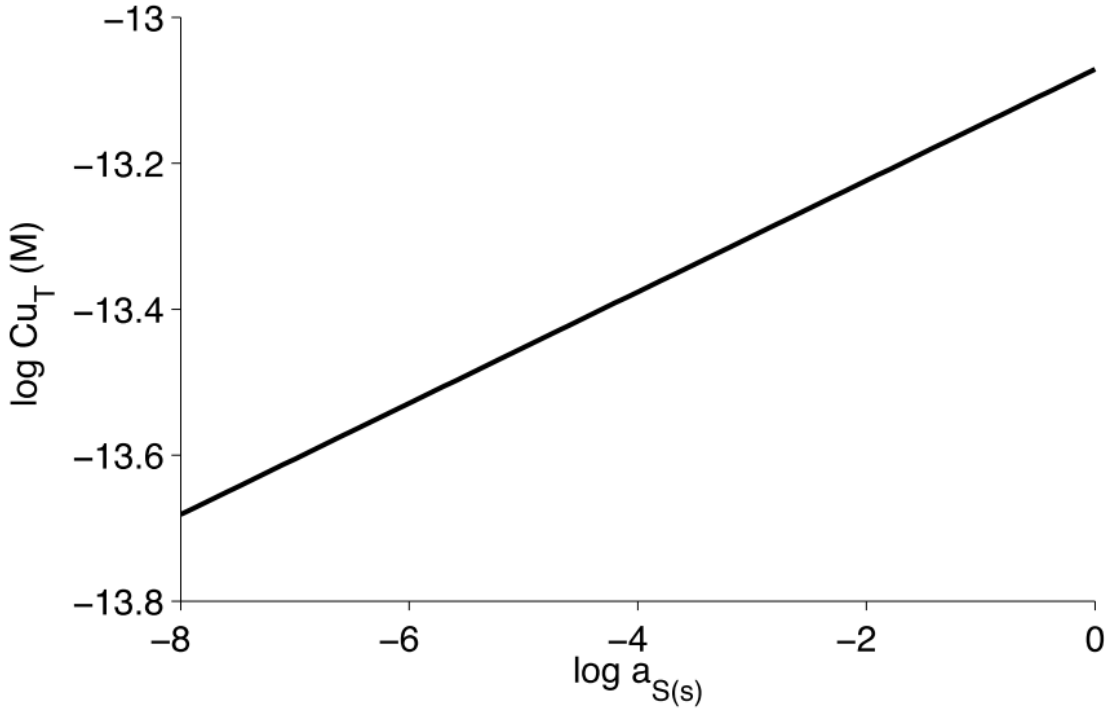

Supplementary Figure A.5. Calculated total soluble copper in equilibrium with poorly crystalline $Cu_{1.18}S$ using the solubility product of Shea and Helz[1] and aqueous stability constants from Benjamin.[2] Model developed for T = 25 °C and I = 0.01 M.

A.12. SUPPLEMENTARY TABLES

Supplementary Table A.1. Sulfide to CuO Molar Ratios and Volumes of 100 mM Na_2S. Each vessel contained 100 mg/L CuO NPs.

Name	S/Cu	100 mM Na_2S (mL)
CuS 1	0.22	1.09
CuS 2	0.43	2.17
CuS 3	0.62	3.10
CuS 4	0.86	4.57
CuS 5	0.94	4.97
CuS 6	2.16	11.41

Supplementary Table A.2. Linear Combination fitting using CuO, Cu_2S and CuS as model compounds (*k* from 2 to 9).

	CuO (%)	Cu_2S (%)	CuS (%)	Sum	R
S/Cu 0.22	80	6	2	88	0.17
S/Cu 0.43	44	7	4	55	0.2
S/Cu 0.62	33	22	6	58	0.27
S/Cu 0.86	11	55	12	78	0.24
S/Cu 0.94	12	57	17	86	0.16
S/Cu 2.16	12	54	21	87	0.15

APPENDIX B:

Assessing the veracity of Precambrian 'sponge' fossils using *in situ* nanoscale analytical techniques

A.D. Muscente, F. Marc Michel, James G. Dale, Shuhai Xiao

Department of Geosciences, Virginia Polytechnic Institute and State University, Blacksburg, VA 24061, USA

Reprinted with permission from *Precambrian Research*, July 2015, 263, pp 142-156.

B.1. ABSTRACT

Paleontological inferences, molecular clocks, and biomarker fossils indicate sponges evolved in the Cryogenian, but Precambrian sponge fossils are rare, poorly substantiated, and controversial. Spiculelike microstructures (SLMs) hosted in phosphatized fossils from the Ediacaran Doushantuo Formation (~635–551 Ma) at Weng'an of South China have been interpreted as cylindrical siliceous monaxons, and their hosting fossils as the oldest demosponges in the fossil record. In order to assess their veracity as the oldest spiculate demosponges, we utilize a suite of in situ nanoscale analytical techniques—including scanning electron microscopy, synchrotron X-ray fluorescence mapping, X-ray absorption near edge structure (XANES) spectroscopy, focused ion beam electron microscopy, and transmission electron microscopy—to evaluate the ultrastructures and elemental, chemical, and mineralogical compositions of the SLMs. Our data decisively shows that the SLMs are carbonaceous in composition and rectangular in transverse sections, and therefore, are not cylindrical siliceous spicules. Instead, the SLMs may be microbial strands, axial filaments of early hexactinellids, or acicular crystals molded by organic matter. Regardless, our new data invalidate the oldest

and only Precambrian demosponges with mineralized spicules. These results indicate that interpretations of Precambrian sponge fossils should be scrutinized with compositional, mineralogical, and ultrastructural data collected using *in situ* analytical techniques. In addition, our conclusions affirm that no unequivocal biomineralizing sponges occur below the Ediacaran–Cambrian boundary. If hexactinellids and demosponges did diverge in the Cryogenian as suggested by molecular clocks and biomarkers, they either evolved biomineralization long after their divergence or their biomineralized spicules were never preserved until after the Ediacaran–Cambrian boundary. In either case, the dearth of biomineralizing sponge fossils in the Precambrian and their abundance in the early Cambrian must reflect a geobiologically significant aspect of the Precambrian–Phanerozoic transition.

B.2. INTRODUCTION

Sponge fossils are common in the Cambrian (Antcliffe et al., 2014; Steiner et al., 1993; Xiao et al., 2005), but conspicuously rare in the Precambrian. The Ediacaran appearances of metazoan reefs (Penny et al., 2014), eumetazoan-grade skeletons (Hua et al., 2005), and bilaterian trace fossils (Chen et al., 2013; Gehling et al., 2014) indicate that sponges, cnidarians, and bilaterians diverged in the Ediacaran Period or earlier. Additionally, molecular clock analyses date the divergence of silica-biomineralizing hexactinellid and demosponge classes at >750 Ma (Erwin et al., 2011; Sperling et al., 2010), and suggest that spiculate demosponge subclades diverged in the Cryogenian or the earliest Ediacaran Period (Sperling et al., 2010). Furthermore, demosponge-specific biomarkers date the origin of demosponges at >635 Ma (Antcliffe, 2013; Love et al.,

2009). However, the Precambrian fossil record includes only dubious and equivocal aspiculate sponges (Maloof et al., 2010; Sperling et al., 2011; Wallace et al., 2014; Wang and Wang, 2011), spiculate sponges (Clites et al., 2012; Du et al., 2014; Gehling and Rigby, 1996; Li et al., 1998b; Serezhnikova and Ivantsov, 2007), and sponge spicules (Allison and Awramik, 1989; Brasier et al., 1997; Du and Wang, 2012; Steiner et al., 1993). Although these controversial fossils could potentially fill the gap between the divergence of sponges in the Cryogenian and the first unequivocal sponge fossils in the early Cambrian, their interpretation as sponge fossils has been questioned (Antcliffe et al., 2014; Yin et al., 2001; Zhou et al., 1998).

Spiculate sponges and sponge spicules have the best potential to be preserved and recognized in the fossil record. In contrast to aspiculate sponge fossils, which problematically resemble other soft-bodied fossils such as macroalgae and microbial mats, spiculate sponges and sponge spicules possess diagnostic mineralogical and morphological characters. They also constitute the majority of Phanerozoic sponge fossils, and are expected to be preserved in the Precambrian, if biomineralizing sponges did evolve prior to the Ediacaran–Cambrian boundary as suggested by the molecular clocks (Erwin et al., 2011; Sperling et al., 2010). Yet, Precambrian spiculate sponges and sponge spicules are rare, poorly substantiated, and controversial. Thus far, none of the spiculate sponges described from the Precambrian have been authenticated on morphological and mineralogical grounds (Antcliffe et al., 2014). Consequently, they could alternatively be macroalgae or microbial mats (Antcliffe et al., 2014) or non-biomineralizing animals (Serezhnikova, 2007). Spicule-like structures disseminated in Precambrian rocks are also problematic (Brasier et al., 1997; Du and Wang, 2012; Steiner

et al., 1993). If they are sponge spicules, they should be cylindrical structures with the axial canals, axial symmetries, and sometimes concentric growth layers that distinguish spicules from abiogenic acicular crystals and organic microfossils (Allison and Awramik, 1989; Antcliffe et al., 2014; Steiner et al., 1993; Yin et al., 2001; Zhou et al., 1998). However, reports of Precambrian spicule-like structures generally contain insufficient data regarding such morphological and mineralogical characters to verify sponge affinities.

In situ analytical techniques allowing for nanoscale characterization of fossils can be used to critically assess the veracity of putative Precambrian sponge fossils. The basic utility of these techniques was recently demonstrated by Antcliffe et al. (2014), who used energy-dispersive X-ray spectroscopy (EDS) to show that spicule-like structures preserved within chert concretions from the Ediacaran Tsagaan Gol Formation (~545 Ma) of southwestern Mongolia—originally interpreted as siliceous hexactinellid spicules (Brasier et al., 1997)—contain higher concentrations of arsenic, iron, and sulfur than surrounding chert, and therefore, are probably cruciform arsenopyrite crystals, as hypothesized by other authors (Zhou et al., 1998). In addition to such fundamental compositional information, analytical techniques can also be used to collect *in situ* data regarding mineralogy (Wacey et al., 2014) and ultrastructure (Schiffbauer and Xiao, 2009), thereby providing a multitude of observations for testing phylogenetic interpretations. Despite the potential of such techniques to generate substantive information pertinent to paleobiological controversies, they have not been widely employed in studies of Precambrian 'sponge' fossils.

In this paper, we demonstrate the utility of *in situ* analytical techniques for studying the compositions, mineralogies, and ultrastructures of putative Precambrian sponge fossils by characterizing spicule-like microstructures (SLMs, <5 m in diameter, 10–100 m in length) occurring within phosphatized fossils from the Ediacaran Doushantuo Formation at Weng'an, South China (Li et al., 1998b). These phosphatized fossils were originally interpreted as the oldest demosponges in the fossil record (Li et al., 1998b), and are purportedly the only Precambrian sponges preserved with mineralized spicules. The SLMs were interpreted as siliceous monaxons on the basis of their supposed acicular shape, purported siliceous composition, and proximity to putative sclerocytes within the phosphatized fossils (Li et al., 1998b). However, the inferred siliceous composition of the SLMs was based on the observation that SLMs survived 4 M hydrochloric acid treatment, not spectroscopic or diffraction data (Li et al., 1998b), and although apparent axial canals have been illustrated in two SLMs (Li et al., 1998a), such diagnostic features have not been observed in other studies (Yin et al., 2001; Zhang et al., 1998). For these reasons, the hypotheses that the phosphatized fossils are demosponges and the SLMs are siliceous spicules have been cursorily questioned (Antcliffe et al., 2014; Yin et al., 2001; Zhang et al., 1998), though never thoroughly tested. Zhang et al. (1998) argued against a spicule interpretation—likening the SLMs to acritarch spines—but did not actually analyze the SLMs. Similarly, Yin et al. (2001) hypothesized that the SLMs are diagenetic crystals, similar to co-occurring fascicular and dumbbell-shaped crystals. However, because the micrometric SLMs are embedded in nanocrystalline apatite, the low-resolution and low-sensitivity analytical techniques used by Yin et al. (2001) were unable to determine the composition and the transverse sectional

morphology of the SLMs; their EDS analysis of SLMs was likely contaminated by surrounding phosphatic material.

Until now, no *in situ* compositional, mineralogical, or ultrastructural data existed to assess the various interpretations of SLMs in the phosphatized fossils at Weng'an. Using light and scanning electron microscopy (SEM), we screened over 100 petrographic thin-sections to locate SLMs for EDS, synchrotron X-ray fluorescence (XRF) elemental mapping, and X-ray absorption near edge structure (XANES) compositional analyses. To study their ultrastructure, we prepared *in situ* transverse sections through SLMs using dual-beam focused ion beam electron microscopy (FIB-EM). A SLM transverse section was also prepared as an ultra-thin (~100 nm thick) foil for mineralogical studies using bright field (BF) transmission electron microscopy (TEM), BF scanning transmission electron microscopy (BF-S/TEM), and selected area electron diffraction (SAED). Data from these analyses show that the SLMs are neither cylindrical nor siliceous, and therefore, the demosponge monaxon interpretation is invalidated. We provide several alternative interpretations for testing in future investigations, and conclude our report by reviewing the Precambrian record of sponge fossils in the context of our results and by discussing causes for the dearth of biomineralizing sponge fossils prior to the Ediacaran–Cambrian boundary.

B.3. GEOLOGICAL SETTING

The fossils in this study were collected from the upper Doushantuo Formation at a phosphorite mine (N 27º 00.948', E 107º 23.221'; elevation: 1200 m) near Weng'an in Guizhou Province, South China. In the Weng'an area, the Doushantuo Formation is

divided into 5 units (Fig. B.1; Muscente et al., 2014; Xiao et al., 2014a,b). Unit 1 (~5–10 m thick)—a cap dolostone—overlies the Cryogenian Nantuo diamictite. Above it, unit 2—the lower phosphorite (~8–15 m thick)—is a thin-bedded, peloidal phosphorite with interbedded dolostone and siltstone. It is overlain by unit 3 (~2–4 m thick), a massive dolostone topped by a prominent karstification surface (Xiao and Knoll, 2000; Xiao et al., 1998). Unit 4—the upper phosphorite bed (~3–10 m thick)—is an intraclastic phosphorite consisting of an organic-rich "black" phosphorite facies (unit 4A, ~0.5–5 m thick) overlain by dolomitic "gray" phosphorite facies (unit 4B, ~1–5 m thick) (Dornbos et al., 2006). This unit contains various three-dimensionally preserved fossils (Xiao et al., 2014a), including filamentous structures (Xiao and Knoll, 1999), multicellular algae (Xiao et al., 2004), acritarchs (Xiao et al., 2014b), putative metazoan embryos (Chen et al., 2014; Xiao et al., 1998), and the purported demosponges containing SLMs (Li et al., 1998b). All these fossils are cellularly replicated by nanometer-sized fluorapatite crystals (Cunningham et al., 2012; Schiffbauer et al., 2012; Xiao and Knoll, 1999). Unit 4 is overlain by unit 5 (~10 m thick), a phosphatic dolostone that may contain a karstification surface (Jiang et al., 2011; Zhu et al., 2007). It is overlain by the thick dolostone of the Dengying Formation.

The maximum age of the Doushantuo is constrained by a zircon U–Pb age of 636.4 ± 4.9 Ma from the Cryogenian Nantuo Formation (Zhang et al., 2008). Published radiometric ages from the Doushantuo Formation at Weng'an include Pb–Pb isochron ages of 599 ± 4 Ma (Barfod et al., 2002) and 576 ± 26 Ma (Chen et al., 2004) from unit 4. Condon et al. (2005) argue that phosphorite diagenesis may have compromised the reliability of the Pb–Pb dates. Instead, they propose that the karstification surface atop

unit 3 may be a glacioeustatic response to the 582–584 Ma Gaskiers glaciation (Hoffman and Li, 2009), implying that the fossils in this study are younger than 584 Ma. Alternatively, the karstification surface in unit 5 at Weng'an may be related to the Gaskiers glaciation—an interpretation that does not contradict the 599 ± 4 Ma age from unit 4. If so, the fossils in this study from unit 4 are 580–600 Ma (Xiao et al., 2014b).

B.4. MATERIALS AND METHODS

Samples were collected from units 4A and 4B. Billets of samples were cut, polished, and mounted to petrographic glass slides to make ~30 μm thick petrographic thin-sections. About one hundred thin-sections were examined via transmitted-light microscopy, and transmitted-light images were collected. High resolution composite transmitted-light images of phosphatized fossils and SLMs (indicated in figure captions) were assembled from multiple higher magnification images taken at the same focal lengths and using the same exposure settings. Forty thin sections with phosphatized fossils containing SLMs were imaged and elementally mapped using a low vacuum Hitachi™ TM3000 Tabletop thermionic (tungsten filament electron source) SEM with backscattered electron (BSE) solid state detector (SSD) and Bruker™ Xflash compact EDS detector. Thin-sections were not coated prior to SEM and EDS analyses. BSE images and EDS elemental maps were acquired at 15 keV accelerating voltage and 12 mm working distance. EDS elemental mapping scan live times were 400–500 s with ~8000 counts/s. Given the operating conditions, the tungsten filament electron source, and the count rate, the dead time should be within an acceptable range (~10–40% live time) for elemental mapping analysis. SEM-based EDS data were processed using the

Quantax 70 Microanalysis Software by Bruker™, designed for the Hitachi TM3000 SEM.

Two thin-sections—each containing two SLMs (or SLM fascicles) located approximately 3 μm below the polished thin section surfaces—were subsequently coated with 10 nm thick Au–Pd in preparation for FIB-EM. All FIB-EM analyses were conducted using a FEI™ DualBeam Helios 600 NanoLab equipped with a fieldemission gun electron source, Everhart-Thornley detector (ETD) of secondary electrons (SEs) and BSEs, a S/TEM detector, and a focused Ga^+ ion beam column for controlled, nanoscale material addition and excavation (Schiffbauer and Xiao, 2009). SE images of the SLMs (or SLM fascicles) were acquired throughout FIB preparation using the ETD (configured with a positively biased Faraday cage) at 5 keV accelerating voltage (Muscente and Xiao, 2015). Milling of the thin section was conducted using the Ga^+ ion beam at 30 kV accelerating voltage. The working distance was adjusted periodically. Thin (~1 μm thick) layers of Pt were deposited on the surfaces of the thin-sections above the SLMs (or SLM fascicle) prior to milling using the Ga^+ FIB. The SLM fascicle transverse section prepared as an ultra-thin foil using FIB-EM was removed from the slide using a micromanipulator probe, secured to a copper TEM grid, and ion polished to ~100 nm thickness. BF-TEM, BF-S/TEM, and SAED analyses of the ultra-thin foil were conducted at 200 keV using a JEOL™ 2100 TEM with thermionic source and high-resolution EDS detector. TEM and BF-S/TEM images were processed using JEOL™ Analysis Program software. TEM-based EDS elemental maps were acquired at 200 keV with a scan time of ~26 min (dwell time, 2 ms; resolution, 1024 × 768 pixels), and were processed using JEOL™ AnalysisStation software package.

Phosphatized fossils were also extracted from unit 4B samples using the standard acetic acid maceration technique (Xiao and Knoll, 2000). Samples were macerated in 10–15% acetic acid for 3–6 days, after which, the maceration residuals were washed, drained, and dried. The fossils were then picked individually from the maceration residue, mounted on copper tape, and coated with ~20 nm thick C for electron imaging using a FEI^{TM} Quanta 600F environmental SEM with field emission gun electron source, ETD, and SSD. SE and BSE images were acquired using the ETD (configured with a positively biased Faraday cage) and SSD, respectively, at 10 mm working distance and 10–20 keV accelerating voltage.

Because EDS elemental analysis showed that SLMs are composed of sulfur-rich carbonaceous material, XANES spectroscopy was used to probe the sulfur K-edge (2472 eV) of SLMs in thinsections in order to determine their chemical compositions. The experiments were performed at the Stanford Synchrotron Radiation Lightsource (SSRL) on beamline 14-3 utilizing a silicon(1 1 0) monochromator crystal; data was collected in fluorescence mode. Gypsum was used as a non-simultaneous calibrant. Linear combination fitting (LCF) of the XANES spectra was performed using the SIXPack interface to the IFEFFIT XAFS analysis package (Webb, 2005). Spectra for the model sulfur compounds (cysteic acid, dibenzothiophene, dimethylsulfoxide, elemental sulfur, glutathione-oxidized, gypsum, L-cystine, lipolic acid, marcasite, methionine methylsulfonium chloride, methionine sulfone, methionine, polyphenylene sulfide, pyrite, pyrrhotite, sodium bisulfite, sodium sulfite, sodium thiosulfate, sodium trichloromethane, sphalerite, taurine, thianthrene) were obtained from the ID21 sulfur XANES spectra database (http://www.esrf.eu). In LCF, species were only included which decreased the

R-value (fit residual) by more than 20%. In additional to EDS elemental maps acquired via SEM, XRF elemental maps were also generated on beamline 2–3 at the SSRL using a silicon(1 1 1) monochromator crystal at 12 keV.

B.5. RESULTS

The SLMs most commonly occur within spheroidal to subspheroidal phosphatized fossils referable to the putative animal embryo *Megasphaera* in unit 4A (Xiao and Knoll, 2000). They are distributed randomly within *Megasphaera* of various developmental stages, including two- and four-cell stages (Fig. B.2A and B). Observed in transmitted-light microscopy of petrographic thin-sections, the SLMs appear more opaque than the surrounding cell lumens of *Megasphaera*, and are usually unbranched and rigid (Fig. B.2C,D). However, rare curved and folded SLMs are also present (Fig. B.2E,F). The SLMs are often aggregated in terminally spreading fascicles (Fig. B.2B), which are sometimes attached to the cell membranes or envelopes of *Megasphaera* (Fig. B.2G,H).

Contrast in BSE images indicates that the SLMs are composed of a material with lower average atomic number (Z) than the apatite in the cell lumens (Fig. B.3). EDS elemental maps acquired via SEM show that this lower-Z material is most likely sulfur-containing carbonaceous material (Fig. B.3I–P). Silicon is absent in the SLMs, generally restricted to minerals found in the matrix around *Megasphaera*. XRF elemental maps—produced with synchrotron X-rays, which interact with samples at greater depths and achieve better energy resolution than EDS maps at the cost of signal heterogeneity in non-homogenous samples—also show that the SLMs contain lower concentrations of

silicon and iron, but higher concentrations of sulfur, than the lumen of *Megasphaera* (Fig. B.3E–H). Normalized S K-edge XANES spectra collected via spot analyses of the SLM fascicle (Fig. B.3C) and of carbonaceous material located in the matrix around *Megasphaera* (Fig. B.3D) generally show three peaks: a peak at ~2474 eV and relatively less intense peaks at ~2476 and ~2479 eV (Fig. B.4). A fourth peak at ~2483 eV is apparent in some spectra and varies in relative intensity among spots, suggesting that multiple sulfur compounds are present and vary in relative abundance among spots. LCF of representative spectra of SLM fascicle and matrix carbonaceous material to spectra of model sulfur compounds indicates that the best two-compound fits for the SLM fascicle and matrix carbonaceous material spectra are, respectively, dibenzothiophene (DBT, a thiophene common in petroleum; Aizenshtat et al., 1995) with polyphenylene-sulfide and DBT with gypsum (Table B.1). Inclusion of spectra of other compounds (*e.g.*, elemental sulfur and pyrite) in LCF did not significantly improve the fits. Traces of sulfate may be present in apatite surrounding the SLM fascicle and matrix carbonaceous material (Shields et al., 2004), responsible for the peak at ~2483 eV. The other peaks in the sulfur XANES spectra likely represent organic sulfur in heterocyclic compounds such as DBT, previously reported from organic structures of Precambrian microfossils (Lemelle et al., 2008) and from organic matter in the Dengying Formation (Duda et al., 2014). Thiophenes are abundant in anoxic environments with bacterial sulfate reduction and cyanobacterial mats influenced by hydrogen sulfide (Philp et al., 1992), such as the sediment pore waters in which the apatite comprising the phosphatized fossils at Weng'an most likely precipitated (Muscente et al., 2014).

FIB-EM (Fig. B.5) and TEM (Fig. B.6) revealed that the SLMs are rectangular in transverse sections, lack axial canals, and are composed of homogenous albeit porous carbonaceous material ("pC" in Fig. B.5P). Pores in the porous carbonaceous material can be 30–100 nm in diameter, but are typically less than 50 nm in diameter (Figs. 5P, 6A,J,K). The porous carbonaceous material in the SLMs closely resembles unassociated porous carbonaceous material located in the cell lumen in terms of contrast and porosity ("upC" in Fig. B.5P). Neither the rectangular shape nor dimensions of SLM transverse sections changed significantly during ion milling and polishing (Fig. B.5K–O). TEM-based EDS elemental mapping of the ultra-thin foil confirms high carbon and sulfur and low silicon, iron, calcium, fluorine, oxygen, and phosphorus concentrations in SLMs relative to surrounding cell lumen (Fig. B.6B–I). Silicon and aluminum peaks are limited to an authigenic aluminosilicate located between the carbonaceous material of the SLM and a micrometersized apatite crystal (5 μm in diameter; "mA" in Fig. B.6A,J,K). SAED analyses corroborate inferences based on electron imaging, EDS, XRF, and XANES, showing that the SLM material weakly scatters electrons throughout reciprocal space (Fig. B.6L), and therefore, is generally amorphous. The phosphatic minerals surrounding the SLMs, on the other hand, yield diffraction patterns containing sharp peaks consistent with nanocrystalline (Fig. B.6M,N) and microcrystalline (Fig. B.6O–Q) apatite.

Three types of apatite mineralization can be observed in the analyzed specimens (Fig. B.6). The cell lumen surrounding the SLMs is filled with randomly oriented apatite nanocrystals (~0.1 μm diameter; "ncA" in Fig. B.6A,J,K). These randomly oriented apatite nanocrystals are in contact with the SLMs in some places. However, they are typically separated from SLMs by voids (possible FIB damage) and isopachous apatite

cement of radially oriented prismatic crystals (0.3–0.6 μm diameter; "icA" in Fig. B.6A,J,K). The third mineralization type is exemplified by the micrometer-sized apatite crystal that cross-cuts the SLM prepared as an ultra-thin foil ("mA" in Fig. B.6A,J,K). Unlike the isopachous apatite cement, which is in contact with porous carbonaceous material, the micrometer-sized apatite crystals is separated from porous carbonaceous material by 0.5 μm thick nonporous compressed carbonaceous material ("cC" in Fig. B.6A,J,K).

B.6. DISCUSSION

The SLMs in the phosphatized fossils at Weng'an are rectangular in transverse sections and carbonaceous (specifically thiophenic) in composition, and therefore, are not cylindrical siliceous sponge spicules. Although carbonaceous fossils from the lower Cambrian have been interpreted as organic sheaths that originally surrounded siliceous spicules (Harvey, 2010), the SLMs do not appear to be organic sheaths that ever encased spicules. In addition, unlike rigid sponge spicules, curved and folded SLMs imply original flexibility (Fig. B.2E,F). Petrographic observations also indicate that the phosphatized fossils containing SLMs do not the match expectancies of demosponge spiculogenesis. Modern siliceous spicules are initially formed within one and later in association with several sclerocytes, but the two- and four-celled *Megasphaera* (Fig. B.2A) that host SLMs do not seem to have had differentiated cell types such as sclerocytes. Putative sclerocytes described from the purported Doushantuo sponges (Li et al., 1998b) resemble subcellular structures interpreted as possible lipid vesicles (Hagadorn et al., 2006; Schiffbauer et al., 2012).

B.6.1. Origin of the spicule-like microstructures

The SLMs may represent carbonized filamentous bacteria, such as sulfur-oxidizing bacteria filaments, which sometimes have rectangular transverse sections (Lacko et al., 1999). Phosphatic filaments—interpreted as possible bacterial filaments, fungal hyphae, and mucous strands (Xiao and Schiffbauer, 2009)—are found inside and attached to *Megasphaera* envelopes in unit 4B (Fig. B.1), and include forms that are sparsely-branching (15–20 μm diameter), anastomosing (3–5 μm diameter), and coated with botryoidal cements (Fig. B.7). The sparsely-branching phosphatic filaments sometimes contain axially located structures (2–7 μm diameter) that are circular or oblong (possibly rectangular) in transverse sections, replicated by radially or randomly oriented nanocrystals (0.1 μm diameter), and coated with radially oriented prismatic microcrystals (0.3–2 μm diameter). The paragenesis of apatite in phosphatized fossils from unit 4B inferred from SEM observations indicates the axially located structures were originally organic filaments that were replicated by nanocrystals and then coated with later diagenetic microcrystals, which variously augmented their overall diameters (Cunningham et al., 2012; Schiffbauer et al., 2012; Xiao and Schiffbauer, 2009). Thus, it is possible that SLMs represent an organic version of those phosphatized filaments with an oblong axial structure.

Alternatively, the SLMs may be sponge axial filaments (~2–5 μm in diameter), which in sponge development, are the organic precursors of spicules (Müller et al., 2007). Hexactinellid axial filaments are square in transverse section (Reiswig, 1971), thus broadly resembling the SLMs; in contrast, demosponge axial filaments are triangular (Reiswig, 1971) or hexagonal (Simpson et al., 1985) in transverse section. Axial

filaments are generally rare in the fossil record, but are sometimes preserved in mineralized spicules (Botting and Muir, 2013). If the SLMs are confirmed to be axial filaments, they could provide evidence of hexactinellids. This possibility, however, does notnecessitate that the sponges that produced such axial filaments were biomineralizing organisms, as organic axial filaments could have evolved prior to—and then were exapted for—spiculogenesis.

The occurrence of fascicles of SLMs seems inconsistent with the filamentous bacterium and axial filament interpretations, and invites comparison with acicular mineral aggregates (Yin et al., 2001). Thus, a third possibility is that the SLMs represent acicular minerals that were diagenetically replaced and molded by organic matter. However, the flexible nature of some SLMs (Fig. B.2F) is inconsistent with the acicular mineral interpretation.

Overall, these hypotheses imply that phosphatized fossils containing SLMs at Weng'an are not crown-group demosponges. Indeed, if the SLMs are bacterial filaments or acicular crystals molded by organic matter, the phosphatized fossils containing SLMs may not be sponges. Alternatively, if the SLMs are axial filaments, they must have been produced by hexactinellids, as crown-group demosponges (Reiswig, 1971) and possibly stem-group siliceans (Botting and Muir, 2013) have triangular or hexagonal axial filaments. Despite this possibility, the phosphatized fossils containing the SLMs possess no diagnostic sponge soft tissue characters (Antcliffe et al., 2014). Given these notable ambiguities, placement of the phosphatized fossils with SLMs among sponges is not supported.

B.6.2. Taphonomy of SLMs

Regardless whether the SLMs are bacterial filaments, axial filaments, or pseudomorphs of acicular crystals, their morphology has been modified, both constructively and destructively, by multiple generations of diagenetic phosphatic mineralization. Randomly oriented apatite nanocrystals ("ncA" in Fig. B.6A,J,K) in cell lumens likely formed rapidly during degradation of the cytoplasm when nucleation sites were abundant and the supersaturation level was high (Xiao and Schiffbauer, 2009). Cement stratigraphy suggests that SLMs predate the formation of the isopachous apatite cements ("icA" in Fig. B.6A,J,K) that constructively encrust SLMs. In contrast, cross-cutting relationship suggests that micrometer-sized apatite crystals ("mA" in Fig. B.6A,J,K) played a destructive role; such micrometer-sized crystals in phosphatized fossils are typically interpreted as late diagenetic overgrowth on pre-existing crystals (Cunningham et al., 2012; Schiffbauer et al., 2012; Xiao and Schiffbauer, 2009). As observed in the ultra-thin foil transverse section of an SLM fascicle (Fig. B.6), growth of a micrometer-sized apatite crystal into the SLM caused displacement of organic matter, compressing porous carbonaceous material into nonporous compressed carbonaceous material. Assuming the micrometer-sized apatite crystal in the ultra-thin foil transverse section of an SLM fascicle is representative of the diagenetic processes affecting all SLMs, variations among SLMs and SLM fascicles may correspond to permutations of several variables: the rate and amount of diagenetic apatite growth, the direction of apatite growth relative to the axes of SLMs, and the space available for SLM carbonaceous material displacement and compression. This hypothetical relationship between diagenetic apatite growth and SLM fascicle shape requires further testing with

comprehensive *in situ* analytical techniques, such as FIB-EM nanotomography or X-ray computed nanotomography.

B.6.3. Implications for other purported Precambrian sponges

Our conclusions regarding the phosphatized fossils containing SLMs affirm the observation that no unequivocal sponge fossils occur below the Ediacaran–Cambrian boundary (Antcliffe et al., 2014). Chambered body fossils containing silica and carbonate minerals from Cryogenian rocks have been interpreted as biomineralizing sponge-grade metazoans (Maloof et al., 2010; Wallace et al., 2014), but they lack spicules and there is no data affirming the biogenicity of the silica and carbonate minerals. For these reasons, placement of the chambered fossils among crown-group sponges is unlikely (Laflamme, 2010), and they may instead be microbial structures (Antcliffe et al., 2014; Wallace et al., 2014). Various other Precambrian aspiculate fossils—such as *Cucullus* from China (Wang and Wang, 2011), *Thectardis* from Newfoundland (Sperling et al., 2011), and *Ausia* from Namibia (McMenamin, 1998)—have been interpreted as sponges based on inferences regarding soft tissue anatomy, biomechanics, and taphonomy. However, such interpretations of aspiculate organisms are inherently subjective, and the affinities of the fossils remain disputed (Antcliffe et al., 2014).

Although spicules are generally considered among the most easily identifiable and most commonly preserved features of crown-group sponges, reports of spiculate sponges and sponge spicules from the Precambrian remain ubiquitously controversial due, in part, to the poor preservation and inadequate characterization of the fossils. The spicule-like structures associated with the purported spiculate sponges—including Fedomia from Russia (Serezhnikova and Ivantsov, 2007) and *Palaeophragmodictya* (Gehling and

Rigby, 1996) and *Coronacollina* (Clites et al., 2012) from South Australia—generally lack the siliceous and calcareous biominerals that constitute modern sponge spicules. Instead, the spicule-like structures are preserved, like co-occurring soft tissues, as casts/molds in siliciclastic rock. Consequently, the spicule-like structures may represent casts/molds of diagenetically dissolved spicules (Gehling and Rigby, 1996) or organic structures (Clites et al., 2012; Serezhnikova and Ivantsov, 2007), which cannot be distinguished in such a preservational state. For this reason, the spicule-like structures on these fossils do not represent diagnostic evidence of biomineralizing sponges. The phosphatized fossils containing SLMs in the Doushantuo Formation were previously considered the only Precambrian sponges preserved with mineralized spicules (Li et al., 1998a,b). However, our new data demonstrate that the SLMs are not siliceous sponge spicules. Thus far, no unequivocal biomineralizing sponges have been reported from Precambrian rocks.

Reports of Precambrian spicule-like structures preserved in the absence of soft tissues are common, but typically provide only non-diagnostic petrographic observations. Without detailed mineralogical and ultrastructural data on these structures, interpretations of these fossils as sponge spicules are unconvincing. For instance, the sponge spicules reported from the Noonday Dolomite in Nevada—which may be a basal Ediacaran cap carbonate (Petterson et al., 2011)—have not been illustrated or described in detail (Reitner and Wörheide, 2002), and have been interpreted as inorganically precipitated acicular crystals (Antcliffe et al., 2014). Similarly, monaxon-like structures from the Neoproterozoic Tindir Group in Alaska and western Canada identified as hexactinellid spicules (Debrenne and Reitner, 2001) have only been superficially described (Allison

and Awramik, 1989). Although reports suggest the Tindir Group spicule-like structures were originally hollow and are comparable to chancellorid sclerites (Allison and Awramik, 1989), they have not received sufficient study to affirm sponge affinities. Other problematic hexactinellid spicules have been reported from the Gangolihat Dolomite of India (Tiwari et al., 2000; Tiwari and Pant, 2009). Most of these Gangolihat Dolomite structures are opaque, and thus do not resemble typical siliceous hexactinellid spicules in thin-sections. Previous reports have described no evidence of axial canals in the Gangolihat Dolomite structures. In addition, the Gangolihat Dolomite may be Mesoproterozoic in age (McKenzie et al., 2011). If so, the structures significantly predate the divergence of biomineralizing sponge classes, as estimated from molecular clocks (Erwin et al., 2011; Sperling et al., 2010). Given these uncertainties, the Gangolihat Dolomite structures do not represent compelling evidence of Precambrian sponges.

Besides the Doushantuo SLMs, the only other putative sponge spicules explicitly described with axial canals from the Precambrian are putative hexactinellid monaxons and triaxons from the lower Doushantuo Formation (Du and Wang, 2012). EDS analyses indicate these purported hexactinellid spicules are siliceous in composition. However, the structures lack clearly defined axial canals (despite the authors' claim of such features), they are not preserved with soft tissues, the previous report provides no evidence of concentrically secreted silica layers, and some of these structures shown in thin sections resemble acicular minerals. Thus, they may be abiotic structures formed via silica encrustation or replacement of diagenetic crystals.

Recently, Du et al. (2014) reported putative sponge gemmules containing gemmosclere-like structures from chert nodules of the Doushantuo Formation in the

Yangtze Gorges area of South China. They interpreted the gemmosclere-like structures (<1 μm diameter) as siliceous based on the presence of Si as detected by electron probe microanalysis. However, as the authors noted, it is difficult to focus the electron probe onto micrometer-sized structures, and their compositional analysis may be inaccurate. In addition, the authors provided no mineralogical data and no evidence of axial canals, axial symmetries, and concentric growth layers. For these reasons, the gemmosclere-like structures do not represent unequivocal evidence of Precambrian biomineralizing sponges. They may alternatively be Si-bearing crystals.

Integration of these observations from the literature indicates that, although many spiculate sponges and sponge spicules have been reported from Precambrian rocks, none have been comprehensively characterized in terms of their compositional, mineralogical, and morphological characters. Future studies should test the veracity of these fossils using *in situ* analytical techniques and cogent evaluation criteria. By doing so, such studies may resolve long-standing controversies, test paleobiologically significant hypotheses, and potentially provide compelling evidence of biomineralizing sponges in the Precambrian. According to Antcliffe et al. (2014), the oldest fossils equivocally attributable to biomineralizing sponges are siliceous stauractines and pentactines in the early Cambrian Soltanief Formation (~535 Ma) of Iran. Unambiguous hexactines and pentactines have also been described as *Hunanospongia* from the basal Cambrian Yangjiaping Member of South China (Ding and Qian, 1988), in association with the *Protohertzina anabarica–Kaiyangites novilis* small shelly fossil assemblage biozone (Steiner et al., 2007). These are among the earliest known, unambiguous sponge spicules by virtue of their diagnostic and clearly defined symmetries (Antcliffe et al., 2014).

B.6.4. Interpreting the Precambrian dearth of biomineralizing sponge fossils

The conspicuous scarcity (or complete absence) of spiculate sponges and sponge spicules in the Precambrian has important implications for the evolution of animals and the Earth system across the Ediacaran–Cambrian transition. Whereas the perceived paucity of aspiculate sponge fossils may reflect the taphonomic biases against soft-tissue preservation and the paleontological difficulties associated with differentiating such fossils from those of other soft-bodied organisms, the dearth of spiculate sponges and sponge spicules—which should be readily preservable and easily identifiable—is enigmatic, particularly given that molecular clocks (Erwin et al., 2011; Sperling et al., 2010) and sponge-specific biomarkers (Love et al., 2009) suggest the hexactinellid-demosponge divergence and the internal divergence of spiculate demosponges may have occurred in the Cryogenian. Several explanations have been proposed to account for the enigma (Sperling et al., 2010). Below, we review these explanations, and provide new hypotheses for the dearth of biomineralizing sponge fossils in Precambrian rocks.

B.6.4.1. Biomarkers and molecular clocks

Perhaps the simplest explanation for the dearth of Precambrian spiculate sponges and sponge spicules is that biomineralizing sponge classes diverged during the early Cambrian, as suggested by the fossil record. If so, this explanation implies that the Cryogenian divergence of silica-biomineralizing sponges based on molecular clocks (Erwin et al., 2011; Sperling et al., 2010) and biomarkers (Love et al., 2009) needs to be re-evaluated.

The detection of abundant 24-isopropylcholestanes in Cryogenian rocks in Oman is taken as evidence for demosponge divergence in the Cryogenian Period or earlier

(Love et al., 2009). The demosponge specificity of 24-isopropylcholestanes has been questioned by some authors (Antcliffe, 2013), although a counter argument has been made (Briggs and Summons, 2014). Thus, it remains possible that 24-isopropylcholesterol evolved along the stem leading to crown-group demosponges (Love et al., 2009; Sperling et al., 2010). If so, then the Cryogenian occurrence of 24-isopropylcholestanes can be used as a minimum age constraint for the demosponge-hexactinellid divergence. However, as pointed out by Antcliffe (2013), the exact age of the Cryogenian 24-isopropylcholestanes from Oman has been miscited by many authors. These 24-isopropylcholestanes are constrained between 645 and 635 Ma according to Antcliffe (2013), rather than 713 Ma as cited by some authors.

Published molecular clock estimates of sponge divergences were calibrated, in part, using the occurrence of Cryogenian 24- isopropylcholestanes in Oman as a calibration point. For example, both Sperling et al. (2010) and Erwin et al. (2011) used the 713 Ma age as a maximum age for the origin of crown-group demosponges. Because the Omani 24-isopropylcholestanes are 645–635 Ma and they may predate the origin of crown group demosponges (Love et al., 2009; Sperling et al., 2010), anchoring the divergence of crown-group demosponges using the 713 Ma age, even as a maximum constraint, may overestimate divergence time. It is important to point out, however, that both Sperling et al. (2010) and Erwin et al. (2011) carried out various sensitivity tests including or excluding the 713 Ma calibration point. For example, Erwin et al. (2011) used a Calibrations-Jackknife analysis—comparing molecular clocks randomly generated using various combinations of 12 out of their 24 available calibration points—to show that their estimated divergence dates of animals, on average, were not significantly

affected by their selection of geochronological calibrants and that their analyses consistently supported a Cryogenian divergence of biomineralizing sponge classes (and internal divergence of spiculate demosponges). Nonetheless, the general problem of using stem-group fossils to calibrate their crown-group counterparts remains, and it may be compounded by phylogenetic uncertainties and taxon sampling problems, particularly when the deepest divergence in the crown-group taxon is not represented in the taxon sampling. Thus, considering the significant discrepancy between molecular clocks and skeletal fossils, more effort needs to be spent to improve the accuracy of both records.

B.6.4.2. Independent origins of sponge biomineralization in the Cambrian

Another explanation for the dearth of spiculate sponges and sponge spicules in the Precambrian is that silica biomineralization may have evolved independently among hexactinellids and demosponges during the early Cambrian, perhaps in response to extrinsic ecological and environmental factors driving animal skeletonization (Marshall, 2006; Zhang et al., 2014). Given that it is uncertain whether the siliceans are monophyletic and that aspiculate demosponges (*e.g.*, Keratosa and Myxospongiae) either form a sister group to spiculate demosponges or branch successively at the base of the demosponge clade (Hill et al., 2013), it is possible that demosponge biomineralization may have evolved independently of hexactinellids. Although it is more difficult to accept that the heteroscleromorphs and haploscleromorphs evolved siliceous spicules independently (Cárdenas et al., 2012; Sperling et al., 2010), if the Heteroscleromorpha-Haploscleromorpha divergence is overestimated by several tens of millions of years, then it is possible that the common ancestor of heteroscleromorphs and haploscleromorphs evolved biomineralization in the Cambrian rather than Cryogenian–Ediacaran interval.

Under such a scenario, silicean biomineralization evolved in the early Cambrian independently among two clades: the hexactinellids and heteroscleromorphs + haploscleromorphs.

Recently, however, there has been paleontological evidence suggesting that spicules may be homologous among siliceans or even among siliceans and calcareans (Botting and Butterfield, 2005). It is proposed that ancestral sponges had bimineralic spicules consisting of both silica and calcite, and if sponges are paraphyletic, then the last common ancestor of metazoans may have been spiculate (Botting et al., 2012). Accepting that spicules are homologous among siliceans, sponges, or even metazoans (Botting et al., 2012), and given that there is abundant evidence supporting the appearance of crown-group animals in the Ediacaran Period (Xiao and Laflamme, 2009), it is rather difficult to explain the dearth of Precambrian sponge spicules without invoking a taphonomic megabias against the preservation of Precambrian siliceous spicules.

B.6.4.3. Taphonomic megabias

There are limited data regarding the taphonomic processes governing siliceous spicule preservation. However, multiple studies have characterized factors affecting dissolution of biosilica in diatoms (Cheng et al., 2009; Dixit et al., 2001; Lewin, 1961; Roubeix et al., 2008). In general, the preservation potential of biosilica depends upon its reactive surface area as well as the pH, temperature, salinity, and dissolved silica concentration of the surrounding bottom/pore waters (Van Cappellen and Qiu, 1997a,b). In addition, the presence of organic and inorganic materials impacts biosilica preservation. Organic material as well as inorganic precipitates (*e.g.*, iron or manganese) can absorb onto biosilica, reduce its reactive surface area, and protect it from dissolution

(Chu et al., 2011; Lewin, 1961). Similarly, dissolution of aluminosilicate minerals provides aqueous Al(III), which becomes absorbed onto biosilica, producing negatively charged aluminosilicate surface sites that reduce interactions with catalytic hydroxyl ions and decrease the solubility of the siliceous material (Cheng et al., 2009; Dixit et al., 2001). Lastly, microbial activity affects biosilica preservation. Experiments using marine bacteria show that bacterial colonization significantly increases biosilica solubility (Bidle and Azam, 1999).

In this context, the impact of the Precambrian–Phanerozoic transition on biosilica preservation can be evaluated. Secular changes in chert precipitation and deposition across the Precambrian–Phanerozoic transition affirm evolving geobiological participation in the silica cycle during this interval (Maliva et al., 1989, 2005). Modeling suggests that, before the diversification of silica-biomineralizing plankton in the early Phanerozoic, seawater and pore water SiO_2 concentrations may have been as high as 60 ppm (Perry and Lefticariu, 2014), roughly ten times higher than modern levels (Racki and Cordey, 2000). Though under these levels SiO_2 would have been undersaturated with respect to amorphous silica (Siever, 1992), everything else being equal, biosilica would have been less soluble in Neoproterozoic than in Phanerozoic seawater. Additionally, biosilica would have been less soluble in low temperature Cryogenian environments than in younger greenhouse analogs. Hence, changes in seawater silica concentrations and temperatures do not account for the purported megabias.

Because incorporation of Al(III) decreases biosilica solubility, the dearth of siliceous spicules may reflect secular changes in bottom/pore water Al(III) concentrations through time. For instance, Sperling et al. (2010) hypothesized that siliceous spicules

were unlikely to be preserved in clay- and Al(III)-deficient Neoproterozoic sediments, and proposed that an increase in the total clay contents of sediments deposited from 850 to 530 Ma opened a taphonomic window for the preservation of siliceous spicules. However, several observations dispute this hypothesis. First, the authors cite increasing X-ray diffraction peak ratios of phyllosilicates to quartz from 850 to 530 Ma in three basins as evidence of global trends in the clay contents of sedimentary rocks (Kennedy et al., 2006). However, these ratios do not distinguish between micaceous clays and pedogenic smectite/kaolinite clays. Micaceous clays would not necessarily be a source of Al(III) in early diagenesis, and hence, should not have factored into the preservation of the siliceous spicules. Second, empirical data derived from additional basins indicate that Neoproterozoic and early Cambrian sedimentary rocks are generally comparable in total clay contents, and exhibit no increase in total clay contents with time (Tosca et al., 2010). Lastly, although micaceous clays dominate most late Neoproterozoic clay mineralogy (Tosca et al., 2010), some Ediacaran successions (*e.g.*, the Doushantuo Formation in the Yangtze Gorges area of South China) have abundant Al-rich smectite clays (Bristow et al., 2009), but preserve no siliceous sponge spicules.

Given the effect of marine bacteria on biosilica dissolution, the transition from Precambrian seafloors with well-developed microbial mats to Phanerozoic-type sediments characterized by greater vertical mixing (Bottjer et al., 2000; Droser et al., 2002) could partially explain the dearth of siliceous sponge spicules. In modern settings, bacteria colonize and hydrolyze the surface mucus membranes of diatoms (Smith et al., 1995), which denudes the siliceous skeletons of their organic coating, thereby significantly increasing their reactive surface area and solubility (Bidle and Azam, 1999).

Microbial mats may have analogously colonized siliceous spicules on Neoproterozoic seafloors, degrading their external organic sheaths (Botting et al., 2012; Harvey, 2010) and the carbonaceous matter absorbed onto their surfaces, thereby enhancing the solubility of the biosilica. In addition, organisms inhabiting microbial mats in proximity to siliceous spicules may have—through their various activities (Callow and Brasier, 2009; Muscente et al., 2014)—modified biosilica dissolution.

Hypothetically, sponge paleoecology could also account for the dearth of spiculate sponges and sponge spicules in the Precambrian. Several key observations of modern sponge ecology and spiculogenesis suggest that, during the Precambrian, spiculate sponges may have been more ecological restricted and may have produced small or weakly mineralized spicules, which may have been rapidly dissolved. First, spicules protect modern sponges from predators (Burns et al., 2003; Hill et al., 2005; Jones et al., 2005), suggesting that predation may have driven the evolution of spicules. If so, spiculate sponges in the Neoproterozoic may have—in the absence of predatory animals—produced ostensibly small spicules with low preservational potential. Only after the diversification of predatory animals during the Cambrian Explosion—when large spicules may have enabled sponges to deter the predators—may extensive biomineralization have become widespread among sponges. Second, due to the energy-dependence of silica transport and sclerocyte production (Frøhlich and Barthel, 1997), environmental nutrient availability affects spicule size and morphology (Liu et al., 2013). Sponges in oligotrophic environments typically form smaller spicules than analogs inhabiting eutrophic settings (Bibiloni et al., 1989), and starvation causes sponges to significantly reduce and sometimes cease spicule production (Frøhlich and Barthel, 1997;

Pe, 1973). Because of this relationship between nutrient availability and spiculogenesis, widespread marine anoxia in Proterozoic oceans may have restricted the ecological distribution of spiculate sponges. In addition, although sponges can survive in dysoxic environments (Mills et al., 2014)—such as those that likely exited in Proterozoic oceans—they tend to produce smaller spicules when oxygen levels are low (Liu et al., 2013). Lastly, low oxygen availability is also associated with low levels of predation (Sperling et al., 2013). Consequently, sponges inhabiting Proterozoic oceans with lower oxygen levels than the present may not have experienced predation pressures that drive evolution of extensive biomineralized skeletons. Overall, these various observations suggest that Neoproterozoic spiculate sponges may have been more ecologically restricted and produced smaller spicules than their Phanerozoic descendants. If so, the evolution of sponges with larger, more easily preserved spicules may have been promoted by secular change in nutrient availability, the progressive oxygenation of the ocean, and the diversification of predatory animals through the Cryogenian-Cambrian interval (Canfield et al., 2007; Lenton et al., 2014; Sahoo et al., 2012).

B.7. CONCLUSIONS

In summary, we have demonstrated that *in situ* analytical techniques—including SEM, FIB-EM, TEM, EDS, XRF, and XANES—can be used to decisively assess the veracity of putative Precambrian sponge fossils. Our analysis shows that SLMs occurring within phosphatized fossils from the Doushantuo Formation154 A.D. Muscente et al. / Precambrian Research 263 (2015) 142–156 at Weng'an in South China are organic filaments with rectangular transverse cross-sections, and therefore, are not cylindrical

siliceous sponge spicules. This conclusion invalidates the descriptions of the oldest demosponges in the fossil record and of the only Precambrian sponges purportedly preserved with mineralized spicules (Li et al., 1998a,b). These results have notable implications for the Precambrian record of sponges. In particular, the analytical techniques in this study represent useful tools to critically assess the veracity of other problematic sponge fossils, specifically those with putative biominerals (Allison and Awramik, 1989; Du and Wang, 2012; Du et al., 2014; Maloof et al., 2010; Reitner and Wörheide, 2002; Tiwari et al., 2000; Wallace et al., 2014). By using the analytical techniques to collect *in situ* compositional, mineralogical, and ultrastructural data on these fossils, future studies may resolve long-standing controversies, test paleobiologically significant hypotheses, and potentially provide compelling evidence of biomineralizing sponges in Precambrian rocks. Thus far, no Precambrian sponge fossils have been demonstrated to have decisive mineralogical and morphological characters in support of biomineralization. Thus, molecular clock data suggesting that spciulate sponges diverged in the Cryogenian and Ediacaran periods need to be scrutinized more closely. If biomineralizing sponge clades did diverge in the Cryogenian–Ediacaran periods, as suggested by molecular clocks and biomarkers (Erwin et al., 2011; Love et al., 2009; Sperling et al., 2010), then we have to consider the possibility of independent origins of biomineralized spicules or a taphonomic megabias. A number of factors—including low sediment pedogenic clay mineral content, prevalence of microbial mats, low predation pressures, low nutrient availability, and oceanic anoxia—may have fostered spicule miniaturization and dissolution in the Neoproterozoic. If so, the molecular and fossil records may represent unique albeit complementary windows to

sponge evolutionary history. Whereas molecular clocks may record the timing and pace of sponge cladogenesis, the fossil record (or lack thereof) may reflect the ecological success, distribution, and preservation of early sponges in Precambrian environments. Regardless, the dearth of biomineralizing sponge fossils before the Cambrian represents a geobiologically significant aspect of the Proterozoic-Phanerozoic transition, and merits detailed investigation.

B.8. ACKNOWLEDGEMENTS

This work was supported by grants from the National Science Foundation (EAR-1250800) to S.X., Geological Society of America, Sigma Xi Scientific Research Society, and Virginia Tech Graduate Student Assembly to A.D.M, and Virginia Tech Department of Geosciences to A.D.M. and F.M.M. Use of the Stanford Synchrotron Radiation Lightsource, SLAC National Accelerator Laboratory, is supported by the U.S. Department of Energy, Office of Science, Office of Basic Energy Sciences under Contract No. DE-AC02-76SF00515. We thank B. Kocar, S. Webb, and the personnel at the SRRL for assistance in XANES and XRF analyses. Also, S. McCartney, M. Meyer, J. Tuggle, and C. Winkler are acknowledged for assistance in electron microscopy. We additionally thank James D. Schiffbauer and Erik Sperling for critical comments that greatly helped us to improve the quality of this report.

B.9. REFERENCES

Aizenshtat, Z., Krein, E.B., Vairavamurthy, M.A., Goldstein, T.P., 1995. Role of sulfur in the transformations of sedimentary organic matter: a mechanistic overview. In: Vairavamurthy, M.A., Schoonen, M.A.A., Eglinton, T.I., Luther III, G.W., Manowitz, B. (Eds.), Geochemical Transformations of Sedimentary Sulfur. American Chemical Society, pp. 16–37.

Allison, C.W., Awramik, S.M., 1989. Organic-walled microfossils from earliest Cambrian or latest proterozoic Tindir Group rocks, Northwest Canada. Precambrian Res. 43, 253–294.

Antcliffe, J.B., 2013. Questioning the evidence of organic compounds called sponge biomarkers. Palaeontology 56, 917–925.

Antcliffe, J.B., Callow, R.H.T., Brasier, M.D., 2014. Giving the early fossil record of sponges a squeeze. Biol. Rev., http://dx.doi.org/10.1111/brv.12090.

Barfod, G.H., Albaréde, F., Knoll, A.H., Xiao, S., Télouk, P., Frei, R., Baker, J., 2002. New

Lu–Hf and Pb–Pb age constraints on the earliest animal fossils. Earth Planet. Sci. Lett. 201, 203–212.

Bibiloni, M.A., Uriz, M.J., Gili, J.M., 1989. Sponge communities in three submarine caves of the Balearic Islands (western Mediterranean): adaptations and faunistic composition. Mar. Ecol. 10, 317–334.

Bidle, K.D., Azam, F., 1999. Accelerated dissolution of diatom silica by marine bacterial assemblages. Nature 397, 508–512.

Botting, J.P., Butterfield, N.J., 2005. Reconstructing early sponge relationships by using the Burgess Shale fossil *Eiffelia globosa*, Walcott. Proc. Natl. Acad. Sci. U.S.A. 102, 1554–1559.

Botting, J.P., Muir, L.A., 2013. Spicule structure and affinities of the Late Ordovician hexactinellid-like sponge *Cyathophycus loydelli* from the Llanfawr Mudstones Lagerstätte, Wales. Lethaia 46, 454–469.

Botting, J.P., Muir, L.A., Xiao, S., Li, X., Lin, J.-P., 2012. Evidence for spicule homology in calcareous and siliceous sponges: biminerallic spicules in *Lenica* sp. from the Early Cambrian of South China. Lethaia 45, 463–475.

Bottjer, D.J., Hagadorn, J.W., Dornbos, S.Q., 2000. The Cambrian substrate revolution. GSA Today 10, 1–7.

Brasier, M., Green, O., Shields, G., 1997. Ediacarian sponge spicule clusters from southwestern Mongolia and the origins of the Cambrian fauna. Geology 25, 303–306.

Briggs, D.E.G., Summons, R.E., 2014. Ancient biomolecules: their origins, fossilization, and role in revealing the history of life. Bioessays 36, 482–490.

Bristow, T.F., Kennedy, M.J., Derkowski, A., Droser, M.L., Jiang, G., Creaser, R.A., 2009. Mineralogical constraints on the paleoenvironments of the Ediacaran Doushantuo Formation. Proc. Natl. Acad. Sci. U. S. A. 106, 13190–13195.

Burns, E., Ifrach, I., Carmeli, S., Pawlik, J.R., Ilan, M., 2003. Comparison of antipredatory defenses of Red Sea and Caribbean sponges. I. Chemical defense. Mar. Ecol. Prog. Ser. 252, 105–114.

Callow, R.H.T., Brasier, M.D., 2009. Remarkable preservation of microbial mats in Neoproterozoic siliciclastic settings: implications for Ediacaran taphonomic models. Earth Sci. Rev. 96, 207–219.

Canfield, D.E., Poulton, S.W., Narbonne, G.M., 2007. Late-Neoproterozoic deep-ocean oxygenation and the rise of animal life. Science 315, 92–95.

Cárdenas, P., Pérez, T., Boury-Esnault, N., 2012. Sponge systematics facing new challenges. In: Mikel, A., Becerro, M.J.U.M.M., Xavier, T. (Eds.), Advances in Marine Biology. Academic Press, pp. 79–209 (Chapter 2).

Chen, D., Dong, W., Zhu, B., Chen, X.P., 2004. Pb–Pb ages of Neoproterozoic Doushantuo phosphorites in South China: constraints on early metazoan evolution and glaciation events. Precambrian Res. 132, 123–132.

Chen, L., Xiao, S., Pang, K., Zhou, C., Yuan, X., 2014. Cell differentiation and germ soma separation in Ediacaran animal embryo-like fossils. Nature (advance online publication).

Chen, Z., Zhou, C., Meyer, M., Xiang, K., Schiffbauer, J.D., Yuan, X., Xiao, S., 2013. Trace fossil evidence for Ediacaran bilaterian animals with complex behaviors. Precambrian Res. 224, 690–701.

Cheng, T., Hammond, D.E., Berelson, W.M., Hering, J.G., Dixit, S., 2009. Dissolution kinetics of biogenic silica collected from the water column and sediments of three Southern California borderland basins. Mar. Chem. 113, 41–49.

Chu, J.W.F., Maldonado, M., Yahel, G., Leys, S.P., 2011. Glass sponge reefs as a silicon sink. Mar. Ecol. Prog. Ser. 441, 1–14.

Clites, E.C., Droser, M.L., Gehling, J.G., 2012. The advent of hard-part structural support among the Ediacara biota: Ediacaran harbinger of a Cambrian mode of body construction. Geology 40, 307–310.

Condon, D., Zhu, M., Bowring, S., Wang, W., Yang, A., Jin, Y., 2005. U–Pb ages from the Neoproterozoic Doushantuo Formation, China. Science 308, 95–98.

Cunningham, J.A., Thomas, C.-W., Bengtson, S., Kearns, S.L., Xiao, S., Marone, F., Stampanoni, M., Donoghue, P.C.J., 2012. Distinguishing geology from biology in the Ediacaran Doushantuo biota relaxes constraints on the timing of the origin of bilaterians. Proc. R. Soc. B: Biol. Sci. 279, 2369–2376.

Debrenne, F., Reitner, J., 2001. Sponges, cnidarians, and ctenophores. In: Zhuravlev, A.Y., Riding, R. (Eds.), The Ecology of the Cambrian Radiation. Columbia University Press, New York, pp. 301–325.

Ding, W., Qian, Y., 1988. Late Sinian to Early Cambrian small shelly fossils from Yangjiaping, Shimen, Hunan. Acta Micropalaeontol. Sin. 5, 39–55.

Dixit, S., Van Cappellen, P., van Bennekom, A.J., 2001. Processes controlling solubility of biogenic silica and pore water build-up of silicic acid in marine sediments. Mar. Chem. 73, 333–352.

Dornbos, S.Q., Bottjer, D.J., Chen, J.Y., Gao, F., Oliveri, P., Li, C.W., 2006. Environmental controls on the taphonomy of phosphatized animals and animal embryos from the Neoproterozoic Doushantuo Formation, southwest China. Palaios 21, 3–14.

Droser, M.L., Jensen, S., Gehling, J.G., 2002. Trace fossils and substrates of the terminal Proterozoic–Cambrian transition: implications for the record of early bilaterians and sediment mixing. Proc. Natl. Acad. Sci. U. S. A. 99, 12572–12576.

Du, W., Wang, X.L., 2012. Hexactinellid sponge spicules in Neoproterozoic dolostone from South China. Paleontol. Res. 16, 199–207.

Du, W., Wang, X.L., Komiya, T., 2014. Potential Ediacaran sponge gemmules from the Yangtze Gorges area in South China. Gondwana Res., http://dx.doi.org/10.1016/j.gr.2014.08.012 (published online).A.D. Muscente et al. / Precambrian Research 263 (2015) 142–156 155

Duda, J.-P., Blumenberg, M., Thiel, V., Simon, K., Zhu, M., Reitner, J., 2014. Geobiology of a palaeoecosystem with Ediacara-type fossils: the Shibantan Member (Dengying Formation, South China). Precambrian Res. 255, 48–62.

Erwin, D.H., Laflamme, M., Tweedt, S.M., Sperling, E.A., Pisani, D., Peterson, K.J., 2011. The Cambrian conundrum: early divergence and later ecological success in the early history of animals. Science 334, 1091–1097.

Frøhlich, H., Barthel, D., 1997. Silica uptake of the marine sponge *Halichondria panicea* in Kiel Bight. Mar. Biol. 128, 115–125.

Gehling, J.G., Rigby, J.K., 1996. Long expected sponges from the Neoproterozoic Ediacara fauna of South Australia. J. Paleontol. 70, 185–195.

Gehling, J.G., Runnegar, B.N., Droser, M.L., 2014. Scratch traces of large Ediacara bilaterian animals. J. Paleontol. 88, 284–298.

Hagadorn, J.W., Xiao, S., Donoghue, P.C.J., Bengtson, S., Gostling, N.J., Pawlowska, M., Raff, E.C., Raff, R.A., Turner, F.R., Yin, C., Zhou, C., Yuan, X., McFeely, M.B., Stampanoni, M., Nealson, K.H., 2006. Cellular and subcellular structure of Neoproterozoic embryos. Science 314, 291–294.

Harvey, T.H.P., 2010. Carbonaceous preservation of Cambrian hexactinellid sponge spicules. Biol. Lett. 6, 834–837.

Hill, M.S., Hill, A.L., Lopez, J., Peterson, K.J., Pomponi, S., Diaz, M.C., Thacker, R.W., Adamska, M., Boury-Esnault, N., Cárdenas, P., Chaves-Fonnegra, A., Danka, E., De Laine, B.-O., Formica, D., Hajdu, E., Lobo-Hajdu, G., Klontz, S., Morrow, C.C., Patel, J., Picton, B., Pisani, D., Pohlmann, D., Redmond, N.E., Reed, J., Richey, S., Riesgo, A., Rubin, E., Russell, Z., Rützler, K., Sperling, E.A., di Stefano, M., Tarver, J.E., Collins, A.G., 2013. Reconstruction of family-level phylogenetic relationships within Demospongiae (Porifera) using nuclear encoded housekeeping genes. PLOS ONE 8, e50437.

Hill, M.S., Lopez, N.A., Young, K.A., 2005. Anti-predator defenses in western North Atlantic sponges with evidence of enhanced defense through interactions between spicules and chemicals. Mar. Ecol. Prog. Ser. 291, 93–102.

Hoffman, P.F., Li, Z.-X., 2009. A palaeogeographic context for Neoproterozoic glaciation. Palaeogeogr. Palaeoclimatol. Palaeoecol. 277, 158–172.

Hua, H., Chen, Z., Yuan, X., Zhang, L., Xiao, S., 2005. Skeletogenesis and asexual reproduction in the earliest biomineralizing animal *Cloudina*. Geology 33, 277–280.

Jiang, G., Shi, X., Zhang, S., Wang, Y., Xiao, S., 2011. Stratigraphy and paleogeography of the Ediacaran Doushantuo Formation (ca. 635–551 Ma) in South China. Gondwana Res. 19, 831–849.

Jones, A.C., Blum, J.E., Pawlik, J.R., 2005. Testing for defensive synergy in Caribbean sponges: bad taste or glass spicules? J. Exp. Mar. Biol. Ecol. 322, 67–81.

Kennedy, M., Droser, M., Mayer, L.M., Pevear, D., Mrofka, D., 2006. Late Precambrian oxygenation: inception of the clay mineral factory. Science 311, 1446–1449.

Lacko, N., Bux, F., Kasan, H.C., 1999. Survey of filamentous bacteria in activated sludge plants in KwaZulu-Natal. Water SA 25, 63–68.

Laflamme, M., 2010. Palaeontology: wringing out the oldest sponges. Nat. Geosci. 3, 597–598.

Lemelle, L., Labrot, P., Salomé, M., Simionovici, A., Viso, M., Westall, F., 2008. In situ imaging of organic sulfur in 700–800 My-old Neoproterozoic microfossils using X-ray spectromicroscopy at the S K-edge. Org. Geochem. 39, 188–202.

Lenton, T.M., Boyle, R.A., Poulton, S.W., Shields-Zhou, G.A., Butterfield, N.J., 2014. Coevolution of eukaryotes and ocean oxygenation in the Neoproterozoic era. Nat. Geosci. 7, 257–265.

Lewin, J.C., 1961. The dissolution of silica from diatom walls. Geochim. Cosmochim. Acta 21, 182–198.

Li, C.-W., Chen, J.-Y., Hua, T.-E., 1998a. Interpreting late Precambrian microfossils: response. Science 282, 1783.

Li, C.-W., Chen, J.-Y., Hua, T.-E., 1998b. Precambrian sponges with cellular structures. Science 279, 879–882.

Liu, G., Feng, Q., Shen, J., Yu, J., He, W., Algeo, T.J., 2013. Decline of siliceous sponges and spicule miniaturization induced by marine productivity collapse and expanding anoxia during the Permian-Triassic crisis in South China. Palaios 28, 664–679.

Love, G.D., Grosjean, E., Stalvies, C., Fike, D.A., Grotzinger, J.P., Bradley, A.S., Kelly, A.E., Bhatia, M., Meredith, W., Snape, C.E., Bowring, S.A., Condon, D.J., Summons, R.E., 2009. Fossil steroids record the appearance of Demospongiae during the Cryogenian Period. Nature 457, 718–721.

Maliva, R.G., Knoll, A.H., Siever, R., 1989. Secular change in chert distribution:a reflection of evolving biological participation in the silica cycle. Palaios 4, 519–532.

Maliva, R.G., Knoll, A.H., Simonson, B.M., 2005. Secular change in the Precambrian silica cycle: insights from chert petrology. Geol. Soc. Am. Bull. 117, 835–845.

Maloof, A.C., Rose, C.V., Beach, R., Samuels, B.M., Calmet, C.C., Erwin, D.H., Poirier, G.R., Yao, N., Simons, F.J., 2010. Possible animal-body fossils in pre-Marinoan limestones from South Australia. Nat. Geosci. 3, 653–659. Marshall, C.R., 2006. Explaining the Cambrian “explosion” of animals. Annu. Rev. Earth Planet. Sci. 34, 355–384.

McKenzie, N.R., Hughes, N.C., Myrow, P.M., Xiao, S., Sharma, M., 2011. Correlation of Precambrian–Cambrian sedimentary successions across northern India and the utility of isotopic signatures of Himalayan lithotectonic zones. Earth Planet. Sci. Lett. 312, 471–483.

McMenamin, M.A.S., 1998. The Garden of Ediacara: Discovering the First Complex Life. Columbia University Press, New York.

Mills, D.B., Ward, L.M., Jones, C., Sweeten, B., Forth, M., Treusch, A.H., Canfield, D.E., 2014. Oxygen requirements of the earliest animals. Proc. Natl. Acad. Sci. U. S. A. 111, 4168–4172.

Müller, W.E.G., Boreiko, A., Wang, X., Belikov, S.I., Wiens, M., Grebenjuk, V.A., Schlo, beta macher, U., Schröder, H.C., 2007. Silicateins, the major biosilica forming enzymes present in demosponges: protein analysis and phylogenetic relationship. Gene 395, 62–71.

Muscente, A.D., Hawkins, A.D., Xiao, S., 2014. Fossil preservation through phosphatization and silicification in the Ediacaran Doushantuo Formation (South China): a comparative synthesis. Palaeogeogr. Palaeoclimatol. Palaeoecol., http://dx.doi.org/10.1016/j.palaeo.2014.10.013 (published online).

Muscente, A.D., Xiao, S., 2015. Resolving three-dimensional and subsurficial features of carbonaceous compressions and shelly fossils using backscattered electron scanning electron microscopy (BSE-SEM). Palaios (in press).

Pe, J., 1973. Etude quantitative de la regulation du squelette chez une eponge d'eau douce. Arch. Biol. (Liege) 84, 147–173.

Penny, A.M., Wood, R., Curtis, A., Bowyer, F., Tostevin, R., Hoffman, K.-H., 2014. Ediacaran metazoan reefs from the Nama Group, Namibia. Science 344, 1504–1506.

Perry, E.C., Lefticariu, L., 2014. 9.5 – Formation and geochemistry of Precambrian Cherts. In: Turekian, H.D.H.K. (Ed.), Treatise on Geochemistry. , second ed. Elsevier, Oxford, pp. 113–139.

Petterson, R., Prave, A.R., Wernicke, B.P., Fallick, A.E., 2011. The Neoproterozoic Noonday Formation, Death Valley region, California. Geol. Soc. Am. Bull. 123, 1317–1336.

Philp, R.P., Suzuki, N., Galvez-Sinibaldi, A., 1992. Early-stage incorporation of sulfur into protokerogens and possible kerogen precursors. In: Whelan, J., Farrington, J.W. (Eds.), Organic Matter: Productivity, Accumulation, and Preservation in Recent and Ancient Sediments. Columbia University Press, New York, USA, pp. 264–282.

Racki, G., Cordey, F., 2000. Radiolarian palaeoecology and radiolarites: is the present the key to the past? Earth Sci. Rev. 52, 83–120.

Reiswig, H.M., 1971. The axial symmetry of sponge spicules and its phylogenetic significance. Cah. Biol. Mar. 12, 505–514.

Reitner, J., Wörheide, G., 2002. Non-Lithistid fossil Demospongiae—origins of their palaeobiodiversity and highlights in history of preservation. In: Hooper, J.N.A., Van Soest, R.W.M., Willenz, P. (Eds.), Systema Porifera. Springer, USA, pp. 52–68.

Roubeix, V., Becquevort, S., Lancelot, C., 2008. Influence of bacteria and salinity on diatom biogenic silica dissolution in estuarine systems. Biogeochemistry 88, 47–62.

Sahoo, S.K., Planavsky, N.J., Kendall, B., Wang, X., Shi, X., Scott, C., Anbar, A.D., Lyons, T.W., Jiang, G., 2012. Ocean oxygenation in the wake of the Marinoan glaciation. Nature 489, 546–549.

Schiffbauer, J.D., Xiao, S., 2009. Novel application of focused ion beam electron microscopy (FIB-EM) in the preparation and analysis of microfossil ultrastructures. Palaios 24, 616–626.

Schiffbauer, J.D., Xiao, S., Sen Sharma, K., Wang, G., 2012. The origin of intracellular structures in Ediacaran metazoan embryos. Geology 40, 223–226.

Serezhnikova, E.A., 2007. *Palaeophragmodictya spinosa* sp. nov., a bilateral benthic organism from the Vendian of the Southeastern White Sea Region. Paleontol. J. 41, 360–369.

Serezhnikova, E.A., Ivantsov, A.Y., 2007. *Fedomia mikhaili*—a new spicule-bearing organism of sponge grade from the Vendian (Ediacaran) of the White Sea, Russia. Palaeoworld 16, 319–324.

Shields, G., Kimura, H., Yang, J., Gammon, P., 2004. Sulphur isotopic evolution of Neoproterozoic-Cambrian seawater: new francolite-bound sulphate $d^{34}S$ data and a critical appraisal of the existing record. Chem. Geol. 204, 163–182.

Siever, R., 1992. The silica cycle in the Precambrian. Geochim. Cosmochim. Acta 56, 3265–3272.

Simpson, T.L., Langenbruch, P.-F., Scalera-Liaci, L., 1985. Silica spicules and axial filaments of the marine sponge *Stelletta grubii* (Porifera, Demospongiae). Zoomorphology 105, 375–382.

Smith, D.C., Steward, G.F., Long, R.A., Azam, F., 1995. Bacterial mediation of carbon fluxes during a diatom bloom in a mesocosm. Deep Sea Res. II: Top. Stud. Oceanogr. 42, 75–97.

Sperling, E.A., Frieder, C.A., Raman, A.V., Girguis, P.R., Levin, L.A., Knoll, A.H., 2013. Oxygen, ecology, and the Cambrian radiation of animals. Proc. Natl. Acad. Sci. U.S.A. 110, 13446–13451.

Sperling, E.A., Peterson, K.J., Laflamme, M., 2011. Rangeomorphs, *Thectardis* (Porifera?) and dissolved organic carbon in the Ediacaran oceans. Geobiology 9, 24–33.

Sperling, E.A., Robinson, J.M., Pisani, D., Peterson, K.J., 2010. Where's the glass? Biomarkers, molecular clocks, and microRNAs suggest a 200-Myr missing Precambrian fossil record of siliceous sponge spicules. Geobiology 8, 24–36.

Steiner, M., Li, G., Qian, Y., Zhu, M., Erdtmann, B.-D., 2007. Neoproterozoic to early Cambrian small shelly fossil assemblages and a revised biostratigraphic correlation of the Yangtze Platform (China). Palaeogeogr. Palaeoclimatol. Palaeoecol. 254, 67–99.

Steiner, M., Mehl, D., Reitner, J., Erdtmann, B.-D., 1993. Oldest entirely preserved sponges and other fossils from the lowermost Cambrian and a new facies reconstruction of the Yangtze Platform (China). Berliner Geowissenschaftliche Abhandlungen (E) 9, 293–329.

Tiwari, M., Pant, C.C., Tewari, V.C., 2000. Neoproterozoic sponge spicules and organic-walled microfossils from the Gangolihat Dolomite, Lesser Himalaya, India. Curr. Sci. 79, 651–654.

Tiwari, M., Pant, I., 2009. Microfossils from the Neoproterozoic Gangolihat Formation, Kumaun Lesser Himalaya: their stratigraphic and evolutionary significance. J. Asian Earth Sci. 35, 137–149.

Tosca, N.J., Johnston, D.T., Mushegian, A., Rothman, D.H., Summons, R.E., Knoll, A.H., 2010. Clay mineralogy, organic carbon burial, and redox evolution in Proterozoic oceans. Geochim. Cosmochim. Acta 74, 1579–1592.

Van Cappellen, P., Qiu, L., 1997a. Biogenic silica dissolution in sediments of the Southern Ocean. I. Solubility. Deep Sea Res. II: Top. Stud. Oceanogr. 44, 1109–1128.156 A.D. Muscente et al. / Precambrian Research 263 (2015) 142–156

Van Cappellen, P., Qiu, L., 1997b. Biogenic silica dissolution in sediments of the Southern Ocean. II. Kinetics. Deep Sea Res. II: Top. Stud. Oceanogr. 44, 1129–1149.

Wacey, D., Saunders, M., Roberts, M., Menon, S., Green, L., Kong, C., Culwick, T., Strother, P., Brasier, M.D., 2014. Enhanced cellular preservation by clay minerals in 1 billion-year-old lakes. Sci. Rep. 4, http://dx.doi.org/10.1038/srep05841.

Wallace, M.W., Hood, A.v.S., Woon, E.M.S., Hoffmann, K.-H., Reed, C.P., 2014. Enigmatic chambered structures in Cryogenian reefs: the oldest sponge-grade organisms? Precambrian Res. 255, 109–123.

Wang, Y., Wang, X., 2011. New observations on *Cucullus* Steiner from the Neoproterozoic Doushantuo Formation of Guizhou, South China. Lethaia 44, 275–286.

Webb, S.M., 2005. SIXpack: a graphical user interface for XAS analysis using IFEFFIT. Phys. Scr. 2005, 1011–1014.

Xiao, S., Hu, J., Yuan, X., Parsley, R.L., Cao, R., 2005. Articulated sponges from the Lower Cambrian Hetang Formation in southern Anhui, South China: their age and implications for the early evolution of sponges. Palaeogeogr. Palaeoclimatol. Palaeoecol. 220, 89–117.

Xiao, S., Knoll, A.H., 1999. Fossil preservation in the Neoproterozoic Doushantuo phosphorite Lagerstätte, South China. Lethaia 32, 219–240.

Xiao, S., Knoll, A.H., 2000. Phosphatized animal embryos from the Neoproterozoic Doushantuo Formation at Weng'an, Guizhou, South China. J. Paleontol. 74, 767–788.

Xiao, S., Knoll, A.H., Yuan, X., Pueschel, C.M., 2004. Phosphatized multicellular algae in the Neoproterozoic Doushantuo Formation, China, and the early evolution of florideophyte red algae. Am. J. Bot. 91, 214–227.

Xiao, S., Laflamme, M., 2009. On the eve of animal radiation: phylogeny, ecology and evolution of the Ediacara biota. Trends Ecol. Evol. 24, 31–40.

Xiao, S., Muscente, A.D., Chen, L., Zhou, C., Schiffbauer, J.D., Wood, A.D., Polys, N.F., Yuan, X., 2014a. The Weng'an biota and the Ediacaran radiation of multicellular eukaryotes. Nat. Sci. Rev. 1, 498–520.

Xiao, S., Schiffbauer, J.D., 2009. Microfossil phosphatization and its astrobiological implications. In: Seckbach, J., Walsh, M. (Eds.), From Fossils to Astrobiology: Record of Life on Earth and Search for Extraterrestrial Biosignatures. Springer, The Netherlands, pp. 89–117.

Xiao, S., Zhang, Y., Knoll, A.H., 1998. Three-dimensional preservation of algae and animal embryos in a Neoproterozoic phosphorite. Nature 391, 553–558.

Xiao, S., Zhou, C., Liu, P., Wang, D., Yuan, X., 2014b. Phosphatized acanthomorphic acritarchs and related microfossils from the Ediacaran Doushantuo Formation at Weng'an (South China) and their implications for biostratigraphic correlation. J. Paleontol. 88, 1–67.

Yin, L., Xiao, S., Yuan, Y., 2001. New observations on spicule-like structures from Doushantuo phosphorites at Weng'an, Guizhou Province. Chin. Sci. Bull. 46, 1828–1832.

Zhang, S., Jiang, G., Han, Y., 2008. The age of the Nantuo Formation and Nantuo glaciation in South China. Terra Nova 20, 289–294.

Zhang, X., Shu, D., Han, J., Zhang, Z., Liu, J., Fu, D., 2014. Triggers for the Cambrian explosion: hypotheses and problems. Gondwana Res. 25, 896–909.

Zhang, Y., Yuan, X., Yin, L., 1998. Interpreting late Precambrian microfossils. Science 282, 1783.

Zhou, C., Yuan, X., Xue, Y., 1998. Sponge spicule-like pseudofossils from the Neoproterozoic Doushantuo Formation in Weng'an, Guizhou, China. Acta Micropalaeontol. Sin. 15, 380–384.

Zhu, M., Zhang, J., Yang, A., 2007. Integrated Ediacaran (Sinian) chronostratigraphy of South China. Palaeogeogr. Palaeoclimatol. Palaeoecol. 254, 7–61.

B.10. FIGURES

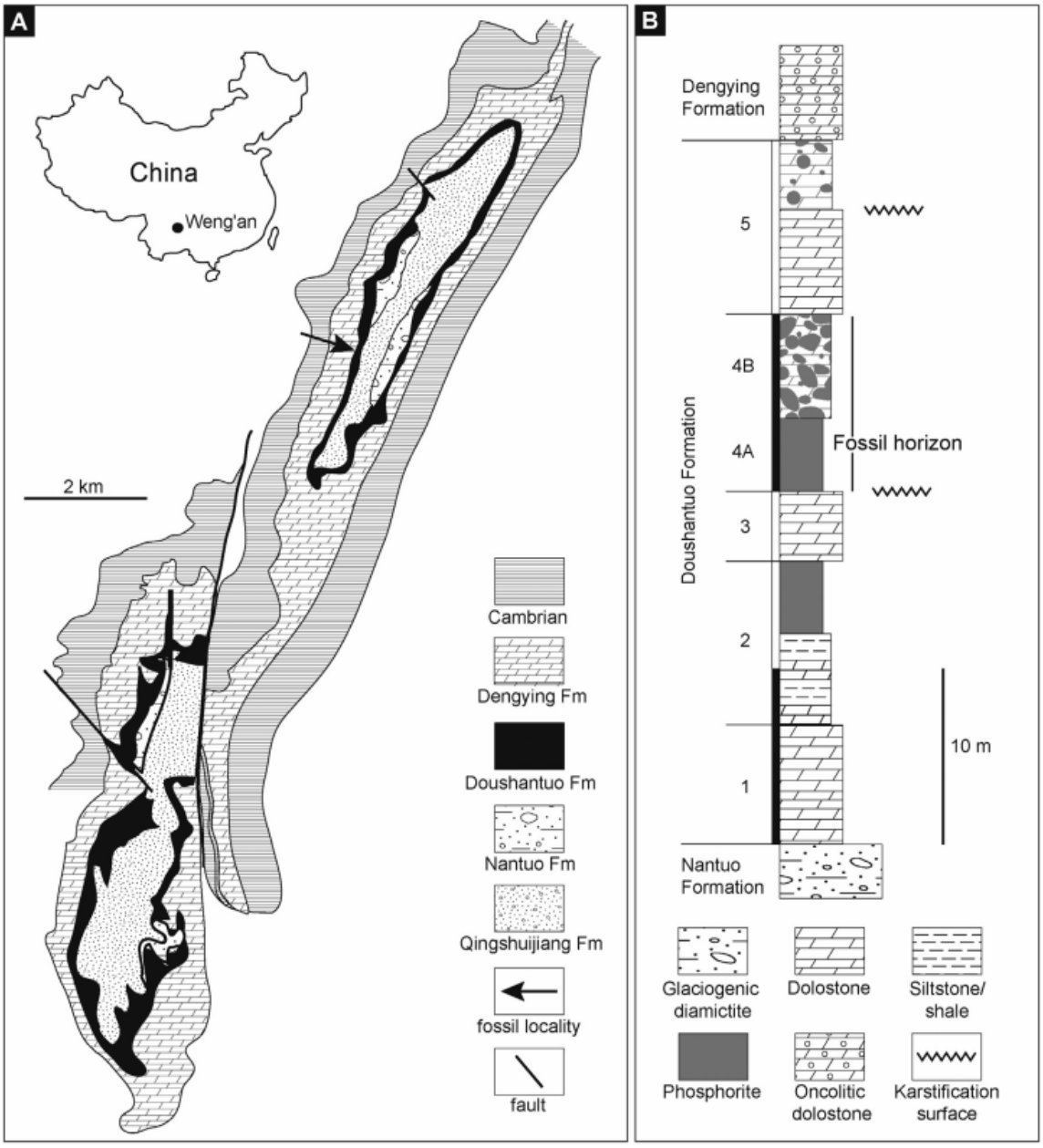

Figure B.1. Geological background of the Doushantuo Formation at Weng'an, Guizhou Province, South China. (A) Geological map of the Weng'an area. (B) Generalized stratigraphy of Doushantuo Formation at Weng'an. Units 4A and 4B represent the fossiliferous black and gray facies, respectively. Modified from Xiao et al. (2014b).

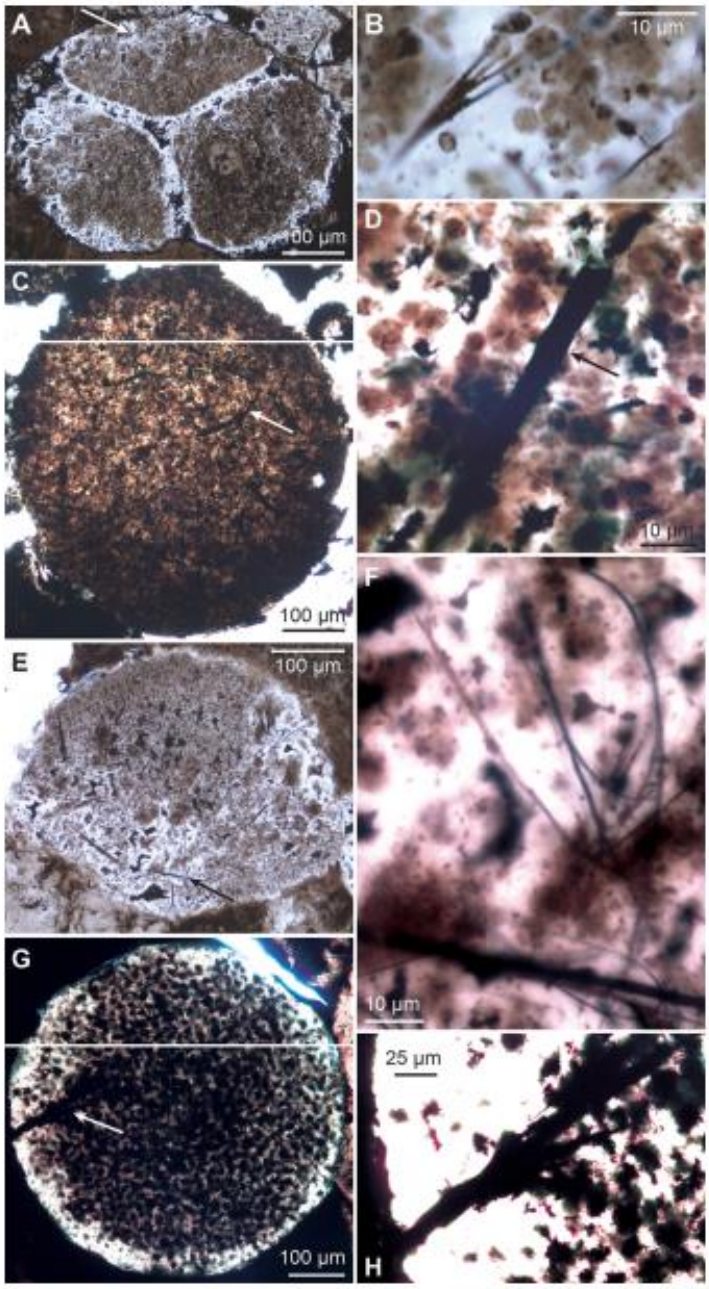

Figure B.2. Transmitted-light microscopy of Doushantuo SLMs in petrographic thin sections. Arrows in (A, C, E, G) indicate areas magnified in (B, D, F, H), respectively. (A) Four-cell *Megasphaera*. (B) Individual SLM (right), SLM fascicle (left), and ellipsoidal sclerocyte-like structures (Li et al., 1998b) interpreted as lipid vesicles (Hagadorn et al., 2006; Schiffbauer et al., 2012). (C) One-celled *Megasphaera*. (D) Relatively thick SLM. Black arrow in (D) indicates location of FIB-EM transverse section illustrated in Fig. B.5P. (E) Poorly preserved spheroidal fossil. (F) SLMs with curved morphologies. (G) *Megasphaera* fossil. (H) SLM fascicle attached to its membrane or envelope. (C, G) are composite transmitted-light images, each assembled from two higher-magnification images (separated by the white lines).

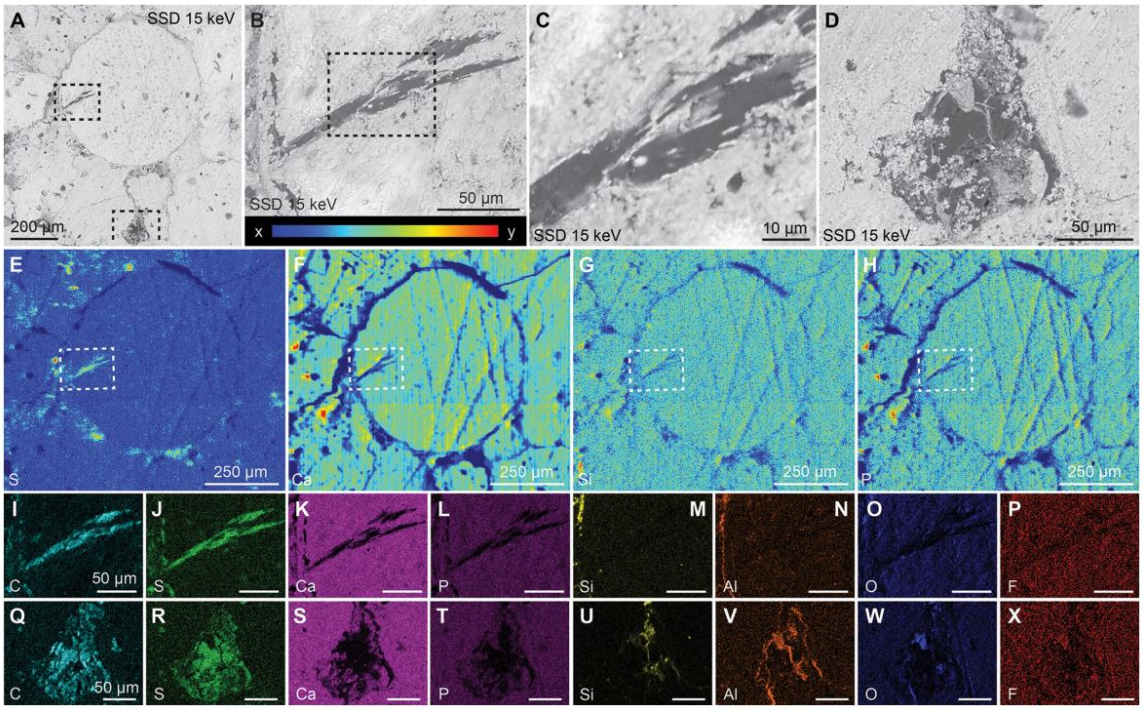

Figure B.3. SEM, EDS, and XRF of SLM fascicle. (A) SEM (SSD) image of *Megasphaera* illustrated in Fig. B.2G. (B) Magnified SEM (SSD) image of SLM fascicle (upper box in A). (C) Magnified image of boxed area in (B), showing the area of the SLM fascicle in (B) that was analyzed with XANES. (D) Magnified image (lower box in A), showing carbonaceous material in matrix around *Megasphaera* analyzed with XANES. (E–H) XRF elemental maps with color scale below (B) showing relative number of counts (x, minimum number of counts; y, maximum number of counts). (E) Sulfur (x < 36 counts; y > 141 counts); (F) Calcium (x < 5596 counts, y > 9326 counts); (G) Silicon (x < 38 counts, y > 149 counts); (H) Phosphorus (x < 110 counts, y > 274 counts). (I–P) SEM based EDS elemental maps of (B). (Q–X) SEM-based EDS elemental maps of (D). Boxes in (E–H) mark area magnified in (I–P). (For interpretation of the references to color in this figure legend, the reader is referred to the web version of this article.)

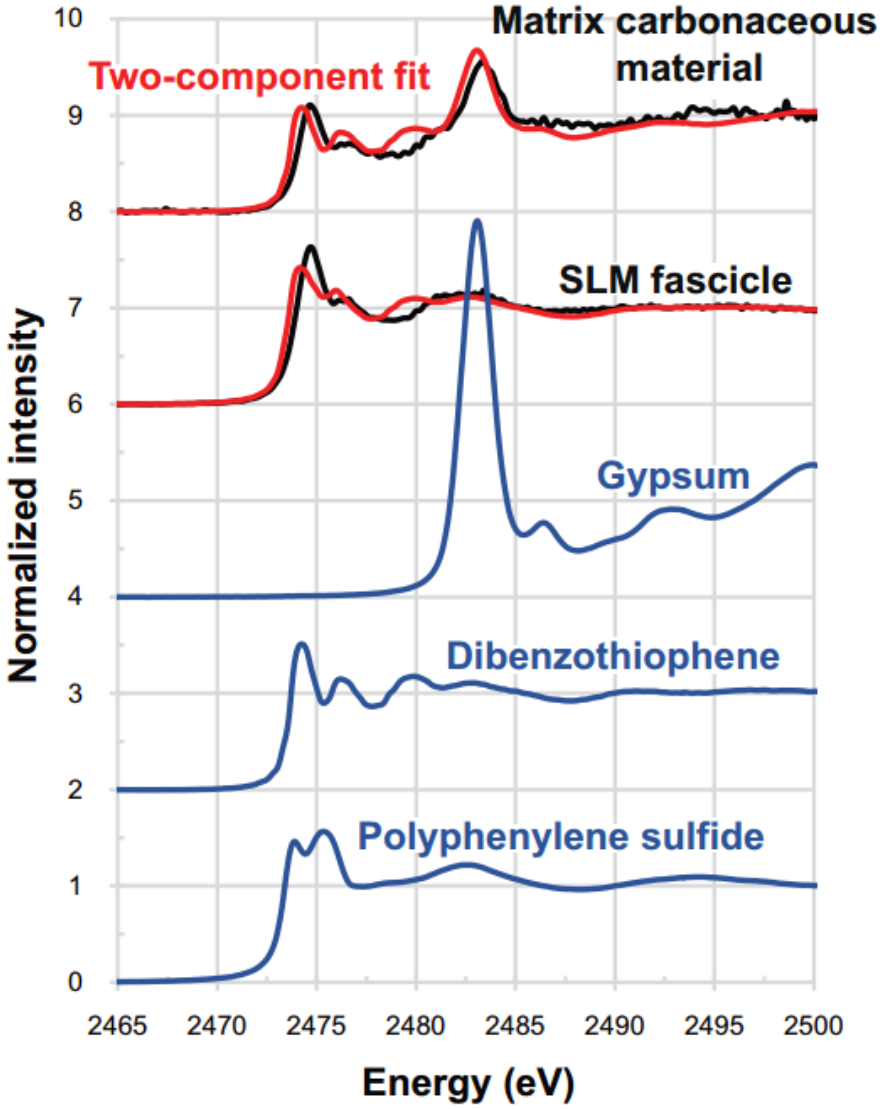

Figure B.4. Representative normalized sulfur K-edge XANES spectra of SLM fascicle and carbonaceous material in matrix around *Megasphaera* (black lines), as well as model sulfur compounds (blue lines). Red lines show best 2-compound fit (dibenzothiophene + gypsum and dibenzothiophene + polyphenylene sulfide in comparison with the matrix carbonaceous material and SLM fascicle spectra, respectively; see Table B.1), as determined by LCF using spectra of various model sulfur compounds. (For interpretation of the references to color in this figure legend, the reader is referred to the web version of this article.)

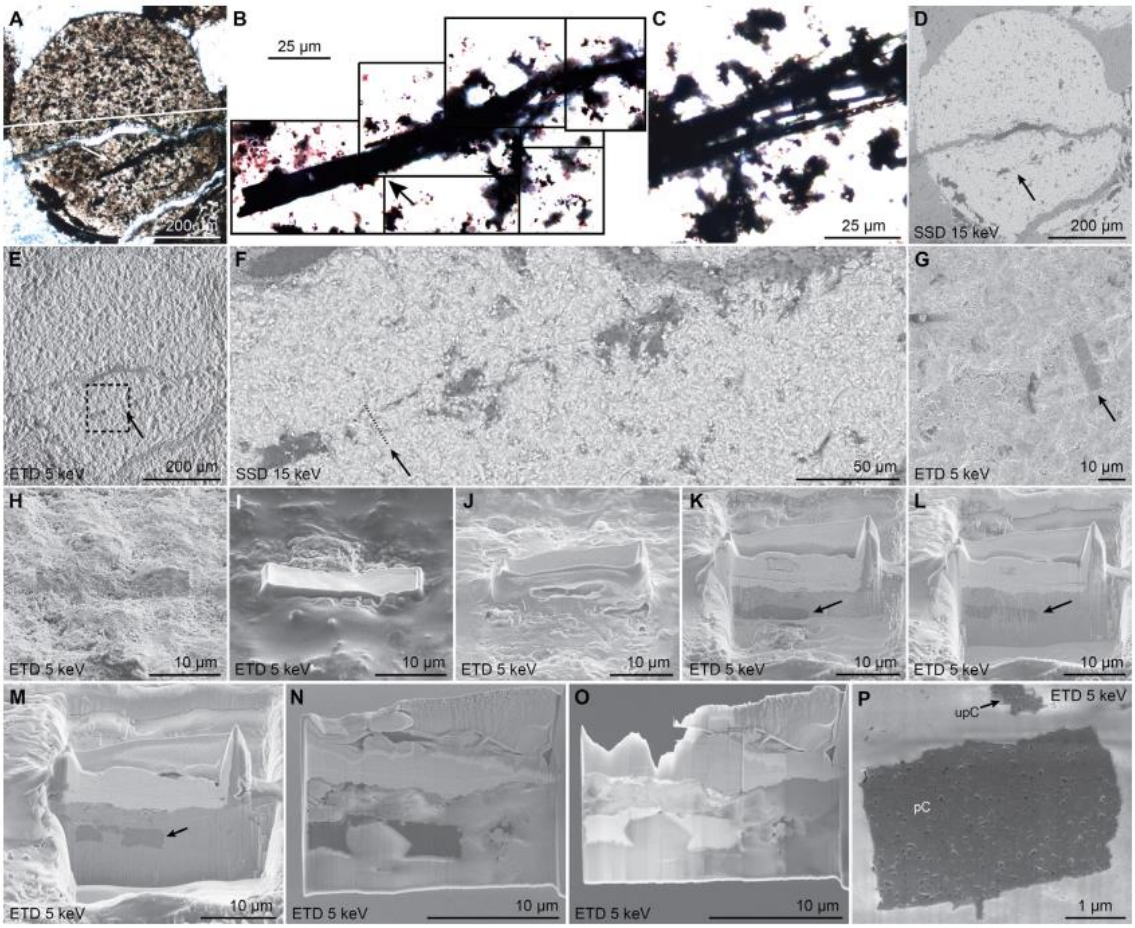

Figure B.5. FIB-EM analysis. (A–O) Preparation and analysis of SLM fascicle transverse section ultra-thin foil. (A) Composite transmitted-light image (assembled from two transmitted-light images separated by line) of phosphatized fossil with SLM fascicle. (B) Composite transmitted-light image (assembled from seven higher magnification images, indicated by boxes), showing SLM fascicle prior to FIB-EM transverse sectioning. (C) Transmitted-light image of the right part of the SLM fascicle in (B) taken at different focal length, showing multiple SLMs in fascicle. (D) SEM (SSD) image and (E) SEM (ETD) images of (A). (F) SEM (SSD) image of SLM fascicle. Arrows in (A, D–F) and dashed line (F) indicate location of FIB transverse section. (G) Magnified SEM (ETD) image of box in (E), showing location targeted for FIB preparation with ion-sputtered rectangle (indicated by arrow in G). (H–N) Sequential SEM (ETD) images acquired during preparation of ultra-thin foil. (H) Location indicated by arrow in (G) magnified and rotated. (I) 1 m thick platinum layer deposited to protect SLM fascicle during ion milling. (J) Initial stages of ion milling. (K) Revelation of SLM fascicle (dark color, indicated by arrow). (L) Toward end of milling process. (M) Rectangular transverse sections of SLMs in fascicle. (N) Ultra-thin foil, after it was removed from thin section and secured to TEM copper grid. (O) SEM (S/TEM) image of ~100 nm thick ultra-thin foil following ion-polishing to electron transparency (also shown in Fig. B.6A). (P) SEM (ETD) image of SLM transverse section (location indicated by arrow in Fig. B.2D). pC, porous carbonaceous material; upC, unassociated porous carbonaceous material in cell lumen.

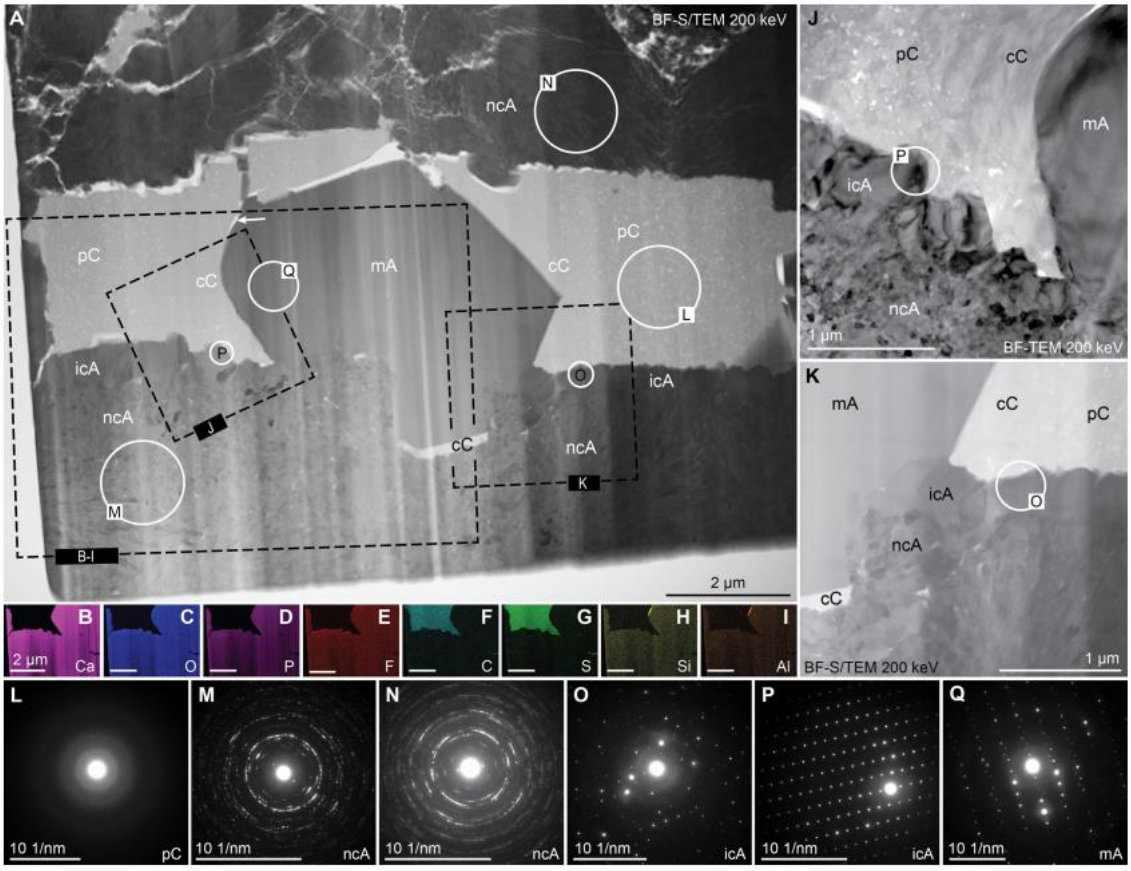

Figure B.6. BF-TEM, BF-S/TEM, and SAED analyses of SLM fascicle transverse section ultra-thin foil. (A) BF-S/TEM image of SLM fascicle transverse section (location indicated by arrow in Fig. B.5F) ultra-thin foil, also illustrated in Fig. B.5O. Arrow in (A) indicates aluminosilicate. (B–I) TEM-based EDS elemental maps of labeled box in (A). (J–K) BF-TEM (J) and BF-S/TEM (K) images of labeled boxes in (A), showing different mineralization types. (L–Q) SAED patterns of carbonaceous material and apatite from labeled circles in (A, J, K). ncA, nanocrystalline apatite; icA, isopachous apatite; mA, micrometer-sized apatite crystal; pC, porous carbonaceous material; cC, nonporous compressed carbonaceous material.

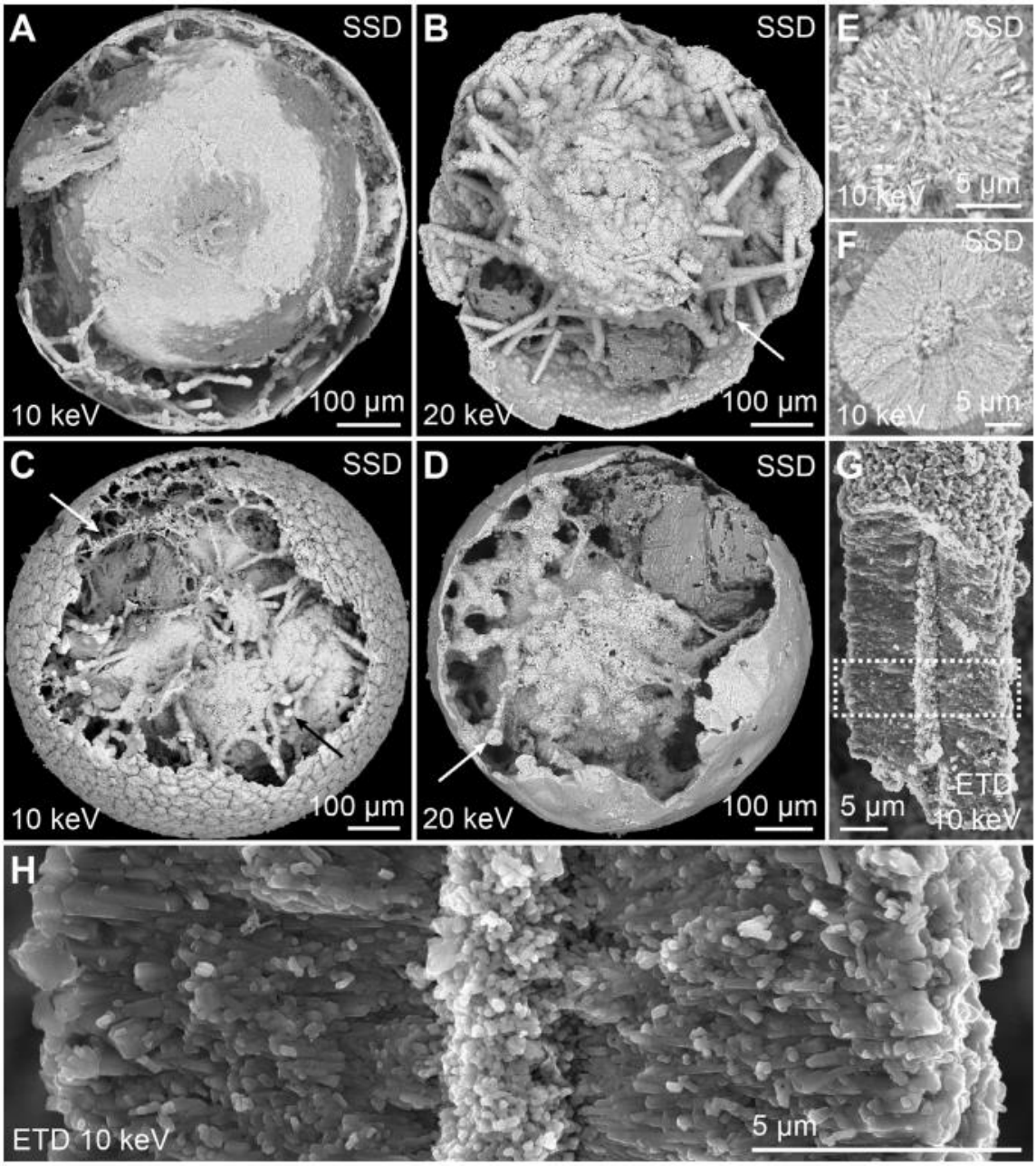

Figure B.7. SEM images of phosphatic filaments within *Megasphaera* fossils extracted from unit 4B. (A) Filaments between internal body and outer envelope. (B) Sparsely-branching filaments. (C) Anastomosing (white arrow) and sparsely-branching filaments. (D) Filaments heavily coated with botryoidal cements. (E) Transverse section through filament without axially located structure (black arrow in C), showing radially oriented crystals. (F) Transverse section through filament (arrow in D), showing oblong (possibly rectangular) axially located structure replicated by randomly oriented nanocrystals. (G) Longitudinal section through filament (arrow in B) showing axially located structure. (H) Magnified view of axially located structure (box in G), showing randomly oriented nanocrystals in axially located structure surrounded by radially oriented prismatic microcrystals.

APPENDIX C:

Speciation of Mercury in Selected Areas of the Petroleum Value Chain

Astrid Avellan[1,2], John Stegemeier[1,2], Ke Gai[1,2], James Dale[2,3], Heileen Hsu-Kim[2,4], Clément Levard[2,7], Dennis O'Rear[5], Thomas P. Hoelen[6], Gregory V. Lowry[1,2]

[1]Carnegie Mellon University, Pittsburgh, PA 15213
[2]Center for Environmental Implications of Nanotechnology, Pittsburgh, PA 15213
[3]Virginia Tech, Geological and Environmental Science, Blacksburg, VA
[4]Duke University, Civil & Env. Eng., Durham, NC
[5]Chevron Energy Technology Company, Richmond CA 94802
[6]Chevron Energy Technology Company, San Ramon CA 94583
[7]Aix Marseille Univ., CNRS, IRD, Coll. France, CEREGE, Aix en Provence, France.

Submitted to *Environmental Science and Technology*.

C.1. ABSTRACT

Petroleum, natural gas, and natural gas condensate can contain low levels of mercury (Hg). The speciation of Hg can affect its behavior during processing, transport, and storage so efficient and safe management of Hg requires an understanding of its chemical form in oil, gas and byproducts. Here, X-ray absorption spectroscopy was used to determine the Hg speciation in samples of solid residues collected throughout the petroleum value chain including stabilized crude oil residues, sediments from separation tanks and condensate glycol dehydrators, distillation column pipe scale, and biosludge from wastewater treatment. In all samples except glycol dehydrators, metacinnabar (β-HgS) was the primary form of Hg. Electron microscopy on particles from a crude sediment showed nano-sized (<100nm) particles forming larger aggregates, and confirmed the co-localization of Hg and sulfur. In sediment from glycol dehydrators, organic $Hg(SR)_2$ accounted for ~63% of the Hg, with ~24% present as β-HgS. β-HgS was the predominant Hg species in refinery biosludge and pipe scale samples. However, the

balance of Hg species present in these samples depended on the nature of the crude oil being processed, i.e. sweet (low sulfur crudes) vs. sour (higher sulfur crudes). This information on Hg speciation in the petroleum value chain can inform management practices.

C.2. INTRODUCTION

Crude oil and natural gas are widely used fossil fuels that can contain low but measureable levels of mercury (Hg).[1] A review of the Hg content measured in 446 crude oil and natural gas condensates samples (i.e., liquid hydrocarbons that formed during natural gas production) from across the world, indicates a Hg median concentration of 1.3 ppb (w/w). Hg concentrations in crude oil range from <0.1 to >1000 ppb[2] depending on the geographical situation, with the highest Hg concentrations occurring in crude oil and natural gas condensate taken from the Pacific and Indian Oceans.[2,3] Even though burning of oil, gas and petroleum refining accounts for a minor fraction (<1.5%) of total anthropogenic atmospheric emissions of Hg,[4] these emissions should be managed during the extraction and refining process to limit their potential release to the environment.

Hg in oil, air, and water can occur as elemental Hg(0), and as a variety of Hg(I) (mercurous) and Hg(II) (mercuric) species depending on redox conditions.[5–11] Each of these species will have a range of volatility, stability, and solubility in oil and in water that will affect its behavior in the oil and gas value chain. Thus, a better understanding of the mercury speciation of solids in crude oil and solid byproducts in the refining process is critical to (*i*) most efficiently manage byproducts to avoid the release of Hg and (*ii*) to the success of strategies used to remove mercury from crude oil, before it is shipped and

refined, thereby collecting the Hg at the initial extraction stage rather than dispersing the Hg into the downstream processing.[12] This can lower costs associated with managing Hg in the petroleum value chain and increase the value of oil and gas products.

To date, the speciation of Hg in solids recovered from upstream (exploration and production) and downstream (refining and retail) byproducts, including oily sludge, pipe corrosion products, glycol dehydrator waste, and wastewater biosludge, has never been reported. Past Hg speciation efforts have relied on operational definitions based on the methods used to separate them, e.g. the Hg fraction that can be centrifuged or filtered out is defined as the "particulate" or insoluble phase.[5,10] Methods such as chemical extractions and a variety of chromatographic methods have been used to speciate Hg in crude oil and condensate. However, these methods can be biased, with results dependent on (*i*) the solubility of the Hg phases present,[13] or (*ii*) background interferences.[7] Thus Hg speciation results can be influenced by the size and crystallinity of the particulate Hg, as well as the nature of the matrix. Moreover; the majority species in crude and gas condensates (~70% of total Hg) is particle-associated,[14] and while speciation of Hg in the hydrocarbon phases (oil and condensate) has been relatively well characterized, the speciation of Hg in the "particulate" fraction has not been well characterized.[7,15]

Mercury can accumulate at different points along the petroleum value chain (see Supplementary Figure C.1). Each point in the value chain can have highly variable conditions, e.g. redox, solvent properties, temperature, pressure that can affect Hg speciation. Produced reservoir fluids can contain crude oil, natural gas, produced water, and solids, which are commonly separated at the production site. After separation of these components, crudes are desalted and distilled at high temperature under

atmospheric or vacuum conditions to produce different hydrocarbon products. Gases from either natural gas wells or from oil producing wells are often dehydrated using glycol, or sweetened and purified by amine treatment for the removal of H_2S and CO_2. Hg that might be present in those gas streams is partially removed in these processes and exits either in the water vapor from a glycol unit or the acid gas from an amine unit.[1] Mercury generally accumulates in the hydrocarbon phases of these processes and in the solids that accumulate, e.g. sludge in tanks, filters, and pipelines, on Hg absorbents, and in metal corrosion products. Wastewater treatment byproducts, i.e. biosludge, may also contain Hg. Given the range of condition that exist in these compartments, Hg can exist as gaseous elemental mercury, various oxidized organic forms (e.g. dialkylmercury species or Hg-thiols), and as particulate forms.[5,10,16,17] As an example, in terrestrial and aquatic environments impacted by anthropogenic mercury inputs, cinnabar (α-HgS) and metacinnabar (β-HgS) are commonly encountered Hg species.[18–23] This is not surprising, since mercury (II) sulfides species are highly stable once they are formed.[24–30] Hg(II) can also bound to thiol complexes forming $Hg(SR)_x$ species in oily phases, crude oil and condensates,[7,31] and with dissolved organic matter (DOM) in aquatic and terrestrial environments,[6,32,33] forming a more soluble and bioavailable compound.[34,35] It is unclear which Hg species will be predominant in solids collected in the petroleum value chain, given the non-aqueous nature of petroleum and gas condensates. Moreover, crude oils can contain different amounts of sulfur and Hg, which may influence Hg speciation. Crude oils are termed either “sour” or “sweet”, depending on their level of sulfur (typically, >0.5% or <0.5%, respectively).

The objective of the present study is to determine Hg speciation in selected samples collected along the petroleum value chain, and to link their speciation with the crude oil nature and potential transformation processes. Samples of Hg-containing solids have been isolated from crude oils and condensate residues collected from storage tanks, and in selected solids byproducts from production and refining. X-ray absorption spectroscopy (XAS) was used to determine the predominant species of Hg present in twelve samples collected from strategic locations and compartments along the production and refining process. Additional analysis of the organic phase associated with the solid phase of some samples was also conducted to distinguish between organic phase Hg species and solids-associated Hg species. Finally, heating and cold vapor atomic fluorescence spectrometry (CVAFS) was used to distinguish between volatile (elemental) and non-volatile Hg species.

C.3. MATERIALS AND METHODS

C.3.1. Chemicals

A 1 ppm Hg standard solution (Brooks Rand Labs, Seattle, WA) was used for calibrating the mercury analyzer over a range from 5 to 10,000 pg total Hg. Bromine monochloride, hydroxylamine and stannous chloride were all purchased from Brooks Rand Labs and were used as specified in EPA method 1631. Toluene (HPLC grade), hexane (ACS Reagent grade) and methylene chloride (ACS Reagent grade) were used for extracting the oil phase from various oily sediments. Trace metal grade hydrochloric acid and nitric acid were used for digesting the sediment samples.

C.3.2. Crude oil and refinery byproduct sampling

Twelve samples were collected from selected production, storage, and refinery operations (Table C.1; Supplementary Figure C.1). Samples were selected based on their location along the petroleum value chain, containing "upstream" samples, including crude oil residue samples (samples 1 to 3), crude oil and condensate sediments (samples 4 to 6) from different locations, and sediment samples from a glycol treatment unit used to condition gas and condensate (samples 7 and 8). Four "downstream" samples were collected from two different refineries (called A and B), including wastewater treatment biosludge (samples 9 and 10) and pipe scale collected from an overhead distillation column (sample 11 and 12). Samples were collected and placed into Hg-free glass bottles, then shipped to Carnegie Mellon University, stored at 4 °C until analysis. Samples of crude oil residue and sediments from crude oil and condensate were taken from stabilized samples. Stabilizing includes heating and separation that can remove volatile Hg species including elemental Hg. Crude oil residue is the solid phase centrifuged from the stabilized crude oils.

C.3.3. Oil and Sediment separation

One goal of the study was to determine the speciation of Hg associated with the oil residue in crude oil sediments and condensate sediments. This was accomplished by extracting the oil residue from the solids using a solvent washing step, using either toluene or methylene chloride (CH_2Cl_2). Approximately 100 to 200 mg of oily sediment was weighed and added to a glass vial containing 10 mL of solvent. The sample was rotated end-over-end for 6 hours to extract the oil. Mercury in the extract was measured as described below. The mercury concentration in the oil phase was calculated from the mass of each phase and the dilution factor according to equation 1,

$$C_{oil} = n\left(\frac{m_{Hg}}{m_{sed_0} - m_{sed_1}}\right) \quad \text{(Eqn 1)}$$

where C_{oil} = Hg concentration in oil phase (mass/mass), n = dilution factor, m_{Hg}: total Hg mass measured in the extracted oil phase, m_{sed_0} = initial sediment mass, m_{sed_1} = sediment mass after removing the oil phase with a solvent wash. To distinguish between particulate and dissolved species in the residue, aliquots of the extracted residue were filtered with a 0.02 micron Anatop syringe filter (Whatman). The filtrate was analyzed for total Hg using EPA Method 1631 as described in supporting information.

C.3.4. Sample drying to determine volatile Hg species

Several mercury species are volatile at 50 °C including elemental mercury, short-chain dialkyl mercury species like dimethyl mercury, and mercuric chloride. In one oil sediment sample (sample 4) and one condensate sediment sample (sample 6) the presence of volatile Hg was assessed by measuring total Hg in the samples before and after heating to 50 °C for 10 hr. About 200 mg samples were weighed into glass vials, and then placed on a hot plate held constant at 50 °C for 10 hours. The dried sediments were digested, diluted, and measured for total Hg according to EPA Method 1631. Comparisons were made on a total Hg mass basis to account for mass loss of other volatile components.

C.3.5. Mercury analysis

Two types of samples were analyzed: 1) solids (as received or washed), and 2) the extracted oil phase. To determine total Hg in solids, approximately 100 to 200 mg of sample was weighed into a glass vial and acid digested overnight using 20 mL of aqua regia. The digestants were diluted for total Hg analysis according to EPA Method 1631. For the extracted oil phase, 4 mL of the extraction solvent was transferred into a 20 mL glass vial with a Teflon-lined cap. Six mL of concentrated HCl solution and 6 mL of an

aqueous BrCl solution were added, and the mixture was vigorously shaken for 30 min to oxidize the Hg in the samples and transfer the Hg(II) into the aqueous phase. The solvent phase and aqueous phase were allowed to separate (Supplementary Figure C.2, supporting information), and 10 µL of the aqueous phase was pipetted into 25 mL of deionized (DI) water for Hg analysis.

C.3.6. Hg Speciation by XAS

The Hg speciation in samples of solids and oily solids was determined using XAS at the Hg L(III) absorption edge (12,282 eV) on beamline 11-2 at the Stanford Synchrotron Radiation Lightsource (SSRL). All measurements were conducted a liquid nitrogen temperature (~77K) to reduce thermal vibrations and potential beam damage of Hg-organic species, as well as to potentially identify elemental Hg. A slow cooling method[36] was used to identify elemental Hg in samples if present. Both transmission and fluorescence spectra were collected. Monochromator and internal energy calibration was made using a $HgCl_2$ salt reference in the SIXpack software suite,[37] version 0.68.13. XAS scans were then background subtracted with E_0 defined as 12,284 eV, converted to frequency (k) space using a spline range of 1 to 9 $Å^{-1}$, and weighted by k^3.

Linear combination fitting (LCF) was performed on k-space of the spectra using a Hg model compound library. The fits were constrained between k = 2 – 8.5 $Å^{-1}$ due to the presence of glitches from the monochromator crystal at k values above 8.5 $Å^{-1}$ or because of the noise due to low Hg concentrations in some samples. During LCF, the energy was not allowed to vary, and the fits were not forced to sum to 100. LCF allows identifying the one component significantly contributing to the EXAFS spectra of a sample. Since we were analyzing the solids fractions from both nan-aqueous (crudes and condensates) and

aqueous (biosludge) compartments, a total of 18 reference compounds containing minerals, salts, or organic species were acquired as model compounds (see EXAFS spectra and provenance of the references in Supplementary Figure C.3) for the LCF, including: α-Hg^0 (slow cooled), cinnabar (α-HgS), metacinnabar (β-HgS), eglestonite ($Hg_6Cl_3O_2H$), schuetite ($Hg_3O_2SO_4$), kleinite ($Hg_2N(Cl, SO_4)$, mosesite ($Hg_2N(Cl, SO_4, MoO_4, CO_3)$), terlinguite ($Hg_2OCl$), $Hg_3S_2Cl_2$, HgCl, HgO, HgSe, $HgSO_4$, $HgCl_2$, Hg-thiosulfate, Hg-tetrathiolate ($Hg(SR)_4$), Hg-cysteine, Hg- glutathione ($Hg(SR)_2$), Hg-phenyl.

A second component contribution was added to the first one if both (*i*) its contribution to the signal was above 10% and (*ii*) it reduced the χ^2 and the R-factor values (i.e. quality factors, the lower their value, the better the fit) by more than 20%. The R-factor (R_f), indicates the variations between fit and the data. We consider a R_f value higher than 0.1 as the indicator of flaws in the fit, or of low quality data. We also used the chi-square (χ^2) value in assessing the statistical quality of the fit. χ^2 is based on the differences between the data and the fit in comparison to the noise of the spectra. A χ^2 close to 10 indicates that the difference between the fit and the data is attributable to data noise.

C.3.7. TEM analysis

Transmission Electron Microscopy coupled to Energy-dispersive X-ray spectroscopy (TEM/EDS) was performed at Virginia Tech on a production sediment sample (sample 6) to determine the morphology of the Hg-containing particles, as well as their chemistry and matrix composition. Samples were prepared by suspending the solids in ethanol, sonicating them for 10 minutes, and then using a ‘drop and wick’ technique

onto a 300 mesh copper grid. TEM images were taken using a JEOL 2100 transmission electron microscope at an accelerating voltage of 200 kV. EDS maps were generated in scanning TEM (STEM) mode and were analyzed using the software package JEOL analysis station. SEM was also collected on these same samples using an FEI Quanta 600 ESEM.

C.4. RESULTS AND DISCUSSION

C.4.1. Trends in total Hg for all samples

Total mercury measured for all of the samples is provided in Table C.2. The total concentration of Hg in most samples ranged from 24 ppm to a few hundred ppm. However, two crude residue samples and two of the three condensate sediments had a higher Hg concentrations than that previously observed in crude oils,[7] even for Southeast Asian crudes which have been shown to contain up to 220 ppb Hg.[2] The two crude residue samples had elevated Hg concentrations because they were centrifuged to concentrate the solids in the samples to have enough Hg content to proceed XAS. The relatively high levels of Hg in the condensate sediment samples indicates that Hg is concentrating in the solids collecting at the bottom of these storage facilities, and suggests that a significant amount of Hg is associated with particulate phases present in crude oil and condensate that will settle and accumulate during storage. The high association of Hg with the particulate phases in crude oil and condensate has already been reported.[5,38]

C.4.2. Hg Speciation

Mercury speciation was determined by XAS to identify the nature of the species present in samples in the petroleum value chain and by heating to assess the presence of volatile Hg species. The Hg speciation is presented depending on their source in the petroleum value chain; "upstream" (samples 1 to 8) or "downstream" (samples 9 to 12) (refer to **Crude oil and refinery byproduct solid/sediment sampling** section in the Material and Methods for more details). All of the LCFs had a sum of component ranging from 84-121%, and had relatively low residuals ($R \leq 0.07$), except for sample 10, which had a noisy EXAFS spectra. The fact that component percentages do not sum to 100% exactly does not indicate that fits are poor. Indeed, the precision of the LCF was assessed on sample numbers 1, 3 and 4. A variation of 10% of the proportion of metacinnabar little affected the fit quality, and the resulting R-factor variation was below 20%. We thus estimated the uncertainties of the LCF at ±15%, i.e. the percentage for which the R-factor variation was higher than 20%, which is consistent with previous studies.[39,40]

Metacinnabar (β-HgS) was a major component in all our samples. Because of its first coordination shell (4 S) and Hg-S first shell bond distance (2.52Å),[41] the β-HgS EXAFS signal was quite similar to the organic $Hg(SR)_4$ compound, exhibiting similar local structure.[42,43] However, we are confident that β-HgS is the right model compound to use. Indeed, LCF indicated β-HgS as the best fit, due to the shoulders present at low *k* on β-HgS but not on $Hg(SR)_4$ (see Supplementary Figures C.4, C.5 and C.6 for more insights). This is also consistent with the results from a KOH chemical extraction of the samples, indicating the presence of little to no organic $Hg(SR)_x$ compounds (Supplementary Figure C.7).

C.4.2.1. Hg speciation in crude oil residues

The speciation of particulate Hg in three crude oil residues (samples 1 to 3) was determined by XAS. The EXAFS spectra were well fit using only β-HgS in all three samples despite their different origins (Figure C.1 and Table C.2). Mercury speciation in crude oils has been previously reported as organic (e.g. pentyl-thiolate-Hg(II)[7] and alkylmercury species[16]) rather than particulate β-HgS. However, these previous studies measured the Hg species dissolved in the oils phase. Here we determined the speciation of Hg present in the solids recovered from the stabilized crude oil, which is primarily β-HgS. Taken together, these two studies provide a comprehensive description of the types of Hg species in stabilized crude oils, including both dissolved and particulate phase species.

C.4.2.2. Sediment samples from crude oil and condensate storage tanks

The Hg speciation was determined in crude oil sediment (sample 4) and condensate sediment (sample 6). These samples contained both a hydrocarbon phase and solids that were primarily quartz (Supplementary Figure C.S8a-b). Heating either sample to 50 °C did not result in any statistically significant loss of Hg (Table C.3). It should be noted that the fairly large sample heterogeneity of these samples (3 each, heated and not heated) precludes an ability to determine if small concentrations of volatile Hg species (e.g. elemental Hg) were present, but it does indicate that elemental Hg is not a significant component of the total Hg in the samples (< ~10 wt%). This was also verified by purging whole samples directly onto the Hg analyzer without addition of BrCl. There were no measureable volatile Hg species in the whole samples suggesting that elemental Hg, if present, would be a small fraction of the total Hg in the sample.

Separation of the hydrocarbon phase from the solids enables the determination of the fraction of Hg associated with the solid or the oil phase (Table C.3), and the corresponding Hg speciation (Figure C.1 and Table C.2). In the crude oil sediment, the solids were approximately 82% of the total sample weight. The oil phase made up the other 18% of the sample. Considering the measured Hg concentrations and the relative mass of each phase, ~90% (w/w) of the Hg was associated with the solids and 10% (w/w) of the Hg with the oil phase (extractable into dichloromethane). The same analysis for the condensate sediment indicates that ~98% of the Hg was associated with the solids, and only 2% of the Hg mass was extractable into dichloromethane. Hg associated with the oil phase in both samples was retained on a 0.02 micron filter, indicating that Hg is bound to (nano)particles rather than present as a dissolved molecular species.

The speciation of Hg in these samples of crude oil tank sediment (sample 4), and in two different condensate tank sediments (samples 5 and 6) was also determined by XAS. In samples with an oil phase (sample 4 and 6), Hg speciation was determined in whole samples (solids plus oil) and in the solvent washed sample (solids only) to assess for differences in Hg speciation between the oil phase and solid phase. Sample 5 was received as a dry solid and did not have an oil phase. The EXAFS data and linear combination fits for sample 4, 5 and 6 are shown in Figure C.1.

All of these samples had a best fit for a mix with metacinnabar (β-HgS) and Hg-glutathione (refereed as Hg-GSH_3 and representing organic Hg-$(SR)_2$ species). These species were found in similar proportion; 75% metacinnabar, 25% Hg-GSH_3; regardless of their source (crude oil or condensate sediment) or their fraction (whole or oil phase), indicating the extraction of both organic and inorganic Hg in equal proportion by the

extraction procedure. Moreover, these samples contained only a small fraction of the Hg in the oil phase as $Hg(SR)_2$ species. This is consistent with Gaulier et al., 2015 who found that Hg in the hydrocarbon phase was associated with C_8 to C_{16} thiols.[7] However, we find that >90 and >99% of the Hg is particle-associated in these two samples. Gaulier et al. 2015[7] found less particulate Hg (~38% maximum) in crude oil and condensate samples. The difference is likely because samples analyzed here were crude tank bottom sediments that had been enriched in particulate phases containing Hg. It is also possible that the enrichment in particulate Hg species is a result of crude oil stabilizing that occurred prior to the sampling point. Stabilizing strips light gases and volatile Hg species, leaving behind primarily the non- volatile particulate β-HgS species found here. The samples analyzed by Gaulier et al. may not have been stabilized.

Thus, overall, the Hg associated with the sediments from stabilized crude oil or condensate is largely particulate in nature, mainly found as a β-HgS (about 80%) species with some amount of Hg associated to thiol groups (about 20%), but does not have a significant mass of elemental Hg. The Hg in these samples is also less oleophilic than the Hg species found dissolved in crude oils because it was not readily removed from the solids by extraction into toluene or dichloromethane (Table C.3).

Since we earlier showed that samples 4 and 6 contained Hg mainly in a particulate form, microscopy (SEM and TEM/EDS) was used to characterize the size of the particulate Hg in solids collected from the condensate holding tank in Southeast Asia (sample 6), and its association with other elements in the sample. This sample was selected because it had a high Hg concentration, making it possible to find the Hg particles in the sample. SEM (backscatter mode) indicated a significant number of

electron dense particles in this samples (SEM image in Figure C.2). These dense particles were associated with other solids and covered a wide range of particle sizes up to ~5 microns. Regions in this image showing high Hg concentrations were explored further using TEM. The dense Hg-rich regions appear to be aggregates of much smaller particles, ~<100nm (Figure C.2, BF). The precipitation of such nano-sized HgS particles has already been shown to occur in the presence of organic matter.[44] In all TEM images, the Hg was co-located with S. Additional regions were explored and all showed strong correlation of Hg and S (Supplementary Figures C.8 and C.9), which is consistent with the XAS findings of β-HgS being the major Hg phase in this sample. Moreover, these HgS nanoparticles were associated with Ba and sometimes Au (Supplementary Figures C.9 and C.10). Indeed, cinnabar (HgS) in the environment is rarely pure and is often associated with other trace elements, including gold[45] and (to a lesser extend) barium.[46] These HgS nanoparticles are embedded in a matrix made of C, O, Al, Si, Fe, As. Aluminosilicates participate in petroleum formation and maturation.[47] The association of As and Fe is also not surprising given the affinity of these elements with aluminosilicates.[48] Figure C.2 also suggest the presence of another phase enriched in Fe, O, As, and could be iron oxide particles with adsorbed arsenic.[49]

In summary, the predominant Hg species in all of the solids isolated from crude oil, and crude oil and condensate sediment samples evaluated here were mainly β-HgS, with Hg- thiol as a minor fraction. The aggregate particles are composed of small particles that are less than 100nm. Selection and development of methods to manage or treat these byproduct streams should consider the properties of β-HgS, namely the high stability against transformation and their nanoparticulate nature.

C.4.2.3. Glycol Dehydrator sediment Samples

The concentrations of Hg in the glycol dehydrator samples (samples 7 and 8) were lower than for most of the stabilized crude oil and condensate sediments (Table C.2). The speciation of Hg in sediment samples from two different glycol dehydrator units, one treating gas (sample 7) and the other treating condensate (sample 8), was determined using XAS (Figure C.1).

Unlike the Hg speciation in stabilized crude oil residue and oil and condensate sediments, the Hg species present in these dehydrator solids is mostly like the Hg-gluthatione model compound, and therefore predominantly $Hg(SR)_2$ species. However, about 24% of the Hg is also present as β-HgS (Table C.2) in both samples. The higher fraction of Hg present as Hg-$(SR)_2$ is most likely a result of the composition of Hg present in the incoming streams (gas vs. stabilized crude oil or condensate). Gas streams have a much larger fraction of mercury present as elemental Hg that can potentially oxidize and subsequently react with organic thiols to form $Hg(SR)_2$ species.[1] In contrast, stabilized crude oil and condensate contain primarily β-HgS species along with some organic $Hg(SR)_2$ species as discussed above. EXAFS analysis provided no evidence of elemental Hg in the samples despite slow cooling the samples in liquid N_2 to identify elemental Hg in the samples.[36] While elemental Hg may leave the dry gas and water streams exiting the dehydrator, the solids leaving the glycol dehydrator are comprised largely of $Hg(SR)_2$ with some β-HgS. Management of this byproduct stream should consider the $Hg(SR)_2$ speciation as it will behave differently in treatment systems and in the environment compared to β-HgS.

C.4.2.4. Selected Refinery Samples

Four samples were collected from the "downstream" oil refining process coming from two different refineries (A and B). Two were pipe scale samples collected from the overhead in a distillation column (sample 11 and 12), and two were biosludge samples from biological wastewater treatment of refinery process water (sample 9 and 10). One set of samples (9 and 11) come from refinery A that processes mostly sweet crudes (low sulfur content), while the second set of samples (10 and 12) come from refinery B that processes a mix of sweet and sour crude oil (i.e. higher sulfur content, and therefore also selenium). The EXAFS LCFs for these samples are also provided in Figure C.1 and Table C.2.

Biosludge samples both contained a majority of the β-HgS species and a small fraction of Hg-thiol (~15%) regardless of their origin. However, the biosludge coming from refinery B also had a significant fraction of Hg (~30%) associated with selenium. Pipe scale samples also predominantly contained β-HgS (72% in refinery A and 63% in B). However, the balance of the Hg species depended on the type of crude oil being processed. The remaining Hg species from pipe scale coming from refinery A (sweet crudes) was associated to chloride (27% HgCl), whereas the remaining Hg species in pipe scale from refinery B (mix of sweet and sour crudes) is Hg associated with HgSe (25%). This speciation is consistent with the greater amount of sulfur (and therefore selenium[50]) present in refinery B compared to refinery A. Given the very high affinity of Hg for Se ($K_{sp}=1x10^{-59}$), it is not surprising to observe HgSe in the pipe scale and in biosolids coming from refineries dealing with higher sulfur (and selenium) content crude oils.

C.4.3. Implications for Managing Hg in the Petroleum Value Chain

Analysis of Hg speciation in samples from the petroleum value chain reveals useful information about the species of Hg in stabilized oil and gas residues, the potential transformations of those species during oil and gas processing, and management options for Hg in the petroleum value chain. First, mercury in stabilized crude oil and condensate residues analyzed here is predominantly associated with the solids and is largely β-HgS. During stabilization, butane and other light gases are removed to meet vapor pressure specifications. The absence of elemental Hg in the samples analyzed suggests that nearly all elemental Hg is purged along with the gas phase during stabilization. With this knowledge of the Hg species in stabilized crude oil and condensate, recommendations can be made to develop and improve processes for Hg removal including filtration (e.g. [51,52]), oxidation followed by extraction into an aqueous phase (e.g. [53–55]), and extraction by sulfidic agents into an aqueous phase (e.g. [56]).

Mercury in glycol dehydrator streams from natural gas or condensate operations is different than in crude oil residue or sediment from crude oil and condensate tanks. The Hg speciation in solids from the glycol dehydrators is mostly $Hg(SR)_2$ species, but also contains some β-HgS. Therefore solids resulting from gas or condensate operations may contain more labile Hg species as compared to those in crude oil sediments. With this knowledge of mercury speciation in gas plants, modifications of approaches to manage mercury (e.g. [14,57]) can be made to continue improving their performance.

Much of the Hg remaining in stabilized crude oil is particle-associated $Hg(SR)_2$ compounds or nanoparticulate β-HgS. However, these particles settle in the crude storage tanks to form tank bottom sediment with elevated Hg concentrations of β-HgS. Particles are also removed in the desalter and transported to a wastewater treatment plant, where

they end up in tank bottoms and biosludge, still largely as β-HgS. The predominance of β-HgS in solids samples along the petroleum value chain is consistent with the high stability of β-HgS observed in environmental samples such as subaquatic sediments.[20,23,58]

Importantly, Hg in solids collected from downstream compartments (distillation column scale and biosludges) showed different speciation. This speciation can be related with the properties of the crude oil being processed. Sweet crudes resulted in solids without HgSe, but contained a reduced Hg species consistent with HgCl. Higher sulfur crudes had a mix of β-HgS and HgSe. The stability of HgSe and HgCl are different, indicating that Hg management strategies in downstream operations may also have to be adapted depending on the mix of crude oil being processed.

Overall, the improved understanding of the speciation of Hg in solids of byproduct streams provided this study, along with the known speciation of Hg species in crude oil and condensate prior to stabilization,[7,17] enables a comprehensive strategy for managing Hg in the petroleum value chain.

C.5. ACKNOWLEDGEMENTS

Portions of this research were carried out at the SSRL beamline 4-3 and 11-2, a national user facility operated by Stanford University on behalf of the U.S. Department of Energy, Office of Basic Energy Sciences. We thank Ryan Davis at SSRL (BL 4-3 and 11-2) for his support. This material is also based on work partially supported by the National Science Foundation (NSF) and the US Environmental Protection Agency (EPA) under NSF Cooperative Agreement EF-1266252, Center for the Environmental

Implications of Nanotechnology (CEINT). Any opinions, findings, conclusions or recommendations expressed in this material are those of the author(s) and do not necessarily reflect the views of the NSF or the EPA. This work has not been subjected to EPA review and no official endorsement should be inferred.

C.6. REFERENCES

(1) Carnell, P. J. H.; Foster, A.; Gregory, J. Mercury matters. *Hydrocarb. Eng.* **2005**, 10 (12), 37–40.

(2) Doll, B.; Knickerbocker, B. M.; Nucci, E. Industry Response to the UN Global Mercury Treaty Negotiations Focus on Oil and Gas; SPE/APPEA International Conference on Health, Safety, and Environment in Oil and Gas Exploration and Production; Society of Petroleum Engineers: Perth, Australia, 2012; Vol. SPE-157572-PP.

(3) Hollebone, B. P.; Yang, C. X. *Mercury in Crude Oil Refined in Canada*; Environment Canada: Ottawa, ON, 2007.

(4) UNEP. *Global Mercury Assessment 2013: Sources, Emissions, Releases and Environmental Transport*; UNEP Chemicals Branch: Geneva, Switzerland, 2013.

(5) Bloom, N. S. Analysis and stability of mercury speciation in petroleum hydrocarbons. *Fresenius J. Anal. Chem.* **2000**, 366 (5), 438–443.

(6) Dyrssen, D.; Wedborg, M. The sulphur-mercury(II) system in natural waters. *Water. Air. Soil Pollut.* **1991**, 56 (1), 507–519.

(7) Gaulier, F.; Gibert, A.; Walls, D.; Langford, M.; Baker, S.; Baudot, A.; Porcheron, F.; Lienemann, C.-P. Mercury speciation in liquid petroleum products: Comparison between on-site approach and lab measurement using size exclusion chromatography with high

resolution inductively coupled plasma mass spectrometric detection (SEC-ICP-HR MS). *Fuel Process. Technol.* **2015**, 131, 254–261.

(8) Schuster, E. The behavior of mercury in the soil with special emphasis on complexation and adsorption processes - A review of the literature. *Water. Air. Soil Pollut.* **1991**, 56 (1), 667–680.

(9) Schwarzenbach, G.; Widmer, M. Die Löslichkeit von Metallsulfiden I. Schwarzes Quecksilbersulfid. *Helv. Chim. Acta* **1963**, 46 (7), 2613–2628.

(10) Wilhelm, S. M.; Liang, L.; Kirchgessner, D. Identification and Properties of Mercury Species in Crude Oil. *Energy Fuels* **2006**, 20 (1), 180–186.

(11) Nriagu, J. O. *The Biogeochemistry of mercury in the environment*; Elsevier/North-Holland Biomedical Press, 1979.

(12) Lord, C. J.; Lambertsson, L. T.; Bjorn, E. L.; Frech, W.; Thomas, S. A. Removing mercury from crude oil. WO 2014143457 A1, September 18, 2014.

(13) Kim, C. S.; Bloom, N. S.; Rytuba, J. J.; Brown, G. E. Mercury speciation by X-ray absorption fine structure spectroscopy and sequential chemical extractions: a comparison of speciation methods. *Environ. Sci. Technol.* **2003**, 37 (22), 5102–5108.

(14) O'Rear, D. J.; Cooper, R. E.; Yean, S.; Gallup, D. L.; Young, L. A. Process, method, and system for removing mercury from fluids. US9023123 B2, May 5, 2015.

(15) O'Rear, D. J.; Cooper, R. E.; Yean, S.; Roby, S. H.; Mogaddedi, H.; Quintana, M. E.; Rovner, J. M. Process, method, and system for removing heavy metals from fluids. US8992769 B2, March 31, 2015.

(16) Pontes, F. V. M.; Carneiro, M. C.; Vaitsman, D. S.; Monteiro, M. I. C.; Neto, A. A.; Tristão, M. L. B. Investigation of the Grignard reaction and experimental conditions for

the determination of inorganic mercury and methylmercury in crude oils by GC–ICP-MS. *Fuel* **2014**, 116, 421–426.

(17) Snell, J. P.; Frech, W.; Thomassen, Y. Performance improvements in the determination of mercury species in natural gas condensate using an on-line amalgamation trap or solid-phase micro-extraction with capillary gas chromatography–microwave-induced plasma atomic emission spectrometry. *Analyst* **1996**, 121 (8), 1055–1060.

(18) Barnett, M. O.; Harris, L. A.; Turner, R. R.; Stevenson, R. J.; Henson, T. J.; Melton, R. C.; Hoffman, D. P. Formation of Mercuric Sulfide in Soil. *Environ. Sci. Technol.* **1997**, 31 (11), 3037–3043.

(19) Harris, L. A.; Henson, T. J.; Combs, D.; Melton, R. E.; Steele, R. R.; Marsh, G. C. Imaging and microanalyses of mercury in flood plain soils of east fork poplar creek. *Water. Air. Soil Pollut.* **1996**, 86 (1–4), 51–69.

(20) Kim, C. S.; Brown Jr., G. E.; Rytuba, J. J. Characterization and speciation of mercury- bearing mine wastes using X-ray absorption spectroscopy. *Sci. Total Environ.* **2000**, 261 (1–3), 157–168.

(21) Lowry, G. V.; Shaw, S.; Kim, C. S.; Rytuba, J. J.; Brown, G. E. Macroscopic and microscopic observations of particle-facilitated mercury transport from New Idria and Sulphur Bank mercury mine tailings. *Environ. Sci. Technol.* **2004**, 38 (19), 5101–5111.

(22) Revis, N. W.; Osborne, T. R.; Holdsworth, G.; Hadden, C. Distribution of mercury species in soil from a mercury-contaminated site. *Water. Air. Soil Pollut.* **1989**, 45 (1–2), 105–113.

(23) Slowey, A. J.; Rytuba, J. J.; Brown, G. E. Speciation of Mercury and Mode of Transport from Placer Gold Mine Tailings. *Environ. Sci. Technol.* **2005**, 39 (6), 1547–1554.

(24) Belzile, N.; Lang, C.-Y.; Chen, Y.-W.; Wang, M. The competitive role of organic carbon and dissolved sulfide in controlling the distribution of mercury in freshwater lake sediments. *Sci. Total Environ.* **2008**, 405 (1–3), 226–238.

(25) Drott, A.; Lambertsson, L.; Björn, E.; Skyllberg, U. Importance of Dissolved Neutral Mercury Sulfides for Methyl Mercury Production in Contaminated Sediments. *Environ. Sci. Technol.* **2007**, 41 (7), 2270–2276.

(26) Liu, G.; Cai, Y.; O'Driscoll, N. *Environmental Chemistry of Mercury*; Wiley, 2012.

(27) Wolfenden, S.; Charnock, J. M.; Hilton, J.; Livens, F. R.; Vaughan, D. J. Sulfide Species as a Sink for Mercury in Lake Sediments. *Environ. Sci. Technol.* **2005**, 39 (17), 6644–6648.

(28) Zhong, H.; Wang, W.-X. Inorganic mercury binding with different sulfur species in anoxic sediments and their gut juice extractions. *Environ. Toxicol. Chem. SETAC* **2009**, 28 (9), 1851–1857.

(29) Morel, F. M. M.; Kraepiel, A. M. L.; Amyot, M. The Chemical Cycle and Bioaccumulation of Mercury. *Annu. Rev. Ecol. Syst.* **1998**, 29 (1), 543–566.

(30) Ullrich, S. M.; Tanton, T. W.; Abdrashitova, S. A. Mercury in the Aquatic Environment: A Review of Factors Affecting Methylation. *Crit. Rev. Environ. Sci. Technol.* **2001**, 31 (3), 241–293.

(31) Cai, C.; Worden, R. H.; Bottrell, S. H.; Wang, L.; Yang, C. Thermochemical sulphate reduction and the generation of hydrogen sulphide and thiols (mercaptans) in

Triassic carbonate reservoirs from the Sichuan Basin, China. *Chem. Geol.* **2003**, 202 (1–2), 39–57.

(32) Nagy, K. L.; Manceau, A.; Gasper, J. D.; Ryan, J. N.; Aiken, G. R. Metallothionein-Like Multinuclear Clusters of Mercury(II) and Sulfur in Peat. *Environ. Sci. Technol.* **2011**, 45 (17), 7298–7306.

(33) Skyllberg, U. Competition among thiols and inorganic sulfides and polysulfides for Hg and MeHg in wetland soils and sediments under suboxic conditions: Illumination of controversies and implications for MeHg net production. *J. Geophys. Res. Biogeosciences* **2008**, 113 (G2), G00C03.

(34) Pinedo-Hernández, J.; Marrugo-Negrete, J.; Díez, S. Speciation and bioavailability of mercury in sediments impacted by gold mining in Colombia. *Chemosphere* **2015**, 119, 1289–1295.

(35) Yu, X.; Li, H.; Pan, K.; Yan, Y.; Wang, W.-X. Mercury distribution, speciation and bioavailability in sediments from the Pearl River Estuary, Southern China. *Mar. Pollut. Bull.* **2012**, 64 (8), 1699–1704.

(36) Jew, A. D.; Kim, C. S.; Rytuba, J. J.; Gustin, M. S.; Brown, G. E. New Technique for Quantification of Elemental Hg in Mine Wastes and Its Implications for Mercury Evasion Into the Atmosphere. *Environ. Sci. Technol.* **2011**, 45 (2), 412–417.

(37) Webb, S. M. SIXPack a Graphical User Interface for XAS Analysis Using IFEFFIT. *Phys. Scr.* **2005**, 1011.

(38) Caumette, G.; Lienemann, C.-P.; Merdrignac, I.; Bouyssiere, B.; Lobinski, R. Element speciation analysis of petroleum and related materials. *J. Anal. At. Spectrom.* **2009**, 24 (3), 263–276.

(39) Singh, B.; Grafe, M. *Synchrotron-based Techniques in Soils and Sediments*; Elsevier, 2010.

(40) Doelsch, E.; Basile-Doelsch, I.; Rose, J.; Masion, A.; Borschneck, D.; Hazemann, J.-L.; Macary, H. S.; Bottero, J.-Y. New combination of EXAFS spectroscopy and density fractionation for the speciation of chromium within an andosol. *Environ. Sci. Technol.* **2006**, 40 (24), 7602–7608.

(41) Charnock, J. M.; Moyes, L. N.; Pattrick, R. A. D.; Mosselmans, J. F. W.; Vaughan, D. J.; Livens, F. R. The structural evolution of mercury sulfide precipitate: an XAS and XRD study. *Am. Mineral.* **2003**, 88 (8–9), 1197–1203.

(42) Warner, T.; Jalilehvand, F. Formation of Hg(II) Tetrathiolate Complexes with Cysteine at Neutral pH. *Can. J. Chem.* **2016**, 94 (4), 373–379.

(43) Manceau, A.; Nagy, K. L. Relationships between Hg(II)–S bond distance and Hg(II) coordination in thiolates. *Dalton Trans.* **2008**, No. 11, 1421–1425.

(44) Pham, A. L.-T.; Morris, A.; Zhang, T.; Ticknor, J.; Levard, C.; Hsu-Kim, H. Precipitation of nanoscale mercuric sulfides in the presence of natural organic matter: Structural properties, aggregation, and biotransformation. *Geochim. Cosmochim. Acta* **2014**, 133, 204–215.

(45) Becker, G. F. Natural solutions of cinnebar, gold, and associated sulphides. *Am. J. Sci*. **1887**, s3-33 (195), 199–210.

(46) Tomashyk, V. *Quaternary Alloys Based on II - VI Semiconductors*; CRC Press., 2014.

(47) Johns, W. D. Clay mineral catalysis and petroleum generation. *Annu. Rev. Earth Planet. Sci.* **1979**, 7, 183–198.

(48) Garcıa-Sánchez, A.; Alastuey, A.; Querol, X. Heavy metal´ adsorption by different minerals: application to the remediation of polluted soils. *Sci. Total Environ.* **1999**, (1–3), 179–188.

(49) Dixit, S.; Hering, J. G. Comparison of Arsenic(V) and Arsenic(III) Sorption onto Iron Oxide Minerals: Implications for Arsenic Mobility. *Environ. Sci. Technol.* **2003**, 37 (18), 4182– 4189.

(50) Meng, X.; Bang, S.; Korfiatis, G. P. Removal of selenocyanate from water using elemental iron. *Water Res.* **2002**, 36 (15), 3867–3873.

(51) Cooper, R. E.; O'Rear, D. J.; Yean, S.; Odueyungbo, S. A. Process, method, and system for removing heavy metals from fluids. US9023196B2, May 5, 2015.

(52) Frankiewicz, T. C.; Gerlach, J. Process for removing mercury from liquid hydrocarbons. US6537443 B1, March 25, 2003.

(53) Gallup, D. L.; Yean, S. Process, method, and system for removing heavy metals from fluids. US8728304 B2, May 20, 2014.

(54) Yean, S.; Gallup, D. L. Process, method, and system for removing heavy metals from fluids. US8673133 B2, March 18, 2014.

(55) Young, L.; Gallup, D. L.; Yean, S.; O'Rear, D. J. Process, method, and system for removing heavy metals from fluids. US8728303 B2, May 20, 2014.

(56) Cooper, R. E.; O'Rear, D. J.; Gallup, D. L.; Young, L. A.; Yean, S. Process, method, and system for removing mercury from fluids. US9023123, May 5, 2015.

(57) O'Rear, D. J.; Cooper, R. E.; Sheu, F.-R.; Belue, J. T. Process, method, and system for removing mercury from fluids. US8790427 B2, July 29, 2014.

(58) Cooke Andrews, J. Mercury Speciation in the Environment Using X-ray Absorption Spectroscopy. In *Recent Developments in Mercury Science*; Atwood, D. A., Ed.; Structure and Bonding; Springer Berlin Heidelberg, 2006; pp 1–35.

C.7. FIGURES

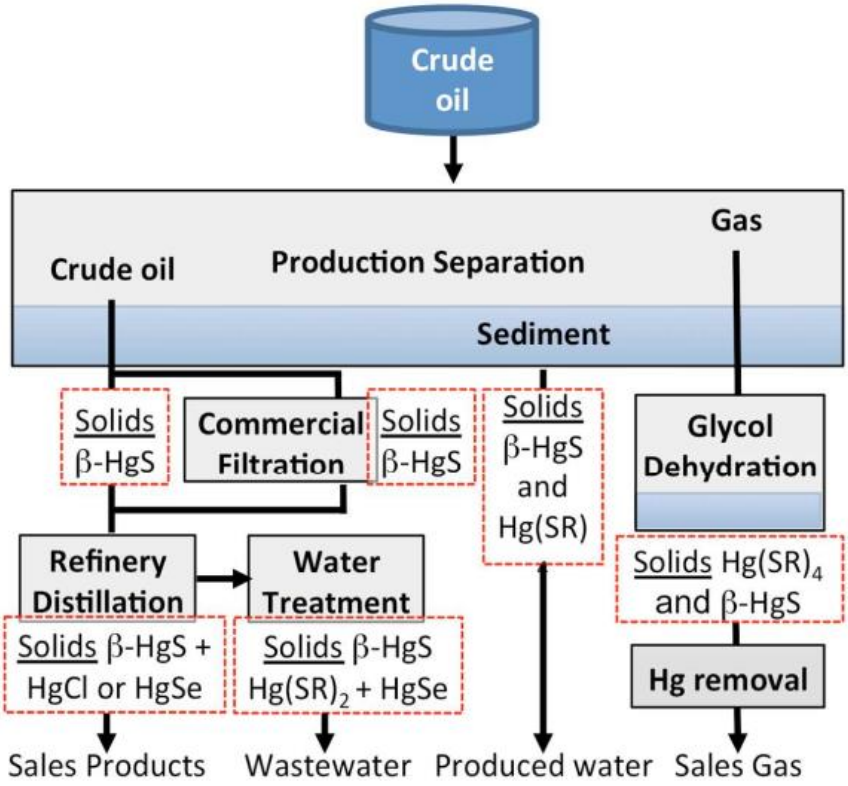

Figure C.0. Abstract figure.

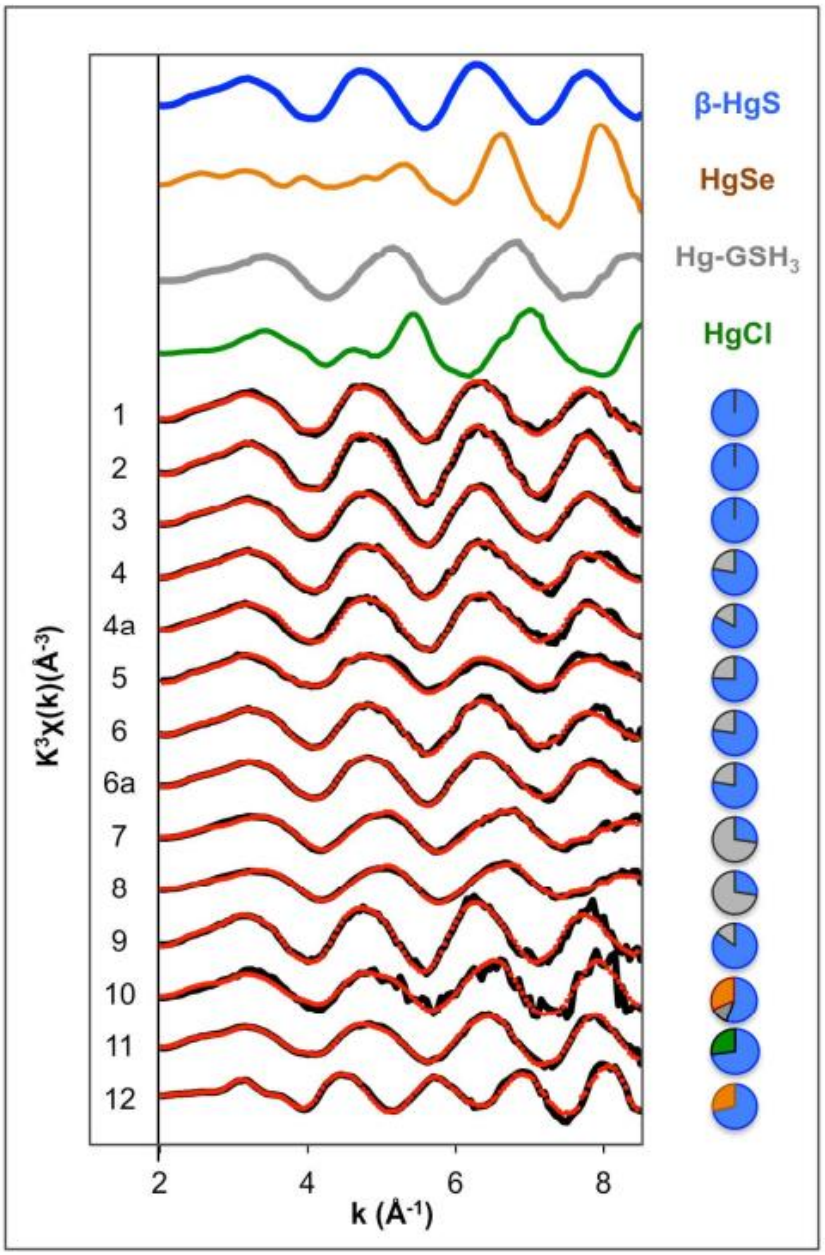

Figure C.1. EXAFS spectra $k^3\chi(k)$ at Hg-L(III) edge of reference compounds β-HgS (metacinnabar), HgSe, Hg-GSH_3 (Hg bounded to glutathione), HgCl, and of samples 1 to 11 (coming from different compartments of the petroleum value chain). 4a and 6a samples were solvent washed. Experimental (black line) and calculated signal (red dotted line) are shown. Blue/grey diagrams are representing the fraction of β-HgS (blue), Hg-GSH_3 (grey) or HgSe (orange) leading to the best linear combination fit results (see Table C.2 for fit details and statistics).

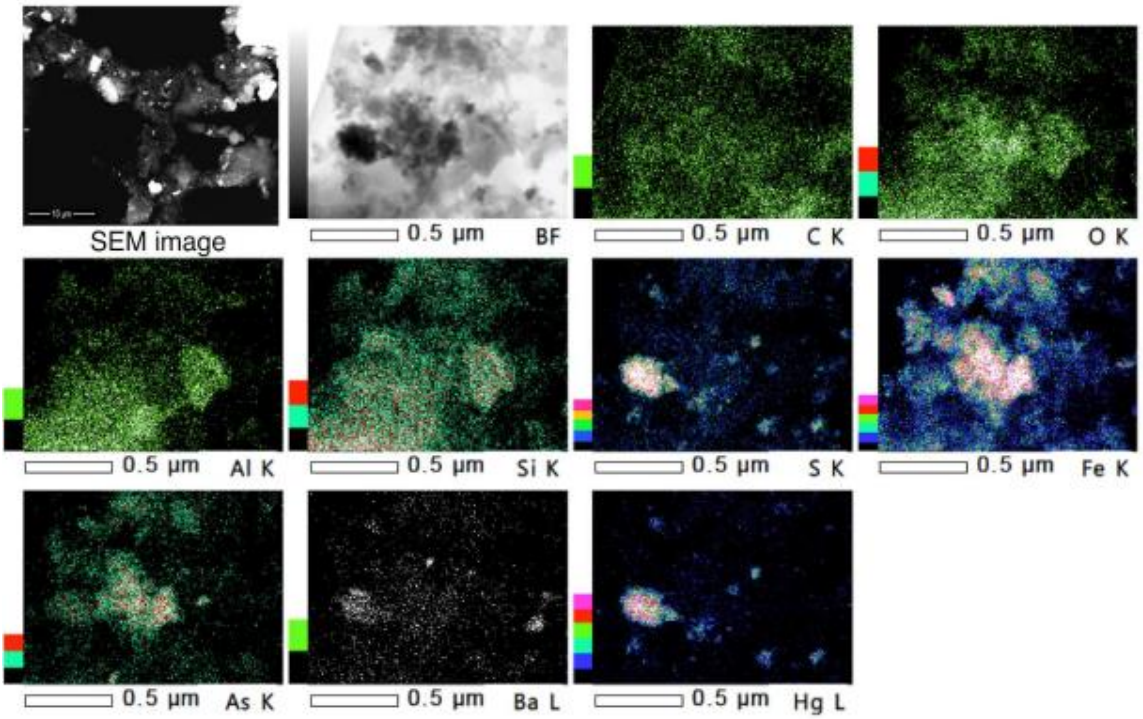

Figure C.2. SEM backscatter image showing a large number of electron dense particles present in the condensate sediment sample (Sample 6). TEM image and K fluorescence emission of C, O, Al, Si, S, Fe, As and L fluorescence emission of B and Hg.

C.8. TABLES

Table C.1. Samples collected from different points in the petroleum value chain (see Supplementary Figure C.1 for more details).

No.	Type	Origin	Fractionation or treatment	
1	Crude oil residue[a]	N. America	Centrifugation of solids from oil samples	
2		SE Asia		
3		S. America		
4	Crude sediment	SE Asia	Sediment 1	Whole
4a		SE Asia		Solvent Washed
5	Condensate sediment	SE Asia	Sediment 2	Whole
6		SE Asia	Sediment 3	Whole
6a		SE Asia		Solvent Washed
7	Glycol Sediments	SE Asia	Sludge-1	Gas-glycol treated
8		SE Asia	Sludge-2	Condensate-glycol treated
9	Refinery	A	Biosludge from water treatment	
10		B	Biosludge from water treatment	
11		A	Pipe Scale from refinery distillation	
12		B	Pipe Scale from refinery distillation	

[a]Crude oil residue samples were concentrated in Hg by centrifugation, they are thus referred to as crude oil residue rather than crude oil.

Table C.2. Hg concentration and speciation in samples collected along the petroleum value chain.

Sample			$[Hg]_{total}$ (ppm) [a]	Speciation assessed by linear combination fit on k^3-wheigted EXAFS spectra						
#	Type	Characteristics		β-HgS (%)	Hg-GSH_3 (%)	HgSe (%)	HgCl (%)	Total (%)	R_f [b]	χ^2 [b]
1	Crude oil residue		12,400	91 ±14	0	0	0	91 ±14	0.03	8.11
2			60	116 ±17	0	0	0	116 ±17	0.03	14.1
3			1,475±25	93 ±14	0	0	0	93 ±14	0.03	8.74
4	Crude sediment	Whole	190±0	80 ±12	23 ±4	0	0	103 ±15	0.04	10.44
4a		Toluene washed	55±3	85 ±13	18 ±3	0	0	103 ±15	0.05	16.15
5	Condensate sediment	Whole	63±9	62 ±9	20 ±3	0	0	82 ±12	0.07	8.64
6		Whole	10,804±1590	78 ±12	23 ±4	0	0	101 ±15	0.04	9.56
6a		CH_2Cl_2 Washed	26,737±310	76 ±11	22 ±3	0	0	98 ±15	0.02	3.91
7	Glycol sediments	Gas-glycol	1,314±270	24 ±4	64 ±10	0	0	88 ±13	0.04	6.14
8		Condensate-glycol	653±128	23 ±4	61 ±9	0	0	84 ±13	0.03	3.87
9	Refinery	Wastewater Biosludg A	13±1	103 ±16	18 ±3	0	0	121 ±18	0.04	15.6
10		Wastewater Biosludge B	112±22	56 ±8	13 ±2	32 ±5	0	101 ±15	0.15	45.7
11		Pipe scale A	14,133	72±4	0	0	27±5	99±9	0.05	3.69
12		Pipe scale B	4,056±52	63±9	0	25 ±4	0	88 ±13	0.02	5.12

[a] Samples without standard deviations were measured using an OHIO Lumex. The ones with standard deviations were measured by method 1631 in duplicate. The concentration measurement on sample 2 was made before centrifugation.

[b] R_f (R-factor) and χ^2 values are quality factors

Table C.3. Mercury Concentrations in the Solid and Oil Phases of the crude oil tank sediment and the condensate tank sediment.

No	Type	Fractionation		Total [Hg] (ppm)	
				20 °C	50 °C
4	Crude oil sediment	whole		190±0	127 ±26
4a		Sediment Washed	Oil (18%[a] w/w)	79.2 ±2	
			Solids (82% w/w)	134.2 ±2	
			0.02 micron filtrate	BD	
6	Condensate Sediment	-whole		10,804 ±1590	10,164 ±3325
6a		Sediment Washed	Oil (59% w/w)	362 ±14	
			Solids (41% w/w)	26,767 ±310	
			0.02 micron filtrate	$1.4x10^{-3}$ $\pm 0.9x10^{-3}$	

BD-below the detection limit of $0.05ng.L^{-1}$.